



Nuclear shell effects in neutron-rich nuclei around $N = 20$ and $N = 32,34$

Inaugural-Dissertation

zur Erlangung des Doktorgrades
der Mathematisch-Naturwissenschaftlichen Fakultät
der Universität zu Köln

vorgelegt von

Michael Seidlitz
aus Hachenburg

Köln – 2012

Berichterstatter:

Prof. Dr. P. Reiter
Prof. Dr. A. Zilges

Tag der mündlichen Prüfung:

04.12.2012

The works of the LORD are great,
sought out of all them that have
pleasure therein.

THE HOLY BIBLE, Psalm 111:2

Abstract

Nuclear shell effects in neutron-rich nuclei around $N = 20$ and $N = 32, 34$ were studied by means of reduced transition probabilities, i.e. $B(E2)$ and $B(M1)$ values. To this end a series of Coulomb-excitation experiments, employing radioactive ^{31}Mg and $^{29,30}\text{Na}$ beams, as well as a precise lifetime experiment of excited states in ^{56}Cr were performed.

The collective properties of excited states of ^{31}Mg were the subject of a Coulomb-excitation experiment at REX-ISOLDE, CERN, employing a radioactive ^{31}Mg beam at a beam energy of 3.0 MeV/u. The beam intensity amounted to 3000 ions/s on average. The highly efficient MINIBALL setup was employed, consisting of eight HPGe cluster detectors for γ -ray detection and a segmented Si-detector for coincident particle detection. The level scheme of ^{31}Mg was extended. Spin and parity assignment of the observed 945 keV state yielded $5/2^+$ and its de-excitation is dominated by a strong collective $M1$ transition. Comparison of the transition probabilities of $^{30,31,32}\text{Mg}$ establishes that for the $N = 19$ magnesium isotope not only the ground state but also excited states are largely dominated by a deformed pf intruder configuration. This implies that ^{31}Mg is part of the so-called “island of inversion”.

Coulomb-excitation experiments of radioactive $^{29,30}\text{Na}$ were carried out at REX-ISOLDE, CERN, at a final beam energy of 2.85 MeV/u. De-excitation γ rays were detected by the MINIBALL γ -ray spectrometer in coincidence with scattered particles in a segmented Si-detector. Despite rather low beam intensities transition probabilities to the first excited states were deduced. Results of very recently published experiments at MSU and TRIUMF could be largely confirmed and extended. The measured $B(E2)$ values agree well with shell-model predictions, supporting the idea that in the sodium isotopic chain the ground-state wave function contains a significant intruder admixture already at $N = 18$, with $N = 19$ having an almost pure $2p2h$ deformed ground-state configuration.

Excited states in ^{56}Cr have been populated after $^{48}\text{Ca}(^{11}\text{B}, p2n)$ reactions at a beam energy of 32 MeV, provided by the Cologne FN tandem accelerator. The Cologne coincidence plunger device surrounded by a γ -ray detector array of one EUROBALL cluster detector and five Ge detectors was employed to determine lifetimes with the recoil distance Doppler-shift method. $\gamma\gamma$ -coincidence data were analyzed using the differential decay curve method and precise lifetimes for the first 2^+ and 4^+ states were extracted. The corresponding $B(E2, 2^+ \rightarrow 0^+)$ value quantifies with a high accuracy the puzzling discrepancy between experimental $B(E2)$ values in $N = 32$ isotones and theoretical results from large-scale shell-model calculations employing modern effective nucleon-nucleon interactions.

Kurzzusammenfassung

Effekte in der Schalenstruktur neutronenreicher Kerne um $N = 20$ und $N = 32, 34$ wurden anhand der reduzierten Übergangswahrscheinlichkeiten, d.h. ihrer $B(E2)$ - und $B(M1)$ -Werte, untersucht. Dafür wurden eine Reihe von Coulombanregungsexperimenten mit radioaktiven ^{31}Mg - und $^{29,30}\text{Na}$ -Strahlen, sowie eine hochgenaue Lebensdauerermessung angeregter Kernzustände in ^{56}Cr durchgeführt.

Die Untersuchung kollektiver Eigenschaften angeregter Kernzustände in ^{31}Mg waren Bestandteil eines Experiments zur Coulombanregung von instabilen ^{31}Mg -Ionen an REX-ISOLDE, CERN, bei einer Strahlenergie von 3.0 MeV/u. Die Strahlintensität betrug durchschnittlich rund 3000 ions/s. Die Messung wurde am hocheffizienten MINIBALL-Aufbau durchgeführt, bestehend aus acht HPGe Cluster-Detektoren zum Nachweis von γ -Quanten und einem segmentierten Si-Zähler zur Detektion koinzidenter Teilchen. Das Termschema von ^{31}Mg konnte somit erweitert werden. Einem beobachteten Zustand bei 945 keV konnten die Spin- und Paritätswerte $5/2^+$ zugewiesen werden. Der Zerfall dieses angeregten Zustands wird durch einen stark kollektiven $M1$ -Übergang dominiert. Der Vergleich der Übergangswahrscheinlichkeiten in den Kernen $^{30,31,32}\text{Mg}$ belegt, dass im Magnesium-Isotop mit $N = 19$ nicht nur der Grundzustand, sondern auch angeregte Zustände weitestgehend von deformierten pf -Intruderkonfigurationen beherrscht werden. Damit ist ^{31}Mg Teil der so genannten „Island of Inversion“.

Experimente zur Coulombanregung von radioaktiven $^{29,30}\text{Na}$ -Ionen in inverser Kinematik wurden an REX-ISOLDE, CERN, bei einer Strahlenergie von 2.85 MeV/u durchgeführt. γ -Strahlung aus der Abregung angeregter Kernzustände wurde vom MINIBALL-Spektrometer in Koinzidenz mit gestreuten Teilchen in einem segmentierten Si-Detektor nachgewiesen. Trotz recht geringer Strahlintensitäten konnten die Übergangswahrscheinlichkeiten zu den ersten angeregten Zuständen bestimmt werden. Ergebnisse erst kürzlich veröffentlichter Experimente an MSU und TRIUMF konnten weitestgehend bestätigt, teilweise sogar noch erweitert werden. Die gemessenen $B(E2)$ -Werte stimmen gut mit den Vorhersagen aus dem Schalenmodell überein. Dies unterstützt die Vorstellung, dass in der Isotopenkette von Na die Wellenfunktion des Grundzustands bereits bei $N = 18$ einen signifikanten Intruder-Anteil besitzt. Für $N = 19$ ergibt sich eine fast reine, deformierte $2p2h$ -Konfiguration im Grundzustand.

Angeregte Kernzustände in ^{56}Cr wurden durch die Reaktion $^{48}\text{Ca}(^{11}\text{B}, p2n)$ bei einer Strahlenergie von 32 MeV am Kölner FN Tandembeschleuniger bevölkert. Der Kölner Koinzidenzplunger ermöglichte die Bestimmung von Lebensdauern mithilfe der so genannten „recoil distance Doppler-shift“ (RDDS) Methode. Emittierte γ -Quanten wurden mit einer Anordnung von einem EUROBALL-Cluster-Detektor und fünf weiteren Ge-Detektoren nachgewiesen. Die aufgenommenen $\gamma\gamma$ -Koinzidenzen wurden anhand der so genannten „differential decay curve“ (DDC) Methode ausgewertet. Präzise Lebensdauern des jeweils ersten angeregten 2^+ und 4^+ Zustands konnten so bestimmt werden. Der entsprechende $B(E2, 2^+ \rightarrow 0^+)$ Wert zeigt mit hoher Präzision die bislang ungelöste Diskrepanz zwischen den experimentell bestimmten $B(E2)$ Werten der $N = 32$ Isotone und theoretischen Vorhersagen aktueller Schalenmodellrechnungen auf, trotz Einbeziehung eines größtmöglichen Modellraums und modernen effektiven Wechselwirkungen zwischen den einzelnen Nukleonen.

Contents

Abstract	v
Kurzzusammenfassung	vii
1 Nuclear structure	1
1.1 The nuclear shell model	1
1.2 The nuclear mean field	3
1.3 Residual interaction	3
1.4 Experimental observables	4
1.4.1 Nuclear masses and binding energies	4
1.4.2 Two-neutron separation energies	5
1.4.3 Ground-state nuclear moments	5
1.4.4 The $E(2^+)$ and $B(E2, 0^+ \rightarrow 2^+)$ strength	6
I Mapping the border of the “Island of Inversion” – Coulomb excitation of exotic Na and Mg isotopes with MINIBALL at REX-ISOLDE	9
2 Motivation and physics case	11
2.1 Vanishing of the $N = 20$ shell gap – the island of inversion	11
2.2 The neutron-rich Mg isotopes	12
2.3 The neutron-rich Na isotopes	15
3 The experimental setup and technique	21
3.1 Introduction	21
3.2 The ISOLDE facility	22
3.2.1 Production of radioactive isotopes	22
3.2.2 Ion sources	24
3.2.3 Mass separation	25
3.3 REX-ISOLDE	26
3.3.1 Charge breeding system	26
3.3.2 The REX-LINAC	28
3.4 The MINIBALL setup	29
3.4.1 The MINIBALL γ -ray spectrometer	30
3.4.2 Particle detectors	31
3.5 Time structure of the beam at REX-ISOLDE	33
3.6 Coulomb excitation	33
3.6.1 Semi-classical approach	34
3.6.2 “Safe” Coulomb excitation	38
3.6.3 Relative measurement of the transition strength	38

4	Data analysis	39
4.1	Acquisition and processing of the data	39
4.2	Detector calibration	39
4.2.1	Energy calibration of the DSSSD	39
4.2.2	Energy- and efficiency calibration of the MINIBALL detectors	40
4.3	Doppler correction	42
4.4	Kinematic considerations	45
4.5	Beam composition	45
4.5.1	Release curve analysis	46
4.5.2	β -decay during charge breeding	48
4.5.3	Measurements with the ionization chamber	49
4.5.4	Measurements with the Bragg detector	50
4.5.5	Measurements with laser ON/OFF	50
4.5.6	Summary of the experimental beam parameters	51
4.6	Particle- γ coincidence	53
5	Results	55
5.1	Coulomb excitation of ^{31}Mg	55
5.1.1	Measurement at 3.0 MeV/u on a 4.0 mg/cm ² thick ^{109}Ag target	55
5.1.2	Measurement at 3.0 MeV/u on a 1.9 mg/cm ² thick ^{109}Ag target	61
5.2	Coulomb excitation of ^{29}Na	63
5.2.1	Measurement at 2.85 MeV/u on a 4.1 mg/cm ² thick ^{104}Pd target	63
5.3	Coulomb excitation of ^{30}Na	67
5.3.1	Measurement at 2.85 MeV/u on a 4.0 mg/cm ² thick ^{120}Sn target	67
5.3.2	Measurement at 2.85 MeV/u on a 4.1 mg/cm ² thick ^{104}Pd target	69
5.3.3	Measurement at 2.83 MeV/u on a 3.6 mg/cm ² thick ^{104}Pd target	73
6	Discussion and Summary	75
6.1	Discussion	75
6.2	Summary	78
7	Outlook	79
7.1	The HIE-ISOLDE project	79
7.2	Coulomb excitation of $^{32,33}\text{Mg}$	79
II	Investigating the subshell closure at N = 32 – Lifetime measurements in the neutron-rich isotope ^{56}Cr with the Cologne plunger	83
8	Motivation and physics case	85
8.1	Evolution of a neutron shell gap at N = 32,34	85
8.2	The neutron-rich Ca, Ti, and Cr isotopes	86
9	The experimental setup and technique	91
9.1	Beam production	91
9.2	The Cologne FN tandem Van de Graaff accelerator	91
9.3	The Cologne plunger setup	92
9.3.1	The Cologne plunger device	92
9.3.2	γ -ray detector setup	93
9.4	Lifetime measurements with a plunger	94
9.4.1	The recoil distance Doppler-shift method	94

9.4.2 $\gamma\gamma$ -coincidences and the differential decay curve method	95
10 Data analysis	97
10.1 Acquisition and processing of the measured data	97
10.2 Calibration measurements	97
10.2.1 Energy calibration of the HPGe detectors	97
10.2.2 Efficiency calibration of the HPGe detectors	98
10.2.3 Time gate for $\gamma\gamma$ -coincidences	98
10.3 Distance calibration of the plunger foils	99
10.4 Yield normalization	99
10.5 Recoil velocity	100
11 Results	103
11.1 Lifetime of the 2^+ state	104
11.2 Lifetime of the 4^+ state	105
12 Discussion and Summary	111
12.1 Shell-model theory and discussion	111
12.2 Summary	112
Bibliography	115
Acknowledgments	123
Erklärung	125
Curriculum vitae	127

Chapter 1

Nuclear structure

1.1 The nuclear shell model

Already during the early 1930s detailed studies of atomic nuclei revealed special numbers of protons and neutrons, that lead to a stabilization of the corresponding nuclei in the isotopic or isotonic chains [1]. Only the first numbers 2, 8, and 20 could be explained by a simple model of non-interacting nucleons, moving independently in an average potential well. An appropriate explanation for the higher numbers failed. The first explanation of all of these so called “magic numbers” 2, 8, 20, 28, 50, 82, and 126 was given by Haxel, Jensen, Suess, and independently by Goeppert-Mayer in 1949, which proposed a strong spin-orbit component of the nucleon-nucleon interaction [2,3]. Every level is split into two orbits with total angular momenta $j = \ell \pm s$ (see Figure 1.1). By this method, nuclear properties on many nuclei reachable at that time, e.g. spins, parities, magnetic moments, and β -decay systematics, could be explained and the model became known as the “nuclear shell model”.

Even today, more than 60 years later, shell structure is one of the most important frameworks for understanding nuclear structure and the properties of atomic nuclei. Special interest has been focused on the evolution of nuclear properties along isotopic or isotonic chains in the vicinity of the magic numbers. It was believed that these magic numbers would be permanent and valid for all nuclei. During the last three decades both experimental and theoretical findings indicated that the known magic numbers are subject to the proton-to-neutron ratio and not universal. Especially for exotic nuclei with large N/Z ratios far from stability new shell closures are expected. Such a new magic

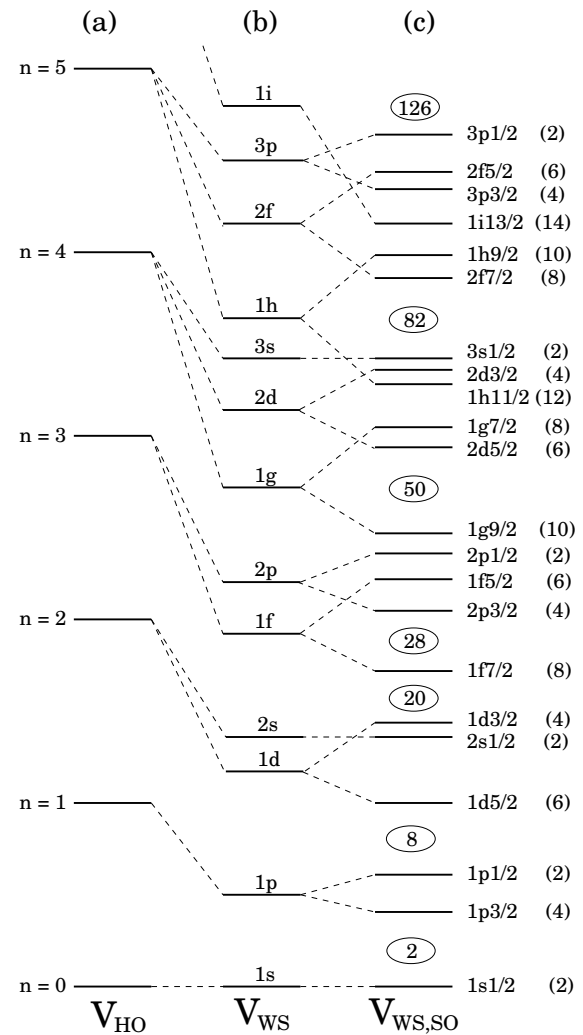


Figure 1.1: Single particle states in the nuclear shell model. (a) Non-interacting nucleons in the potential well of a harmonic oscillator. (b) Breakup of the ℓ -degeneracy using a Woods-Saxon potential. (c) Due to the spin-orbit coupling orbits are split into $j = \ell \pm s$ and the magic numbers can be reproduced. The figure was adapted from [4].

number was proposed at $N = 16$ for some nuclei between $Z = 8$ (oxygen) and $Z = 14$ (sili-

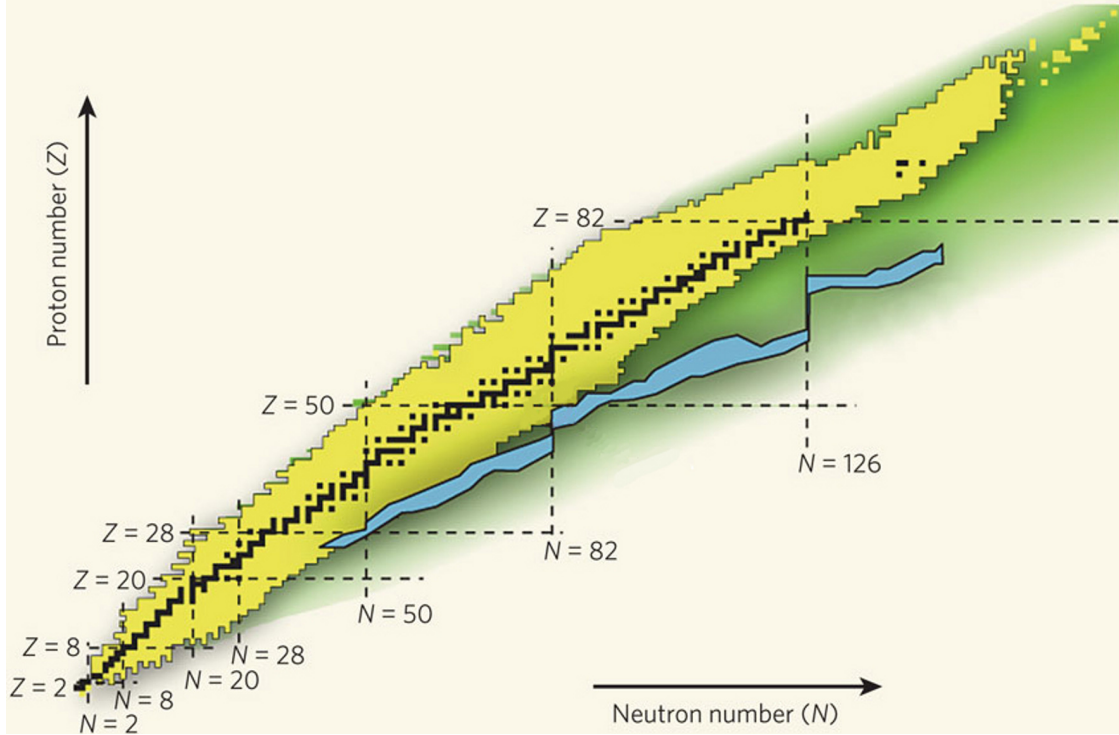


Figure 1.2: The chart of nuclides. Black boxes indicate stable nuclides, whereas the known unstable isotopes are colored in yellow. The region colored in green indicates all nuclides, that are believed to exist but have not been observed yet (“terra incognita”). Blue boxes mark the isotopes that may be produced by nucleosynthesis in the *r*-process. The classical magic numbers are denoted by dashed lines, even though they might change for exotic nuclei (adapted from [10]).

con) [5–7] and confirmed in a series of experiments and most recently by Kanungo *et al.*, that revealed the doubly magic character of ^{24}O [8].

The evolution of nuclear shells for very exotic nuclei is important for the understanding of astrophysical processes. Most elements heavier than Fe are produced in very rapid or even explosive scenarios (e.g. supernovae) by neutron captures and subsequent β -decays. For high neutron densities $n_n > 10^{20} \text{ cm}^{-3}$ nucleosynthesis of very neutron-rich takes place via the so-called *r*-process [9]. A sequence of fast neutron captures generates isotopes with high N/Z -ratios far from stability (see Fig. 1.2). Depending on the nuclear structure of the isotopes involved in the process, the resulting abundances will show a certain structure. In fact the solar *r*-abundance of nuclei is mainly dominated by decay products of the so-called “waiting point” nuclei at the neutron shell closures at $N = 50, 82, 126$ (see Fig. 1.3). The relatively long lifetimes of these nuclei delay the progression of the *r*-process. Recent experiments

with the $N = 82, 126$ waiting point nuclei have shown that changes in the shell structure – such

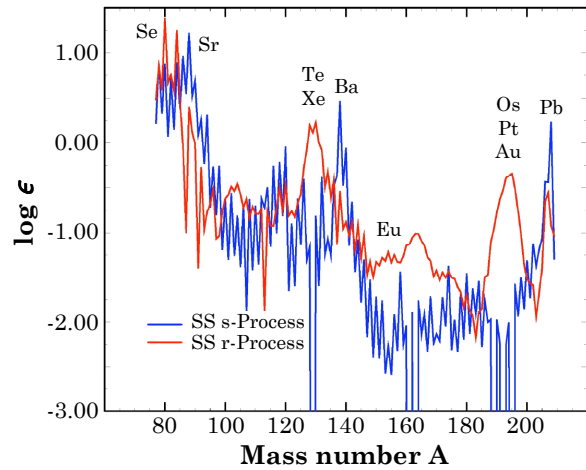


Figure 1.3: Abundances of nuclides in the solar system, depending on their synthesis mechanism: *s*- and *r*-process. The peak-like structure in the *r*-abundance is caused by the “waiting point” nuclei at the neutron shell closures. Some elements corresponding to the approximate mass numbers are noted (adapted from [11]).

as shell quenching – affect the r -abundances in that region significantly [12–14].

The shell-model modifications and the occurrence of new magic numbers are traced back to the residual nucleon-nucleon interaction.

1.2 The nuclear mean field

The atomic nucleus is a complex system of A strongly interacting quantum particles. Shell-model calculations, using accurate two-body and three-body interactions by QCD or *ab initio* approaches, have been performed for light nuclei with $2 \leq A \leq 16$ to study their structure and reactions. Due to the enormous computing power that would be required to study heavier nuclei truncations and approximative solutions have to be used in order to reduce the computed model space.

The Hamiltonian for A interacting nucleons can be written as a sum over the kinetic energy terms T_i and the two-body nucleon-nucleon (NN) interaction V_{ij} . Based on the superposition of all NN interactions the last term can be approximated by an effective average single-particle potential $U(\vec{r})$:

$$\begin{aligned} H &= \sum_{i=1}^A T_i + \sum_{i<j} V_{ij} \\ &= \sum_{i=1}^A (T_i + U(\vec{r}_i)) + \left(\sum_{i<j} V_{ij} - \sum_{i=1}^A U(\vec{r}_i) \right) \\ &= H_0 + H_R. \end{aligned}$$

H_0 describes an ensemble of A independent particles moving in an average single-particle potential $U(\vec{r})$ generated by the nucleons themselves. H_R corresponds to the residual interaction between the so-called valence nucleons outside a closed shell (“inert core”). In the vicinity of the valley of stability H_R can be neglected by an appropriate choice of H_0 and the properties of atomic nuclei can be described well by H_0 .

1.3 Residual interaction

To study the residual NN interaction, the corresponding Hamiltonian can be decomposed sub-

sequently into a multipole expansion [15]:

$$H_R = H_{\text{monopole}} + H_{\text{dipole}} + H_{\text{quadrupole}} + \dots$$

Usually the monopole part has the highest amplitude and contributes most to the nucleus wave function. According to the decomposition of the general potential between two nucleons, the monopole interaction can be separated into central and non-central parts and depends on the three vector coordinates of radius \vec{r} , spin $\vec{\sigma}$ and isospin $\vec{\tau}$ [16]:

$$\begin{aligned} V_{1,2} &= V(\vec{r}_1, \vec{\sigma}_1, \vec{\tau}_1, \vec{r}_2, \vec{\sigma}_2, \vec{\tau}_2) \\ &= V_{1,2}^C + V_{1,2}^{LS} + V_{1,2}^T \end{aligned}$$

The **central** part contains four terms:

$$\begin{aligned} V_{1,2}^C &= V_0(r) + V_\sigma(r) \vec{\sigma}_1 \cdot \vec{\sigma}_2 + V_\tau(r) \vec{\tau}_1 \cdot \vec{\tau}_2 \\ &\quad + V_{\sigma\tau}(r) (\vec{\sigma}_1 \cdot \vec{\sigma}_2) (\vec{\tau}_1 \cdot \vec{\tau}_2) \end{aligned}$$

with the distance $r = |\vec{r}_1 - \vec{r}_2|$ between both nucleons.

The two-body **spin-orbit** potential is defined as

$$V_{1,2}^{LS} = (V_{\text{isocal.}}^{LS}(r) + V_{\text{isovect.}}^{LS}(r) \vec{\tau}_1 \cdot \vec{\tau}_2) \vec{L} \cdot \vec{S}$$

where \vec{L} is the relative orbital momentum between the two interacting nucleons and \vec{S} their total intrinsic spin, with $\vec{S} = \frac{1}{2}(\vec{\sigma}_1 + \vec{\sigma}_2)$.

The **tensor** part of the interaction is given by

$$\begin{aligned} V_{1,2}^T &= (V_{\text{isocal.}}^T(r) + V_{\text{isovect.}}^T(r) \vec{\tau}_1 \cdot \vec{\tau}_2) \\ &\quad \times \frac{3}{r^2} (\vec{\sigma}_1 \cdot \vec{r})(\vec{\sigma}_2 \cdot \vec{r}) - (\vec{\sigma}_1 \cdot \vec{\sigma}_2) \end{aligned}$$

The monopole tensor interaction can affect the so-called nucleon effective single-particle energies (ESPEs), i.e. the energy differences caused by adding a nucleon to an empty single-particle orbit or by removing a nucleon from an occupied orbit. Two nucleons in two different orbits j and j' will couple to a state with spin J and isospin T . It was shown by Otsuka *et al.* that the interaction between protons and neutrons ($T = 0$), occupying orbits with $j = \ell \pm \frac{1}{2}$ and $j' = \ell' \mp \frac{1}{2}$ ($S = 0$, spin-flip) is attractive and strongest for $\Delta L = 0$ (spin-orbit partners) [17]. For nucleons in the $j = \ell \pm \frac{1}{2}$ and $j' = \ell' \pm \frac{1}{2}$ orbits ($S = 1$) the interaction is repulsive.

While the previous sections have given an overview over the theoretical frameworks for

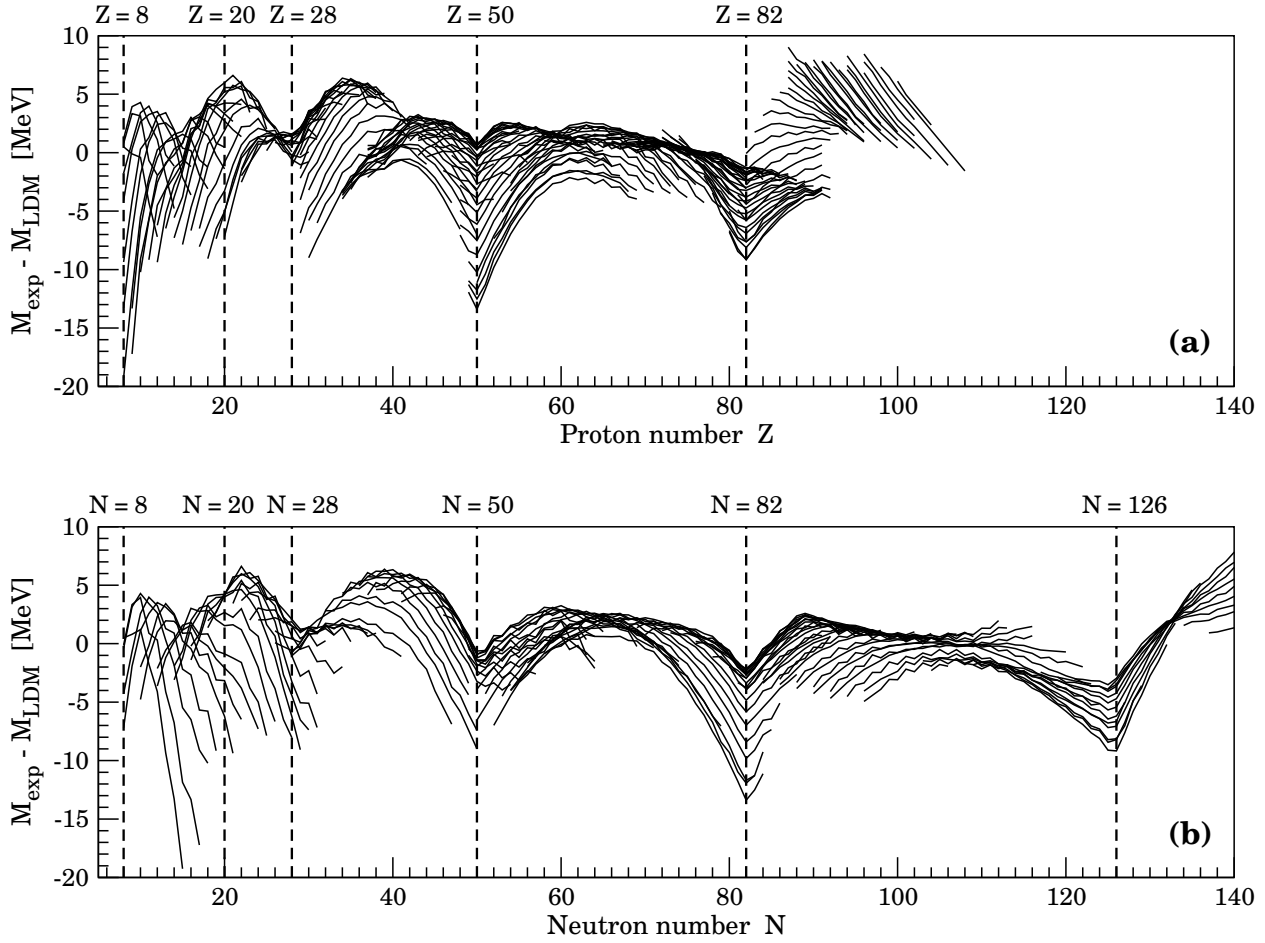


Figure 1.4: Deviations of the measured nuclear masses from the calculated masses of the liquid drop model (LDM, Weizsäcker mass formula) as a function of (a) proton number Z and (b) neutron number N , respectively. Due to the enhanced binding of the nuclear system near closed shells the mass is lowered for many isotones/isotopes (connected by solid lines). The conventional magic numbers are indicated by dashed lines. Experimental masses were taken from [18].

understanding nuclear shell structure, the following sections will focus on the experimental observables which can provide information on nuclear shell structure and the location of shell closures across the nuclear landscape.

1.4 Experimental observables

As previously discussed the energy gap between nuclear orbits and the location of nuclear shell closures is not static but is subject of the proton-to-neutron ratio. To probe nuclear structure models and theory it is necessary to have unambiguous experimental observables for the location of shell and subshell closures. Therefore experimental analysis has been focused on the evolution of specific quantities across isotopic or

isotonic chains, which will be discussed in the following paragraphs.

1.4.1 Nuclear masses and binding energies

Nuclear masses and binding energies provide a fundamental testing ground for the study of nuclear structure and shell closures. Due to the enhanced binding of the nucleons near closed shells, the mass of the nuclear system is consequently lowered. In Figure 1.4 the mass difference between the measured mass and the calculated mass from the liquid drop model (LDM, Weizsäcker mass formula) is shown as a function of Z and N , respectively. The biggest deviations can be observed for nuclei near the magic numbers, for which the measured masses are sig-

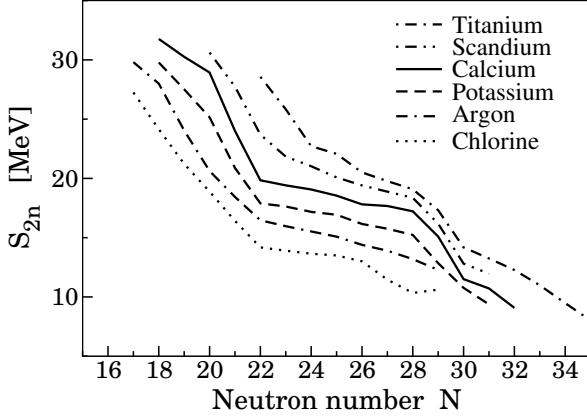


Figure 1.5: Trends of the two-neutron separation energies across the isotopic chains of Cl, Ar, K, Ca, Sc, and Ti. The dramatic drop in S_{2n} for $N \geq 20$ and $N \geq 28$ can be seen for most elements, indicating shell closures at $N = 20, 28$. Values were taken from [18].

nificantly lower than the ones calculated using the liquid drop model, indicating the underlying shell structure of the atomic nucleus.

1.4.2 Two-neutron separation energies

The trend of the two-neutron separation energies S_{2n} across isotopic chains provide a fundamental indication for completely filled neutron shells. It can be calculated out of the binding energies using $S_{2n} = BE(A, Z) - BE(A - 2, Z)$. Neutrons in a (nearly) closed neutron shell are more strongly bound and more energy is needed to remove them out of the nuclear medium. Neutrons populating orbits outside closed shells are less bound and therefore S_{2n} drops dramatically at the shell closures (see Figure 1.5).

1.4.3 Ground-state nuclear moments

The nuclear **electrical quadrupole moment** Q depends on the nuclear charge distribution. Thus it is sensitive to the nuclear shape. Nuclei near closed shells are expected to be spherical. Therefore their ground-state quadrupole moments should be small. Midshell nuclei may be axially deformed, having a large magnitude quadrupole moment. For pure single-particle configurations it can be shown that a particle outside a closed shell causes an oblate mass distribution ($Q < 0$), whereas a hole corresponds to a prolate mass distribution ($Q > 0$) [4]. Thus,

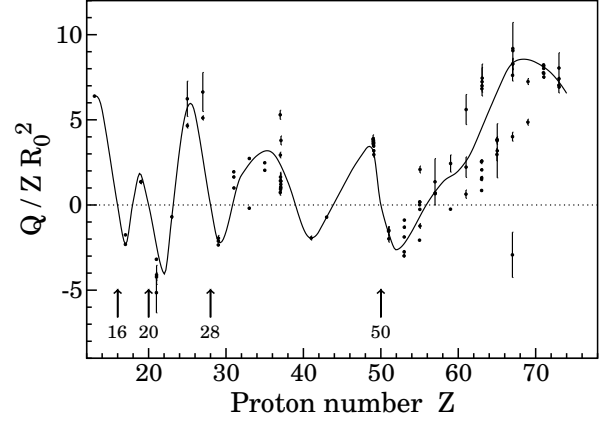


Figure 1.6: Experimental deduced nuclear ground-state electrical quadrupole moments for odd-even nuclei as a function of Z for $12 < Z < 74$. To give a measure of the nuclear deformation independent of the size of the nucleus, the quantity Q/ZR_0^2 was chosen. At closed shells Q always changes its sign from a prolate to an oblate deformation, as indicated by arrows. The solid line was drawn to guide the eye. Data taken from [19].

the quadrupole moment changes its sign at the shell closures, as it can be seen in Figure 1.6. The evolution of the ground-state nuclear moments provide an indication of changes in the nuclear structure, especially of shell closures.

The nuclear **magnetic dipole moment** μ for a state with spin I is given by $\mu = g_I I \mu_N$, where g_I is called the “gyromagnetic ratio”, and μ_N is the nuclear magneton. Due to its origin in the motion of the (charged) protons on their orbits and the spin of the nucleons, giving rise to an orbital and an intrinsic magnetic field, respectively, the magnetic moment is a sensitive probe to the wave function of a nuclear state. Within the shell-model picture the magnetic moments of odd- A nuclei near closed shells are affected by the unpaired valence nucleon. The magnetic moments of the nucleus’ states can therefore be calculated using the free nucleon magnetic moments for protons and neutrons $\mu_\pi = +2.793 \mu_N$ and $\mu_\nu = -1.913 \mu_N$, respectively. This approximation works well for most of the light isotopes. In heavier nuclei the magnetic moment is influenced by the presence of the other nucleons, and “effective” g -factors have to be used as well as further correction factors in the calculations [20]. Measurements of the g -factors in isotopic/isotonic chains allows

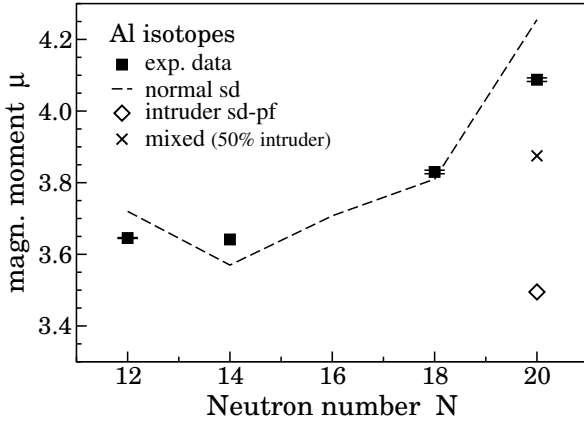


Figure 1.7: Experimental magnetic moments for odd-A aluminum isotopes as a function of N , compared to different shell-model calculations in the sd - pf space, assuming a “normal” ground state, an “intruder” ground state or a “mixed” ground state for ^{33}Al . More detailed information is given in the text. All data taken from [22].

to investigate small changes in the nuclear structure with changing N/Z ratio. In Figure 1.7 the experimentally deduced nuclear ground-state magnetic moments for odd-A aluminum isotopes are compared to different shell-model calculations. The magnetic moment of $^{25,27,31}\text{Al}$ can be well described by a “normal” ground-state configuration with consecutively filled neutron orbits in the sd -shell [21]. The more neutron-rich ^{33}Al should be in line with these results, due to its magicity $N = 20$. However, it turns out that the deduced g -factor is significantly lower than the assumption of a pure sd -shell configuration. This leads to the conclusion that, due to the vanishing of the $N = 20$ shell closure for neutron-rich nuclei, ^{33}Al must contain a contribution of almost 25% from neutron excitations into the pf -shell, so called $2p2h$ intruder configurations, in the ground-state wave function [22].

1.4.4 The $E(2^+)$ and $B(E2, 0^+ \rightarrow 2^+)$ strength

Not only the ground-state properties are useful indicators for the evolution of nuclear structure, but also excited nuclear states can be used to reveal the underlying shell structure. As seen in the previous section, quadrupole collectivity is a very sensitive quantity to probe nucleon shell closures. The energy of the first excited 2^+ state,

$E(2^+)$, and the reduced transition probability of the transition between the first excited 2^+ state and the 0^+ ground state, $B(E2; 2^+ \rightarrow 0^+)$, are the most common measures for quadrupole collectivity in even-even nuclei, even far from stability.

The first excited 2^+ state in even-even nuclei is formed by a two quasi-particle excitation, i.e. by the breaking of a nucleon-nucleon pair and excitation of one nucleon to the next higher orbit. For magic nuclei the energy needed to excite nucleons across the shell gap is large, thus the energy of the first excited 2^+ state is large. For mid-shell nuclei the level density of possible excitations is much higher. Due to the mixing of the N levels ϕ_1, \dots, ϕ_N the state with the most coherent wave function $\psi_I = \frac{1}{\sqrt{N}} (\phi_1 + \dots + \phi_N)$ is lowered in energy [23]. Thus, lowering of the $E(2^+)$ is an indication for increasing coherence in the wave function, which in turn is the microscopic basis for increased collectivity in the structure [23]. In Figure 1.8(a) the energy of the first 2^+ state of even-even calcium isotopes is plotted as a function of N , showing the characteristic peak-like structure at the shell closures $N = 20, 28$ and a more constant trend in between.

Due to the pairing interaction the ground state in even-even nuclei is always 0^+ . Thus, the first excited 2^+ state can only decay by electric quadrupole radiation, i.e. an $E2$ transition to the ground state. In general, the transition probability of an (electric or magnetic) transition of multipolarity λ is given by

$$B(\sigma\lambda, I_i \rightarrow I_f) = \frac{1}{2I_i + 1} \left| \langle \psi_f || \mathfrak{M}(\sigma\lambda) || \psi_i \rangle \right|^2$$

with the total angular momentum I of the initial state $|\psi_i\rangle$ and the final state $|\psi_f\rangle$, respectively [24]. $\langle \psi_f || \mathfrak{M}(\sigma\lambda) || \psi_i \rangle$ is the reduced transition matrix element with the electromagnetic multipole operator $\mathfrak{M}(\sigma\lambda)$, which can have either an electric ($\sigma = E$) or a magnetic ($\sigma = M$) character. The transition matrix element $\mathfrak{M}(\sigma\lambda)$ of an electromagnetic decay of an excited state is the same transition matrix element as of the excitation process with the same $\sigma\lambda$ character. Therefore the transition strength of the excitation and de-excitation between two

states with I_i and I_f is connected by

$$B(\sigma\lambda, I_i \rightarrow I_f) = \frac{2I_f + 1}{2I_i + 1} B(\sigma\lambda, I_f \rightarrow I_i)$$

The value of $B(E\lambda)$ is usually expressed in terms of $e^2 b^\lambda = 10^4 e^2 \text{fm}^{2\lambda}$, whereas $B(M\lambda)$ is given in $\mu_N^2 b^{\lambda-1} = 10^4 \mu_N^2 \text{fm}^{2(\lambda-1)}$, with μ_N the nuclear magneton. In a single-particle picture, where only one single nucleon contributes to the electromagnetic transition, the so called “Weisskopf unit” (W.u.) can be defined [24]:

$$B(E\lambda)_W = \frac{1}{4\pi} \left(\frac{3}{\lambda + 3} \right)^2 (1.2A^{1/3})^{2\lambda}$$

$$B(M\lambda)_W = \frac{10}{\pi} \left(\frac{3}{\lambda + 2} \right)^2 (1.2A^{1/3})^{2\lambda-2},$$

where $B(E\lambda)$ is given in $e^2 \text{fm}^{2\lambda}$ and $B(M\lambda)$ is given in $\mu_N^2 \text{fm}^{2\lambda-2}$. Expressed in Weisskopf units the $B(\sigma\lambda)$ -values are a rough estimate of the number of nucleons contributing to the transition. Thus, the $B(E2)$ -value is a measure of collectivity in the nucleus. For example $B(E2) \approx 1$ W.u. indicates a pure single-particle transition, whereas for collective transitions in spherical vibrational nuclei $B(E2) \approx 10$ -50 W.u. can be expected. Figure 1.8(b) displays the evolution of the $B(E2; 2^+ \rightarrow 0^+)$ for even-even calcium isotopes as a function of the neutron number. At midshell, the transition strength is large, which can be explained by an increased coherence in the nucleons’ wave functions, i.e. increased collectivity. At the shell closures the number of valence nucleons is reduced, which lessens the collectivity of the system and lowers the $B(E2)$ -value [23].

Shell-model calculations of the transition strength are performed typically within a reduced model space, including a limited number of valence nucleons outside a closed shell (cf. section 1.2). These valence nucleons are proposed to move in selected valence orbits, totally decoupled from the inert core. Due to polarization effects, in which the valence nucleons polarize the underlying core, effective proton and neutron charges, e_π^{eff} and e_ν^{eff} , respectively, are defined. Thus, the reduced transition probability $B(E2)$ can be written as a sum of proton and neutron amplitudes:

$$B(E2, I_i \rightarrow I_f) = \frac{1}{2I_i + 1} (e_\pi^{\text{eff}} A_\pi + e_\nu^{\text{eff}} A_\nu)^2$$

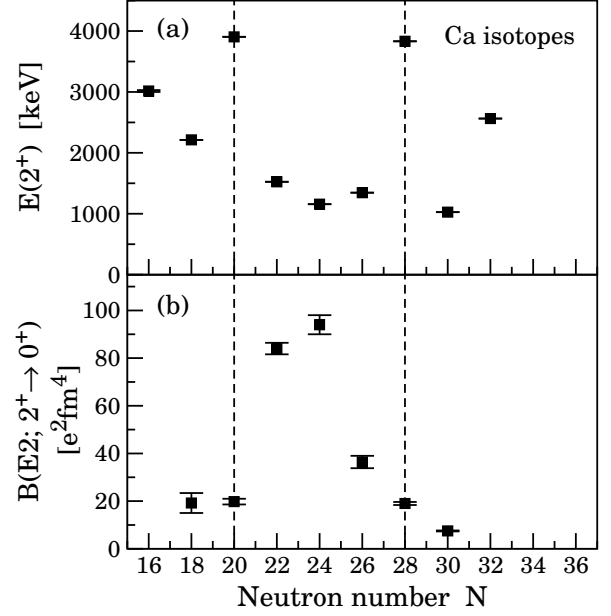


Figure 1.8: (a) Energy of the first excited 2^+ state and (b) transition strength $B(E2; 2^+ \rightarrow 0^+)$ for even-even Ca isotopes, as a function of N . At the neutron shell closures (dashed lines) $E(2^+)$ peaks, whereas the $B(E2)$ value reaches its maximum at midshell. Values taken from [25–27].

where the nucleon amplitudes are defined as

$$A_\pi = \langle I_f | \mathfrak{M}(E2) | I_i \rangle_\pi$$

$$A_\nu = \langle I_f | \mathfrak{M}(E2) | I_i \rangle_\nu$$

In the case of a closed shell the corresponding nucleon amplitude will be zero.

In many experiments the lifetime τ of an excited state is measured to determine the transition probability. The probability for the emission of a γ ray of multipolarity λ from an excited state I_i into a lower-lying state I_f is connected to the $B(\sigma\lambda)$ value and is expressed by [24]

$$T(\sigma\lambda; I_i \rightarrow I_f) = \frac{8\pi(\lambda + 1)}{\lambda[(2\lambda + 1)!!]^2} \frac{1}{\hbar} \left(\frac{E_\gamma}{\hbar c} \right)^{2\lambda+1} \times B(\sigma\lambda; I_i \rightarrow I_f)$$

The lifetime of a state I_i , which can decay into several final states I_f by emission of λ -pole radiation, is given by

$$\tau(I_i) = \left(\sum_{I_f} \sum_{\lambda} T(\sigma\lambda; I_i \rightarrow I_f) [1 + \alpha(\lambda)] \right)^{-1},$$

including the usual λ -pole conversion coefficient $\alpha(\lambda)$. In the special case of a pure $E2$ transition

from the first excited 2^+ state to the 0^+ ground state, the lifetime of the 2^+ state is

$$\tau(2^+) = \frac{8.16 \times 10^{-14}}{[1 + \alpha(E2)] E_\gamma^5 B(E2; 2^+ \rightarrow 0^+)} \text{ [s]}$$

where E_γ is given in MeV, and the $B(E2)$ in units of e^2b^2 .

Part I

**Mapping the border
of the “Island of Inversion” –**

**Coulomb excitation
of exotic Na and Mg isotopes
with MINIBALL at REX-ISOLDE**

Chapter 2

Motivation and physics case

Shell structure is one of the most important frameworks for understanding nuclear structure and the properties of atomic nuclei. Contrary to the opinion some years ago that magic numbers are permanent and valid for all nuclei, recent experimental and theoretical findings indicate that magic numbers are subject to the proton-to-neutron ratio. Thus, well-known shell closures vanish and new magic numbers are revealed when going to more exotic nuclei far from the valley of stability.

2.1 Vanishing of the $N = 20$ shell gap – the island of inversion

A first indication for such a vanishing of a shell closure was found in early mass measurements for $^{31,32}\text{Na}$ at ISOLDE (CERN), which found deviations from the expected binding energies for a closed shell at $N = 20$ [28]. Campi *et al.* suggested a deformed ground state for these nuclei [29]. Further evidence for this interpretation was provided by studies of mean square nuclear charge radii [30] and β -decay spectra of the neutron-rich sodium isotopes around $N = 20$ [31, 32]. Later shell-model calculations by Warburton *et al.* [33] assumed that the $1f_{7/2}$ orbital becomes lower in energy, reducing the sd shell gap and an anomalous inverted level structure was proposed, which is based on 2-particle 2-hole ($2p2h$) neutron cross shell configurations in the ground state. Recent shell-model calculations trace this phenomenon back to the residual nucleon-nucleon interaction [5–7, 34]. The monopole term of the strongly attractive tensor interaction between protons and neutrons is strongest for $S = 0$ (spin-flip), $\Delta L = 0$ (spin-

orbit partner) and $T = 0$ (isospin-flip) [17] (cf. Sec. 1.3). In the case of silicon, protons in the $\pi d_{5/2}$ orbital strongly interact with neutrons in $\nu d_{3/2}$. Moreover the monopole interaction $V_{d_{5/2}d_{3/2}}^{T=0}$ is the most attractive in the sd shell [5]. As pointed out by Sorlin *et al.* the $V_{d_{5/2}f_{7/2}}^{T=0}$ proton-neutron interaction is weaker firstly due to the different angular momenta of proton and neutron ($\Delta L = 1$), i.e. due to the weaker overlap of their wave functions. Secondly the interaction contains a repulsive tensor force due to the spin alignment ($S = 1$) [16]. Thus, the $\nu d_{3/2}$ orbital becomes lower in energy with respect to the $\nu f_{7/2}$ orbital, resulting in the classical magic number $N = 20$. By removing protons from the $\pi d_{5/2}$ orbital the $V_{d_{5/2}d_{3/2}}^{T=0}$ residual interaction decreases due to the missing $S = 0$ partner protons and the $\nu d_{3/2}$ orbital is shifted

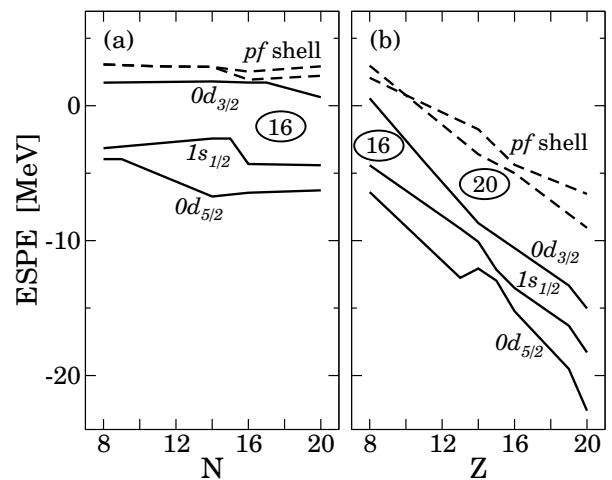


Figure 2.1: Calculated effective single particle energies (ESPE) of neutrons (a) in the $Z=8$ isotopic chain of oxygen and (b) in the $N=20$ isotonic chain with $8 < Z < 20$. Explanation is given in the text. The figure was adapted from Ref. [7].

to higher energies. The energy gap to the pf shell becomes smaller, causing a new (sub)shell closure at $N = 16$, as shown in Figure 2.1.

The neutron-rich isotopes of Ne, Na and Mg are located at this transition from a shell closure at $N = 20$ to a shell closure at $N = 16$. Compared to ^{34}Si the shell gap between the neutron $d_{3/2}$ and the pf orbitals is reduced by about 1 MeV for the Mg isotone and about 2 MeV for the Ne isotone [35]. Thus, excitation of $2p2h$ intruder configurations of sd and pf orbits is increased for the neutron-rich Ne, Na and Mg isotopes. The intruder configurations gain correlation energy, i.e. deformation energy, comprising proton-neutron and neutron-neutron monopole and quadrupole terms [36]. If this gain of correlation energy largely compensates the loss of energy promoting two neutrons from the $d_{5/2}$ orbital across the $N = 20$ shell gap to a pf orbital ($2E_{\text{gap}}$), the ground-state wave function contains a dominant $2p2h$ admixture. Thus, normal ($0\hbar\omega$) and intruder ($2\hbar\omega$) configurations are inverted in those nuclei, triggering the name “island of inversion”. Moreover, due to deformation of the ground state, nuclei which reside in the region of the island of inversion, show largely collective behavior, e.g. reduced $E(2^+)$ and increased $B(E2, 0^+ \rightarrow 2^+)$ values for even-even isotopes. Besides the shell-model calculations the low-lying 2_1^+ states and increased $B(E2)$ values were reproduced also by the quasiparticle random-phase approximation [37] and configuration mixing with angular-momentum projection [38, 39]. Mean-field calculations result in a spherical shape for the ground state of ^{32}Mg [40, 41]. However, it is calculated to be very soft against quadrupole deformation. Investigations in the following nuclei evince that $^{29,30,32}\text{Ne}$ [42–44], $^{30,31}\text{Na}$ [45, 46] and $^{31-34,36}\text{Mg}$ [47–53] are part of the island of inversion (see Figure 2.2).

Many efforts have been made in experimental and theoretical studies to understand the coexistence of normal $0\hbar\omega$ and intruder $1\hbar\omega$ and $2\hbar\omega$ configurations at low energies for different isotopes in the region of the island of inversion. However, the driving mechanisms are not fully understood yet and the predictive power of most theories is not good enough to provide reliable information on the low-energy structure and ex-

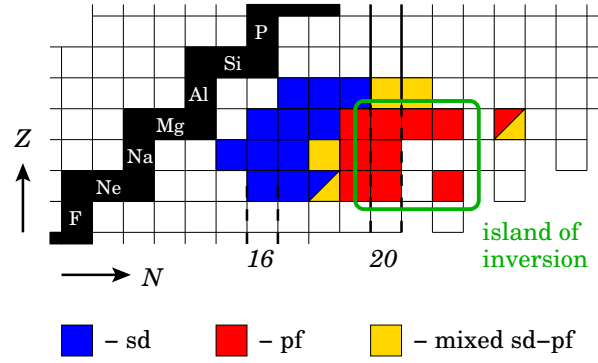


Figure 2.2: Location of the “island of inversion” inside the chart of nuclides, summarizing recent experimental results [22, 42–63]. Nuclides colored in blue show normal sd shell structure, whereas nuclides found to have a pf intruder ground state are marked in red. Yellow boxes indicate transitional nuclei with a mixed sd - pf configuration in the ground state.

perimental observables for many nuclei in this region. Especially for nuclei with odd N and/or odd Z detailed theoretical information is rare, although these nuclei are a much more sensitive probe for the competing structure of $0\hbar\omega$, $1\hbar\omega$ and $2\hbar\omega$ configurations at low energies. Thus, the experiments presented in this work will focus on the study of collective properties and the low-energy structure of the neutron-rich odd-mass magnesium isotope ^{31}Mg and the neighboring odd- Z sodium isotopes $^{29,30}\text{Na}$.

2.2 The neutron-rich Mg isotopes

Shortly after the first observation of the anomalous behavior of the neutron-rich sodium isotopes around $N = 20$ [28, 30], experimental studies focused on the neighboring magnesium isotopes. β -decay studies of neutron-rich ^{32}Na nuclei found a low-lying 2^+ state in ^{32}Mg [31]. Its low excitation energy of only 886 keV pointed to a largely deformed nucleus. Early mass measurements of $^{31,32}\text{Mg}$ supported this suggestion, finding the neutrons in the $\nu d_{3/2}$ orbital to be less bound than expected for a nucleus at the $N = 20$ shell closure [64, 65]. During the last two decades different experimental methods were employed to study the structure of the neutron-rich Mg isotopes at the region of the island of inversion in detail.

As stated in the first chapter, the energy of

the first excited 2^+ state and the reduced transition probability $B(E2, 0^+ \rightarrow 2^+)$ are the most accessible observables to study the properties of excited states in exotic even-even nuclei. Therefore the quadrupole collectivity of the $N = 20$ nucleus ^{32}Mg was determined by Motobayashi *et al.*, employing for the first time the method of intermediate-energy Coulomb excitation to nuclei far from stability [50]. The experiment yielded $B(E2, 0^+ \rightarrow 2^+) = 454(78) \text{ e}^2\text{fm}^4$, corresponding to a large quadrupole deformation of the ground state with $\beta_2 = 0.522(41)$, caused by the highly deformed pf intruder state. These values were confirmed by a series of independent Coulomb-excitation experiments and inelastic scattering experiments [51, 52, 66–68]. The most recent of these Coulomb-excitation experiments was performed at REX-ISOLDE, proving the deformed sd - pf intruder configuration dominating the ground state of ^{32}Mg [68]. In contrast Coulomb-excitation experiments in the $N = 18$ isotope ^{30}Mg [59, 66] revealed an excitation strength of $B(E2) = 280(20) \text{ e}^2\text{fm}^4$ for the 2^+ state at 1483 keV, which is consistent with a spherical $0\hbar\omega$ ground-state configuration. An excited 0_2^+ state in ^{30}Mg was identified at an excitation energy of 1789 keV by measuring its $E0$ ground-state decay $0_2^+ \rightarrow 0_{\text{gs}}^+$ [69]. The configuration of this state was found to be dominated by a deformed $2\hbar\omega$ intruder configuration of two neutrons excited across the sd - pf shell gap. Recently a similar shape coexistence was observed in ^{32}Mg , employing the $^{30}\text{Mg}(t,p)^{32}\text{Mg}$ 2n-transfer reaction in inverse kinematics at REX-ISOLDE [70]. Beside the deformed 0_{gs}^+ the first excited 0_2^+ was identified at 1058 keV, supporting the idea of an inversion of normal and intruder configurations for nuclei residing inside the island of inversion. Further investigations in the even more neutron-rich nuclei $^{34,36}\text{Mg}$ found low-lying 2_1^+ states at 657(7) keV [51, 52, 71] and 660(6) keV [53], respectively, pointing to well deformed nuclei. For ^{34}Mg this was supported by several intermediate-energy Coulomb-excitation experiments, yielding a large quadrupole collectivity of $B(E2, 0^+ \rightarrow 2^+) = 570(100) \text{ e}^2\text{fm}^4$ [51, 52, 66], which corresponds to a deformation parameter $\beta_2 = 0.58(6)$.

All these findings are summarized in Fig-

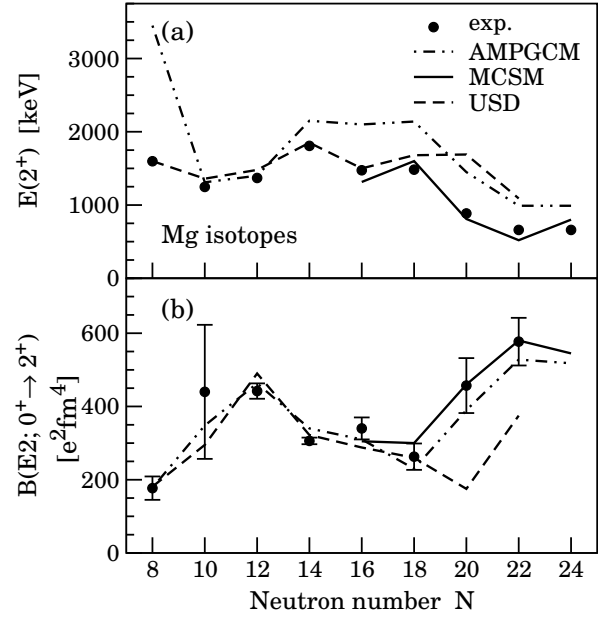


Figure 2.3: (a) Energies of the first excited 2^+ states and (b) their $B(E2)$ values for even-even Mg isotopes. While for $N \leq 18$ the experimental values [72] are well reproduced by USD shell-model calculations [73], large deviations are found for $N \geq 20$. This can be explained by dominant $2p2h$ configurations in the ground state of $^{32,34,36}\text{Mg}$, which were taken into account in MCSM [35] and AMPGCM [38] calculations.

ure 2.3, showing the energies of the first excited 2^+ states and their $B(E2)$ values for even-even Mg isotopes. For $Z \leq 18$ the experimental values [72] are well reproduced by shell-model calculations using the usual sd shell-model space of the USD interaction [73]. For $N \geq 20$ the values can no longer be reproduced by the USD interaction. A dominant mixing of intruder configurations, exciting neutrons across the $N = 20$ shell gap, has to be taken into account, which was performed in the framework of Monte-Carlo shell model (MCSM) calculations [35] and beyond-mean-field calculations [38].

The measurement of low-lying 2_1^+ states and large $B(E2, 0^+ \rightarrow 2_1^+)$ values in even-even nuclei residing inside the island of inversion has meanwhile established the picture of highly deformed intruder ground states. However, the details of the underlying single-particle structure can be preferentially addressed by studying nuclei with odd neutron or proton number. A relevant case is given by the $N = 19$ nucleus ^{31}Mg , which is located at the boundary of the island

J^π	E_x [keV]	Q_s / Q [efm ²]	$B(E2)$ [e ² fm ⁴]	μ [μ_N]	$B(M1)$ [μ_N^2]
$1/2^+$	0	—	—	-0.98	—
$3/2^+$	101	-17 / 84	106	+0.56	0.06
$5/2^+$	988	-17 / 59	127	-0.30	0.38
$7/2^+$	1236	-25 / 75	151	+0.94	0.04

Table 2.1: Predicted energies, electromagnetic moments, and reduced transition probabilities of the positive-parity yrast states in ^{31}Mg , calculated by shell-model calculations in the sd - pf model space [48].

of inversion. Early β -decay studies of $^{31,32}\text{Na}$ determined a $3/2^+$ ground state for ^{31}Mg due to the measured $\log ft$ value [74]. Thus, the ground-state wave function was assumed to be dominated by a normal sd shell configuration, placing ^{31}Mg outside of the island of inversion. In a recent hyperfine structure and β -NMR measurement by Neyens *et al.* the spin and nuclear moment of the ground state in ^{31}Mg were mea-

sured directly, yielding $J^\pi = 1/2^+$ [47] in contradiction to previous findings (cf. Figure 2.4). Maréchal and collaborators performed a complementary β -decay experiment on ^{31}Mg [48, 75] and observed very weak feeding to the ^{31}Al ground state ($J^\pi = 5/2^+$) and lowest excited states ($J^\pi = 1/2^+, 3/2^+$). Both observations agree well with the $1/2^+$ ground state of ^{31}Mg . The absence of strong β -decay feeding into the lowest-lying $J^\pi = 1/2^+, 3/2^+$ states indicates very different single-particle structures of mother- and daughter nuclei in agreement with a strong $2p2h$ component in the ^{31}Mg ground-state wave function.

These experimental results were supported by shell-model calculations in the sd - pf valence space, reproducing the low-lying level scheme of ^{31}Mg remarkably well for the first time [48]. The ground state and the first excited $3/2^+$ state were found to be largely dominated by $2p2h$ intruder configurations, and ^{31}Mg has to be placed inside the island of inversion. Furthermore, theoretical results on the collective properties of excited states in ^{31}Mg predict a deformed positive-parity yrast band – built on the $1/2^+$ ground state – with a collective transition to a $J = 5/2$ state just below 1 MeV. A corresponding $B(E2, 5/2^+ \rightarrow 1/2^+) = 127 \text{ e}^2\text{fm}^4$ value is given [48]. Further predicted observables of the positive-parity states are summarized in Table 2.1. Additional calculations were done by Kimura [76], which yielded an intruder dominated $5/2^+$ state at 0.89 MeV. The electric quadrupole moment of this strongly deformed and largely collective state was predicted to be $Q = -19.1 \text{ efm}^2$ and $Q_s = -21.6 \text{ efm}^2$, calculated by the AMD+GCM wave function and the rigid rotor approximation, respectively [76]. More detailed information on the calculated properties of the positive-parity states in ^{31}Mg

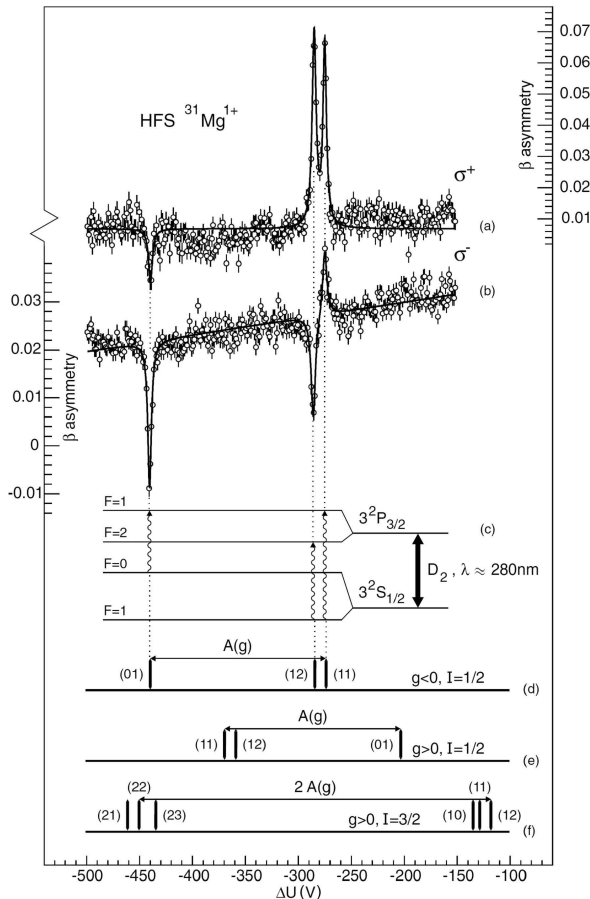


Figure 2.4: Discovery of the $I = 1/2$ spin value of ^{31}Mg by the measured hyperfine structure (HFS) spectra of σ^+/σ^- optically polarized ^{31}Mg ions, observed in the asymmetry of the β -decay. The figure was taken from the original publication in [47].

J^π	E_x [MeV]	Q [efm ²]	Q_s [efm ²]	$0p1h$ [%]	$2p3h$ [%]
$1/2_1^+$	0.0	—	—	0	93
$3/2_1^+$	0.14	-18.9	-17.1	25	61
$3/2_2^+$	0.81	8.2	7.4	68	20
$5/2_1^+$	0.89	-19.1	-21.6	21	63
$7/2_1^+$	1.39	-23.2	-22.5		
$5/2_2^+$	1.85	4.8	-2.7	67	11
$7/2_2^+$	2.23	-2.4	-5.3		
$9/2_1^+$	2.93	-17.2	-19.5		

Table 2.2: Predicted energies, configuration mixings, and electric quadrupole moments of the positive-parity states in ^{31}Mg , calculated by the AMD+GCM wave function (Q) and the rigid rotor approximation (Q_s) [76].

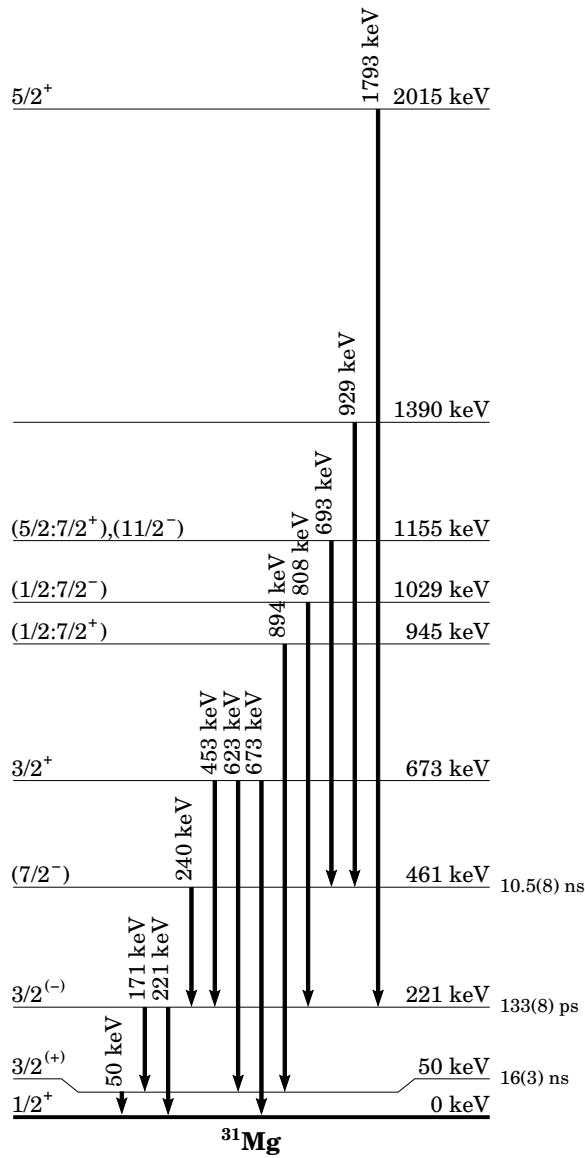


Figure 2.5: Levelscheme of ^{31}Mg up to 2 MeV, deduced from β -decay, fast timing $\beta\gamma\gamma$ measurements, and proton-knockout reactions [72, 77, 78].

by AMD-GCM calculations can be found in Table 2.2.

So far detailed structure information on the low-lying levels of ^{31}Mg have been provided by β -decay, fast timing $\beta\gamma\gamma$ measurements [77], and proton-knockout reactions [78], the latter ones allowing for determination of transitions strengths and spin and parity assignments of the first excited levels, respectively. Three promising candidates for a strongly deformed and largely collective $5/2^+$ state remain between 900 keV and 1400 keV [72, 77, 78], but spin and parity assignments are not available from β -decay experiments (cf. Figure 2.5). The unknown $5/2^+$ state and the predicted collective properties of the first excited positive-parity states in ^{31}Mg motivated a first Coulomb-excitation experiment with a ^{31}Mg beam in inverse kinematics at REX-ISOLDE, CERN, performed by the MINBALL collaboration. The intruder configurations also at higher excitation energy are the subject of this investigation to clarify the placement of ^{31}Mg inside the island of inversion. Reduced transition probabilities, i.e. $B(E2)$ and $B(M1)$ values, will be presented and compared to recent theoretical results in this work.

2.3 The neutron-rich Na isotopes

Besides the exotic magnesium isotopes around $N = 20$ neutron-rich sodium isotopes played the most important role in the discovery and understanding of the island of inversion. The first indication for a vanishing $N = 20$ shell gap was found in early mass measurements for $^{26-32}\text{Na}$ at ISOLDE (CERN) [28]. The observed excess

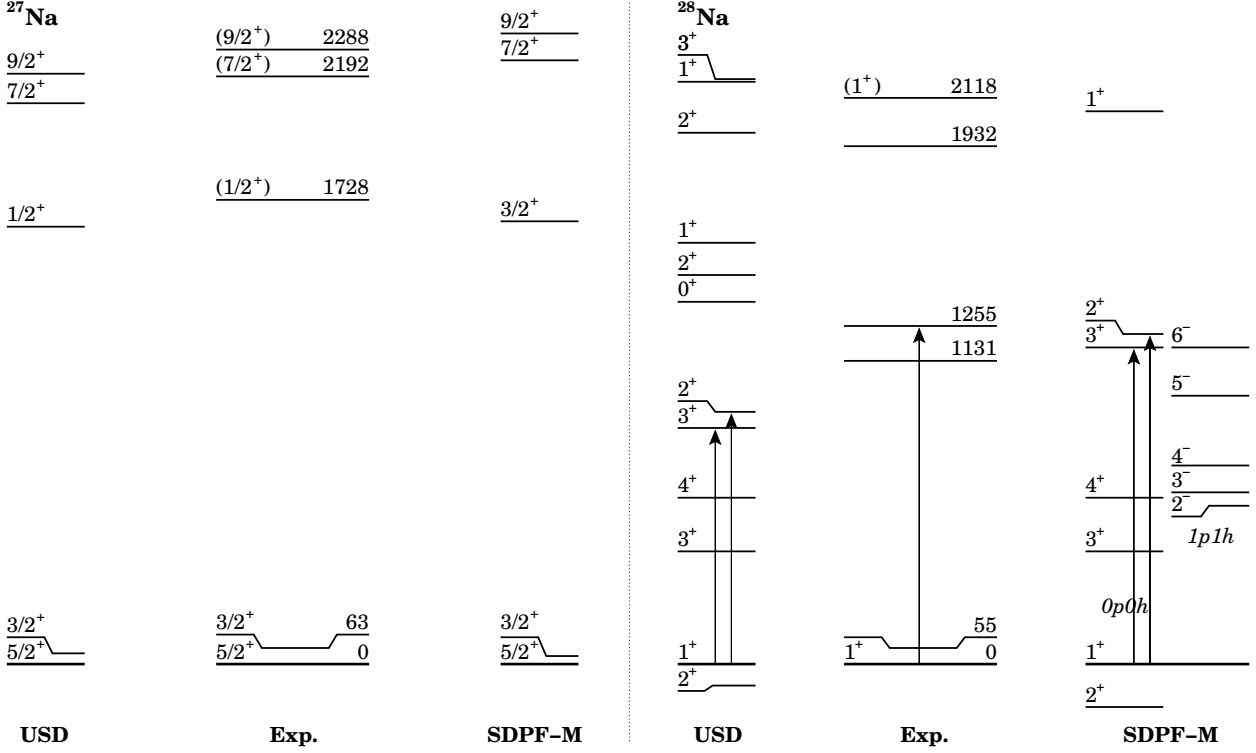


Figure 2.6: Comparison of the energy levels of $^{27,28}\text{Na}$, deduced by experiment (middle) and by shell-model calculations using the USD (left) and SDPF-M interactions (right). The E2 excitation strengths from the ground state are indicated by the width of the arrows. The figure was adapted from Refs. [54, 57].

in the two-neutron separation energy pointed to the onset of deformation (at $N = 20$) in the ground state of exotic Na isotopes. Thus, $^{31,32}\text{Na}$ were proposed to have an intruder-dominated ground state. Later this was confirmed by different experimental findings, e.g. the ground-state spin $J = 3/2$ as well as a significantly reduced magnetic moment [80] and enhanced quadrupole collectivity [46, 56, 79] of ^{31}Na .

For the $N = 16$ and $N = 17$ isotopes $^{27,28}\text{Na}$ level schemes were investigated mainly by β -decay experiments [57, 81] and a recent fusion experiment employing both radioactive ^{14}C beams and targets [82]. The ground-state spin of ^{28}Na was measured to be $J^\pi = 1^+$ by laser spectroscopy [30] and deduced $\log ft$ values of the ^{28}Ne β -decay [57]. The results agree well with shell-model calculations in the sd model space using the USD interaction [54], which show energetically very close lying states. A normal shell-model configuration is assumed for the low-lying 1_1^+ , 2_1^+ , 3_1^+ , and 4_1^+ states, where a neutron in the $\nu d_{3/2}$ orbital couples weakly with a proton in the $\pi d_{3/2}$ or $\pi d_{5/2}$ orbital.

Thus $B(E2)$ values from the ground state to the other low-lying states are expected to be small. Utsuno *et al.* predicted transition strengths of $19 \text{ e}^2\text{fm}^4$ and $27 \text{ e}^2\text{fm}^4$ for the excitation from the ground state into the 2_1^+ and 3_1^+ states, respectively [54]. For the excitation of one neutron from the $\nu 1s_{1/2}$ orbital into the $\nu 0d_{3/2}$ orbital MCSM calculations with the SDPF-M interaction yielded $B(E2, 1_1^+ \rightarrow 2_2^+) = 69 \text{ e}^2\text{fm}^4$ and $B(E2, 1_1^+ \rightarrow 3_2^+) = 47 \text{ e}^2\text{fm}^4$. An indication for the latter ones was observed in a Coulomb-excitation experiment at MSU [56]. Within the energy resolution of the NaI detector array used one γ ray was observed at 1.24 MeV with $B(E2)^\uparrow = 54(26) \text{ e}^2\text{fm}^4$ which is quite close to the predictions.

The nuclear masses and two-neutron separation energies of the $N = 18, 19$ sodium isotopes $^{29,30}\text{Na}$ did not show any major deviations compared to predicted values from standard shell-model calculations in the sd shell [28]. However, measurements of the magnetic dipole moments and electric quadrupole moments revealed significant deviations from the USD

spectively [83]. Additional MCSM calculations obtained 65% and 77% $2p2h$ admixture for the $3/2_2^+$ state and $5/2_2^+$ state, respectively [83]. Due to the large intruder mixing in the ground state these states are supposed to have a noticeable overlap with the ground state in their wave functions. Thus the related $B(E2)$ values are sensitive probes related to the intruder content and the $N = 20$ shell gap. A value of $B(E2, 3/2_{gs}^+ \rightarrow 7/2_2^+) = 57 \text{ e}^2\text{fm}^4$ is given exemplarily [54], awaiting experimental verification.

The magnetic dipole moment of ^{30}Na was experimentally deduced by Keim *et al.* to be $2.069(2) \mu_N^2$, which is significantly lower than the predicted value from USD model calculations, yielding $\mu = 2.687 \mu_N^2$ [80]. Moreover, an anomalous electric quadrupole moment was measured [56, 79]. The deduced value and also its sign is quite different from the USD prediction. MCSM calculations with the SDPF-M interaction reproduce the measured μ and Q_0 values very well [54]. Thus, the properties of the electromagnetic moments indicate that already at $N = 19$ the ground state in ^{30}Na is dominated by intruder configurations. A rotational $K = 2$ band was obtained by the MCSM calculations, built upon the 2^+ ground state, characterized by highly collective $E2$ intra-band transitions. The reduced transition probabilities amount to a $B(E2, 2_1^+ \rightarrow 3_1^+) = 168 \text{ e}^2\text{fm}^4$ and $B(E2, 2_1^+ \rightarrow 4_1^+) = 90 \text{ e}^2\text{fm}^4$ [54]. To probe these values intermediate-energy Coulomb-excitation experiments of ^{30}Na were performed at the NSCL, MSU. Employing a highly efficient NaI(Tl) array a value of $E_\gamma = 433(16) \text{ keV}$ with $B(E2) \uparrow = 130_{-65}^{+90} \text{ e}^2\text{fm}^4$ was deduced by Pritychenko *et al.* [56]. A recently published experiment with a segmented germanium detector array by Ettenauer *et al.* measured $E_\gamma = 424(3) \text{ keV}$ and $B(E2) \uparrow = 147(21) \text{ e}^2\text{fm}^4$ [45]. Both results agree well with the predicted decay of the first excited 3_1^+ state. Collective transitions of higher-lying states were not observed. The particle-rotor model describes the strong prolate deformation with an intrinsic state, which couples the deformed ^{28}Ne rotor with a proton in the $\pi[211]3/2^+$ Nilsson orbit and a neutron in the $\nu[200]1/2^+$ orbit, allowing for a $K = 1$ or $K = 2$ yrast band. The MCSM calculations predict the $K = 2$ band to be energetically fa-

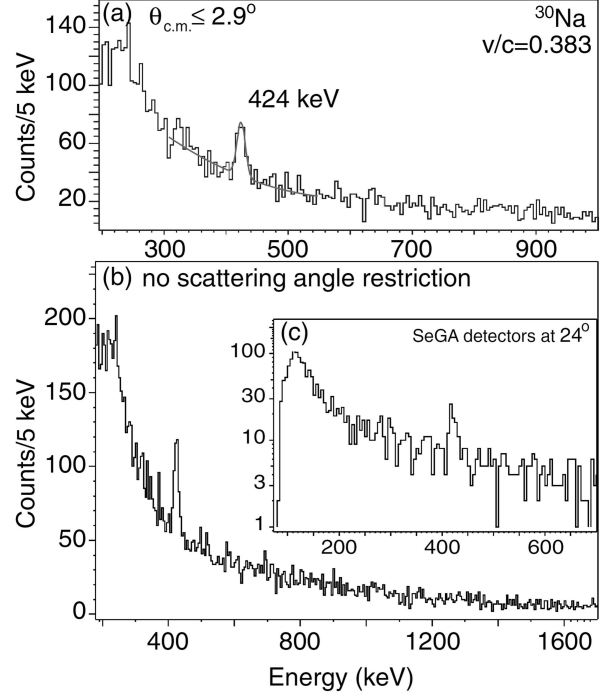


Figure 2.9: Particle- γ coincident and event-by-event Doppler-corrected γ -ray spectra observed in the intermediate-energy Coulomb-excitation experiment of ^{30}Na by Ettenauer *et al.*. The figure was taken from the original publication in [45].

vored with respect to the $K = 1$ band [54], which is consistent with the measured ground-state spin. The $K = 1$ band head is calculated at 0.31 MeV and its $J = 2$ and 3 members at around 1 MeV excitation energy. A promising candidate for the $K = 1$ band head was found by a new β -decay experiment, which observed a 1^+ state at 150 keV [83]. Excited states dominated by a normal, spherical $0p0h$ configuration are expected at around 1-1.5 MeV. Moreover, the MCSM calculations predict rather low-lying negative-parity states, which are dominated by $1p1h$ excitations across the $N = 20$ shell gap [54]. Thus, in ^{30}Na normal and intruder configurations are supposed to compete with each other at low excitation energies. Detailed experimental studies of these states would reveal excellent information on the underlying shell-model modifications around $N = 20$.

For ^{29}Na a Coulomb-excitation experiment in inverse kinematics was proposed at REX-ISOLDE, CERN, in 2008, employing a post-accelerated radioactive ^{29}Na beam at “safe” energies and the MINIBALL γ -ray spectrometer and

particle detector setup, to probe the predicted collective properties of the first excited $5/2_1^+$ state and of the unknown higher-lying $3/2_2^+$, $5/2_2^+$, and $7/2_1^+$ states. A few months after the proposal was accepted, Hurst and collaborators published the results of their Coulomb-excitation experiment which was performed at TRIUMF [58]. However, compared to their experiment the experiment with MINIBALL at REX-ISOLDE would gain from the much more intense radioactive ion beam of about 1×10^4 ions/s and a slightly higher beam energy. Thus, the new experiment intended to measure the much less intense transitions of the proposed higher-lying $3/2_2^+$, $5/2_2^+$, and $7/2_1^+$ states, even with the predicted moderately large $B(E2)$ values. A confirmation of those values by experiment would establish the onset of significant intruder mixing in the ground-state wave function of the sodium isotopes already at $N = 18$.

The unknown higher-lying states of the $K = 2$ and $K = 1$ bands in ^{30}Na and their predicted collective properties motivated a precise Coulomb-excitation experiment with a ^{30}Na beam in inverse kinematics at REX-ISOLDE, CERN. Compared to the very recent measurements, performed at NSCL, MSU [45, 56], the new experiment with the MINIBALL setup would provide (i) the high energy resolution of the MINIBALL HPGe detectors, (ii) the enlarged energy range for γ -ray detection, which goes down to a lower threshold of 50 keV, (iii) the high efficiency of the 8 triple cluster detectors of MINIBALL and (iv) the advantage of much lower background at energies below 250 keV in an ISOL beam experiment compared to measurements utilizing the in-flight production technique. The intruder configurations also at higher excitation energy are the subject of this investigation to obtain new information about the underlying shell structure and the evolution of the shell gaps far from stability.

In this work reduced transition probabilities, i.e. $B(E2)$ and $B(M1)$ values, of $^{29,30}\text{Na}$ will be presented and compared to recent theoretical predictions.

Chapter 3

The experimental setup and technique

3.1 Introduction

A total number of about 3000 different nuclides have been experimentally observed so far, of which less than 10% are stable (cf. Fig. 1.2). All other nuclides are radioactive and an overwhelming part of it needed to be produced by nuclear reactions, to be studied in experiments. During the last decades special interest in nuclear physics has focused on the properties of radioactive nuclei with extreme N/Z ratios far off stability. Production cross sections and resulting yields for these nuclei are small compared to the large amount of possible background reactions, often orders of magnitude more numerous. Thus, experimental techniques have to be very selective and efficient, to provide a pure and intense radioactive ion beam beam. The main task is the transport of the beam of interest, away from its place of production to a specific scientific setup, to eliminate the primary reaction background. Furthermore, in the course of transport, selective methods (e.g. mass separation) can suppress contaminants. Generally, the following experimental conditions should be met by any radioactive ion beam (RIB) facility: (i) The radioactive ions should be produced in a sufficient rate. (ii) The extraction technique has to be selective to the ions' A and Z . (iii) The method for extraction and preparation of the radioactive ions has to be fast, to produce RIBs of very short-lived isotopes. (iv) All stages of the RIB preparation have to be highly efficient.

Two different types of RIB facilities fulfill these requirements: The “In-Flight separation” (IF) facilities such as the FRS@GSI, BigRIPS@RIKEN, NSCL@MSU, and LISE@GANIL. The “Isotope Separation On-

Line” (ISOL) facilities such as ISOLDE@CERN, ISAC@TRIUMF, and SPIRAL@GANIL.

The IF method uses an intermediate energy or relativistic heavy ion beam (typically several 100 MeV/u up to 4.5 GeV/u), impinging on a low-mass primary production target (e.g. ^9Be). Reaction products are emitted in forward direction with energies of still a few 100 MeV/u. Isotopes of interest are selected and identified with a fragment separator, consisting of electromagnetic field combinations, a degrader, scintillators, and ionization chambers [84,85]. With this fast technique, isotopes with lifetimes down to the sub-microsecond range can be investigated.

The basic principles of the ISOL method and the feasibility of the separation of short-lived radioactive nuclei were first demonstrated by O. Kofoed-Hansen and K.O. Nielsen already in 1951 [86]. The “classic” ISOL facility consists of a thick, heavy target, which is irradiated with a high-energetic ion beam, typically protons at several 100 MeV, or neutrons. By heating the target to temperatures up to 2500°C, the radioactive nuclei can diffuse out of the target material and into an ion source. After ionization

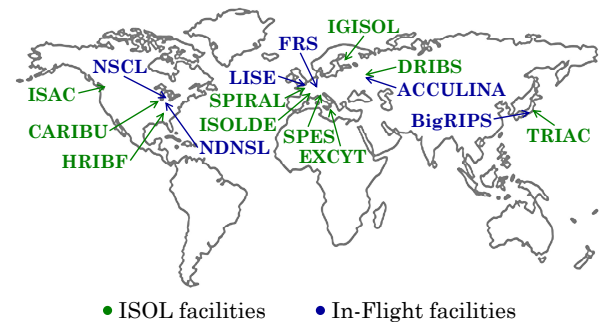


Figure 3.1: Overview of the current and upcoming radioactive ion beam facilities in the world.

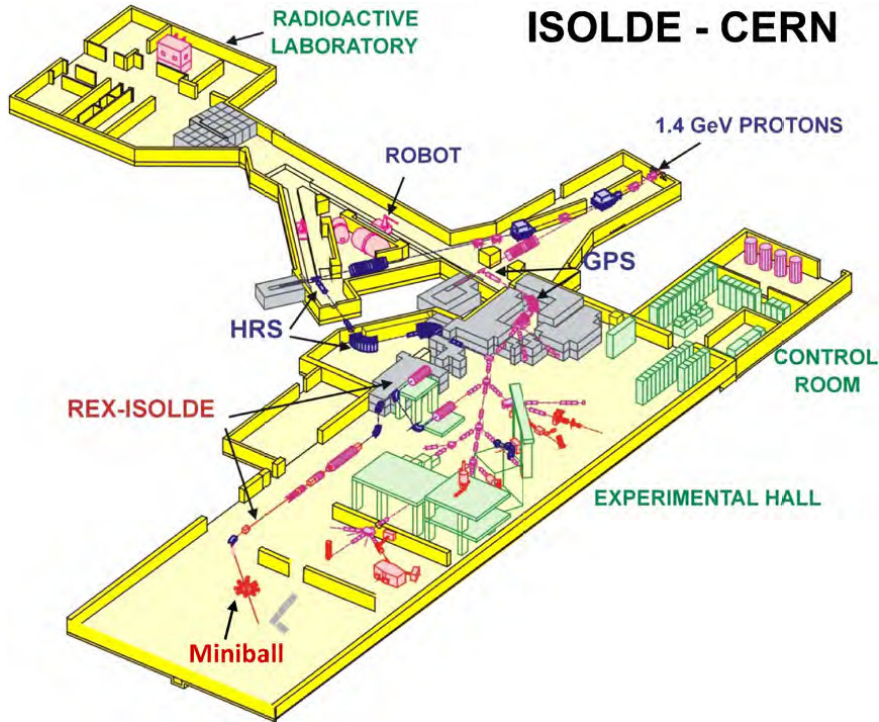


Figure 3.2: The schematic layout of the ISOLDE facility at CERN is shown. 1.4 GeV protons from the PS Booster are delivered to one of the primary target stations, coupled to two different mass separators (GPS and HRS). Post-acceleration up to 3.0 MeV/u of the RIB is possible by the REX-ISOLDE setup. Picture taken from [92].

the isotopes of interest are accelerated and mass separated [87]. Due to the long time needed to get the radioactive nuclei out of the target material, the number of nuclei is reduced to those with typically $T_{1/2} \geq 10$ ms. However, the beam quality (i.e. emittance, size of the beam spot) of the RIB is generally better for the ISOL method, than for the IF method.

The Coulomb-excitation experiments presented in this work, have been performed at the ISOLDE facility at CERN, making use of the Radioactive beam EXperiment (REX-ISOLDE) [88], providing post-accelerated neutron-rich Na, Mg, and Al beams with a maximum energy of approximately 3.0 MeV/u. In the following sections the ISOLDE facility and the experimental setup will be discussed in detail.

3.2 The ISOLDE facility

The ISOLDE facility at CERN started operation in 1967. The first “driver” accelerator was CERN’s synchro-cyclotron (SC), providing a 600 MeV proton beam with up to 4 μ A intensity [89]. In 1992 ISOLDE was integrated into CERN’s ac-

celerator complex, making use of 1.0-1.4 GeV proton pulses, delivered by the Proton Synchrotron Booster (PSB) with an averaged maximum intensity of 2 μ A. ISOLDE is a world leading ISOL facility, providing isotopically pure radioactive ion beams of more than 70 elements (with $2 \leq Z \leq 92$) and more than 700 isotopes with intensities ranging from 10^{-1} to 10^{12} ions/s [90, 91]. Besides low-energy physics (e.g. mass spectroscopy, laser spectroscopy, solid state and biophysics) radioactive ions can be post-accelerated up to 3.0 MeV/u by the REX-ISOLDE accelerator, to study nuclear properties in nuclear reactions. A schematic layout of the present ISOLDE facility can be found in Figure 3.2.

3.2.1 Production of radioactive isotopes

ISOLDE’s driver accelerator is the CERN PS Booster (PSB), providing 1.4 GeV protons with a maximum intensity of 3.2×10^{13} p/pulse. The pulses were spaced in time by integer multiples of 1.2 s, at an average of 2.4 s. Thus, the average proton beam intensity is up to 2 μ A at the ISOLDE target station. ISOLDE provides

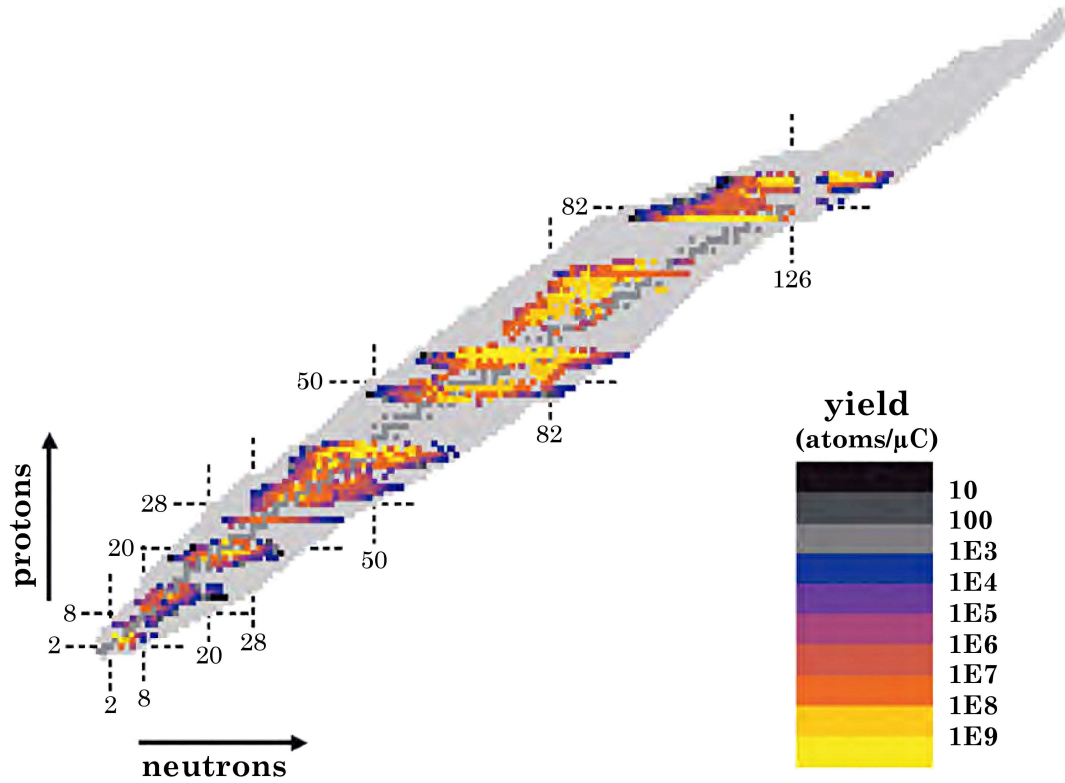


Figure 3.3: Chart of nuclei produced at ISOLDE. The color code illustrates the yield of the radioactive nuclei provided for experiments (adapted from [92]).

two target stations, each of them coupled to a mass separator (cf. Section 3.2.3). Different targets and target materials have been developed to allow the production of a large variety of high-intensity radioactive ion beams (see Fig. 3.3). The standard ISOLDE target, as seen in Fig. 3.4(a), consists of a tantalum cylinder, 20 cm long and 2 cm in diameter, connected to the ion source by a thin tube, the so-called transfer line. The tantalum cylinder contains 2-200 g/cm² of either refractory metal powders, metals or carbides at temperatures of up to 2400°C (Fig. 3.4(b)), or molten metals kept at temperatures between 700°C and 1400°C [95]. Impinging the high-energy proton beam from the PSB directly on the heavy target, exotic ions are generated by fragmentation, spallation and fission reactions. While proton-rich isotopes are especially produced by fragmentation of the target nuclei, neutron-rich isotopes are well produced by spallation or fission of neutron-rich heavy nuclei. For some isotopes higher beam purity can be achieved, doing neutron induced fission (generally of a U target), rather than proton induced fission. For this purpose the proton

beam is directed on a heavy metal rod (e.g. Ta, W), the so-called proton-to-neutron converter, placed next to the fission target. Low-energy spallation neutrons are emitted at large angles, inducing fission reactions in the ISOL target.

The produced radionuclides have to be released out of the target material and transported to the ion source quickly. Therefore the target and transfer line are electrically heated to high temperatures, to assure fast diffusion and effusion processes of the exotic atoms. Molten metal targets show a slow release of the produced isotopes, typically in the range of several 10 s. Release times of metals or carbides at 2000°C are much faster, in the order of a second or even less. Figure 3.4(c) shows a Monte-Carlo simulation of the path of one single atom from production to release inside the ISOLDE target. Detailed information on the production and release of radioactive nuclei in ISOL targets can be found in [95, 96].

The short-lived radioactive Na and Mg beams described in this work, were produced by bombarding a 50 g/cm² UC_x target directly with 1.4 GeV protons from the CERN PS Booster. Typ-

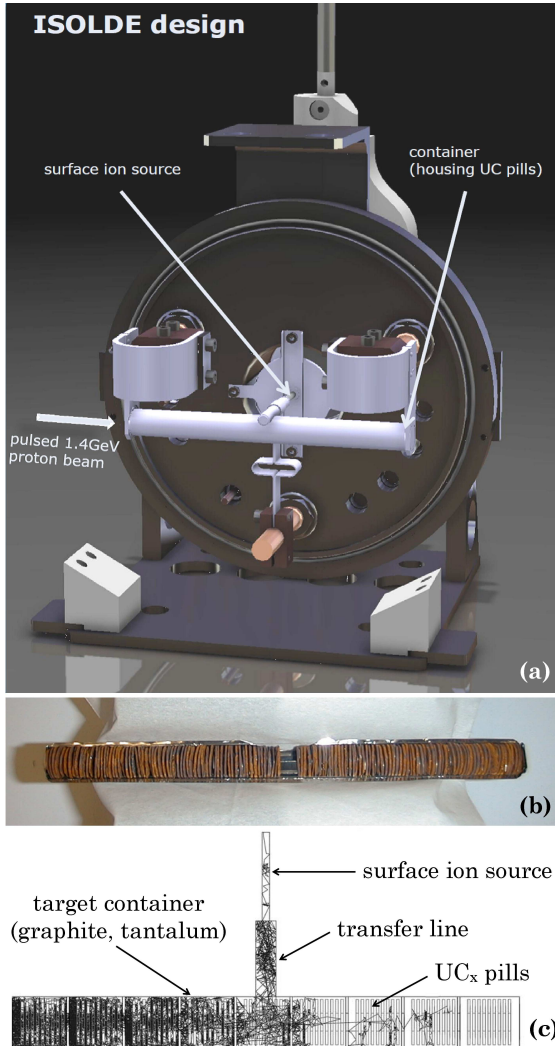


Figure 3.4: (a) Standard ISOLDE target unit, containing an UC_x target and a surface ion source. (b) About 120 individual UC_x pills are used in an ISOLDE target, each with 3.5 g/cm^3 density, grain sizes of $3\text{-}50 \text{ }\mu\text{m}$, and high porosity for improved release properties. (c) Monte-Carlo simulation of the path of one single atom from production to release inside the ISOLDE target. Pictures adapted from [93, 94].

ical release times of Na and Mg isotopes are about 200 ms and 190 ms, respectively [97, 98].

3.2.2 Ion sources

To assure the production of intense and pure radioactive ion beams, the combination of target and ion source should be able to produce ion beams which preferably should contain only isotopes from one chemical element. At ISOLDE three different types of ion sources are currently

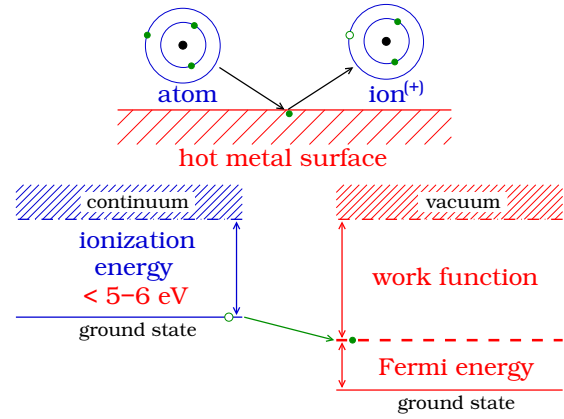


Figure 3.5: Schematic drawing of the principles of positive surface ionization (adapted from [96]).

in operation: surface ion sources, plasma ion sources, and laser ion sources. The first and the last one have been used in this work and will therefore be discussed in more detail in the following paragraphs.

Surface ion source

The most simple setup for ionizing atoms is the surface ion source. It consists only of a metal tube, the so-called “line”, which can be heated up to 2400°C , just hot enough to desorb the atoms of interest thermally. Usually the line is made out of tantalum, tungsten or rhenium, which have a high work function ϕ . If an atom with a low ionization potential W_i hits the hot surface of the line, the atom can get ionized upon desorption by giving a valence electron to the metal (see Fig. 3.5). The probability for the positive surface ionization of an element X can be derived by the so-called Saha-Langmuir equation (from [99]):

$$\alpha_s = \frac{X^{(+)}}{X^{(0)}} = \frac{2J_+ + 1}{2J_0 + 1} \exp\left(\frac{\phi - W_i}{k_B T}\right)$$

Here T is the temperature of the ionizer, and J_+ and J_0 are the (electronic) angular momenta of the ionic and atomic ground state of X , respectively (e.g. for alkalis $J_0 = 1/2$ for the $^2S_{1/2}$ atomic ground state and $J_+ = 0$ for the 1S_0 ionic ground state). For most elements $(\phi - W_i)$ is negative, even with very noble metal ionizers. Thus, the ionization efficiency can be enhanced by increasing the temperature of the line. Figure 3.6 shows the ionization potentials of el-

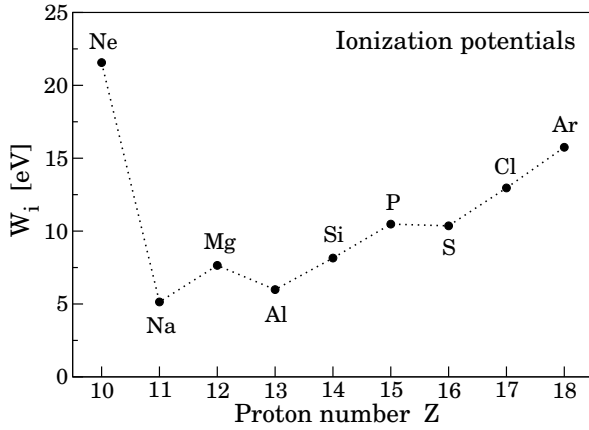


Figure 3.6: Ionization potentials W_i of elements with $10 \leq Z \leq 18$. W_i is lowest for Na and Al, explaining their enhanced efficiency for surface ionization. The ionization potential of Mg is almost 30% higher compared to Al, illustrating the need for resonant laser ionization in the Mg experiment.

elements with $10 \leq Z \leq 18$. It illustrates the enhanced efficiency for surface ionization of Na and Al due to their low ionization potential, as it was observed and used in the present experiments.

Laser ion source

As shown in Figure 3.6, most chemical elements have relatively high ionization potentials >6.5 eV. Thus, these elements can either not be surface ionized or not in a sufficient amount. Another powerful, element selective ionization technique is the Resonance Ionization Laser Ion Source (RILIS) [100]. It utilizes the element specific atomic excitation energies of the isotope of interest. The excitation of the atom is induced by intense, pulsed laser light, which is tuned in resonance to strong atomic transitions. Thereby ionization is achieved in two or three succeeding excitation steps. Other chemical elements are hardly ionized, because the laser light is out of resonance to their atomic transitions. During the time between two laser pulses, typically about 100 μ s, the atoms have to be stored, to allow multi-step excitation and a maximum overlap of the atoms and the laser beam during the ionization process. Therefore the ions have to effuse through a thin, hot tube, referred to as “hot cavity” or “line”. At ISOLDE the RILIS provides ionization schemes of more than 30 dif-

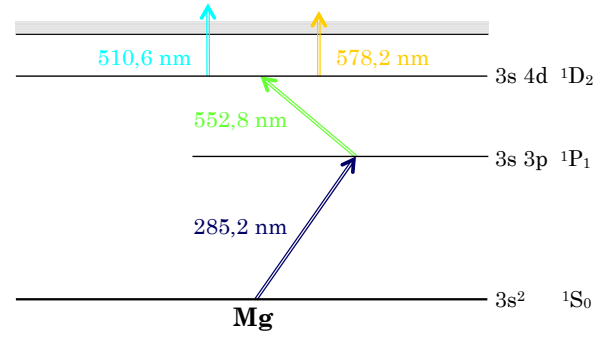


Figure 3.7: RILIS three-step ionization scheme of Mg (adapted from [91]).

ferent chemical elements, which are currently available [91]. For the preparation of the ^{31}Mg ion beam, used in this work, a three-step laser ionization scheme was employed, which is presented in Figure 3.7. The quoted ionization efficiency was up to 9.8% [91].

3.2.3 Mass separation

After ionization the 1^+ ions are extracted from the ion source by applying a voltage of up to 60 kV, and are guided to the mass separator. Each of the ISOLDE target stations is coupled to one of the ISOLDE mass separators, either to the General Purpose Separator (GPS) or to the High Resolution Separator (HRS), sketched in Figure 3.8. Both magnetic mass separators feed the radioactive beams into a common beam distribution system, to which almost all of the ISOLDE experiments are connected.

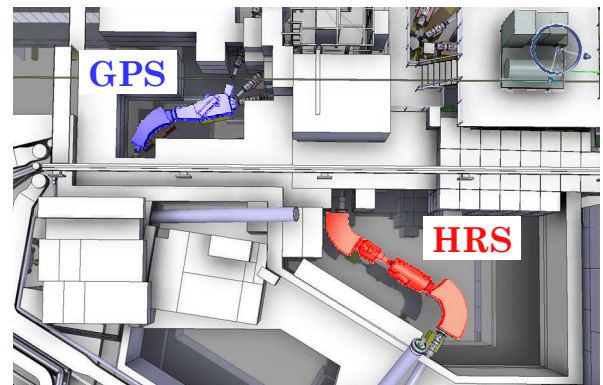


Figure 3.8: Schematic picture of the ISOLDE mass separators: the General Purpose Separator (GPS) and the High Resolution Separator (HRS). Additional information is given in the text (adapted from Ref. [101]).

General Purpose Separator (GPS)

The General Purpose Separator (GPS) consists of a 70° double focussing magnet. Its mass resolving power is specified as $M/\Delta M = 2400$ [102]. A special arrangement of movable, cylinder-shaped electrostatic deflectors, the so-called switchyard, enables the GPS to select and deliver simultaneously three different beams within a certain mass range into three different beam lines (i.e. central mass, low mass and high mass beam line). The designed mass range of the low and high mass beams is $\pm 15\%$ of the central mass. Thus, up to three different experiments can be operated simultaneously on one mass separator. The GPS was used for the experiment on ^{30}Na in 2011, presented in this work.

High Resolution Separator (HRS)

ISOLDE's second mass separator has been constructed as a High Resolution Separator (HRS). It is built up of a two stage magnetic analysis, consisting of a 90° and a 60° magnet. Higher order image aberrations could be corrected by special electrostatic multipole elements, i.e. 32-poles in octopole configuration as well as pole face windings in the magnet in hexapole configuration. A mass resolving power of typically $M/\Delta M = 5000$ is achieved in normal operation. In high resolution mode a value even of up to $M/\Delta M = 11000$ is possible [102]. The HRS was used for most experiments described in this work.

3.3 REX-ISOLDE

Low-energy physics with short-lived radioactive nuclei has been the main field of activity in the ISOLDE collaboration for more than 30 years. To study the properties of radioactive nuclei by reactions at moderate beam energies, e.g. Coulomb excitation and transfer reactions, the Radioactive beam EXperiment (REX) at ISOLDE was proposed in 1994 [103]. Operational in 2001 [104], REX-ISOLDE was originally designed for post-acceleration of neutron-rich light isotopes (e.g. Li, Na, K). So far more than 90 different radioactive isotopes, ranging from the light ^8Li up to the heavy ^{224}Rn ,

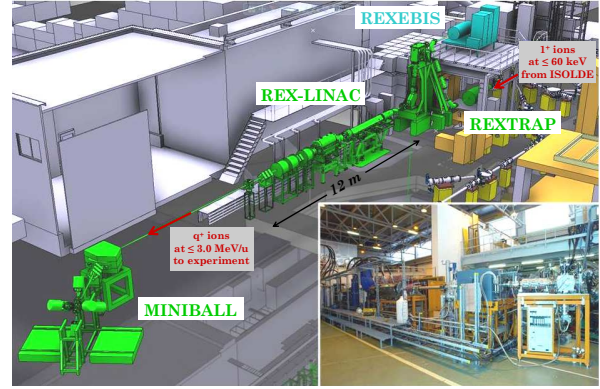


Figure 3.9: Schematic diagram and picture of the REX-ISOLDE setup. Additional information is given in the text (adapted from [101]).

have been efficiently post-accelerated and studied with the REX-ISOLDE setup at beam energies up to 3.0 MeV/u [91].

The complex REX-ISOLDE setup is shown in Figure 3.9. Singly charged radioactive ions coming from ISOLDE are first cooled and bunched in a Penning trap (REXTRAP) before they are charge bred to higher charge states, using an electron beam ion source (REXEBS). The ions with $A/q < 4.5$ are post-accelerated in a compact linear accelerator (REX-LINAC) up to 3.0 MeV/u and delivered to the experimental area [88].

3.3.1 Charge breeding system

To post-accelerate singly charged ions to beam energies of up to several MeV/u, very extensive, large-scale acceleration structures are required. Thus, the production of highly charged ions is absolutely necessary, to ensure the installation of a compact, efficient and cost-effective experimental setup [88, 103]. In principle there are two different ways for effective charge breeding [105], either with an Electron Cyclotron Resonance Ion Source (ECRIS) using a continuous ion beam [106], or with an Electron Beam Ion Source (EBIS) using a bunched ion beam [107]. At REX-ISOLDE the latter one has been installed successfully, receiving its bunched beam by a cylindrical Penning trap (REXTRAP). The total transmission rate of the charge breeding system of REX is typically 10-15% for light ions and about 5% for ions with $A > 150$.

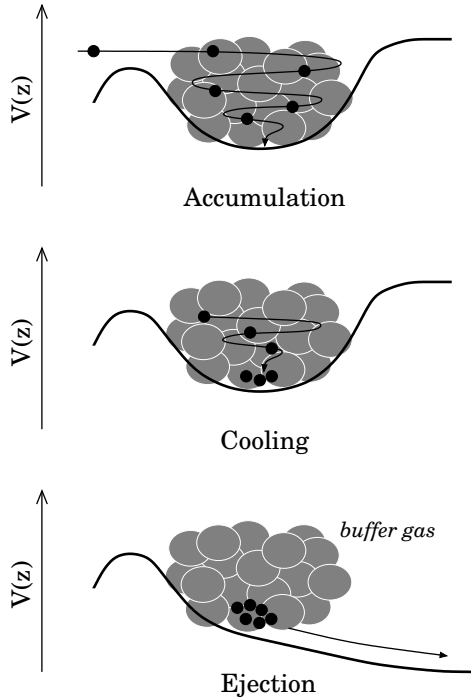


Figure 3.10: Accumulation, cooling, and bunching of a continuous ion beam in the gas-filled Penning trap REXTRAP (adapted from [108]).

Penning trap (REXTRAP)

The ion beam of ISOLDE is continuously injected into a 1 m long cylindrical Penning trap, the so-called REXTRAP (Figure 3.11), where it is stored by a specific arrangement of electric and magnetic fields. Within the trap the ions are first decelerated to some eV by the applied high voltage (typically 30-60 kV). Further cooling can be achieved by collisions with the atoms of a buffer gas, usually Ne and Ar at a pressure of 10^{-4} to 10^{-3} mbar. The time needed to cool the ions down to room temperature is typically in the range of a few ms [108]. By this cooling the transversal emittance is considerably improved. Further improvement of the emittance and the beam purity is possible by mass-selective side band cooling [109, 110]. By the cooling all ions are first driven to magnetron orbits larger than the diameter of the extraction hole of the trap, due to collisions with the buffer gas. Applying an RF-field with cyclotron frequency $\omega_c = q/mB$ in the trap, only the ions of interest are recentered. Finally, the ions are cooled and collected in the trap center, where from they can be extracted as short ion bunches

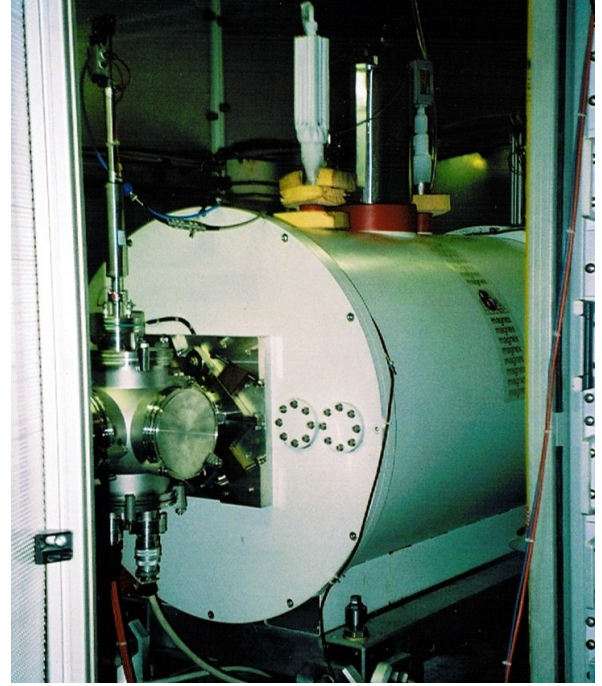


Figure 3.11: Picture of the REXTRAP. The white de-war contains the liquid helium for cooling of the 3 T superconducting solenoid inside.

(typically 10-20 μ s bunch width) and injected into the EBIS (cf. Fig. 3.10). The mass selectivity of the side band cooling technique at REXTRAP is typically $M/\Delta M \approx 500$, and can be pushed up to $M/\Delta M \approx 30000$ under certain circumstances [110]. Due to space charge effects, the capacity of REXTRAP is limited to $<10^8$ ions/bunch.

Electron Beam Ion Source (REXEBS)

The bunched ion beam coming from REXTRAP is injected into the Electron Beam Ion Source (REXEBS) for charge breeding, shown in Figure 3.12. Highly charged ions with mass-to-charge ratios of $A/q < 4.5$ are bred by electron impact ionization, due to collisions of the ions with a dense electron beam. For this an electron gun provides a mono-energetic beam of 3-6 keV electrons with usually 200-250 mA beam current. The electron beam is focused by a 2 T magnetic field of a superconducting solenoid, to gain a current density of typically 150 A/cm² [111, 112]. The negative space charge of the electrons forms a potential well, in which the injected ions are confined radially. In the longitudinal direc-

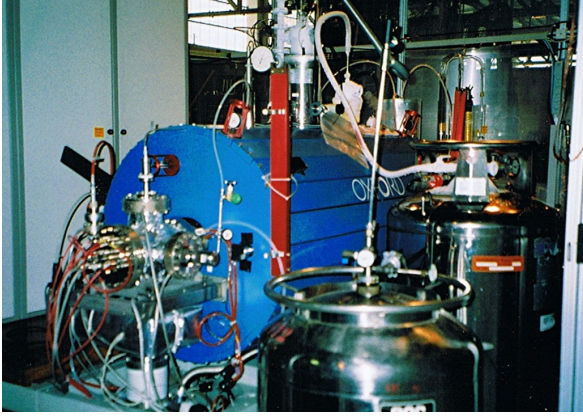


Figure 3.12: Picture of the REXEBIS. The blue cylinder contains the liquid helium for cooling of the 2 T superconducting solenoidal magnet. The electron gun is placed inside the vacuum cross at the front.

tion, confinement is arranged by potential barriers generated by electrodes on the front and on the back side of the EBIS (cf. Fig. 3.13). Thus, the phase space overlap of the injected ions and the electron beam is increased and a high ionization efficiency can be achieved. With the EBIS an $A/q < 4.5$ can be bred within timescales of 20 ms (for light ions with $A < 40$) up to about 200 ms (for heavy ions with $A \sim 200$) [105]. For extraction the potential of the EBIS is decreased to about 20 kV, to allow the injection of the beam into the linear post-accelerator at 5 keV/u beam energy. The ions are extracted as bunch with a typical bunch length of about 100-200 μs , which can be extended to almost 800 μs for high intensity beams (“slow extraction”).

Inside the EBIS an ultra-high vacuum (UHV) better than 10^{-11} mbar is needed to ensure efficient charge breeding and to reduce the contamination of the extracted RIB by ionized residual gas atoms (e.g. C, N, O, Ne, Ar).

The A/q separator

Despite the UHV inside the EBIS, the amount of contaminants in the EBIS beam, stemming from ionized residual gas atoms, can be some orders of magnitude larger than the yield of the isotopes of interest. Thus, it is necessary to select the desired mass according to a special A/q value, before injecting into the linear accelerator. Due to the potential depression caused by the electrons in the EBIS, the extracted ions have

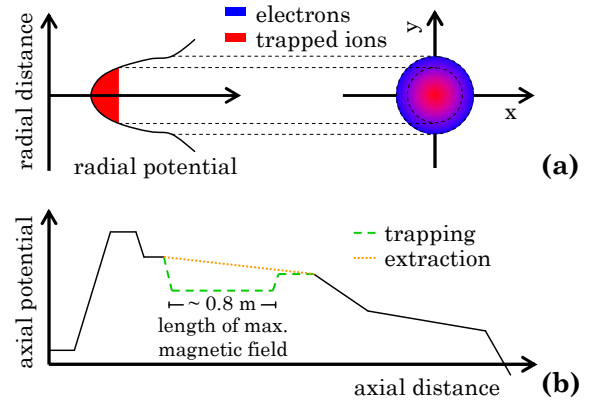


Figure 3.13: (a) Radial potential for the confinement of the ions, caused by the negative charges of the electrons. (b) Electrical potential along the beam axis for closed trap and extraction (not to scale; figure was adapted from Ref. [91]).

a large energy spread of $\Delta E/E \approx 5 \times 10^{-3}$. This limits the A/q resolution of an ordinary magnetic separator system. Therefore an S-shaped combination of an electrostatic deflector and a 90° dipole magnet has been installed downstream of the EBIS [113]. The electrostatic deflector separates the ions according to their energies irrespective of their masses, while the correct A/q value is selected using the magnetic deflector. With this system an A/q resolution of ~ 150 can be achieved, which is enough to select the rare radioactive ions and to suppress the residual gas contaminants in the post-accelerated beam significantly.

3.3.2 The REX-LINAC

The aim of the compact REX linear accelerator (REX-LINAC) is to post-accelerate the charge bred ions with $A/q < 4.5$ stepwise from 5 keV/u to the final beam energy of up to 3.0 MeV/u. It consists of four different types of resonant structures at room temperature, operating at 101.28 MHz and 202.56 MHz, respectively, with 10% duty cycle [88]. In a first stage the ions are accelerated from 5 keV/u to 300 keV/u by a 4-rod Radio Frequency Quadrupole (RFQ). Subsequent acceleration to 1.1-1.2 MeV/u is obtained by an Interdigital-H-type (IH)-structure with 20 accelerating gaps. To match the requirements of a wide range of physics experiments, the ions can either be decelerated down

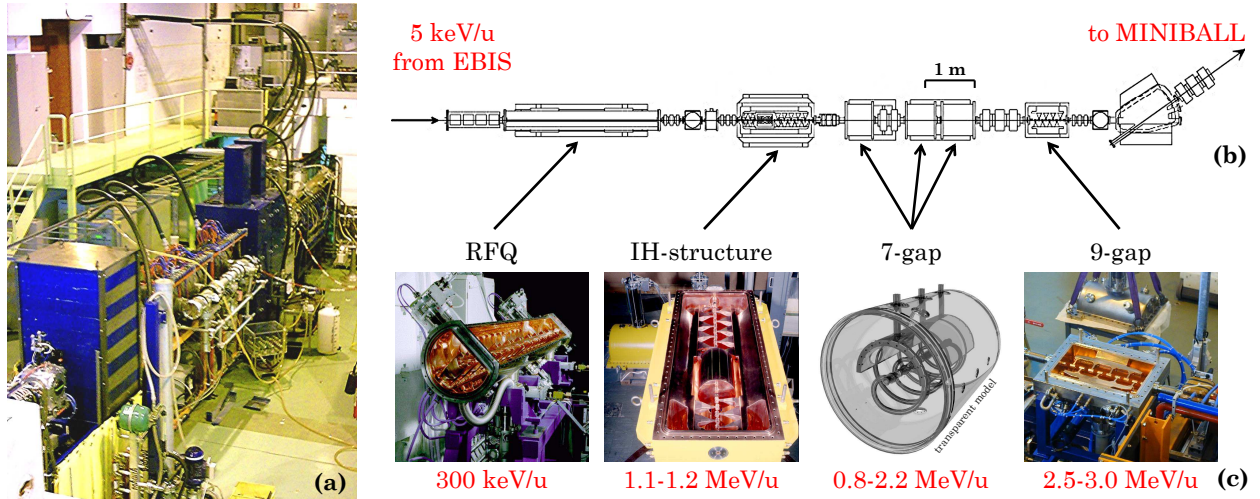


Figure 3.14: (a) Picture of the linear accelerator of REX-ISOLDE in operation (in 2007). The direction of the beam is from the top right to the bottom left. (b) Layout of the REX-LINAC [91] and (c) of its RF accelerating structures (all opened for test/maintenance purposes). Further information is given in the text.

to 0.8 MeV/u or accelerated up to 2.25 MeV/u in three 7-gap resonators. In the final acceleration stage a 9-gap IH-structure provides beam energies of 2.55-3.0 MeV/u. The typical energy spread after the 9-gap amounts to 0.7% [91]. The experiments on neutron-rich Mg and Na isotopes, presented in this work, were performed at beam energies of 3.0 MeV/u and 2.85 MeV/u, respectively. A 65° bending magnet directs the post-accelerated ion beam to the MINIBALL setup.

Since 2009/2010 the REX-LINAC is housed in a concrete bunker to shield the experiments against the high X-ray background from bremsstrahlung, caused by accelerated electrons in the RF-resonating structures.

3.4 The MINIBALL setup

To study the nuclear properties of the post-accelerated radioactive ions after Coulomb excitation or transfer reactions, a very efficient spectrometer for emitted γ rays and particles is necessary. For γ -ray detection the highly efficient MINIBALL spectrometer was developed [114]. In coincidence with particles, detected in Si detectors, advanced Doppler correction for rare radioactive ion beams with beam velocities of $\beta = 0.08$ can be realized as well as an excellent background suppression. For the study of transfer reactions the so-called T-

REX setup was designed recently [115]. For experiments using projectile Coulomb excitation the MINIBALL array is combined with a CD-shaped double-sided silicon strip detector (DSSSD) [116] for scattered particles in forward direction, as shown in Figure 3.17. Two additional particle detectors can be used downstream after the scattering chamber to monitor the position of the beam and the beam composition, respectively. A position-sensitive parallel-plate avalanche counter (PPAC), can be placed right into the beam axis 1.2 m behind the target for measurement of the beam profile in x and y direction [117]. Permanent monitoring of the beam composition in mass A and charge Z is allowed either by a ΔE - E telescope, consisting of a gas cell and a silicon detector, or by a Bragg ionization chamber [118], mounted close to the beam dump position.

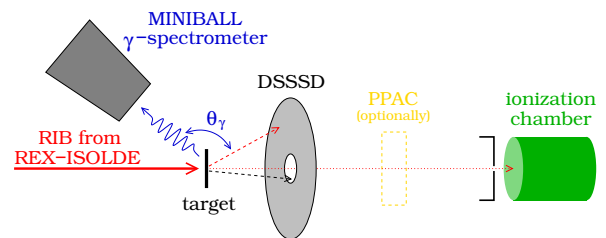


Figure 3.17: Schematic view of the experimental MINIBALL setup for Coulomb-excitation experiments at REX-ISOLDE. Further information on the detector systems is given in the text.

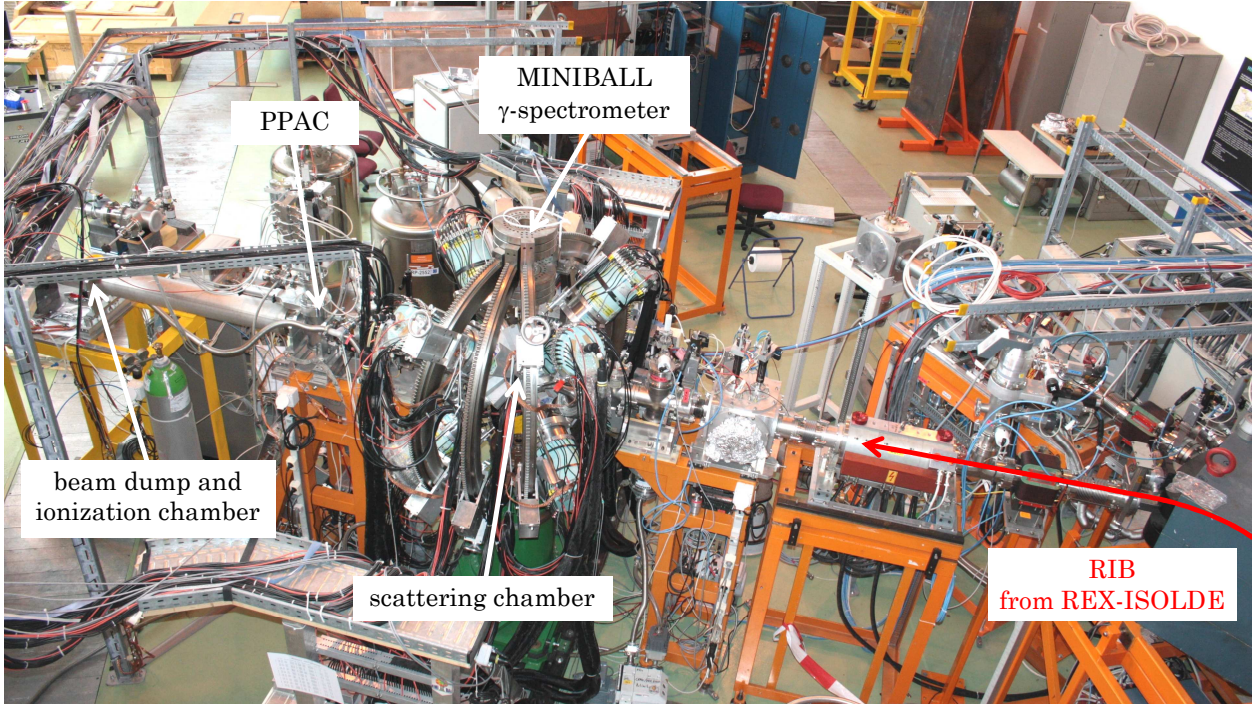


Figure 3.15: Picture of the MINIBALL setup in 2010. The radioactive ion beam delivered by REX-ISOLDE is coming from the bottom right, hitting the secondary target right in the middle of the MINIBALL γ -ray spectrometer. Downstream of the scattering chamber additional detector systems are installed to monitor the position of the beam and its composition.

3.4.1 The MINIBALL γ -ray spectrometer

In the first REX-ISOLDE proposal a newly developed γ -ray spectrometer was already intended [103], to study de-excitation γ rays following the induced nuclear processes. Several technical demands have to be met by this detector array: (i) Due to the low beam intensities the reactions to be observed are very rare. Thus, the spectrometer has to be highly efficient. (ii) The isotopes of interest are radioactive, creating a large amount of background radiation. Therefore high-resolution detectors are needed, to improve the peak-to-total. (iii) Scattering nuclei will recoil at velocities of almost 8% of the speed of light, causing significant Doppler shifts and broadening. Therefore a high granularity is absolutely necessary, to reduce the opening angle of the detector in a compact configuration.

As a result the high-resolution and highly efficient MINIBALL γ -ray spectrometer was developed [114]. It consists of eight triple cluster detectors, mounted on movable arms (“MINIBALL frame”) around the target chamber to allow a compact geometry. Each cryostat con-

tains three individually encapsulated six-fold segmented high-purity germanium crystals (see Figure 3.16). The hexagonal shaped crystals have a length of 78 mm and a diameter of 70 mm. The total number of $8 \times 3 \times 6 = 144$ individual segment signals plus the signals from the 24 central electrodes, referred to as “cores”, are processed using digital electronics (“Digital Gamma Finder” DGF, XIA electronics), enabling count rates of up to 20 kHz per detector. With close distances between target and Ge-detectors of almost 12 cm, the array covers a solid angle of about 60% of 4π . The photopeak efficiency of MINIBALL at 1.3 MeV is 8% after cluster addback. The detectors and the “cold” preamplifier FETs are operated near the temperature of liquid nitrogen (about 80-100 K), giving rise to an average energy resolution of 2.3 keV at $E_\gamma = 1.33$ MeV. The azimuthal electrical segmentation of the detector increases the granularity and ensures a proper Doppler correction for in-flight γ -ray emission at $\beta \sim 8\%$ even at the very close distances between target and detector. Further improvement of the position resolution can be achieved by Pulse Shape Analysis

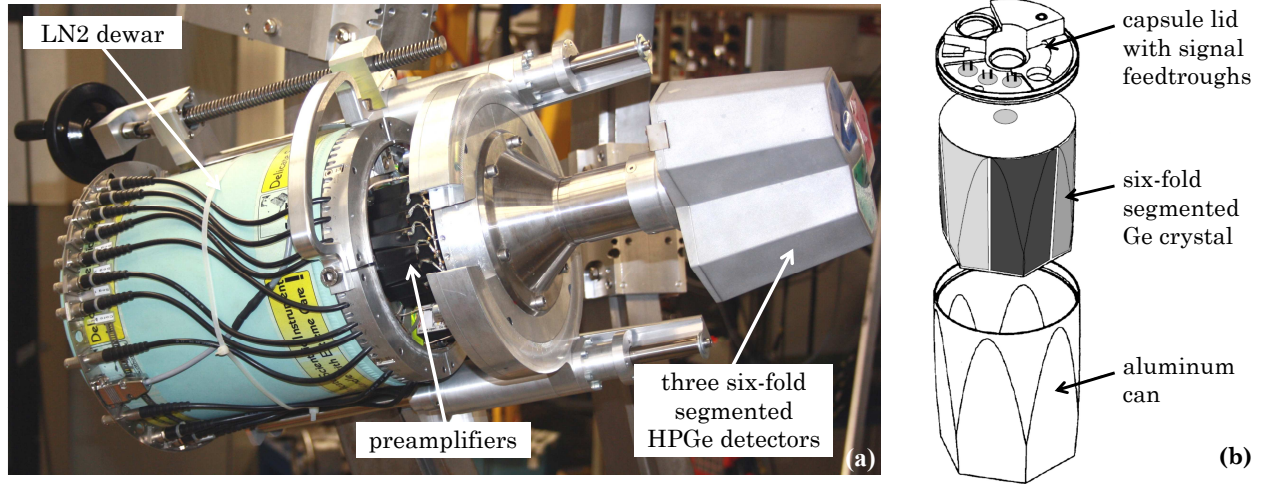


Figure 3.16: (a) Picture of a MINIBALL triple cryostat, containing three segmented high-purity germanium detectors, mounted in the MINIBALL frame. (b) Layout of the six-fold segmented encapsulated MINIBALL HPGe detector (adapted from [114]).

(PSA) [114]. Combining the information of the time-dependent charge collection at the central electrode and at the segments, the interaction point of the γ ray can be reconstructed in radial and azimuthal direction. Thus, a position resolution of about 5 mm can be achieved. This feature of PSA was not used in the present work.

3.4.2 Particle detectors

Double-sided Silicon Strip Detector (DSSSD)

To ensure a proper Doppler correction for in-flight γ -ray emission at $v/c \sim 8\%$, the angular information of the γ ray provided by MINIBALL, has to be combined with the direction and velocity of the scattered beam particle that was detected in coincidence. Therefore the scattered beam and recoiling target nuclei are detected by a CD-shaped double sided silicon strip detector (DSSSD), consisting of four identical quadrants with thicknesses between 35 and 500 μm [116]. As shown in Figure 3.18, each quadrant comprises 16 annular strips at 2 mm pitch at the front side and 24 radial strips at 3.5° pitch at the back side for identification and reconstruction of the trajectories of the scattered nuclei. The inner radius of the active area is 9 mm, the outer radius is 40.9 mm. Thus, the total area of the CD detector is 50 cm^2 , of which approximately 93% is active. The distance between the scattering target and the DSSSD is typically about

30 mm. This corresponds to a forward angle between 16.8° and 53.7° in the laboratory system, which is covered by the CD detector.

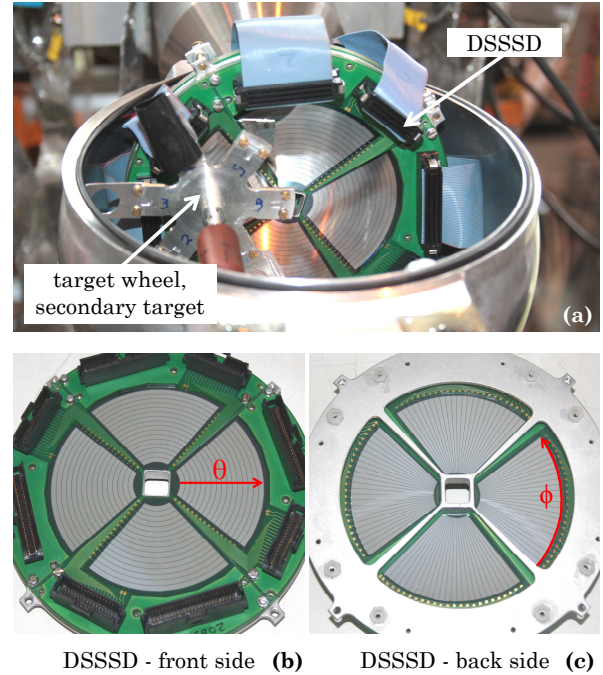


Figure 3.18: (a) Four quadrants of the double-sided silicon strip detector, mounted on the holder inside the scattering chamber. (b) Front view of the detector, showing the 16 annular segments to obtain the θ angle of the scattered particle. (c) Back view of the CD with the mounting frame and the central hole for the beam. The 4×24 radial segments for detection of the ϕ angle can be seen.

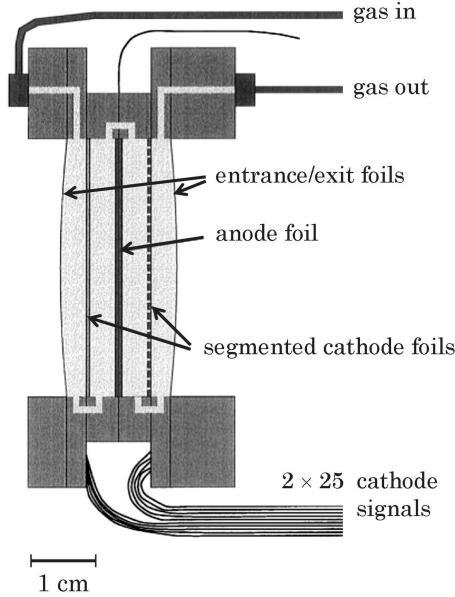


Figure 3.19: Schematic view of the parallel plate avalanche counter (PPAC), used at REX-ISOLDE (adapted from [117]).

Parallel Plate Avalanche Counter (PPAC)

A position-sensitive parallel-plate avalanche counter (PPAC), can be placed right into the beam axis 1.2 m behind the target for measurement of the beam profile in x and y direction (cf. Figure 3.15) [117]. It consists of a central anode foil and two segmented cathode foils, mounted inside a gas volume with a thickness of 17 mm and a diameter of 40 mm. Both cathode foils are segmented into 25 strips at 1.6 mm pitch, to allow a position-sensitive readout of the particle flux in x and y direction, respectively. Figure 3.19 shows a schematic view of the PPAC design. A constant gas flow of CF_4 at a pressure of typically ~ 10 mbar enables counting rates of up to 10^9 ions/s for all heavy ion beams with a proton number $Z \geq 2$.

Bragg detector

Close to the beam dump position a Bragg ionization chamber can be mounted, to allow a permanent monitoring of the beam composition in mass A and charge Z [118]. The detector consists of a gas volume with a length of 70 mm and an aperture of 30 mm, filled with tetrafluoromethane (CF_4) at a pressure of typically 420 mbar. A homogeneous electrical

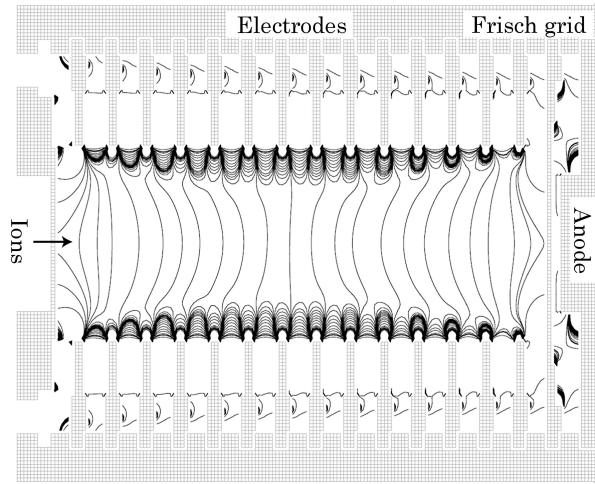


Figure 3.20: Schematic view of the Bragg ionization chamber. Calculated field gradients are drawn, demonstrating the homogeneity of the electrical field inside the detector (adapted from [118]).

field can be applied along the gas volume on 20 electrodes, each separated by 3 mm, as it is shown in Figure 3.20. The incoming ions lose their energy in the gas, following the characteristic dE/dx curve derived by the Bethe formula [119]. Due to the applied longitudinal homogeneous electrical field the generated charges drift with a constant velocity towards the anode. From the time evolution of the anode pulse the mass A and charge Z of the incoming particle can be derived. The Bragg detector was used successfully in the Coulomb-excitation experiment of ^{31}Mg , presented in this work.

Ionization chamber

Another possibility to monitor continuously the composition of the RIB delivered by REX-ISOLDE, is the installation of a ΔE - E_{res} detector, the so-called “ionization chamber”. It consists of a gas-filled ionization chamber with CF_4 at a pressure of 300-450 mbar, generating a Z dependent energy loss signal, coupled to a silicon detector for the measurement of the residual energy E_{res} . Assuming that all ions have the same energy per nucleon, the mass A can be derived from E_{res} . An adjustable collimator is put in front of the entrance windows of the ionization chamber to attenuate the beam to prevent pile-up.

3.5 Time structure of the beam at REX-ISOLDE

The radioactive ion beam provided by REX-ISOLDE is not a continuous flux of particles, but it is delivered in short particle bunches with a characteristic time structure. It is caused by the time-dependent yield of the ions of interest due to their release and radioactive decay and by the duty cycles of the charge breeding and accelerating systems, as mentioned in the previous sections (see Figure 3.21). Experiments can benefit from this feature by efficient background suppression and thus increasing the peak-to-background ratio. To synchronize the data acquisition at the MINIBALL setup with the production and acceleration of the radioactive ions, different time signals are available at ISOLDE.

The first periodic time signal is the time pulse at the beginning of each supercycle of the PS Booster. Its periodicity is $n \times 1.2$ s, with n the total number of proton pulses in the supercycle. This time signal can be used in experiments with laser ion sources, to drive a shutter which periodically blocks the laser light towards the ionization tube. From these so-called Laser ON/OFF measurements the amount of beam contaminants can be derived, as it is shown in section 4.5.5.

Immediately before a proton beam from the PSB impinges on the ISOLDE target, the T1 signal is generated. Since the radionuclides are only produced at the time of the proton beam impact, the amount of short-lived species detected by the MINIBALL particle detectors will decrease with increasing time difference between T1 and the detection time. Thus, the analysis of such isotopes is typically restricted to time differences of a few half-lives with respect to the T1 signal, to suppress long-lived or stable contaminants substantially.

An additional time signal is related to the injection of the charge bred ions from the EBIS into the REX-LINAC. On the one hand it is used as a hardware trigger to synchronize the accelerator with the incoming particle bunches. On the other hand it is used to trigger a 1 ms time gate in the data acquisition of MINIBALL, referred to as “On Beam” window. Due to the typical bunch length of the ion beam of 150 μ s, all particles

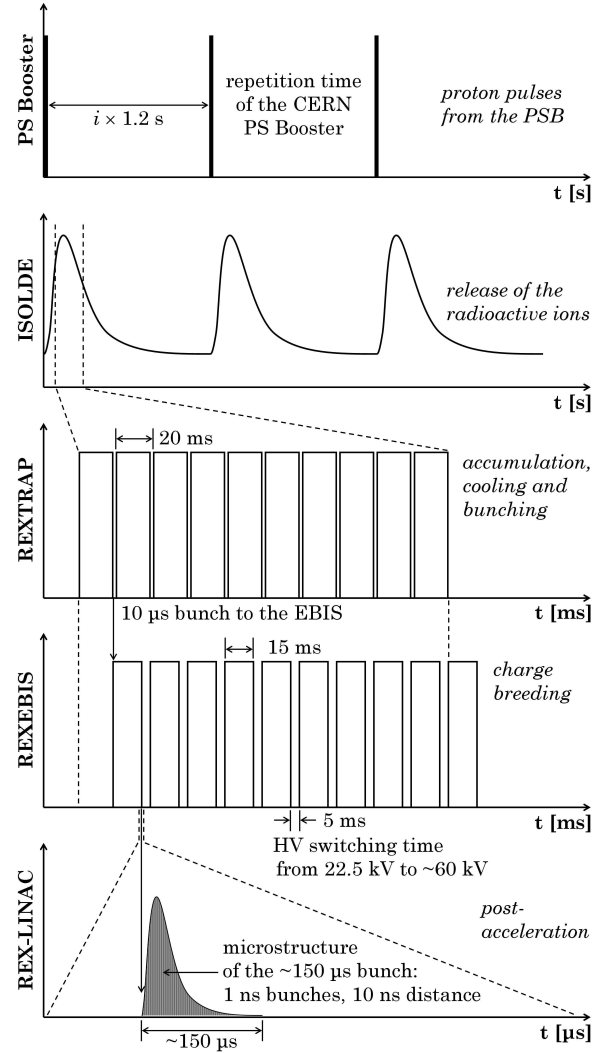


Figure 3.21: Schematic view of the time structure of REX-ISOLDE, using the example of a short-lived light ion beam (adapted from [88]). More detailed information is given in the entire text of this chapter.

arrive at the MINIBALL target within 150 μ s after the EBIS signal. For longer time differences only background should be detected. Therefore the analysis of the nuclear reaction events could be limited to $\Delta t_{\text{EBIS}} \leq 150$ μ s for background suppression.

3.6 Coulomb excitation

In general, the reduced transition probability $B(E2)$ can be determined by different experimental methods. One common possibility, which was already mentioned on page 7, is to measure the lifetime of the excited nuclear state via the recoil distance Doppler-shift (RDDS) or the

Doppler-shift attenuation method (DSAM). The former method was used to study the properties of ^{56}Cr , which will be discussed in the second part of this work. For rare exotic nuclei far off stability, usually the Coulomb-excitation technique in inverse kinematics is applied to determine the $B(E2)$ value. For pure Coulomb interaction between the projectile and target nuclei, the excitation can be expressed by the same electromagnetic transition matrix elements characterizing the de-excitation of the states that are involved. Thus, measurements of the Coulomb-excitation cross sections allows a detailed study of the nuclear structure of the low-lying nuclear states.

The following sections will give an overview of the underlying theory in a semi-classical approach, which is commonly used in coupled-channel codes for the calculation of the theoretical Coulomb-excitation cross sections (e.g. CLX [120, 121], GOSIA [122, 123]). A more detailed description can be found in Alder *et al.* [124, 125], where also the fully quantum-mechanical approach is given.

3.6.1 Semi-classical approach

Elastic and inelastic scattering

In the semi-classical approach of the Coulomb excitation it is assumed, that the particles follow classical Rutherford trajectories during the scattering process, as indicated in Picture 3.22. The excitation process itself is treated quantum-mechanically. Thus the Coulomb-excitation cross section is given by

$$\left(\frac{d\sigma}{d\Omega}\right)_{\text{CE}} = \left(\frac{d\sigma}{d\Omega}\right)_{\text{ruth}} P_{i \rightarrow f}$$

where $\left(\frac{d\sigma}{d\Omega}\right)_{\text{ruth}}$ is the classical Rutherford cross section. $P_{i \rightarrow f}$ is the quantum-mechanical probability of the excitation from an initial state $|i\rangle$ to a final state $|f\rangle$ in a collision in which the particle is scattered into the solid angle element $d\Omega$. The Rutherford cross section of elastic scattering can be written classically as

$$\left(\frac{d\sigma}{d\Omega}\right)_{\text{ruth}} = \left(\frac{a_0}{2}\right)^2 \left(\sin^4\left(\frac{\theta_{\text{CM}}}{2}\right)\right)^{-1}.$$

θ_{CM} is the scattering angle in the center-of-mass system and $2a_0 = d_{\text{min}}$ is the distance of closest

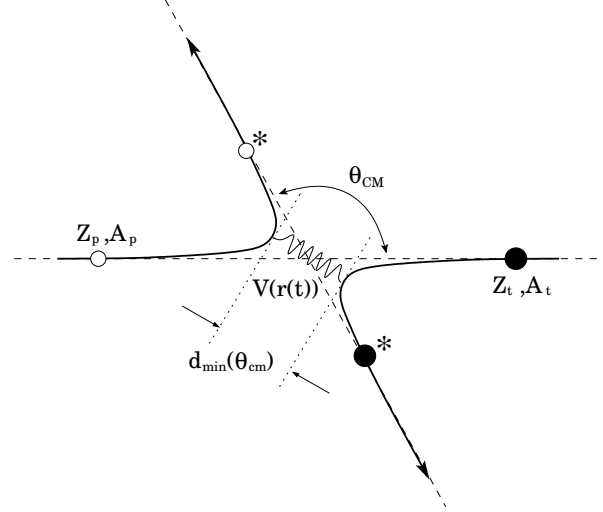


Figure 3.22: Schematic diagram of the Coulomb-excitation process of a projectile nucleus (Z_p, A_p), scattering inelastically on a target nucleus (Z_t, A_t), in the center-of-mass system.

approach between the projectile and target nuclei in a scattering process with impact parameter $b = 0$. a_0 can be expressed in terms of the proton numbers Z_p and Z_t for projectile and target nuclei, respectively, the reduced mass m and the velocity $\beta = v/c$:

$$\begin{aligned} a_0 &= \frac{1}{2} \frac{Z_p Z_t e^2}{E_{\text{CM}}} = \frac{Z_p Z_t e^2}{mc^2 \beta^2} \\ &\approx 0.71999 \left(1 + \frac{A_p}{A_t}\right) \frac{Z_p Z_t}{E_p} [\text{fm}]. \end{aligned}$$

To ensure the validity of the semi-classical description, the size of the scattering nuclei, taken as a wave packet with the de Broglie wavelength λ , has to be small compared to the dimensions of the classical orbit. Since such a wave packet will move along the classical trajectory, the semi-classical approach is justified. Therefore the so-called **Sommerfeld parameter**

$$\eta = \frac{a_0}{\lambda} = \alpha \frac{Z_p Z_t}{\beta}$$

is introduced, where $\alpha = 1/137$ is the fine structure constant. For the semi-classical approach the condition

$$\eta \gg 1$$

has to be fulfilled. Moreover, in heavy ion collisions well below the Coulomb barrier it guarantees that the distance of closest approach is large

compared to the dimensions of the nuclei, preventing the nuclei to come into reach of the nuclear interaction or even penetrate the Coulomb barrier. In the present work the Sommerfeld parameters were $\eta \approx 52$ for a ^{31}Mg beam onto a ^{109}Ag target at a beam energy of 3.0 MeV/u and $\eta \approx 48$ for a $^{29,30}\text{Na}$ beam onto a ^{104}Pd target at a beam energy of 2.85 MeV/u, respectively.

First-order perturbation theory

Due to the movement of the projectile the electromagnetic field between the incoming projectile and the target nucleus will change in time and can be described by a time-dependent interaction potential $V(\vec{r}(t))$. If the interaction is weak, the excitation amplitude for an excitation from a state $|i\rangle$ to a state $|f\rangle$ can be approximated by first-order perturbation theory [124]:

$$a_{i \rightarrow f} = \frac{1}{i\hbar} \int_{-\infty}^{\infty} e^{\frac{i}{\hbar} \Delta E_{if} t} \langle f | V(\vec{r}(t)) | i \rangle dt$$

where ΔE_{if} is the energy difference between the involved states. The probability for Coulomb excitation is given by

$$P_{i \rightarrow f} = |a_{i \rightarrow f}|^2.$$

The differential and absolute excitation cross sections are derived by a multipole expansion of the interaction potential $V(\vec{r}(t))$. It contains both electric and magnetic parts. Thus, the Coulomb excitation of the projectile nucleus¹ can be caused either by the electric or the magnetic field of the target nucleus. Both excitation mechanisms can be treated separately. For the multipole expansion of the electrostatic part of $V(\vec{r}(t))$ the excitation probability is

$$a_{i \rightarrow f}^{E\lambda} = \frac{4\pi Z_t e}{i\hbar} \sum_{\lambda\mu} \frac{\langle I_i m_i | \mathcal{M}(E\lambda, \mu) | I_f m_f \rangle^*}{2\lambda + 1} S_{E\lambda\mu}$$

The factor $S_{E\lambda\mu}$ contains the time integral along the classical trajectory of the scattered particle and depends on the parameters of the scattering process. In contrast the matrix element

¹The target excitation can be explained in an completely analog way. Only the expressions for projectile and target have to be interchanged: $Z_p \rightleftharpoons Z_t, \dots$

$\langle I_i m_i | \mathcal{M}(E\lambda, \mu) | I_f m_f \rangle$ depends only on the nuclear properties of the scattered particle. For the absolute excitation cross section of the multipole order λ it follows:

$$\sigma_{E\lambda} = \left(\frac{Z_t e}{\hbar v} \right)^2 a_0^{-2\lambda+2} B(E\lambda; I_i \rightarrow I_f) f_{E\lambda}(\xi),$$

where

$$f_{E\lambda}(\xi) = \int_{\theta_{\min}}^{\theta_{\max}} \frac{df_{E\lambda}(\theta, \xi)}{d\Omega} d\Omega$$

is the integrated non-relativistic Coulomb-excitation function over the range of the solid angle, that is covered by θ_{\min} and θ_{\max} of the particle detector (in the CM system). The so-called adiabaticity parameter ξ will be explained at the end of this section.

The total cross section for magnetic excitation of multipole order λ can be derived in an analog way:

$$\sigma_{M\lambda} = \left(\frac{Z_t e}{\hbar c} \right)^2 a_0^{-2\lambda+2} B(M\lambda; I_i \rightarrow I_f) f_{M\lambda}(\xi).$$

Compared to the cross section of electric excitation of the same multipole order, magnetic excitation is suppressed by a factor of $(v/c)^2 = \beta^2$. For the typical beam energies of ≤ 3.0 MeV/u at REX-ISOLDE the maximum velocity of the incoming particle is $\beta \approx 0.08$. Thus, electric excitations will dominate in the Coulomb-excitation experiments presented in this work.

In an inelastic scattering process, the collision time $\tau_{\text{coll}} = a_0/v$ has to be of the same order of magnitude, or even shorter than the time of the internal motion of the nucleus $\tau_{\text{nucl}} = \hbar/\Delta E_{if}$, to excite a final state $|f\rangle$ from a state $|i\rangle$. The **adiabaticity parameter** ξ is given by the ratio of both times:

$$\begin{aligned} \xi &= \frac{\tau_{\text{coll}}}{\tau_{\text{nucl}}} = \frac{a_0 \Delta E_{if}}{\hbar v} \\ &= \frac{Z_1 Z_2 e^2 c}{\hbar} \left(\frac{1}{\beta_f} - \frac{1}{\beta_i} \right) \stackrel{!}{\leq} 1 \end{aligned}$$

where β_i and β_f is the velocity of the incoming nucleus before and after the Coulomb-excitation process, respectively [125]. If the velocity of the projectile is too slow, i.e. the collision time is comparatively long, the nucleus can follow

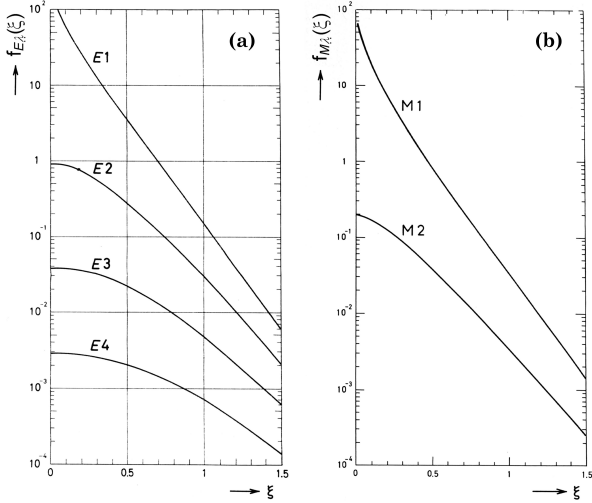


Figure 3.23: Logarithmic plotting of the integrated non-relativistic Coulomb-excitation function $f_{\pi\lambda}(\xi)$ for (a) electric transitions ($\lambda = 1,2,3,4$) and for (b) magnetic transitions ($\lambda = 1,2$) [125].

the perturbation caused by $V(\vec{r}(t))$ adiabatically and thus, no excitation will occur. As shown in Figure 3.23, the Coulomb-excitation functions $f_{\pi\lambda}(\xi)$ decrease exponentially with increasing adiabaticity ξ . Therefore the excitation probability is reduced significantly for slow impact velocities or high excitation energies. In experiments with low-energy Coulomb excitation at beam energies of a only few MeV/u, as described in the present work, the possible excitation energies are limited to typically 1-2 MeV by the adiabatic cutoff.

The excitation probability is not only affected by the adiabaticity of the transition of order $\pi\lambda$ from a state $|i\rangle$ to $|f\rangle$, but also by the so-called **excitation strength parameter** χ . Following [125] it is defined as

$$\chi_{i \rightarrow f}^{(E\lambda)} = \frac{\sqrt{16\pi} Z_t e}{\hbar v} \frac{(\lambda - 1)!}{(2\lambda + 1)!!} \frac{\langle I_f || \mathcal{M}(E\lambda) || I_i \rangle}{a_0^\lambda \sqrt{2I_i + 1}}$$

for electric excitations. An analog expression is found for magnetic excitations:

$$\chi_{i \rightarrow f}^{(M\lambda)} = \frac{\sqrt{16\pi} Z_t e}{\hbar c} \frac{(\lambda - 1)!}{(2\lambda + 1)!!} \frac{\langle I_f || \mathcal{M}(M\lambda) || I_i \rangle}{a_0^\lambda \sqrt{2I_i + 1}}$$

The excitation strength can be interpreted as the possible total angular momentum $\lambda\hbar$ which can be transferred in a head-on collision of the two

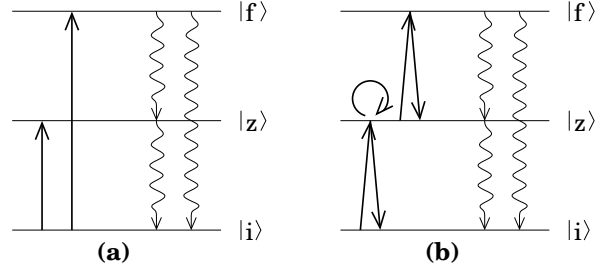


Figure 3.24: (a) Schematic diagram of one-step Coulomb excitation from a state $|i\rangle$ to states $|z\rangle, |f\rangle$. (b) Possible multi-step excitations to the final states, including some virtual excitations and de-excitations.

nuclei. An estimation is given by

$$\chi_{i \rightarrow f}^{(\pi\lambda)} \approx \frac{V^{(\lambda)}(a_0) \tau_{\text{coll}}}{\hbar}$$

where $V^{(\lambda)}(a_0)$ is the interaction potential of multipole order λ between projectile and target at half the distance of closest approach a_0 , which is proportional to $a_0^{-(\lambda+1)}$. In experiments with beam energies below the Coulomb barrier, excitation strengths of $\chi^{(E2)} \leq 10$ are possible for electric quadrupole transitions. Due to these rather large excitation strengths multi-step Coulomb excitations are possible (see Fig. 3.24). A sufficient condition for the applicability of first-order perturbation theory in the Coulomb excitation is, that all possible excitation probabilities are small. Obviously this is no longer the case for multi-step Coulomb excitation. Thus, perturbation expansion of higher order has to be considered.

Higher-order perturbation theory

Assuming an excitation from a state $|i\rangle$ to a state $|f\rangle$ via intermediate states $|z\rangle$, the total excitation amplitude is given to second order by [125]

$$a_{i \rightarrow f} = a_{i \rightarrow f}^{(1)} + \sum_z a_{i \rightarrow z \rightarrow f}^{(2)}$$

where the first term is the excitation amplitude of first order and the second term $a_{i \rightarrow z \rightarrow f}^{(2)}$ is defined as

$$a_{i \rightarrow z \rightarrow f}^{(2)} = \frac{1}{i\hbar} \int_{-\infty}^{\infty} e^{\frac{i}{\hbar} \Delta E_{zf} t} \langle f | V(\vec{r}(t)) | z \rangle dt \times \frac{1}{i\hbar} \int_{-\infty}^{\infty} e^{\frac{i}{\hbar} \Delta E_{iz} t} \langle z | V(\vec{r}(t)) | i \rangle dt$$

where ΔE_{iz} and ΔE_{zf} are the energy differences between the involved states. In order to simplify the summation over all intermediate states $|z\rangle$, some important cases with only one intermediate state will be discussed in the following paragraphs.

In the first case a final state with spin I_f can be excited directly or via another, low-lying state with spin I_z (cf. Fig. 3.24). As given in [125] a pure two-step excitation through an intermediate state $|z\rangle$ can be observed if the direct excitation $I_i \rightarrow I_f$ is small or vanishing:

$$\chi_{i \rightarrow f} \ll \chi_{i \rightarrow z} \chi_{z \rightarrow f}$$

A typical example for such a two-step excitation is the excitation of the 4^+ state in even-even nuclei. Due to the strong hindrance of a direct $E4$ excitation to this level (cf. Fig. 3.23(a)), it will be populated preferably by two succeeding electric quadrupole transitions through the 2^+ state:

$$0^+ \xrightarrow{E2} 2^+ \xrightarrow{E2} 4^+$$

Another application of the second-order perturbation theory is the effect of the quadrupole moments of the involved states on the excitation cross section. In this case the intermediate state $|z\rangle$ is one of the magnetic sub-states of the initial or the final level. The transition between the final state and its magnetic sub-state occurs through the interaction with its quadrupole moment. The transition strength depends on the magnitude of the matrix element $\langle I_f || \mathcal{M}(E2) || I_z \rangle$, which is directly proportional to the spectroscopic quadrupole moment Q_s^I :

$$Q_s^I = \sqrt{\frac{16\pi I(2I-1)}{5(I+1)(2I+1)(2I+3)}} \times \langle I || \mathcal{M}(E2) || I \rangle$$

where $I = I_f = I_z$ [24]. In the case of a rotational nucleus, the spectroscopic quadrupole moment Q_s of a state with spin I is related to the intrinsic quadrupole moment Q_0 by [24]

$$Q_s = \frac{3K^2 - I(I+1)}{(I+1)(2I+3)} Q_0$$

For transitions within such a rotational band the reduced transition probability is linked to the intrinsic quadrupole moment Q_0 by [24]

$$B(E2, I_i \rightarrow I_f)_{\text{rot}} = \frac{5}{16\pi} e^2 Q_0^2 \left| \langle I_i 2K0 | I_f K \rangle \right|^2$$

The effect of the quadrupole moment on the differential Coulomb-excitation cross section of a state I is illustrated in Figure 3.25, using the example of the $5/2^+$ state in ^{31}Mg . The cross section was calculated, using a constant $B(E2)$ value of $0.018 \text{ e}^2\text{b}^2$ but three different quadrupole moments (0 eb and $\pm 0.59 \text{ eb}$). For a prolate (oblate) deformation, the differential Coulomb-excitation cross section will increase (decrease) significantly with respect to the spherical configuration. Hence, for the experiment presented in this work, a change of the total integrated Coulomb-excitation cross section of about $\pm 4.3\%$ could be expected.

For nuclei with ground-state spin equal to 0 or $1/2$ it is possible to determine the quadrupole moment Q of an excited state by a measurement of the relative cross sections for different scattering angles. If the ground-state spin is equal to 1 or even larger, only a linear combination of the static moment of the excited state and the quadrupole moment of the ground state can be deduced by this method, due to interference terms arising from both moments. A detailed analysis of these effects is given in [125].

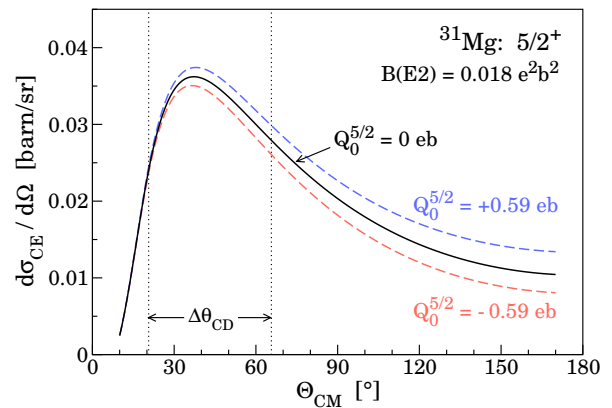


Figure 3.25: Differential Coulomb-excitation cross section for population of the $5/2^+$ state of ^{31}Mg , impinging a ^{31}Mg beam at 3.0 MeV/u onto a 4.0 mg/cm^2 thick ^{109}Ag target. Depending on a possible prolate (or oblate) deformation of the nucleus, the integrated cross section obtained in the experiment will change by about $\pm 4.3\%$, as indicated by the dashed lines. The calculation was done using the classical Coulomb-excitation code CLX [120, 121].

3.6.2 “Safe” Coulomb excitation

In a scattering process the minimum distance $d_{\min}(\theta_{\text{CM}})$ between the incoming projectile and the target nucleus depends on the scattering angle θ_{CM} (cf. Fig. 3.22). As long as the strong interaction is negligible, the semi-classical theory of Coulomb excitation gives

$$d_{\min}(\theta_{\text{CM}}) = a_0 \left(1 + \frac{1}{\sin^4 \left(\frac{\theta_{\text{CM}}}{2} \right)} \right).$$

To fulfill the basic idea of Coulomb excitation, the interaction between the colliding nuclei has to be purely electromagnetic. To ensure the negligibility of any contribution from the nuclear interaction to the excitation process, the minimum distance between projectile and target in a head-on collision has to exceed the sum of both nuclear radii R_p and R_t , plus an additional safe distance Δ_s :

$$2a_0 > R_p + R_t + \Delta_s$$

Cline *et al.* found that for a safe distance of $\Delta_s = 5$ fm and $R_i = 1.25A_i^{1/3}$ the contribution of the nuclear interaction to the total excitation cross section is less than 0.1% [126]. This condition corresponds to beam energies below 4.5 MeV/u for heavy ions (e.g. ^{208}Pb) decreasing to less than 4.1 MeV/u for light ions (e.g. ^{40}Ar). If the beam energy exceeds these “safe” bombarding energies, Coulomb-nuclear interference effects can be minimized by a restriction of the scattering angle to forward angles well below the grazing angle. Thus, classical trajectories can be chosen where the distance of closest approach exceeds the safe distance mentioned above [126].

3.6.3 Relative measurement of the transition strength

In a Coulomb-excitation experiment the number of inelastically scattered projectile and target nuclei is a direct measure of the excitation probability between states $|i\rangle$ and $|f\rangle$ in the respective nuclei. This number can be determined experimentally by the detection of the de-exciting γ rays of the transition $|f\rangle \rightarrow |f'\rangle$. For projectile

excitation the number of detected γ rays is

$$N_{\gamma,\text{proj}}(f \rightarrow f') = \epsilon_{\gamma,\text{proj}} b_{f \rightarrow f'} \sigma_{\text{proj}}(f) \frac{\rho d_t N_A}{A_t} I,$$

where $\epsilon_{\gamma,\text{proj}}$ is the absolute detection efficiency of the γ rays, $b_{f \rightarrow f'}$ is the branching ratio of the transition, $\sigma_{\text{proj}}(f)$ is the absolute Coulomb-excitation cross section of the state $|f\rangle$ and I is the beam intensity. The number of scattering centers in the target is expressed in terms of the target thickness ρd_t in mg/cm², the mass A_t of the target nuclei and Avogadro’s constant N_A .

In experiments with radioactive ion beams the beam intensity is normally not well known or has a rather large uncertainty. Therefore, the absolute Coulomb-excitation cross section is typically measured in relation to another, well-known excitation cross section, e.g. the excitation of the target nuclei. Analog to the number of detected γ rays of the projectile mentioned above, the number of γ rays, de-exciting a state $|f\rangle$ of the Coulomb-excited target nucleus, is given by

$$N_{\gamma,\text{target}}(f \rightarrow f') = \epsilon_{\gamma,\text{target}} b_{f \rightarrow f'} \sigma_{\text{target}}(f) \frac{\rho d_t N_A}{A_t} I.$$

The ratio of projectile and target excitation is independent of the physical properties of the beam and the target (e.g. intensity, thickness, mass):

$$\frac{N_{\gamma,\text{proj}}(f \rightarrow f')}{N_{\gamma,\text{target}}(f \rightarrow f')} = \frac{\epsilon_{\gamma,\text{proj}} b_{f \rightarrow f'} \sigma_{\text{proj}}(f)}{\epsilon_{\gamma,\text{target}} b_{f \rightarrow f'} \sigma_{\text{target}}(f)}$$

Thus, the unknown Coulomb-excitation cross section of a state $|f\rangle$ of the (radioactive) projectile can be derived from the ratios of the numbers of detected γ rays, the detection efficiencies and the branching ratios, and of the well known target excitation cross section, which can be calculated with coupled-channel codes like CLX or GOSIA.

Chapter 4

Data analysis

Modern experiments in nuclear and particle physics record all the relevant information on an event-by-event basis. To characterize a physical event in an experiment, all information on energy, position and time of different sub-events is collected by the complex detector system of various particle- and γ -ray detectors, described in the last chapter. The information of the different detectors then has to be re-combined to the original event, for example a particle- γ coincidence. This process is referred to as “event-building”. Thus, the raw data have to be preprocessed efficiently, before the experimental data can be analyzed in detail. The following sections will therefore concentrate on the sorting of the data (Sec. 4.1) as well as careful calibration of the detector systems (Sec. 4.2 and 4.3). Due to the low beam intensities of radioactive beams, background suppression is crucial in the advanced analysis. A detailed investigation of the beam composition and the application of reasonable energy and time gates will be presented in Sections 4.5 and 4.6.

4.1 Acquisition and processing of the data

The data acquisition system MAR_aBQU [127] of MINIBALL is based on the GSI front-end system MBS [128] combined with the ROOT framework developed at CERN [129] for the back-end visualization. Recorded list mode data are (pre-)processed, using C/C++ based codes, and stored in the efficient, user-optimized ROOT format. In principle three different steps are implemented in the sorting routines:

1. All particle events in the DSSSD are cali-

brated and correlated to the corresponding time stamps. The registered γ -ray events are calibrated. Coincident events in neighboring segments are expected to belong to a single, Compton-scattered γ ray and are added up (“add-back routine”). The segment with the highest detected energy deposition is assumed to be the point of interaction for this γ -ray event.

2. All γ -ray events within a time window of typically 4-6 μ s with respect to a detected particle are correlated to this particle. This information on particle- γ coincidence is stored in a ROOT tree.
3. User-defined time gates are set, according to prompt and random particle- γ coincidences. Random coincidences are expected to contain mostly background radiation. The information on each particle is stored in a special ROOT tree with a parameter, indicating whether this particle is in prompt or random coincidence to a γ ray.

4.2 Detector calibration

4.2.1 Energy calibration of the DSSSD

Calibration of all 160 individual segments of the DSSSD was done with an α -source, containing ^{148}Gd , ^{239}Pu , ^{241}Am , and ^{244}Cm . Thus, the energies of the α particles used for calibration were 3.183 MeV, 5.157 MeV, 5.486 MeV, and 5.805 MeV. In Figure 4.1 an α -calibration spectrum is shown, using the example of a single ring of the first quadrant.

The relevant energy range of the scattered particles detected in the present experiments is about 20-70 MeV. Due to the extrapolation of

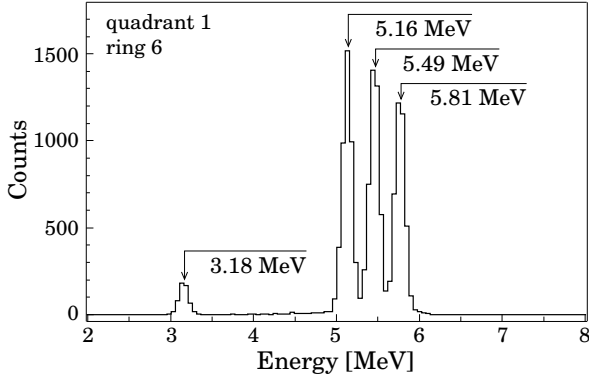


Figure 4.1: Detail of the calibration spectrum of the DSSSD, using the example of ring 6 of quadrant 1. The α -lines of ^{148}Gd , ^{239}Pu , ^{241}Am , and ^{244}Cm are well separated, demonstrating the excellent energy resolution of the detector.

the calibration data up to this energy range, the α -calibration might cause large deviations of about 2-5 MeV. Thus, an optional energy offset was implemented in the analysis, to compensate possible energy differences at high energies.

4.2.2 Energy- and efficiency calibration of the MINIBALL detectors

To calibrate the MINIBALL clusters and to determine their absolute detection efficiency ϵ_{abs} , radioactive ^{60}Co , ^{152}Eu and ^{133}Ba sources were mounted onto the target frame at the target position. A sum spectrum of all MINIBALL cluster detectors can be found in Figure 4.2.

The absolute efficiency at 1.33 MeV was derived from the ratio of the intensities of the 1173 keV peak and the sum peak at 2506 keV of

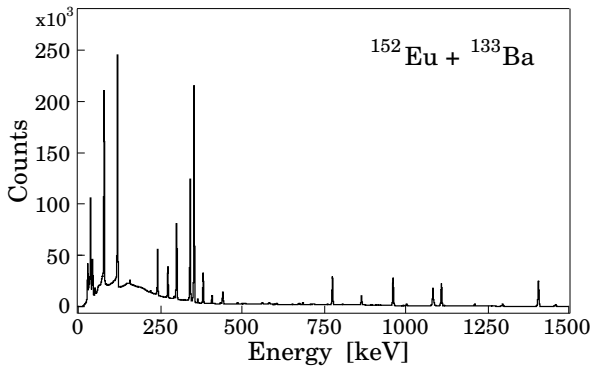


Figure 4.2: Sum spectrum of all eight MINIBALL cluster detectors, containing ^{152}Eu and ^{133}Ba γ -ray decay transitions used for calibration.

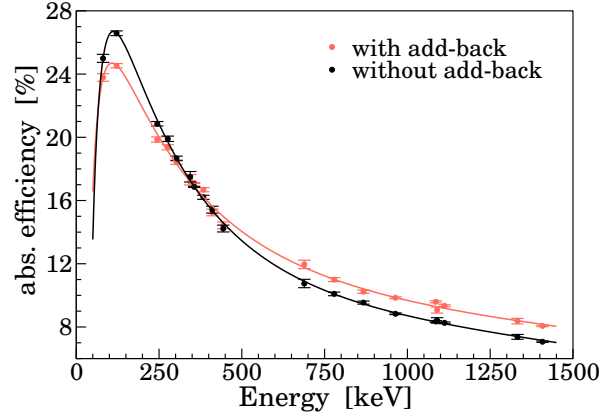


Figure 4.3: Absolute detection efficiency of the MINIBALL array as a function of the γ -ray energy. For $E_\gamma > 500$ keV the add-back correction increases the efficiency by 10-15% compared to the non-corrected efficiency.

^{60}Co . Without the addback correction a value of $\epsilon'_{\text{abs}} = 7.374 \pm 0.153\%$ can be achieved, while the addback correction increases the absolute detection efficiency of the MINIBALL array up to $\epsilon_{\text{abs}} = 8.369 \pm 0.174\%$. The relative efficiency was determined as a function of the γ -ray energy in the range of 80 keV to 1.4 MeV, using Eu and Ba sources, and fitted to the absolute efficiency at 1.33 MeV (see Fig. 4.3). For the fit the function of the absolute efficiency

$$\epsilon_{\text{abs}} = \sum_{i=0}^4 a_i (\ln(E_\gamma))^i$$

was used. For the addback corrected spectra the parameters are $a_0 = -946.6$, $a_1 = 639.0$, $a_2 = -153.5$, $a_3 = 15.97$, and $a_4 = -0.614$, where E_γ is given in keV.

Due to recoil velocities of typically $v \approx 0.05 c$ and the compact geometry of the setup, states with lifetimes of several nanoseconds will decay in rest after implantation of the scattered ion in the DSSSD. Hence, the γ rays are not emitted by a “point-like” source at target position in the center of the MINIBALL spectrometer, but by a much larger area located downstream of the target. Therefore, the efficiency of each MINIBALL detector depends highly on its position in the frame, relative to the position of the implanted ion in the DSSSD. To account for this effect, the detection efficiency of each individual MINIBALL cluster detector was measured as a function of the position of a radioactive source

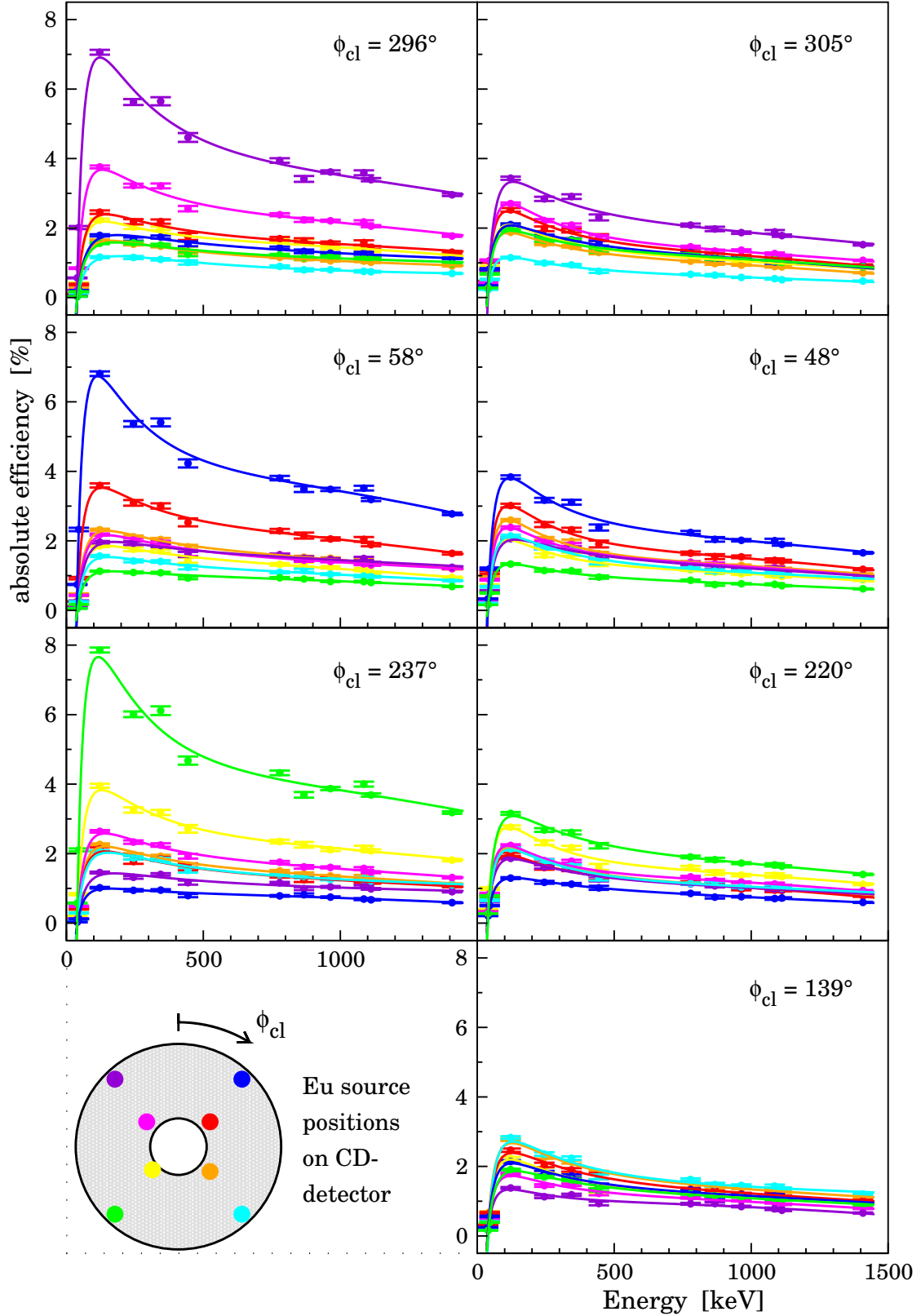


Figure 4.4: Energy-dependent detection efficiency of 7 individual MINIBALL cluster detectors in add-back mode, depending on the position of a ^{152}Eu source. The source was mounted in front of the DSSD at eight different positions (see color code). MINIBALL detectors are labeled by their ϕ_{cl} angle, as they are mounted in the frame. The left column shows detectors placed in forward direction, whereas the right column shows detectors placed in backward direction.

in front of the DSSSD. Therefore the “active” parts of the DSSSD, i.e. the silicon wafers and its mounting PCBs, were replaced by a special plastic disc for safer handling. An ^{152}Eu source was mounted on the disc at eight different positions, corresponding to the center of the innermost and outermost rings of each quadrant of the DSSSD, as displayed in the bottom left part of Fig. 4.4.

The spectra show a significantly increased efficiency of the cluster detectors in forward direction for γ -ray sources in the nearby quadrant of the DSSSD. For example the absolute detection efficiency of a 500 keV γ ray is a factor of 2 higher for the detector in forward direction ($\phi = 296^\circ$), compared to the one in backward direction ($\phi = 305^\circ$), if the source is placed at the outermost position of the top left CD quadrant (see first row of Fig. 4.4). In a first approximation the evolution of the efficiency of a backward cluster detector, depending on the position \vec{r}_{source} of the source, can be described by the simple variation of the distance between source and detector:

$$\epsilon(\vec{r}_{\text{source}}) = \epsilon_0 \left(\frac{|\vec{r}_0 - \vec{r}_{\text{det}}|}{|\vec{r}_{\text{source}} - \vec{r}_{\text{det}}|} \right)^2,$$

where ϵ_0 is the efficiency at a reference point \vec{r}_0 . For detectors in forward direction the explanation of the observed efficiencies is much more complex, due to additional material in the line of sight between source and detector. The amount of this material, e.g. the silicon wafers, PCBs, copper cables, and the massive aluminum mounting frame of the DSSSD, depends highly on the position. Furthermore it attenuates especially low-energy γ radiation. Thus, in forward direction the efficiency at around 100-200 keV is lower than in backward direction for distances, that exceed the distance between the center of the DSSSD and the cluster detector (cf. Fig. 4.4).

4.3 Doppler correction

If a γ ray is emitted in-flight ($\beta > 0$), the detected energy $E_{\gamma,\text{lab}}$ is Doppler shifted:

$$E_{\gamma,\text{lab}} = \frac{\sqrt{(1 - \beta^2)}}{1 - \beta \cos \theta_\gamma} E_{\gamma,0},$$

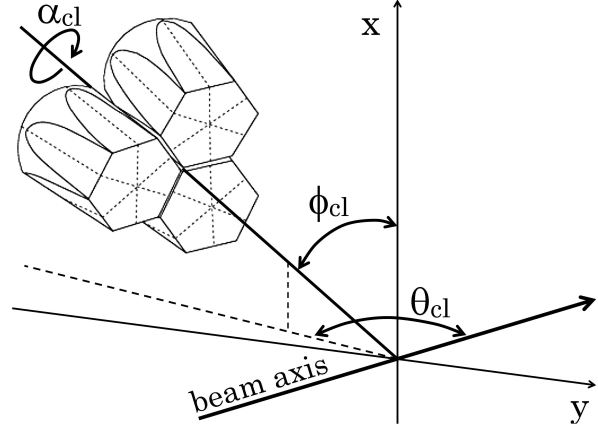


Figure 4.5: Definition of the three angles θ_{cl} , ϕ_{cl} and α_{cl} , which indicate the exact position of each individual MINIBALL cluster detector. The scattering target is in the center.

where $E_{\gamma,0}$ is the original energy of the γ ray in the rest frame of the emitting nucleus and θ_γ is the angle between the de-exciting nucleus and the γ ray. To determine θ_γ , the exact position coordinates of both, the detected γ ray and the emitting nucleus have to be known. If the nucleus is detected in the DSSSD with position coordinates $(\theta_{\text{part}}, \phi_{\text{part}})$ and the γ ray is detected in a MINIBALL detector with $(\theta_{\gamma,\text{lab}}, \phi_{\gamma,\text{lab}})$, the angle is given by

$$\cos \theta_\gamma = \sin \theta_{\text{part}} \sin \theta_{\gamma,\text{lab}} \cos(\phi_{\text{part}} - \phi_{\gamma,\text{lab}}) + \cos \theta_{\text{part}} \cos \theta_{\gamma,\text{lab}}$$

All eight MINIBALL cluster detectors were mounted on movable arms around the scattering chamber (“MINIBALL frame”) and could be rotated in three angular directions: θ_{cl} , ϕ_{cl} and α_{cl} , as indicated in Figure 4.5. For Doppler correction, all angles of the cluster detectors had to be known exactly. Due to the construction of the MINIBALL frame and the mounting devices of the cluster detectors in the frame, only ϕ_{cl} can be read at the frame with an appropriate accuracy. To determine θ_{cl} and α_{cl} an angle-calibration measurement was performed, using Doppler-shifted γ rays after the pick-up reactions $d(^{22}\text{Ne}, ^{23}\text{Ne})p$ and $d(^{22}\text{Ne}, ^{23}\text{Na})n$ (see Fig. 4.6). A stable ^{22}Ne beam with an energy of 2.2 MeV/u was impinged on a typically 100 μm thick deuterated polyethylene target. Due to the maximum scattering angle of 4.3° of the ejectile, the angle of the emitted γ ray could be approximated by $\theta_\gamma = \theta_{\gamma,\text{lab}}$.

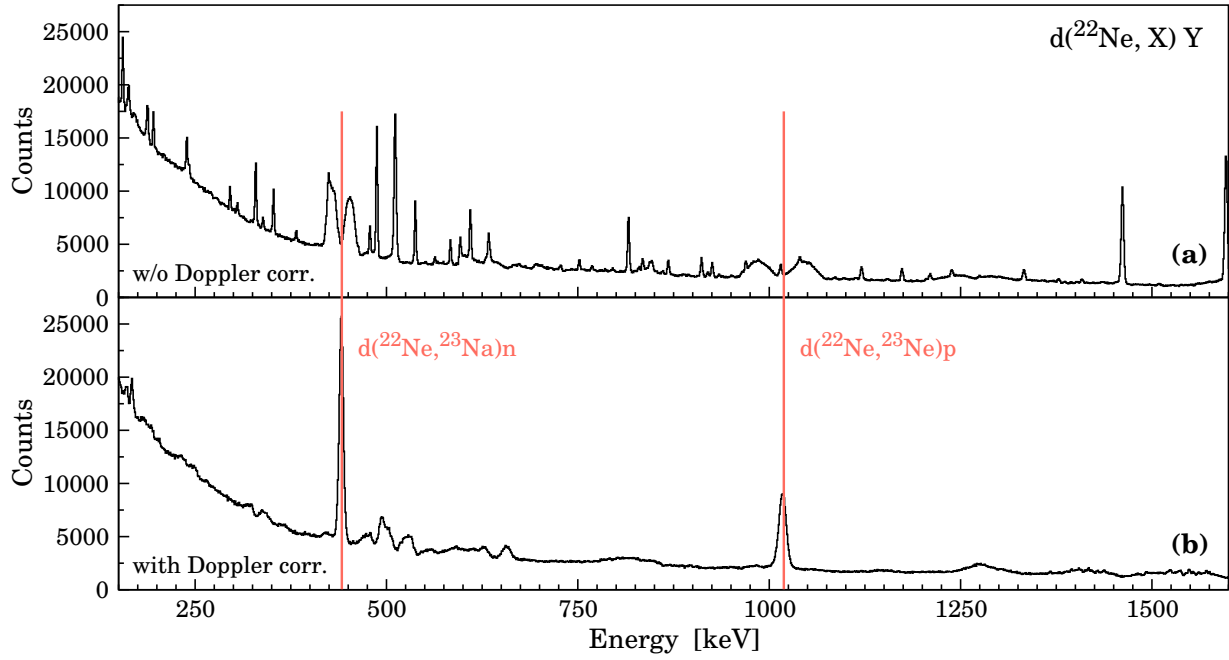


Figure 4.6: Sum spectrum of all MINIBALL cluster detectors containing γ -ray transitions of the $d(^{22}\text{Ne}, ^{23}\text{Ne})p$ and $d(^{22}\text{Ne}, ^{23}\text{Na})n$ reactions. The spectrum in (a) is not Doppler corrected. Various narrow background decay transitions can be observed as well as broad bumps at around 440 keV and 1020 keV. (b) In the Doppler-corrected spectrum the prompt γ -ray transitions of both reaction channels, emitted in-flight, are clearly visible.

The neutron pick-up reaction populated the first excited $1/2^+$ state in ^{23}Ne at an energy of 1016.95(9) keV, which has a lifetime of 178(10) ps [130]. The de-excitation γ ray was emitted in-flight, hence it was Doppler shifted and could be used for angular calibration. To determine the optimum angular parameter set of

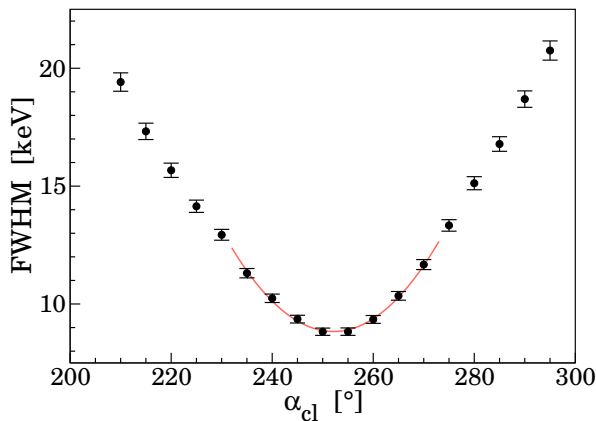


Figure 4.7: Evolution of the line width (FWHM) of the 1017 keV transition of ^{23}Ne as a function of the angle α_{cl} for one MINIBALL cluster detector. The optimum position was found to be $252(2)^\circ$. Detailed information is given in the text.

each individual MINIBALL cluster detector, the angles θ_{cl} , ϕ_{cl} and α_{cl} were varied recursively to optimize the peak position and to minimize the line width of the Doppler-corrected γ -ray transition. Figure 4.7 shows the evolution of the line width (FWHM) of the 1017 keV transition for different angles α_{cl} , which were assumed in the analysis for the positioning of one MINIBALL cluster detector. This implies an imaginary rotation of the detector between 200° and 300° around its axis of symmetry. The angle with the minimum line width indicates the optimum positioning parameter of the cluster detector, in this case $\alpha_{cl} = 252(2)^\circ$.

Figure 4.8 demonstrates the improvement of the energy resolution after Doppler correction, including the segment information of the MINIBALL detectors. Due to the close geometry of the MINIBALL clusters, the opening angle of a single detector is quite large, approximately 30° . Due to the six-fold segmentation of the detectors, the position resolution of the interaction is increased, giving rise to a much narrower opening angle for the γ -ray detection ($<15^\circ$). Thus, Doppler correction on the segment level gives an optimized energy resolution for the 1017 keV

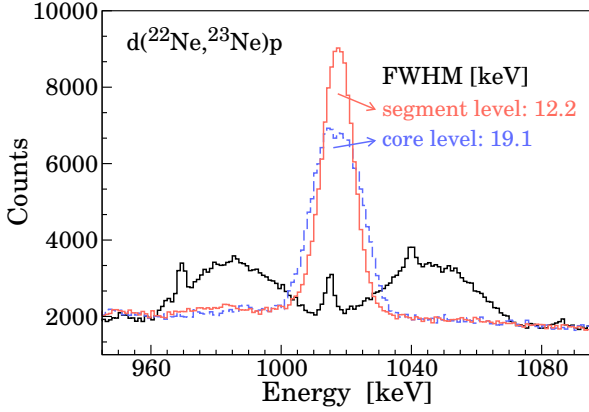


Figure 4.8: Detail of the γ -ray spectrum of the neutron pick-up reaction at different stages of the Doppler correction. The uncorrected spectrum is plotted in black (solid line). Applying Doppler correction on the core level (dashed line, blue), the 1017 keV transition becomes visible. Including the segment information of the MINIBALL detectors (red), the resolution is further improved.

transition of about 12 keV, which could be further improved by the use of pulse shape analysis (not implemented in this work).

To get a proper Doppler correction it is necessary to determine the precise angles of the different segments of the CD detector as well as all cluster angles. θ_{CD} could be calculated out of the dimensions of the detector and the distance between target and detector, which amounted to about 30.0 ± 0.5 mm. Thus, θ_{CD} covered typically the laboratory angle from 16.7° to 53.7° . To determine the exact azimuth angle ϕ_{CD} , the

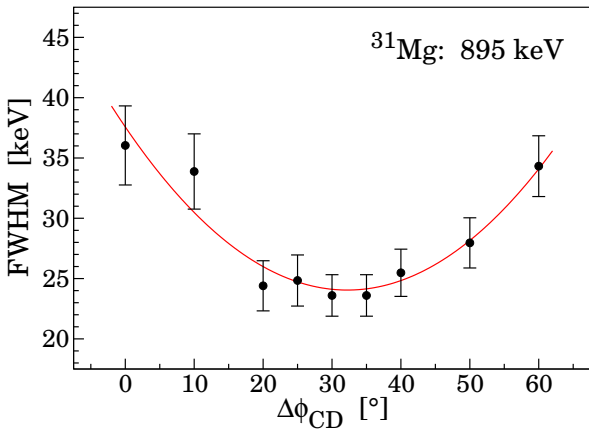


Figure 4.9: Evolution of the line width (FWHM) of the 895 keV transition of ^{31}Mg as a function of the angular offset $\Delta\phi_{CD}$. The optimum value was found to be $32(5)^\circ$. For detailed information see text.

895 keV transition of the Coulomb excitation of ^{31}Mg was used. As a first estimate it was assumed that the first strip of the first quadrant of the DSSSD was pointing upwards ($\phi_{CD} = 0^\circ$). Now the evolution of the line width of the Doppler-corrected transition was studied as a function of an angular offset $\Delta\phi_{CD}$ in the analysis, implying an imaginary rotation of the par-

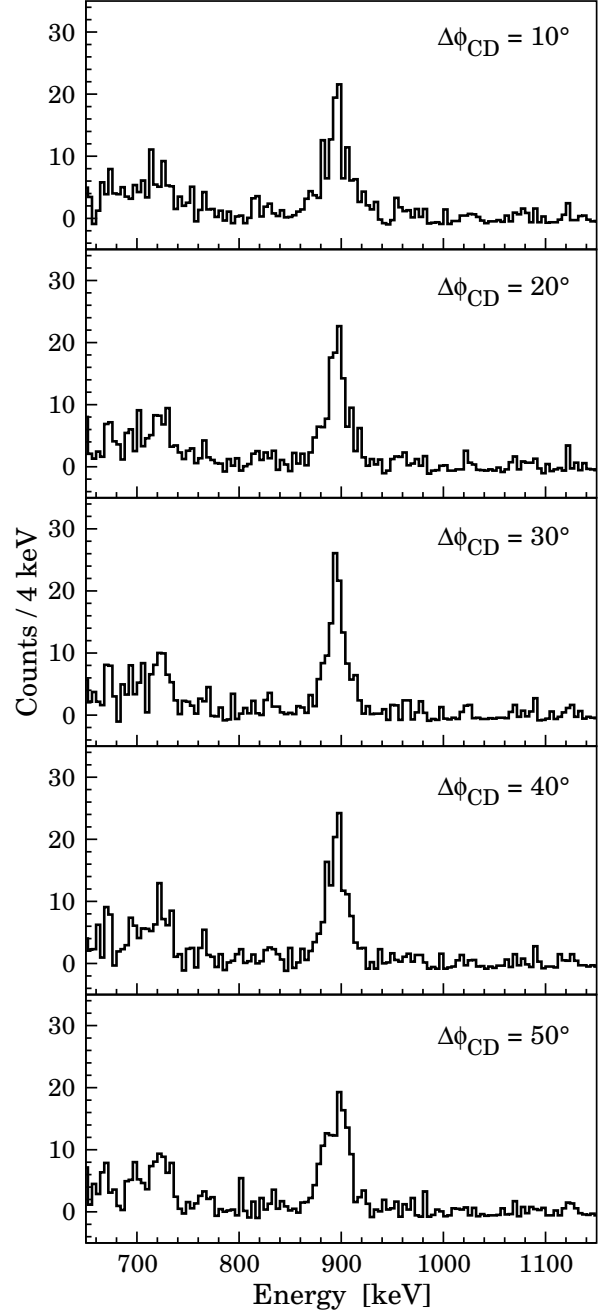


Figure 4.10: γ -ray spectra of the 895 keV transition of ^{31}Mg for five different angular offsets $\Delta\phi_{CD}$ between 10° and 50° , implying an imaginary rotation of the DSSSD around its axis of symmetry.

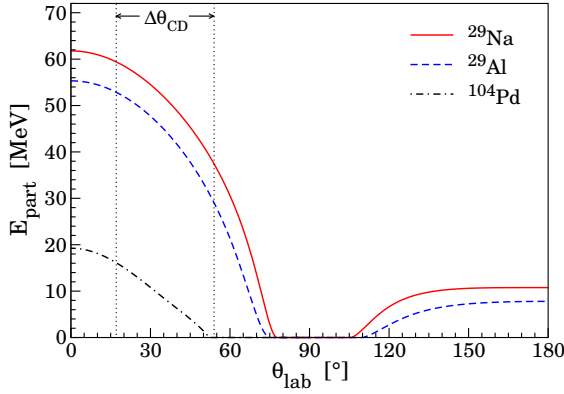


Figure 4.11: Calculated energy of ^{29}Na , ^{29}Al and recoiling ^{104}Pd nuclei as a function of the scattering angle, for scattering of an $A=29$ beam with an energy of 2.85 MeV/u on a 4.1 mg/cm² thick ^{104}Pd target. The spacial dimensions of the beam were neglected in the calculation. The dotted vertical lines indicate the angular range covered by the DSSSD.

ticle detector between 0° and 60°. Again the angle with the minimum line width indicates the optimum angular parameter of the detector, here yielding $\Delta\phi_{\text{CD}} = 32(5)^\circ$ (cf. Fig. 4.9 and 4.10).

4.4 Kinematic considerations

A correct Doppler correction depends largely upon the identification of the scattered projectile and target nuclei in the DSSSD. Necessary information can be obtained from the kinematics of the scattering process. Measuring the correlation of particle energy and scattering angle, different beam components can be identified and partially separated, as well as the recoiling target nuclei.

As an example the scattering of ^{29}Na and ^{29}Al nuclei with an energy of 2.85 MeV/u on a 4.1 mg/cm² thick ^{104}Pd target was calculated. Figure 4.11 shows the calculated energy after the target as a function of the scattering angle. Due to the Z -dependent energy loss inside the target, the energy of the sodium nuclei should be slightly higher (approx. 6 MeV) than the energy of the isobaric aluminum nuclei at the entrance of the particle detector. The measured spectrum of the particle energy versus the scattering angle (see Fig. 4.12) showed the expected characteristics. The energy of the ions

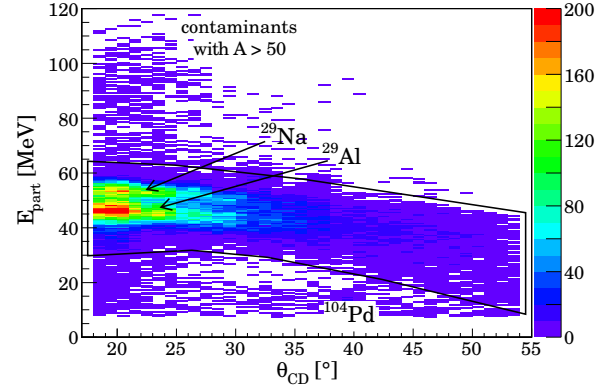


Figure 4.12: Measured particle energy at the CD detector as a function of the scattering angle θ_{CD} for scattering of the $A=29$ beam on a 4.1 mg/cm² thick ^{104}Pd target. ^{29}Na and ^{29}Al can be identified and partially separated. For the analysis of Coulomb-excitation events, the indicated particle gate was used, to select $A=29$ nuclei only.

detected in the DSSSD was slightly lower than proposed by the calculations, which was due to disregarded energy straggling and angular straggling, as well as the spatial dimensions of the beam spot. Moreover, these properties lower the resolution, making it impossible to separate the ^{29}Na and ^{29}Al ions completely, especially for the higher scattering angles. Thus, the analysis of the Coulomb-excitation data was done applying a particle gate, which covered all possible isobars (Na, Mg, Al, and Si), as indicated in Figure 4.12.

4.5 Beam composition

In Coulomb-excitation experiments with radioactive ion beams possible beam contaminations have to be carefully investigated, because all beam components contribute to Coulomb excitation of the target material, which is used for normalization. For the extraction of the transition probabilities it was mandatory to monitor and to determine the exact beam composition during the experiment. Different sources of beam contamination were identified: Isobaric contaminants occur by β -decay of the radioactive nuclei during accumulation and charge breeding at REX-ISOLDE. Isobaric contaminants, directly produced in the primary ISOLDE target, were surface ionized due to the high tem-

Element	λ_r^{-1} [ms]	λ_f^{-1} [ms]	λ_s^{-1} [ms]	α
Mg	66	190	860	0.98
Al	(100)	(500)	22000	(0.5)

Table 4.1: Release parameters of magnesium and aluminum for a standard ISOLDE UC_x target with W ionizer at a temperature of about 2000° C/2200° C, as given in Ref. [96, 98]. For a definition of the parameters see the text.

perature of the hot cavity and were not separated completely in the HRS due to the small mass differences. An additional beam component in the Coulomb-excitation experiment of ³¹Mg stemmed from residual argon gas in the REX-Trap and EBIS. After charge breeding, the ³⁸Ar¹¹⁺ had almost the same A/q ratio and was accelerated together with the ³¹Mg⁹⁺ ions.

The beam composition was carefully monitored during the experiment using different techniques, which will be discussed in detail in the following sections.

4.5.1 Release curve analysis

Due to the pulsed proton beam impinging onto the primary ISOLDE target and due to the radioactive decay of the nuclei of interest, the intensity of the radioactive ion beam at the MINIBALL setup had a characteristic time-dependent shape, as already mentioned in Section 3.5. In general the release curve of an element can be described with an empirical formula, including four element-specific parameters [131]:

$$P(t, \lambda_r, \lambda_f, \lambda_s, \alpha) = \frac{1}{\text{Norm.}} \left(1 - e^{-\lambda_r t} \right) \times \left[\alpha e^{\lambda_f t} + (1 - \alpha) e^{-\lambda_s t} \right]$$

The release process starts with a sharp rise of intensity (λ_r), followed by a steep fall with a fast and a slow component, characterized by the parameters λ_f and λ_s , respectively. The relative intensity of the fast component is given by the parameter α . As mentioned in Section 3.2.1 alkali metals and alkaline earths (e.g. Na, Mg, ...) are released very fast after proton beam impact [97, 98]. In contrast, the release of aluminum is dominated by the slow component of the fall time [98]. The corresponding release parameters for magnesium and aluminum are given in Table 4.1 as an example. Please note that the release parameters can vary signifi-

cantly due to the chosen macroscopic and microscopic target and ion source characteristics (e.g. temperature, material, “grain size”). For exotic isotopes the release function is superimposed by

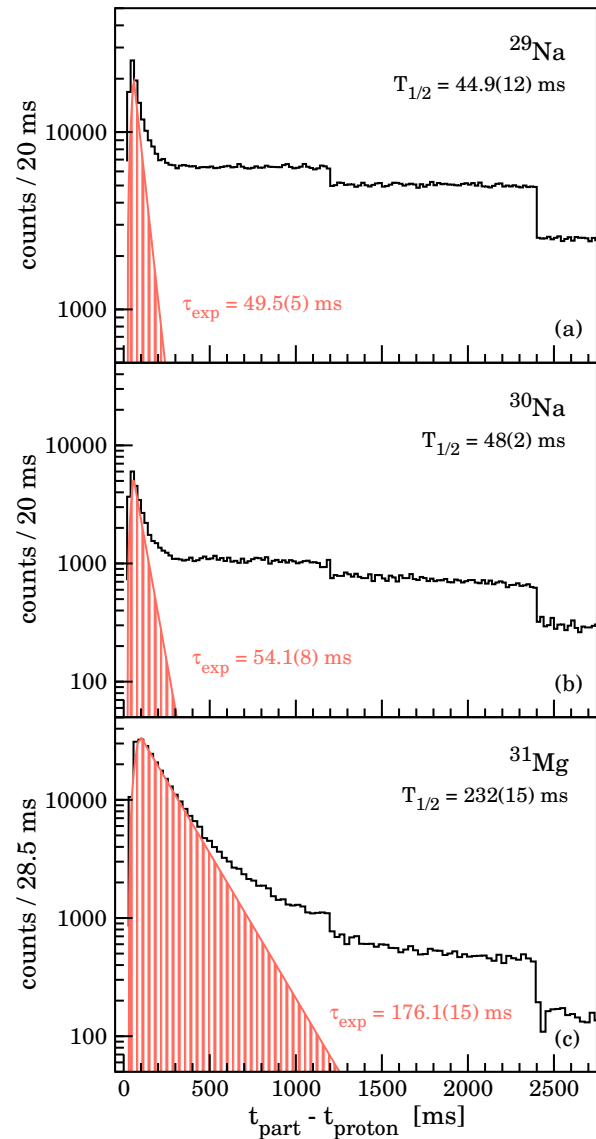


Figure 4.13: Time-dependent intensity of the RIB with respect to the last proton beam impact onto the ISOLDE target for the ^{29,30}Na and ³¹Mg runs. The experimentally deduced release curves for the isotopes are indicated in red.

the radioactive decay of the nuclei with decay constant λ_d :

$$P'(t) = e^{-\lambda_d t} P(t, \lambda_r, \lambda_f, \lambda_s, \alpha)$$

To determine the beam composition in the MINIBALL experiments and to optimize the background suppression in the analysis, the pulse shape of the radioactive ion beam delivered by REX-ISOLDE was studied. Therefore the number of scattered beam particles detected in the DSSSD was measured as a function of the time interval since the last proton impact on the primary ISOLDE target. The binning of the measurement was given by the repetition rate of the charge breeding system of REX-ISOLDE. Figure 4.13 shows the time-dependent intensity of the radioactive ion beam with respect to the last proton beam impact onto the ISOLDE target for $^{29,30}\text{Na}$ and ^{31}Mg , taken during the Coulomb-excitation runs at REX-ISOLDE in 2007 (c) and 2009 (a-b). Both, sodium and magnesium ions were released very fast out of the primary target. Thus, the post-accelerated beams had their maximum intensity 60-80 ms after the proton beam impact, as it was expected. The decrease of intensity was dominated by the fast component of the fall and the radioactive decay of the isotope of interest and could be described by an exponential function:

$$P'(t) \approx Ce^{-(\lambda_f + \lambda_d)t} = Ce^{-t/\tau}, \text{ for } t > 1/\lambda_r$$

The experimentally deduced release constants τ_{exp} are summarized in Table 4.2 and compared to the expected values τ_{ref} by superimposing λ_f and λ_d . The values are in reasonable agreement. Due to their fast release out of the primary target and their short lifetimes, the main intensity of $^{29,30}\text{Na}$ and ^{31}Mg was delivered within several 100 ms after the proton impact (cf. Figure 4.13). Thus, long-lived and stable contami-

Isotope	τ_{exp} [ms]	τ_{ref} [ms]
^{29}Na	49.5(5)	48.9(14)
^{30}Na	54.1(8)	51.4(23)
^{31}Mg	176.1(15)	121.2(41)

Table 4.2: The experimentally deduced release constants τ_{exp} , compared to the expected values τ_{ref} for $^{29,30}\text{Na}$ and ^{31}Mg by superimposing λ_f and λ_d .

nants dominated the beam composition for most of the time, producing a large amount of background. To reduce this background and to improve the relative intensity of the isotope of interest, the analysis had to be restricted to reasonable time differences $\Delta t = t_{\text{part}} - t_{\text{proton}}$. An appropriate time gate had to be found, to accumulate as much intensity of the relevant isotopes as well as to guarantee an optimum background suppression. Therefore Figure 4.14 shows the time-dependent evolution of the relative intensity of $^{29,30}\text{Na}$ and ^{31}Mg with respect to the integrated intensity of the beam and to the totally delivered intensity of the isotope. As expected, a saturation of the relative amount of these isotopes accumulated at the MINIBALL setup was found a few 100 milliseconds after the proton pulse. 99% of the total intensity of the isotope

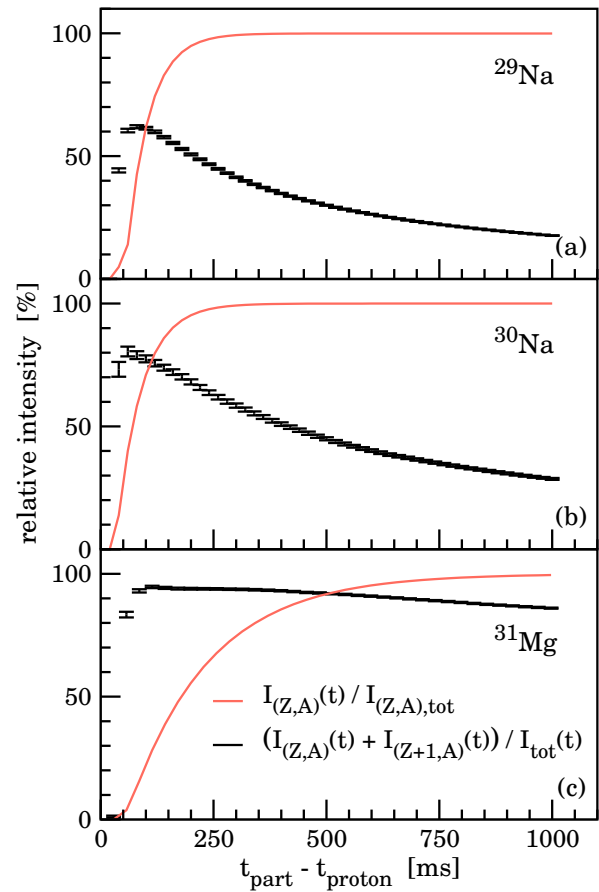


Figure 4.14: Relative intensity of $^{29,30}\text{Na}$ and ^{31}Mg with respect to the integrated intensity of the beam (black) and to the totally delivered intensity of the isotope (red) as a function of the time difference to the proton beam impact. Radioactive decay during charge breeding is not taken into account.

Isotope	t_{99} [ms]	$r(t_{99})$ [%]	$r(t_{\text{tot}})$ [%]
^{29}Na	275(10)	43.52(34)	6.65(4)
^{30}Na	285(10)	59.69(87)	13.85(17)
^{31}Mg	850(20)	87.65(24)	75.77(20)

Table 4.3: After the time t_{99} the accumulated intensity amounts 99% of the total intensity of the isotopes of interest. The relative intensity $r(t)$ of the isotope with respect to the integrated intensity of the beam is given for $\Delta t = t_{99}$ and for the total beam intensity (t_{tot}). For further analysis β -decay of the radioactive beam during charge breeding has to be taken into account (see Section 4.5.2).

of interest was accumulated within the time t_{99} after the proton pulse, as given in Table 4.3. Furthermore t_{99} provided an improved relative intensity

$$r(t) = \frac{I_{(Z,A)}(t) + I_{(Z+1,A)}(t)}{I_{\text{tot}}(t)}$$

with respect to the unrestricted ratio $r(t_{\text{tot}})$. For the short-lived ^{29}Na the improvement of the relative intensity exceeded even a factor of 6.5, while for ^{31}Mg it was still a factor of almost 1.2 (cf. Table 4.3). Thus, the analysis could be restricted to time differences $\Delta t \leq t_{99}$ after the proton pulse. Due to radioactive decay during the charge breeding process, which will be discussed in detail in the following Section 4.5.2, the relative intensities derived by the release curve method were not only caused by the isotope of interest (Z,A), but also by its daughter isotope ($Z+1,A$).

4.5.2 β -decay during charge breeding

For accumulation and charge breeding at ISOLDE the radioactive ions have to be stored in the ion traps REXTRAP and REXEBIS for some time. If these trapping times are long compared

to the half-lives of the ions, a significant amount of the stored ions decays during trapping and charge breeding. This process is referred to as “in-trap decay” [132]. According to the storage of the radioactive ions in two different ion traps, the total amount of in-trap decay can be calculated in two consecutive steps. Due to a continuous injection of the ions from the primary target into REXTRAP for accumulation and bunching, the trapping times depend on the arrival of the ions at REXTRAP. Thus, the exponential decay has to be averaged over the time the ions are injected into REXTRAP [132]:

$$r_{\beta,\text{TRAP}}(T) = \frac{1}{T} \int_0^T e^{-\lambda_d t} dt$$

Typically the maximum trapping time T is given by the repetition time of the charge breeding system. For charge breeding the bunched ion beam is transferred from REXTRAP to the REXEBIS and stored for a certain so-called breeding time t_{breed} . Thus, neglecting any decay losses, the exponential decay in the EBIS can be calculated straightforward and the total ratio for the isotope of interest is given by:

$$\begin{aligned} r_{\beta,\text{tot}} &= r_{\beta,\text{TRAP}}(T) \cdot r_{\beta,\text{EBIS}}(t_{\text{breed}}) \\ &= \frac{1}{\lambda_d T} (1 - e^{-\lambda_d T}) e^{-\lambda_d t_{\text{breed}}} \end{aligned}$$

Table 4.4 summarizes $r_{\beta,\text{tot}}$ for the $^{29,30}\text{Na}$ and ^{31}Mg runs as well as the particular breeding and repetition times. However, the processes of in-trap decay are still not fully understood. Large discrepancies between the calculated and experimentally observed beam composition were already found by [132]. Possible explanations were losses of the daughter nuclei due to the recoil energy as well as multiply

Mass A	T [ms]	t_{breed} [ms]	$r_{\beta,\text{tot}}^{(\text{Na})}$ [%]	$r_{\beta,\text{tot}}^{(\text{Mg})}$ [%]	$r_{\beta,\text{tot}}^{(\text{Al})}$ [%]	$r_{\beta,\text{tot}}^{(\text{Si})}$ [%]
29	20	13	70.4	28.8	0.8	—
30	20	13	72.0	27.8	0.2	—
31	30	28.5	—	87.7	12.0	0.3

Table 4.4: Repetition and breeding times of REXTRAP and REXEBIS for the $^{29,30}\text{Na}$ and ^{31}Mg runs. The calculated ratios $r_{\beta,\text{tot}}$ of the different isotopes and decay products (up to 3rd generation) after in-trap decay are given.

charged (n^+ , $n \geq 2$) ions after β -decay, inducing insufficient cooling in REXTRAP and thus a poor injection into the EBIS, differences in the charge state distributions of mother and daughter nuclei after charge breeding, or collisions of the recoiling daughter nuclei with the installations inside the trap, e.g. with inner walls and electrodes. [132].

4.5.3 Measurements with the ionization chamber

For a more direct investigation of the beam composition at MINIBALL, a $\Delta E_{\text{gas}}-E_{\text{res}}$ detector was installed at the beam dump position. Furthermore the ionization chamber allowed for a continuous monitoring of the beam composition during the experiments with the radioac-

tive sodium beams. Figure 4.15 shows $\Delta E_{\text{gas}}-E_{\text{res}}$ spectra, taken during the $^{29,30}\text{Na}$ beam times without a scattering target in place. Due to the good resolution of both, the gas detector (ΔE_{gas}) and the silicon detector (E_{res}), the different isobars at $A = 29, 30$ could be well separated and identified. Heavier contaminants in the beam could be identified as stable isotopes (e.g. $^{58,60}\text{Ni}$, $^{83,86}\text{Kr}$), partially stemming from residual gas in the EBIS, matching almost the same A/q ratio of 4.143 and 4.286 for the $A = 29$ and $A = 30$ beams, respectively. The excellent background suppression by applying the time gate $\Delta t = t_{99}$, discussed in Section 4.5.1, is demonstrated. Due to their high ionization potential of 7.61 eV, magnesium isotopes will not be ionized by a surface ion source. Thus, any magnesium isotopes detected at the MINIBALL

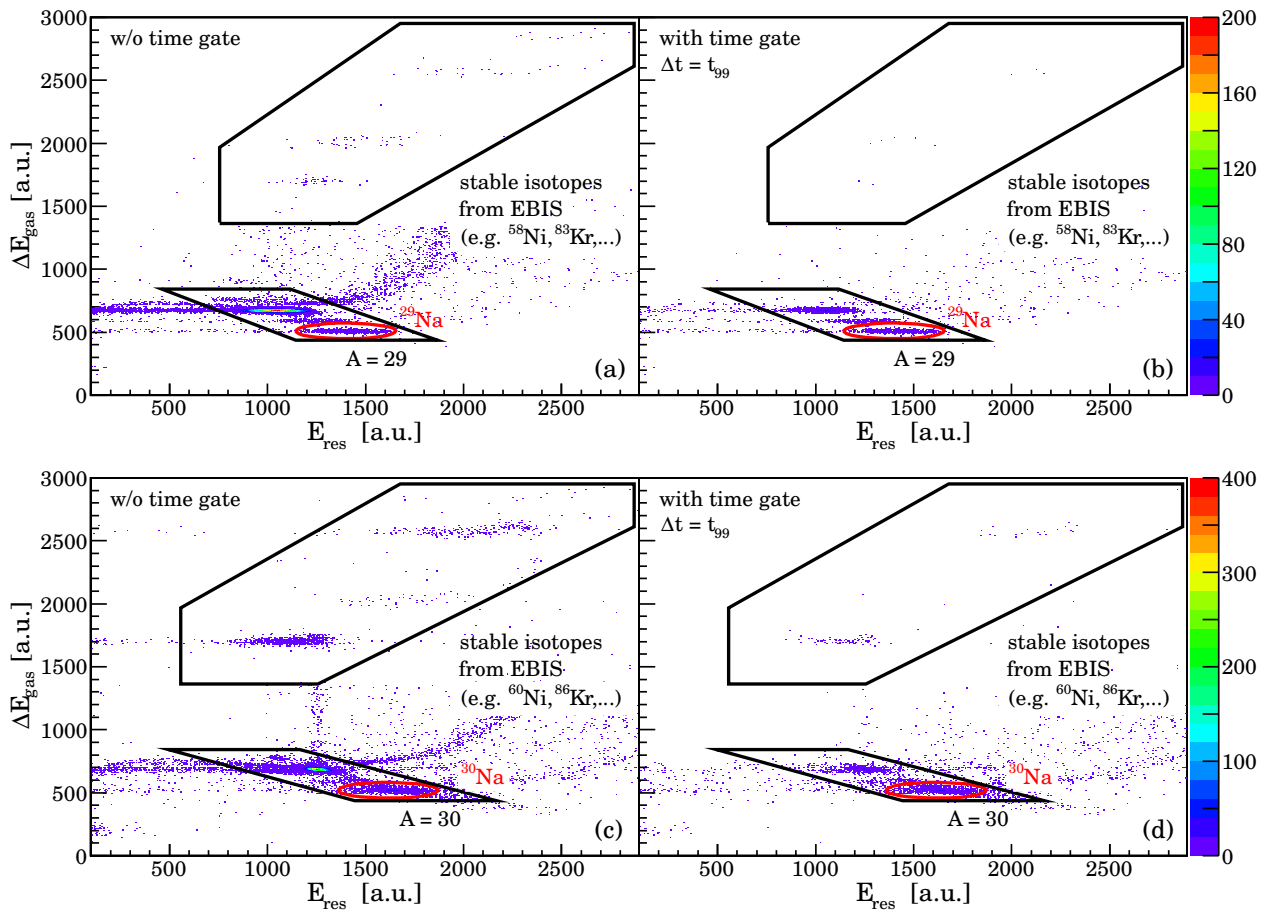


Figure 4.15: $\Delta E_{\text{gas}}-E_{\text{res}}$ spectra of the beam composition, taken with the ionization chamber during the ^{29}Na (top) and ^{30}Na beam times (bottom). The $A=29,30$ isobars are well separated and can be clearly identified. Some heavier stable contaminants are observable, e.g. $^{58,60}\text{Ni}$ and $^{83,86}\text{Kr}$, partially from residual gas. While for the spectra (a,c) no time gate is applied, the spectra (b,d) contain only those ions, which arrive at the ionization within $\Delta t = t_{99}$. The suppression of the stable and long-lived components is well demonstrated.

Mass A	Coulex target	$r_{IC}^{(Na)} [\%]$	$r_{IC}^{(Mg)} [\%]$	$r_{IC}^{(Al)} [\%]$	$r_{IC}^{(Si)} [\%]$
29	^{104}Pd	28.3(6)	11.6(3)	58.5(8)	1.6(1)
30	^{104}Pd	53.5(9)	5.8(3)	39.7(7)	1.0(1)
30	^{120}Sn	50.0(28)	14.5(13)	34.5(22)	1.0(3)

Table 4.5: Relative ratio $r_{IC}(t_{99})$ of the different isotopes, measured with the ionization chamber for the three experiments with $A=29,30$ radioactive ion beams.

setup were caused by in-trap decay of short-lived Na isotopes during the accumulation and charge breeding process (cf. Section 4.5.2). For the silicon isotopes $^{29,30}\text{Si}$ detected at the ionization chamber it is much the same. Silicon can not be extracted out of an ISOL target, and thus any silicon detected was caused by the in-trap decay of the isobaric aluminum isotopes $^{29,30}\text{Al}$, the most abundant beam components.

To account for time-dependent effects (e.g. slightly changing extraction and ionization yields, aging of the production target material), the beam composition was typically measured every 8-16 hours for about 20-30 minutes with the ionization chamber. Then the overall relative ratio $r_{IC}(t)$ of the isotopes is given by the time-averaged value of all measurements. Assuming a homogeneous distribution of the different beam components over the geometrical beam profile, the composition measured at the ionization chamber without a scattering target in place, should be the same as at the MINIBALL target position. Table 4.5 summarizes $r_{IC}(t_{99})$ of the $A = 29, 30$ isobars, obtained with the ionization chamber during the different runs with the $^{29,30}\text{Na}$ beams. Due to the particle gate applied in the Coulomb-excitation analysis (cf. Section 4.4), heavier contaminants with $A > 50$ can be neglected.

4.5.4 Measurements with the Bragg detector

During the ^{31}Mg beam time the Bragg detector (see p. 32) was mounted at the beam dump position at MINIBALL, to monitor the beam composition. In particular it was used to identify the different beam components on-line for a given A/q value. In the beginning of the experiment the beam was a mostly pure ^{31}Mg beam, due to laser ionization, with a small fraction of surface ionized ^{31}Al , as shown in Figure 4.16(a,c). Af-

ter 52 hours of beam time an additional beam component appeared, which was not an isobar of ^{31}Mg . To identify this contaminant, several measurements with the Bragg detector were performed at the end of the experiment (see Fig. 4.16(b,d)). It could be shown that the isotope had to be stable, stemming from residual gas in the EBIS, and it had a slightly higher mass A and higher proton number Z than ^{31}Mg . Furthermore, the contaminant had to match an A/q ratio of 3.444. Thus, it was identified as $^{38}\text{Ar}^{11+}$, which was part of the buffer gas in the REXTRAP.

Due to $Z = 18$, the energy loss of ^{38}Ar was higher than for ^{31}Mg on its way through the scattering target, and the residual energy of ^{38}Ar , detected in the DSSSD, was similar to the residual energy of the $A = 31$ isotopes. Thus, the contaminant matched the particle gate, which was applied to select the $A = 31$ ions, and the relative abundance of ^{38}Ar in the beam had to be analyzed accurately.

4.5.5 Measurements with laser ON/OFF

As already mentioned above, magnesium isotopes cannot be surface ionized due to their high ionization potential. Therefore the ISOLDE RILIS was used, to selectively laser-ionize ^{31}Mg . Due to the design of the RILIS ionizer tube, consisting of a very hot metal cavity, some elements with a low ionization potential (e.g. Na, Al, ...) could get surface ionized and could contaminate the beam. The surface ionization happens continuously and completely independent from the laser ionization, so there is a possibility to investigate this source of contamination in detail. Therefore the ratio of laser ionized ^{31}Mg over surface ionized ^{31}Al in the beam was checked by switching the laser on and off periodically every 2.5 hours for about 30 minutes. While the laser was on, ^{31}Mg was elastically scattered into the DSSSD as well as ^{31}Al (see Fig. 4.17(a)). When

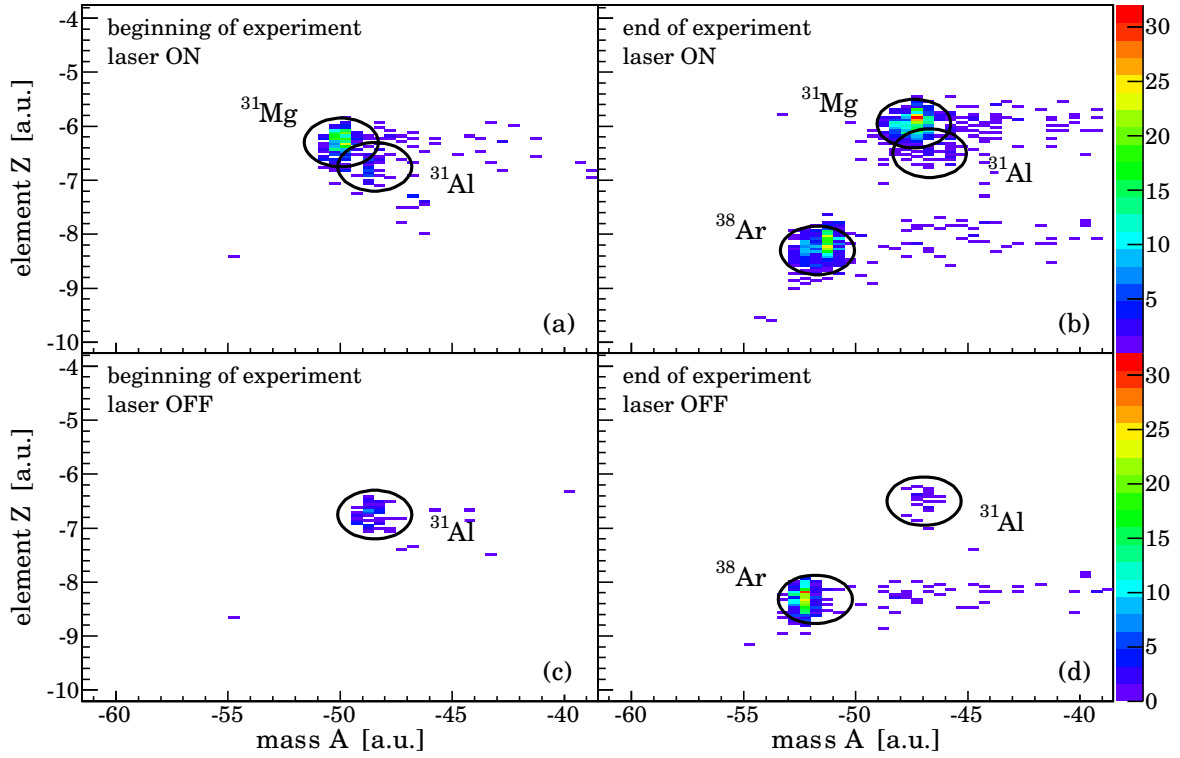


Figure 4.16: Spectra taken with the Bragg detector at the beginning (left) and at the end (right) of the ^{31}Mg beam time, respectively. Z rises from the top to the bottom, A lowers from left to the right. To be sure to have a mostly pure, laser ionized ^{31}Mg beam, spectra were taken with laser on (top) and laser off (bottom). ^{31}Al and ^{38}Ar can be identified as contaminants (see text).

the laser light was blocked, only the surface ionized contaminant was detected (Fig. 4.17(b)). Again, β -decay during charge breeding has to be taken into account. The fraction r_{laser} of laser-ionized magnesium ions and their daughter products in the beam was calculated out of the intensities I_{on} with laser on and I_{off} with laser off as

$$r_{\text{laser}} = \frac{I_{\text{on}} - I_{\text{off}}}{I_{\text{on}}}.$$

Hence, the surface ionized fraction of the beam was given by $r_{\text{surface}} = 1 - r_{\text{laser}}$. To

achieve the exact beam composition, the different scattering cross sections $\sigma_{\text{ruth}}^{\text{Mg}} = 30.0$ mb, $\sigma_{\text{ruth}}^{\text{Al}} = 31.0$ mb, and $\sigma_{\text{ruth}}^{\text{Ar}} = 55.6$ mb had to be taken into account. The results, obtained for the different parts of the experiment on ^{31}Mg , are summarized in Table 4.6.

4.5.6 Summary of the experimental beam parameters

In Table 4.7 the most important beam parameters of the $^{29,30}\text{Na}$ and ^{31}Mg beam times at REX-ISOLDE are summarized. The beam

target	thickness	$r_{\text{laser}}^{\text{Mg+Al}}$ [%]	$r_{\text{surface}}^{\text{Al+Si}}$ [%]	$r_{\text{EBIS}}^{\text{Ar}}$ [%]	amount of statistics
^{109}Ag	1.9 mg/cm ²	91.1(9)	8.9(9)	—	14.0%
^{109}Ag	4.0 mg/cm ²	93.4(3)	6.6(3)	—	34.5%
^{109}Ag	4.0 mg/cm ²	87.5(4)	6.2(6)*	6.3(6)*	51.5%

Table 4.6: Beam compositions of the $A=31$ beam, deduced by the laser ON/OFF measurements for the two different enriched ^{109}Ag targets. To get the average beam composition, the different parts of the experiment have to be weighted according to their accumulated amount of statistics. To calculate the relative amount of ^{38}Ar it was assumed, that the ratio of laser ionized and surface ionized ions was constant in time (marked with *).

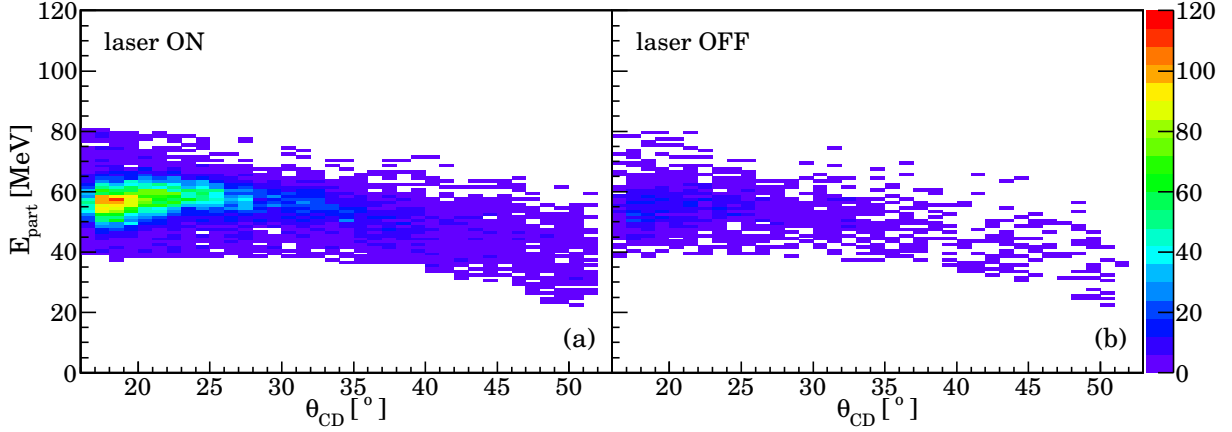


Figure 4.17: Energy of elastically scattered ^{31}Mg , ^{31}Al and ^{38}Ar ions in the DSSSD, depending on the scattering angle θ_{CD} , measured during the laser ON/OFF runs. An adequate particle gate was applied, to select beam-like particles only. Furthermore the time gate $\Delta t = t_{99}$ was selected again. In (a) the laser was on, while for spectrum (b) the laser light was blocked by a shutter.

intensities were derived by the use of the Coulomb-excitation events of the target nuclei, detected with the MINIBALL detectors in coincidence with a scattered beam-like particle in the DSSSD. Thus, the beam intensity I_{beam} of the nucleus of interest is given by

$$I_{\text{beam}} = \frac{N_{\gamma} \cdot r_{\text{total}}}{\sigma_{\text{CE}} \cdot \epsilon_{\text{MB}} \cdot N_{\text{target}} \cdot T},$$

where N_{γ} is the number of detected γ rays following Coulomb excitation of the target nuclei, r_{total} is the relative ratio of the nucleus of interest on the total beam intensity, σ_{CE} is the Coulomb-excitation cross section of the target nuclei, ϵ_{MB} is the energy dependent efficiency of the MINIBALL array, N_{target} is the number of target nu-

clei, and T is the duration of the measurement. The individual beam composition for each experiment was derived by the different experimental methods discussed in the last section, i.e. by release curve analysis, measurement with the ionization chamber or with laser ON/OFF. For the final beam composition the average of the individual beam compositions was calculated, taking into account the β -decay.

All beam components Coulomb excite the target material, which is used for normalization. Thus, this effect has to be taken into account carefully. Isobaric contaminants with higher Z lose more energy inside the target and have a larger distance of closest approach, compared to the isotopes of interest. Therefore, the

nucleus of interest	^{29}Na	^{30}Na		^{31}Mg	
A/q ratio	4.143	4.286	4.286	3.444	3.444
beam energy [MeV/u]	2.85	2.85	2.85	3.0	3.0
beam intensity [ions/s]	2700(100)	750(250)	550(60)	3500(200)	2600(150)
beam time [hours]	63.7	46.4	37.8	29.0	58.0
target nucleus	^{104}Pd	^{120}Sn	^{104}Pd	^{109}Ag	^{109}Ag
target thickness [mg/cm ²]	2.2+1.9	4.0	2.2+1.9	1.9	4.0
beam composition [%]	Na	29.5(7)	46.5(29)	48.2(12)	—
	Mg	12.1(3)	15.5(13)	11.2(4)	78.4(10)
	Al	57.7(9)	37.4(24)	40.0(13)	20.8(10)
	Si	0.7(1)	0.6(3)	0.6(1)	0.8(2)
	Ar	—	—	—	0.5(2)
					3.5(7)

Table 4.7: Summary of the most important beam parameters of the different beam times, using $^{29,30}\text{Na}$ and ^{31}Mg beams at REX-ISOLDE.

Coulomb-excitation cross sections for target excitation are slightly lower for the contaminant, than the one of the desired isotope. In the case of ^{31}Mg and its contaminant ^{31}Al , impinging onto a 4.0 mg/cm^2 thick ^{109}Ag target, the difference in the cross section is about 2.5% at a beam energy of 3.0 MeV/u. The heavier contaminant ^{38}Ar has a target excitation cross section, which is increased by about 25% with respect to that of ^{31}Mg , due to its higher mass and therefore higher beam energy. Thus, the final beam compositions have to be normalized by the dedicated target excitation cross sections.

4.6 Particle- γ coincidence

In experiments using radioactive ion beams, γ -ray spectroscopy often suffers from the massive amount of background radiation, caused by the radioactive decay of the beam particles, which covers the very rare events of interest almost completely. Thus, in the Coulomb-excitation experiments described in the present work, digitized data were recorded using particle- γ coincidences. To select the prompt Coulomb-excitation events and to suppress random coincidences from room background, i.e. β -decay and bremsstrahlung, a restrictive time window

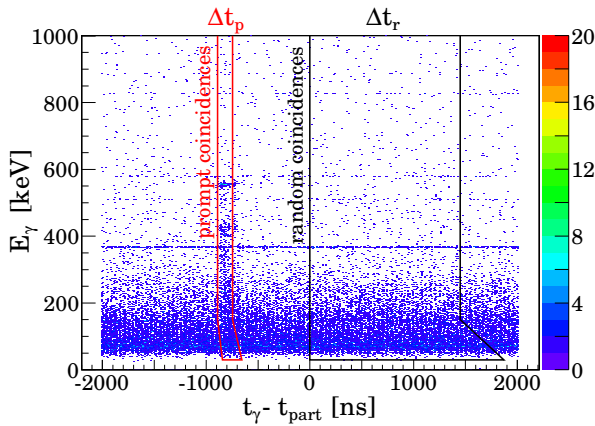


Figure 4.18: Detected γ -ray energy as a function of the time difference between the detected particle and the coincident γ ray, measured during the ^{30}Na experiment. Background radiation is characterized by continuous, horizontal lines. The time gates for prompt (Δt_p) and random (Δt_r) coincidences are given exemplarily for the first quadrant of the DSSSD.

with a width of typically $\Delta t_p = 120 \text{ ns}$ up to 250 ns between the particle and the γ ray was applied in the offline analysis, as shown in Figure 4.18. For γ -ray energies below 150 keV the coincidence window was chosen slightly broader and shifted to later times, to account for the walk effect. To minimize statistical fluctuations, background radiation was analyzed using a long time window of typically $\Delta t_r = 10 \times \Delta t_p$. As shown in Figure 4.19(a-c), the prompt Coulomb-excitation spectrum for further analysis is par-

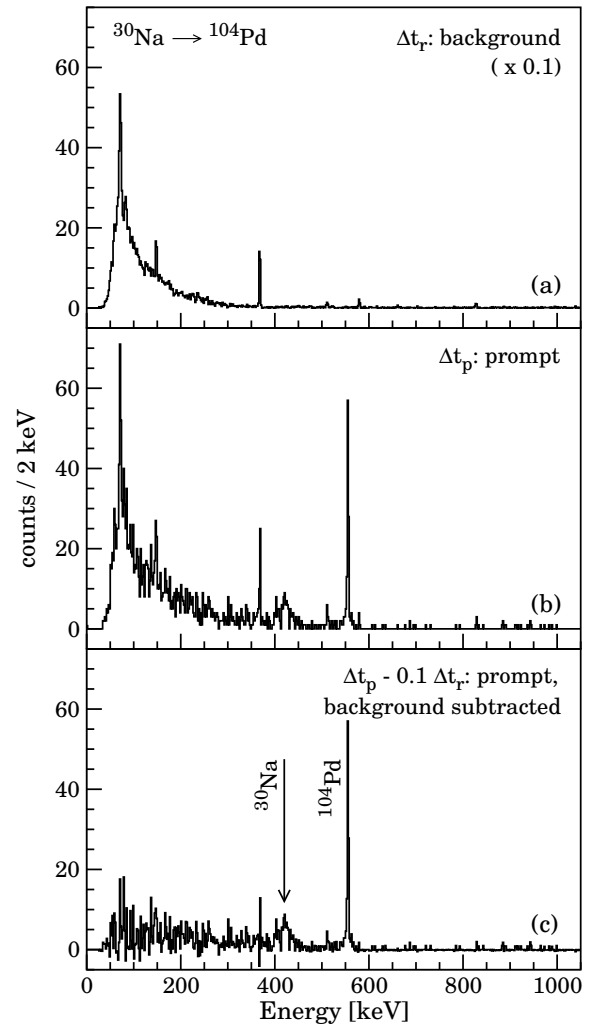


Figure 4.19: Non-Doppler-corrected γ -ray spectra for the different coincidence gates, taken during the ^{30}Na experiment. (a) The spectrum contains random coincidences (Δt_r), i.e. only background radiation, which is dominated by the bremsstrahlung coming from the 9-gap resonator. (b) Applying the prompt time gate Δt_p , Coulomb-excitation events can be observed besides the background. (c) After background subtraction the prompt spectrum is particularly clean of any background transitions.

ticularly clean of any background transitions after background subtraction. All observed γ -ray transitions are due to Coulomb excitation of either beam or target nuclei.

Chapter 5

Results

The results of all different Coulomb-excitation experiments of radioactive $^{29,30}\text{Na}$ and ^{31}Mg beams with MINIBALL at REX-ISOLDE, CERN, will be presented in this chapter. Observed γ -ray transitions were allocated in the level schemes of the nuclei. Reduced transition probabilities were determined for the different nuclei, using the coupled-channel codes GOSIA [122, 123] and CLX [120, 121]. In the case of ^{31}Mg assignments of spin and parity of the levels participating in transitions could be facilitated by the calculated transition strengths.

5.1 Coulomb excitation of ^{31}Mg

To determine transition strengths of the neutron-rich odd-mass magnesium isotopes $^{29,31}\text{Mg}$ a Coulomb-excitation experiment was proposed employing the MINIBALL setup at REX-ISOLDE. A first experiment on ^{31}Mg in 2006 found a hint for a prominent transition at 895 keV [133]. Its transition strength could not be deduced due to several technical problems.

Therefore, another Coulomb-excitation experiment of ^{31}Mg was scheduled and carried out at REX-ISOLDE. The radioactive ^{31}Mg beam was delivered with a final energy of 3.0 MeV/u and an average intensity of around 3×10^3 ions/s onto the secondary target. During the experiment two enriched ^{109}Ag targets were used with thicknesses of 1.9 mg/cm² and 4.0 mg/cm², respectively, to maximize the yield. The beam on target time added up to about 29 hours for the 1.9 mg/cm² target and 58 hours for the 4.0 mg/cm² target. Due to the fast release and the short half-life of ^{31}Mg ($T_{1/2} = 232(15)$ ms [72]) the analysis was restricted to the first 850 ms after each proton impact at the

primary ISOLDE target (cf. Sec. 4.5.1). More information on the experimental details and the beam compositions can be found in the previous chapter in Table 4.7.

5.1.1 Measurement at 3.0 MeV/u on a 4.0 mg/cm² thick ^{109}Ag target

Coulomb-excitation data analysis commenced by identifying and selecting scattered ^{31}Mg ions, which were identified by the CD detector (DSSSD). As shown in Section 4.4, the kinematics of the scattered beam or target nuclei is clearly separated by the measured correlation of particle energy and scattering angle. Despite increased straggling in the thick target, these characteristics could be clearly observed for the ^{31}Mg beam, incident on the 4.0 mg/cm² thick ^{109}Ag target at a beam energy of 3.0 MeV/u, as shown

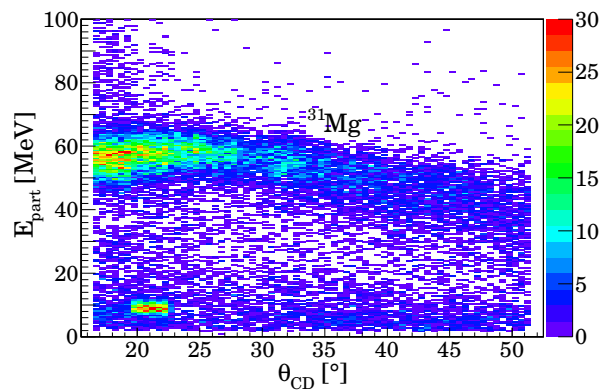


Figure 5.1: Particle energy versus scattering angle, measured in the DSSSD for the ^{31}Mg beam, incident on the 4.0 mg/cm² thick ^{109}Ag target at a beam energy of 3.0 MeV/u. Only those events are plotted, which coincide with at least one prompt γ -ray event detected at MINIBALL. The broadened energy distribution of the beam-like particles is mainly caused by straggling in the thick target.

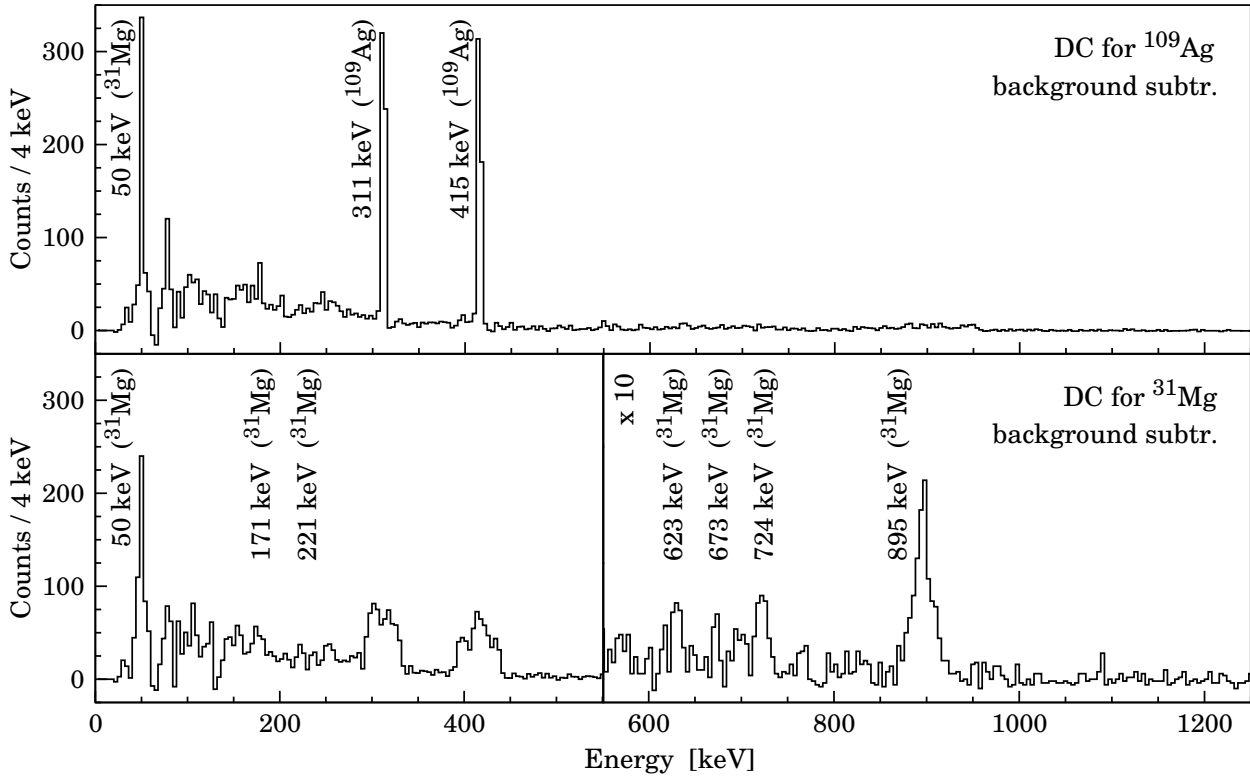


Figure 5.2: Doppler-corrected (DC) and background-subtracted γ -ray spectra in coincidence with scattered beam particles. Several γ -ray transitions from the Coulomb excitation of projectile and target nuclei were detected. For γ -ray energies above 550 keV the scale was zoomed in by a factor of 10 for visibility reasons. Further information is given in the text.

in Figure 5.1. A particle gate was applied, to select the scattered ^{31}Mg ions. Using the position and energy information of the scattered particle, a proper Doppler correction of the coincident γ rays was performed for the detected ^{31}Mg projectile and the corresponding recoiling ^{109}Ag target nucleus, respectively. Prompt γ -ray events were corrected for random background coincidences, as described in Section 4.6. The resulting γ -ray spectra are shown in Figure 5.2.

Analysis of the γ -ray spectra

Applying Doppler correction for scattered ^{109}Ag target nuclei, strong γ -ray transitions are observed in the background-subtracted γ -ray spectra at 311 keV and 415 keV, depopulating Coulomb-excited states in ^{109}Ag [134]. Doppler correction for beam-like particles gives rise to two transitions at 50 keV and 895 keV, already observed in β -decay studies of $^{31,32}\text{Na}$ [74, 135] and assigned to the transitions of a known excited state at 945 keV in ^{31}Mg . The small

Doppler-broadening of the 50 keV transition in the spectrum corrected for ^{31}Mg is due to the long half-life of 16(3) ns [74]. The time of flight between target and CD-detector is only 1.7-3.2 ns, thus these γ rays were emitted at rest after implantation in the detector. There is evidence for some more transitions de-exciting states in ^{31}Mg . Despite high background radiation, coming from bremsstrahlung, there is clear indication for two transitions at 171 keV and 221 keV, which are assigned to transitions of a known excited $3/2^{(-)}$ state at 221 keV [74, 77, 78, 135]. Two more transitions at 623 keV and 673 keV were already established by the β -decay studies as depopulating transitions of an excited state at 673 keV into the $3/2^{+}$ state at 50 keV and the ground state, respectively. The transition at 724 keV was observed for the first time in this work. To identify this γ -ray transition unambiguously and to place it into the level scheme, information on coincident transitions has been evaluated. Multiple γ -ray events, that are in prompt

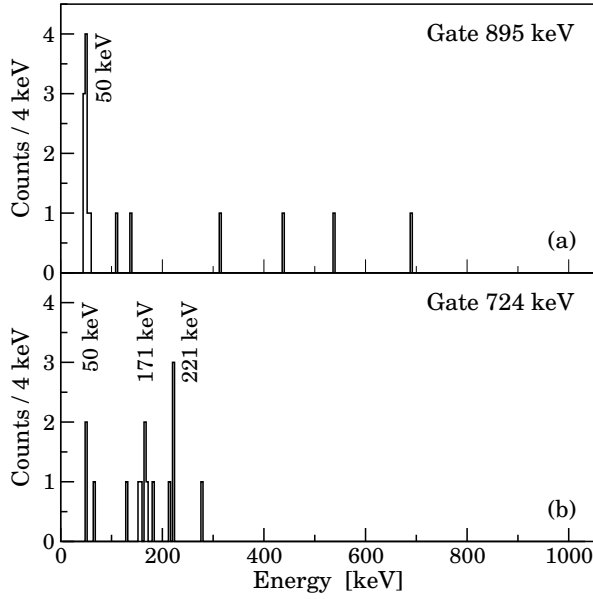


Figure 5.3: Prompt γ -ray coincidences in the Coulomb-excitation spectrum of ^{31}Mg , (a) for the 895 keV transition and (b) for the 724 keV transition, respectively. Coincident γ rays can be observed at 50 keV, 171 keV and 221 keV. Doppler correction was done for the detected ^{31}Mg nucleus.

coincidence with a detected beam particle, have been sorted into a $\gamma\gamma$ -matrix. The known coincident transitions at 895 keV and 50 keV from a $5/2^+ \rightarrow 3/2^+ \rightarrow 1/2^+$ cascade are confirmed by coincidence relations, as shown in Figure 5.3(a). Despite low statistics of 2-3 counts on a mean background of about 0.02 count/keV, which is in good agreement with the MINIBALL γ -ray efficiency of $\sim 10\%$, the cut spectrum on the 724 keV transition shows clear evidence for coincident γ rays at 50 keV, 171 keV and 221 keV (see Figure 5.3(b)). These transition energies are all known to belong to the low-energy level scheme of ^{31}Mg [74, 135]. The new 724 keV transition can be inserted clearly into the level scheme of ^{31}Mg as de-exciting transition of the 945 keV state, feeding a known $3/2^{(-)}$ state at 221 keV [77, 78]. The direct decay of the 945 keV state into the ground state was not observed. A summary of the observed transitions and relative intensities can be found in Figure 5.4.

The shape of the 895 keV line in the measured γ -ray spectrum does not follow a simple Gauss distribution, but has a slightly broader base (see Figure 5.5). This characteristic can

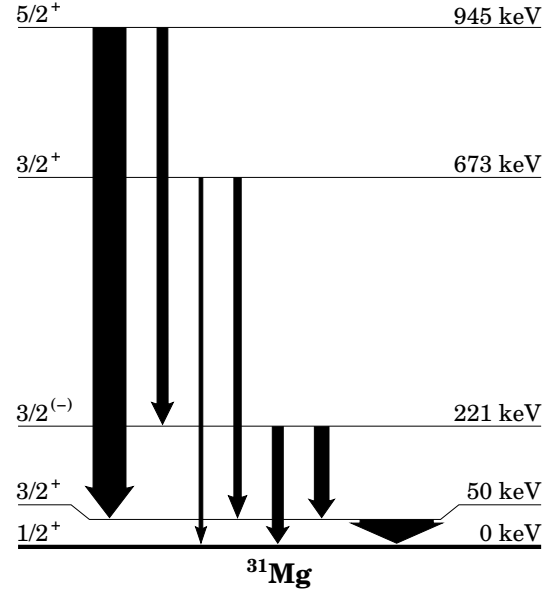


Figure 5.4: Measured γ -ray energies and relative intensities of the transitions observed in the Coulomb-excitation experiment of ^{31}Mg . The spin and parity assignments of the states will be discussed later in the text.

be explained by the fact that the lifetime of the 945 keV state is of the same order of magnitude than the time of flight of the excited nucleus through the target. If the Coulomb-excitation reaction takes place towards the end of the target, almost all excited nuclei will de-excite in-flight after the target. The detected energies E_{CD} of the nuclei in the CD detector correspond directly

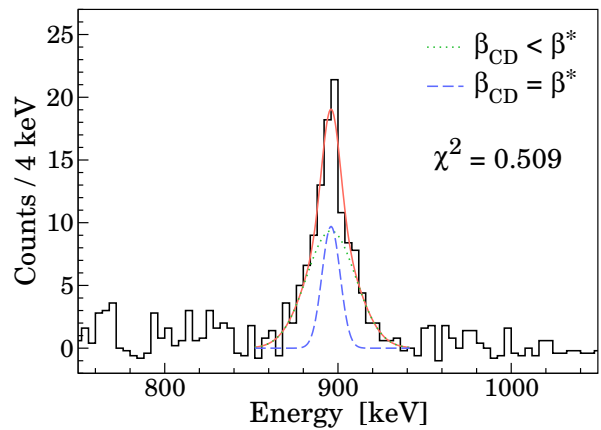


Figure 5.5: Shape of the 895 keV line of ^{31}Mg , indicating a lifetime of the level of the same order of magnitude than the time of flight through the target. The peak is fitted with contributions from the ^{31}Mg decaying after the target ($\beta_{\text{CD}} = \beta^*$) and during slowing down inside the target ($\beta_{\text{CD}} < \beta^*$).

to the velocities β^* of the nuclei at the moment of de-excitation. These events are Doppler corrected properly, resulting in a narrow contribution to the peak. If the nuclei get Coulomb excited right in the beginning or in the middle of the target, de-excitation may occur even during the slowing down process in the target. In the present case the maximum energy loss in the target after the reaction is about 40.3 MeV for a scattering process with $\theta = 53.7^\circ$ at the beginning of the target. Thus, the detected particle energies E_{CD} might be significantly lower, yielding slower velocities $\beta_{CD} < \beta^*$, than at the moment the γ ray was emitted. For these events the Doppler correction fails, leading to a slight shift of the detected energies to higher or lower values, depending whether the γ rays were emitted in forward or backward direction. Figure 5.6 shows the distribution of the Doppler-corrected 895 keV γ rays detected in forward ($\theta_{\gamma_{CM}} < 90^\circ$) and in backward direction ($\theta_{\gamma_{CM}} > 90^\circ$), respectively. The maximum time of flight through the target is about 0.45 ps. Thus, the ratio of the intensities of the narrow and broad contributions gives an estimation of the lifetime of the level at 945 keV, which yields only a few tenths of a picosecond.

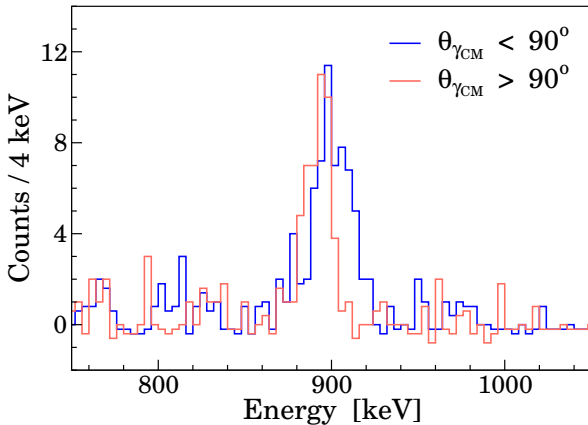


Figure 5.6: Distribution of the Doppler-corrected γ rays at 895 keV, detected in forward direction ($\theta_{\gamma_{CM}} < 90^\circ$) and in backward direction ($\theta_{\gamma_{CM}} > 90^\circ$), respectively. The asymmetry of the 895 keV line, i.e. the shift to higher/lower energies, depending on the detection angle is due to γ -ray emission during slowing down in the target and hence, an overestimation of the Doppler correction.

Reduced transition probabilities

The measured de-excitation yields of the γ -ray transitions in ^{31}Mg were used to determine the experimental Coulomb-excitation cross sections, which depend on the unknown reduced transition probabilities. These cross sections were normalized to the well-known cross sections for exciting the $3/2^-$ and $5/2^-$ states in the ^{109}Ag target, as shown in Section 3.6.3. According to Section 4.5.6, each isotope in the beam has a different cross section for excitation of the target nuclei. Therefore, the de-excitation yields of the γ -ray transitions in ^{109}Ag were corrected with the deduced effective beam composition, yielding a ^{31}Mg fraction of 77.4% for the excitation of the $3/2^-$ state and 77.7% for the excitation of the $5/2^-$ state. The fit of the experimental data was performed using the coupled-channels Coulomb-excitation code GOSIA [122]. The electromagnetic transition matrix elements were fitted using a least squares fit. The calculation took into account: the energy loss of the projectile in the target material, the angular distribution of the emitted γ ray, internal conversion coefficients, the position and efficiency of each MINIBALL cluster detector, and an integration over the scattering angle range of $\Theta_{CM} = 21.4-67.0^\circ$, which is covered by the CD detector.

Due to the unknown spin and parity values of excited states in ^{31}Mg , different scenarios for the spin and parity of the 945 keV state and different excitation modes were assumed:

- (i) The 945 keV state has a spin and parity of $5/2^+$ or $7/2^+$. Excitation takes place by a pure 2-step excitation, i.e. via $M1$ or $E2$ excitation $1/2_{g.s.}^+ \rightarrow 3/2^+$ and a subsequent $E2$ excitation $3/2^+ \rightarrow (5/2^+, 7/2^+)$.
- (ii) The 945 keV state has a spin and parity of $1/2^-$ or $3/2^-$ and is excited via an $E1$ excitation from the ground state.
- (iii) The 945 keV state has a spin and parity of $5/2^-$ or $7/2^-$ and is excited via an $E3$ excitation from the ground state.
- (iv) The 945 keV state has a spin and parity of $3/2^+$ and is excited via an $E2$ excitation from the ground state.
- (v) The 945 keV state has a spin and parity of

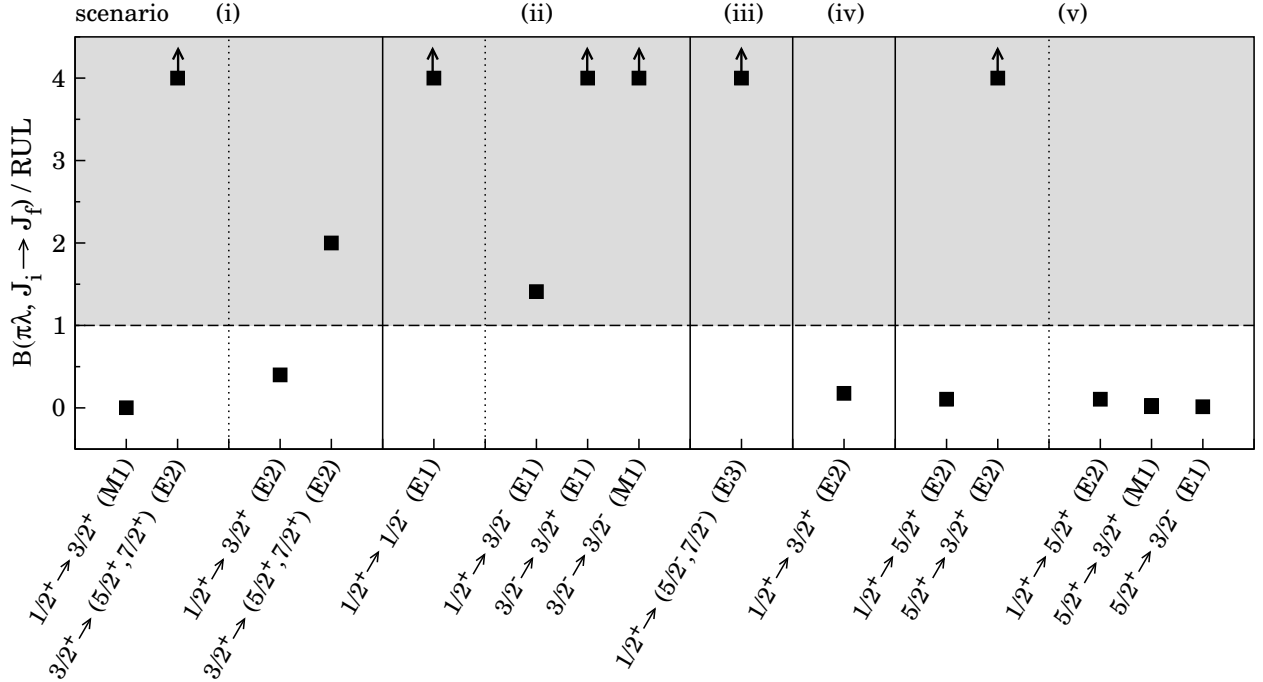


Figure 5.7: Calculated transition strengths of the Coulomb-excited ^{31}Mg . Due to the unknown spin and parity value of the 945 keV state different scenarios were tested to reproduce the measured Coulomb-excitation cross section. All values are given in terms of the recommended upper limits (RUL) for transition strengths [136], i.e. transitions with values > 1 can be excluded (shaded interval). The only scenario giving reasonable values is a direct E2 excitation from the $1/2^+$ ground state into a $5/2^+$ state at 945 keV, followed by a strong M1 de-excitation into the $3/2^+$ state at 50 keV. Detailed information is given in the text.

$5/2^+$ and is excited via a direct E2 excitation from the ground state.

To limit the model space of the Coulomb-excitation calculation a truncated level scheme of ^{31}Mg was used at this point, containing the following states and connecting transitions that are relevant for excitation of the 945 keV state: the $1/2^+$ ground state, the $3/2^+$ state at 50 keV, and the 945 keV state. Other levels contribute less than 10% to the excitation schemes and were neglected.

First, a possible 2-step excitation into the 945 keV state via the two consecutive transitions with 50 keV and 895 keV, respectively: $1/2^+_{g.s.} \rightarrow 3/2^+ \rightarrow (5/2^+, 7/2^+)$ is clearly excluded. The known $B(M1, 3/2^+ \rightarrow 1/2^+_{g.s.}) = 0.0190(37) \mu_N^2$ value [72] for the M1 excitation implies a M1 Coulomb-excitation cross section of 0.05 mb for the 50 keV state. Consequently the next excitation to the 945 keV state, even with an E2 matrix element far beyond the recommended upper limit (RUL) of 100 W.u. for E2 strengths [136], would yield

a nanobarn cross section, which is orders of magnitude less than the measured value of around 130 mb. Therefore the M1 contribution to the excitation is negligible. A large E2 component of $B(E2, 1/2^+ \rightarrow 3/2^+) = 460 \text{ e}^2\text{fm}^4$ was assumed for the first excitation step, which is comparable to the E2 strength of the collective $0^+ \rightarrow 2^+$ transition in ^{32}Mg . In order to reproduce the measured γ -ray yields, the second excitation into the 945 keV state would have to have an excitation strength of $B(E2, 3/2^+ \rightarrow 7/2^+) \approx 2300 \text{ e}^2\text{fm}^4$ which is again significantly higher than the RUL for E2 strengths (cf. Fig. reftrans-prob-calc). Consequently scenario (i), a 2-step excitation process, can only play a negligible role in exciting the 945 keV state. Thus, the main contribution of the excitation comes from direct excitation from the $1/2^+$ ground state into the 945 keV state.

In the case of a 1-step excitation via E1 the 945 keV level would have negative parity and the spin would be limited to $1/2$ or $3/2$. For the assumption of a $1/2^-$ state at

945 keV GOSIA calculated excitation probabilities of $0.466 \text{ e}^2\text{fm}^2$, which exceeds the RUL of 0.1 W.u. for $E1$ transitions [136] by more than a factor 7. For a $3/2^-$ state GOSIA calculated a reduced excitation probability of $B(E1, 1/2^+ \rightarrow 3/2^-) = 0.224 \text{ e}^2\text{fm}^2$. For de-excitation into the $3/2^+$ state at 50 keV the calculation yielded $B(E1) = 3.3 \text{ W.u.}$ and $B(M1) = 71.3 \text{ W.u.}$ for de-excitation into the $3/2^{(-)}$ state at 221 keV, respectively. All these values are significantly higher than the recommended upper limits of each transition and scenario (ii) can be excluded. Also an excitation via $E3$ to a $5/2^-$ or $7/2^-$ state would yield a similar disproportionately huge value of $B(E3) \uparrow > 40000 \text{ e}^2\text{fm}^6$, which exceeds the RUL by at least a factor of 4. Thus, a negative parity state, i.e. scenario (iii), can be excluded.

The remaining possibilities to get consistent values for the excitation of the 945 keV state are the scenarios (iv) and (v). Hence, the 945 keV state has to be a $3/2^+$ or a $5/2^+$ state and the population has to proceed via a direct (1-step) $E2$ excitation from the ground state. Now the full known level scheme of ^{31}Mg up to 1 MeV and all known and newly observed transitions were taken into account for the calculation, with adopted $B(E1)$, $B(E2)$, and $B(M1)$ values for the states up to 500 keV [72, 77]. Predicted spectroscopic quadrupole moments Q_s and their reduced matrix elements for the $3/2^+$ and $5/2^+$ states [48, 76], so-called re-orientation matrix elements, were included into the calculation, using

$$Q_s^{al} = -\sqrt{\left(\frac{16\pi I(2I-1)}{5(I+1)(2I+1)(2I+3)}\right)} \times M_{al,al}(E2),$$

where $M_{al,al}(E2) = -\langle \alpha I || \mathfrak{M}(E2) || \alpha' I' \rangle$ is the reduced matrix element [24].

For the assumption of a $3/2^+$ state at 945 keV the reduced transition probability was calculated to be $B(E2, 1/2^+ \rightarrow 3/2^+) = 198 \text{ e}^2\text{fm}^4$. De-excitation was investigated using the measured branching ratios of 74(12)% for the 895 keV transition, 24(7)% for the 724 keV transition, and an upper limit of $< 2.6(8)\%$ for the unobserved direct transition to the ground state. De-excitation of a $3/2^+$ state at 945 keV

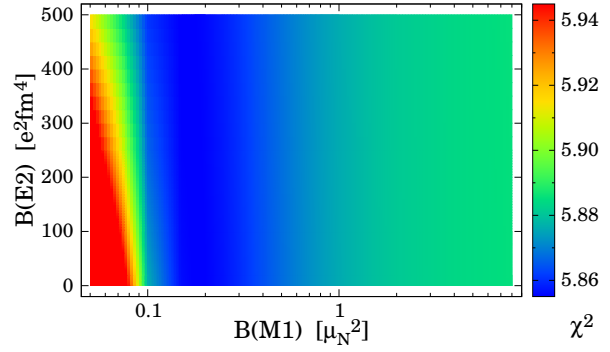


Figure 5.8: Calculated, total χ^2 as a function of the $B(E2)$ and $B(M1)$ values of the 895 keV transition, de-exciting the 945 keV state in ^{31}Mg . A minimum was found at $B(M1) = 0.18(5) \mu_N^2$. The χ^2 depends weakly on the $B(E2)$ for a given $B(M1)$ value. More information is given in the text.

would have to proceed via $E2+M1$ transitions to the ground state and the $3/2^+$ state at 50 keV, respectively. The investigated branching ratios yield a ground-state transition via $M1+E2$ with a reduced transition probability that is hindered by a factor of about 10^{-4} compared to the 895 keV transition. This is very unlikely due to the similar $2p3h$ configuration of the ground state and the first $3/2^+$ excited state at 50 keV [48]. Thus, scenario (iv), i.e. a $3/2^+$ state at 945 keV can be rejected.

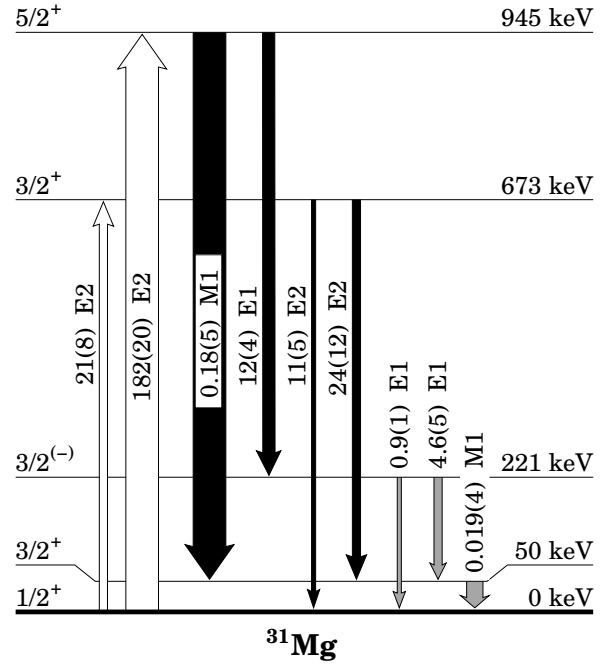
The only remaining possibility is that the 945 keV is a $5/2^+$ state, i.e. scenario (v). The analysis yielded a reduced transition probability of $B(E2) \uparrow = 182 \pm 17 \text{ (stat.) } {}^{+9}_{-13} \text{ (syst.) e}^2\text{fm}^4$. The error bar is dominated by the statistical error on the number of counts in the observed γ -ray transitions. The systematic error includes mainly the uncertainty on the beam composition, as well as the uncertainties on the $B(E2)$ values of the ^{109}Ag target excitation. Investigating de-exciting transitions, a pure $E2$ transition to the 50 keV state would imply an unreasonably high $B(E2)$ value of about $2700 \text{ e}^2\text{fm}^4$, which is in fact about $4.7 \times \text{RUL}$, to reproduce the measured intensities. Thus, de-excitation to the 50 keV state proceeds via a strong $M1$ transition. The magnitude of the $M1$ strength depends mostly on the multipole mixing ratio δ of the transition and its absolute $E2$ strength. To fix these parameters, the excitation and de-excitation process was calculated for different $B(E2)$ and $B(M1)$ values of the 895 keV tran-

sition. Figure 5.8 shows the magnitude of the resulting total χ^2 , depending on the $E2$ and $M1$ strengths. The χ^2 contains mostly the deviation of the calculated and measured γ -ray yields, as well as of known branching ratios, lifetimes, and transition strengths. Obviously the χ^2 depends weakly on the $B(E2)$ for a given $B(M1)$ value. Thus, the absolute $E2$ strength has to be determined by another technique, for example a measurement of the multipole mixing ratio δ via the angular distribution of the emitted γ rays. For the $M1$ strength of the 895 keV transition the calculated χ^2 has its minimum at $B(M1, 5/2^+ \rightarrow 3/2^+) = 0.18(5) \mu_N^2$. The additional de-excitation to the $3/2^{(-)}$ state at 221 keV had to proceed via an $E1$ transition with $B(E1) = 12(4) \times 10^{-4} \text{ e}^2\text{fm}^2$. A brief summary of the transition strengths calculated for the different scenarios of the spin and parity of the 945 keV state is given in Figure 5.7.

The deduced transition strengths can be used to calculate the lifetimes of the populated states. For the 945 keV state GOSIA gives an average lifetime of $\tau_{5/2^+} = 0.32(9)$ ps, assuming an $E2$ strength of $60 \text{ e}^2\text{fm}^4$ for the 895 keV transition, which is of the same order as the $E2$ strength of the ground-state transition. This result agrees well with the lifetime, which was estimated using the observed line shape of the 895 keV transition (cf. pages 57f).

For the 673 keV state, which is a $3/2_2^+$ state with a $0p1h$ configuration [78], the analysis yielded a reduced transition probability of $B(E2, 1/2^+ \rightarrow 3/2_2^+) = 21(8) \text{ e}^2\text{fm}^4$. Assuming purely $E2$ de-excitation from this state as well, the calculation gives $B(E2) = 11(5) \text{ e}^2\text{fm}^4$ and $B(E2) = 24(12) \text{ e}^2\text{fm}^4$ for the 673 keV and 623 keV transitions, respectively. For the lifetime of this state GOSIA gives $\tau_{3/2_2^+} = 80(30)$ ps. The $B(E2)$ value of the 50 keV transition could not be determined due to feeding and a complex, non-uniform efficiency for these 50 keV γ rays in the MINIBALL detectors, as stated in Section 4.2.2.

All reduced transition probabilities that were deduced in this experiment are presented in Figure 5.9. For the first time a clear spin and parity assignment was done for the 945 keV state. This $5/2^+$ state is part of a strong collective $K^\pi = 1/2^+$ band in ^{31}Mg .



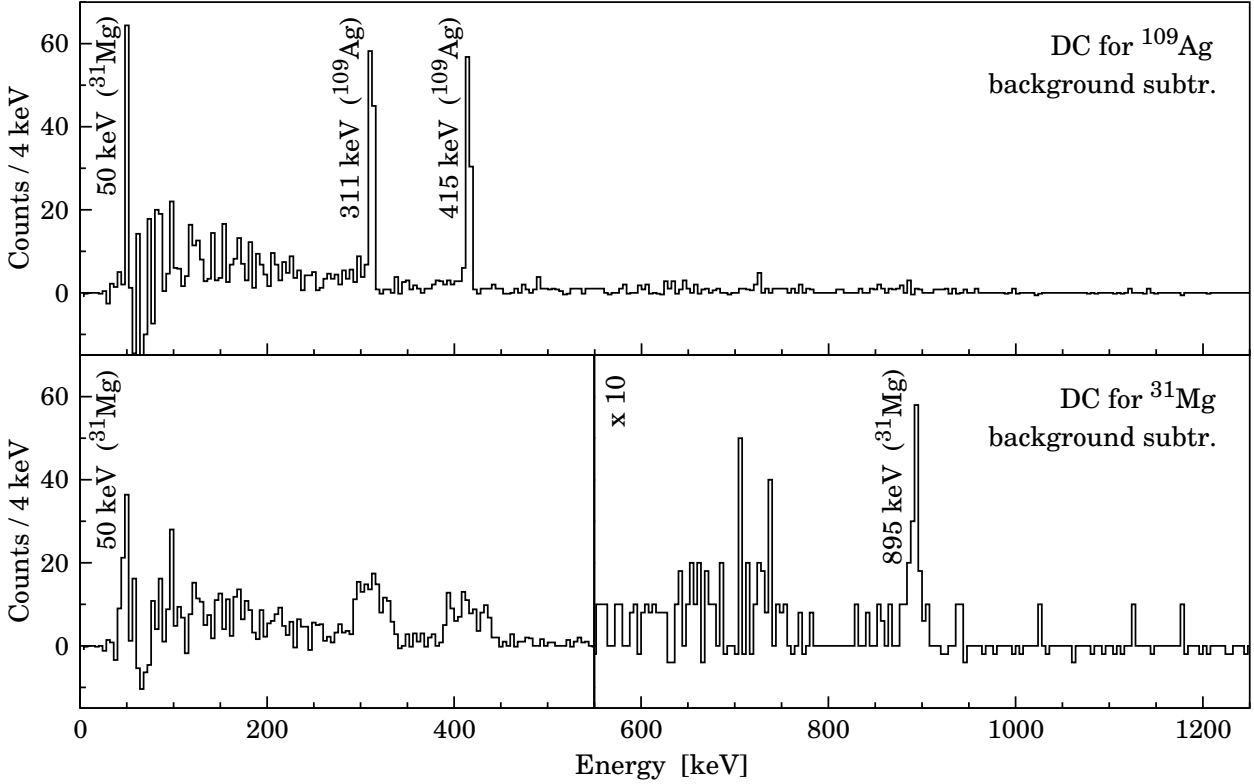


Figure 5.11: Doppler-corrected (DC) and background-subtracted γ -ray spectra in coincidence with scattered beam particles. γ -ray transitions from the Coulomb excitation of projectile and target nuclei were observed. For γ -ray energies above 550 keV the scale was zoomed in by a factor of 10 for visibility reasons. Further information is given in the text.

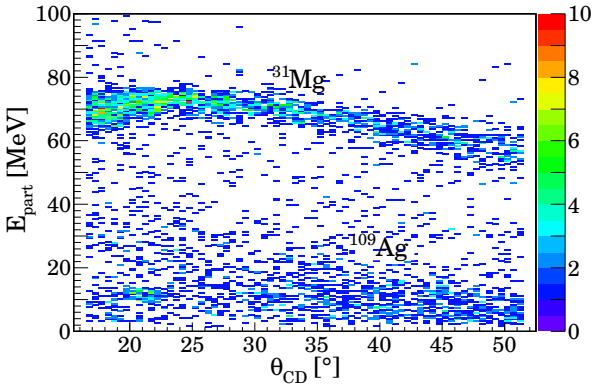


Figure 5.10: Particle energy versus scattering angle, measured in the DSSSD for the ^{31}Mg beam, incident on the 1.9 mg/cm^2 thick ^{109}Ag target at a beam energy of 3.0 MeV/u . Only those events are plotted, which coincide with at least one prompt γ -ray event detected at MINIBALL. Compared to Fig. 5.1 straggling is reduced significantly due to the thinner target. Thus, also some scattered target nuclei can be observed at energies below 20 MeV.

background-subtracted and Doppler-corrected spectra for both, Coulomb-excited projectile and

target nuclei. For ^{109}Ag the well known transitions at 311 keV and 415 keV are identified, depopulating Coulomb-excited $3/2^-$ and $5/2^-$ states, respectively [134]. Applying Doppler correction for scattered ^{31}Mg nuclei, the two transitions at 50 keV and 895 keV are visible, which are assigned to the known transitions of the 945 keV state in ^{31}Mg [74, 135]. Also the newly observed 724 keV transition (cf. p.56) can be found, even though there is poor statistics of only 5.6(2.4) counts.

Reduced transition probabilities

The measured intensities of the γ -ray transitions depopulating Coulomb-excited states in the ^{109}Ag target and ^{31}Mg projectile nuclei, respectively, were used to determine the excitation strength of the 945 keV state of ^{31}Mg . Deduced Coulomb-excitation cross sections were normalized to the well-known cross sections for exciting the 311 keV and 415 keV states in the ^{109}Ag target nuclei. Spin and parity assignments for

the different states of ^{31}Mg , which could be deduced in the detailed analysis of the experiment with the 4.0 mg/cm^2 thick ^{109}Ag target, were taken into account. Finally the GOSIA calculations yielded a reduced transition probability of $B(E2)^\dagger = 138 \pm 42 \text{ (stat.)} \pm 21 \text{ (syst.) } e^2\text{fm}^4$ for the excitation of the $5/2^+$ state in ^{31}Mg . The obtained value agrees well with the transition strength of $B(E2) = 182(20) e^2\text{fm}^4$ deduced with the thicker target.

5.2 Coulomb excitation of ^{29}Na

After the successful experiment on neutron-rich ^{31}Mg , another Coulomb-excitation experiment was proposed with the MINIBALL setup at REX-ISOLDE to study the $N = 19$ isotope of ^{31}Mg , which is ^{30}Na , as well as the $N = 18$ sodium isotope ^{29}Na . The aim was to determine their reduced transition probabilities.

The Coulomb-excitation experiment of ^{29}Na was carried out at REX-ISOLDE at a final beam energy of 2.85 MeV/u . Due to the very short half-life of $44.1(9) \text{ ms}$ [137] special attention had to be paid on the optimization of the working cycle of the REX-ISOLDE charge breeding system in order to minimize losses caused by in-trap decay. Therefore the charge breeding and repetition times were set to 13 ms and 20 ms , respectively. The fast release of the sodium ions out of the primary target enables the use of a very restrictive time gate of only $275(10) \text{ ms}$ after the proton impact on the primary target in the off-line analysis. Thus, the average relative amount of ^{29}Na in the post-accelerated radioactive ion beam was increased to $29.5(7)\%$, which is equivalent to an absolute value of $2700(100) \text{ ions/s}$ at the MINIBALL scattering target. To maximize the yield of the Coulomb-excitation reaction, the scattering target consisted of a stack of two ^{104}Pd targets with thicknesses of 1.9 mg/cm^2 and 2.2 mg/cm^2 , respectively. The beam on target time added up to almost 64 hours . For γ -ray detection seven MINIBALL triple cluster detectors were available. More information on the experimental details and the beam composition can be found in Chapter 4.5.

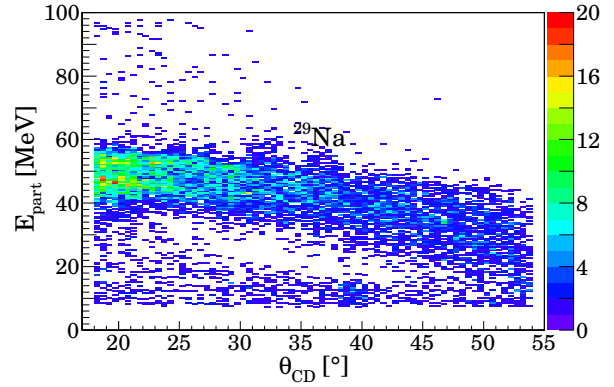


Figure 5.12: Particle energy versus scattering angle, measured in the CD detector for the $A=29$ beam, incident on the 4.1 mg/cm^2 thick ^{104}Pd target at a beam energy of 2.85 MeV/u . Due to the distinctive, Z -dependent energy loss in the target ^{29}Na and ^{29}Al can be identified and partially separated. Only those events are plotted, which coincide with at least one prompt γ -ray event detected at MINIBALL.

5.2.1 Measurement at 2.85 MeV/u on a 4.1 mg/cm^2 thick ^{104}Pd target

Scattered ^{29}Na ions were selected by a particle gate on the measured correlation of particle energy and scattering angle in the CD-detector, according to Section 4.4. As shown in Figure 5.12 the isobars ^{29}Na and ^{29}Al can be well identified and partially separated due to their distinctive energy losses in the target. Nevertheless the particle gate includes all $A = 29$ nuclei. Using the position and energy information of the scattered particle, a proper Doppler correction of the coincident γ rays was performed for the detected $A = 29$ projectile and the corresponding recoiling ^{104}Pd target nucleus, respectively. The resulting prompt, background-subtracted γ -ray spectra are shown in Figure 5.13.

Analysis of the γ -ray spectra

De-excitation γ rays of excited states of both projectile and target nuclei were observed in the spectra, shown in Figure 5.13. The well-known $2^+ \rightarrow 0^+$ transition in ^{104}Pd at 555.8 keV [138] was the strongest γ -ray transition in the prompt, background-subtracted spectrum. Due to the slow velocities of the scattered target nuclei ($\beta \approx 0$), which were mostly stopped in the target, no Doppler correction was necessary. Additionally at 767.8 keV the de-exciting transition of

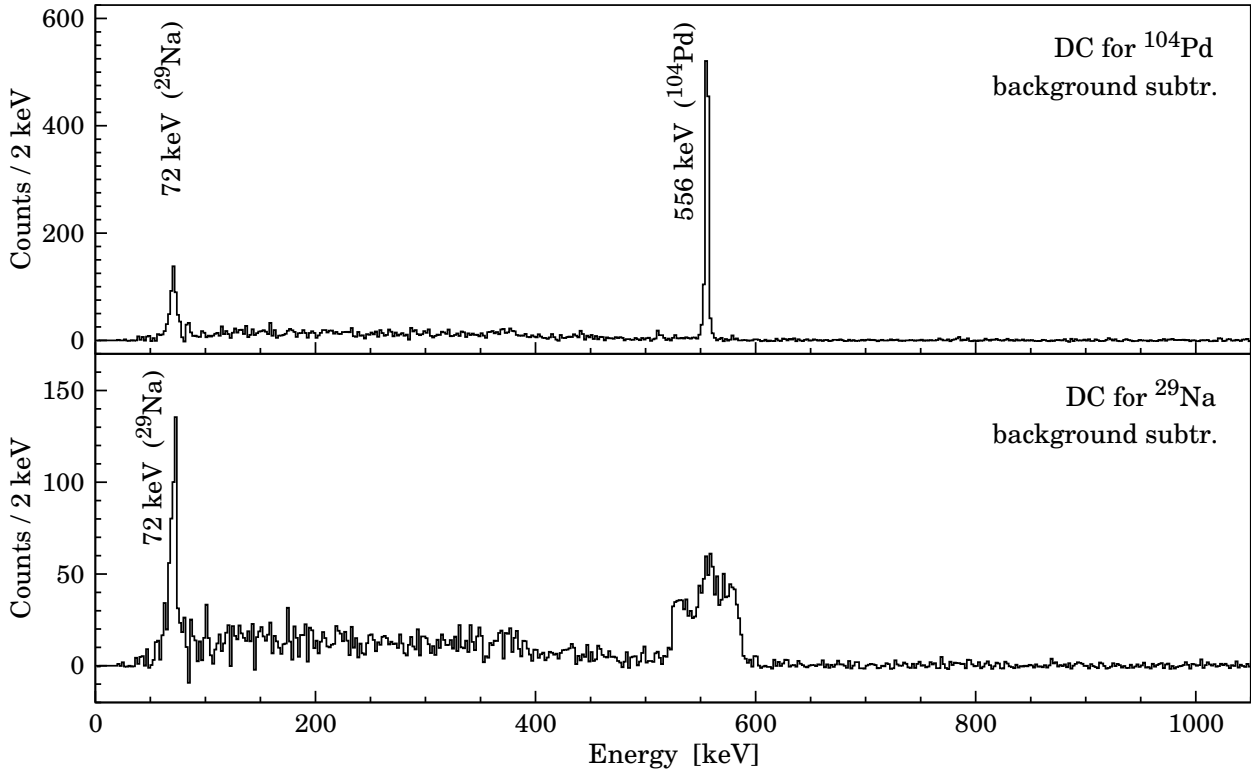


Figure 5.13: Doppler-corrected (DC) and background-subtracted γ -ray spectra in coincidence with beam particles. γ -ray transitions from the Coulomb excitation of projectile and target nuclei were detected. Further information is given in the text.

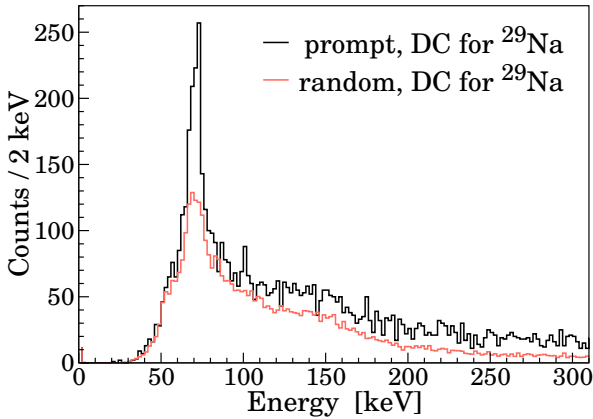


Figure 5.14: Prompt Coulomb-excitation spectrum of ^{29}Na , compared to the random background X-ray radiation, both including Doppler correction for the scattered projectile. The excess of prompt 72 keV γ rays is clearly visible.

the 4^+ state to the 2^+ state [138] was observed, even though it contained only 5(2) counts.

Prior to the Coulomb-excitation experiment on the neutron-rich Na isotopes an experiment on ^{200}Po was performed at the MINIBALL setup. Therefore in the analysis of the γ -ray spectra

special attention had to be paid to the background radiation, coming from the long-lived decay products of ^{200}Po . Strong X-ray radiation following β -decay of ^{200}Pb and ^{200}Tl matched the γ -ray energy of a known transition in ^{29}Na at 72 keV [81]. Thus, careful investigation of the low-energy spectra of prompt (Coulomb excitation) and random (background) γ -ray events was mandatory (see Figure 5.14). It was possible to determine the γ -ray yield of the 72 keV transition, depopulating the Coulomb-excited proposed $5/2^+$ state in ^{29}Na with reasonable accuracy.

A detailed analysis of the line-shape of the 72 keV transition similar to the analysis of the line shape of the 895 keV transition in ^{31}Mg (cf. Fig. 5.5,5.6) revealed information on the lifetime of the 72 keV state in ^{29}Na . The prompt, Doppler-corrected and background-subtracted γ -ray events were plotted depending on the angle $\theta_{\gamma\text{CM}}$ between scattered nucleus and γ ray. The resulting spectrum for backward angles ($\theta_{\gamma\text{CM}} > 90^\circ$) is shown in Figure 5.15. Whereas the ^{31}Mg spectrum for this angular

range showed events that were slightly shifted to lower energies due to γ -ray emission during slowing-down in the target, the line shape of the 72 keV transition shows some events that were

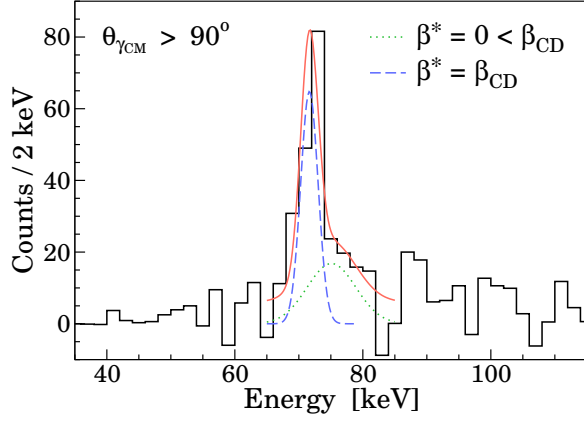


Figure 5.15: Shape of the Doppler-corrected 72 keV line of ^{29}Na for γ -ray emission in backward direction ($\theta_{\gamma\text{CM}} > 90^\circ$). The peak is fitted with two contributions from decay at rest after implantation in the DSSSD ($\beta^* = 0$) and in flight ($\beta^* = \beta_{\text{CD}}$).

shifted to slightly higher energies after Doppler correction. For $\theta_{\gamma\text{CM}} < 90^\circ$ some events were shifted to lower energies. Thus, most γ rays were emitted in flight ($\beta^* = \beta_{\text{CD}}$), but some of them had to be emitted in rest after implantation in the DSSSD ($\beta^* = 0 < \beta_{\text{CD}}$), for which the Doppler correction failed. Depending on the scattering angle and velocities of $\beta_{\text{CD}} = 4.9\text{--}6.4\%$ for the scattered ^{29}Na nuclei, the time-of-flight (TOF) from the target to the CD detector was between 1.7–3.5 ns. The ratio of the shifted and unshifted component, indicated in Figure 5.15, gives an estimate of the lifetime of the 72 keV state: $\tau \approx 0.90 \text{ TOF}_{\text{mean}} \approx 1.8$ ns.

Monte-Carlo shell model (MCSM) calculations by Utsuno *et al.* predicted γ -ray transitions depopulating deformed $3/2_2^+$, $5/2_2^+$, and $7/2_1^+$ states in ^{29}Na at around 2 MeV, which could be Coulomb excited with a moderately large excitation strength [54]. For instance a possible $7/2_1^+$ state might be excited with a transition strength of $B(E2, 3/2_1^+ \rightarrow 7/2_1^+) = 57 \text{ e}^2\text{fm}^4$ [54]. No

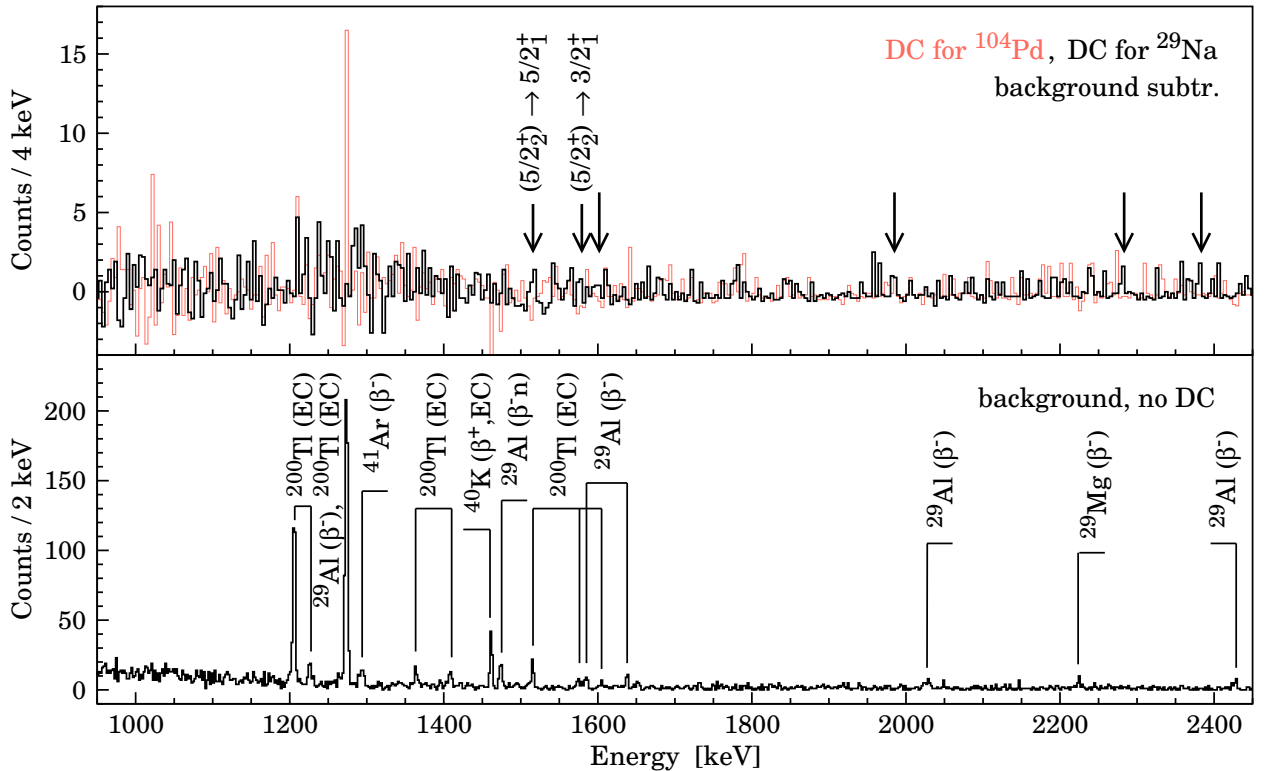


Figure 5.16: Doppler-corrected and background-subtracted γ -ray spectra in coincidence with beam particles (top) compared to the background spectrum (bottom) for γ -ray energies above 1 MeV. No peak from a γ -ray transition depopulating high-lying Coulomb-excited states in ^{29}Na was found. Possible candidates for weak transitions are indicated, e.g. the $(5/2_2^+) \rightarrow 5/2_1^+$ transition at 1516 keV. The structure at around 1200–1400 keV is caused by statistical fluctuations of Doppler-broadened background decay transitions.

clear experimental sign was found for such transitions due to the low beam intensity of about 3500 ions/s, which was more than three times less than expected from known ISOLDE yields. Possible candidates for weak transitions were found at several energies in the range of 1500-2400 keV, as indicated in Figure 5.16. The most promising one at 1518(4) keV was already known from β -decay studies as depopulating transition of a $(5/2^+)$ state at 1588 keV [81].

Reduced transition probabilities

Following the method presented in 3.6.3 the unknown reduced transition probabilities of excited states of ^{29}Na were determined using the relative de-excitation γ -ray yields between ^{29}Na and the Coulomb-excited, well known 2^+ state of ^{104}Pd . The de-excitation yield of the 555.8 keV transition of ^{104}Pd was corrected with the deduced effective beam composition, including the different Coulomb-excitation cross sections of the isobars for excitation of the target material, yielding a ^{29}Na fraction of 32.2(10)% for the excitation of the 2^+ state. To fit the electromagnetic transition matrix elements to the experimental data the coupled-channels Coulomb-excitation codes CLX and GOSIA were used. The calculations were performed integrating over the scattering angle range of $\Theta_{\text{CM}} = 20.9\text{-}66.2^\circ$, which is covered by the CD detector, and the energy loss of the projectile in the target material. Corrections of the measured γ -ray yields for angular distribution effects and internal conversion were taken into account as well as position and efficiency of the MINIBALL cluster detectors.

The spin and parity of the 72 keV state were determined to be $J^\pi = 5/2^+$ [83] in agreement with MCSM calculations which favor a $5/2^+$ above the $3/2^+$ ground state [54]. The spectroscopic quadrupole moment of the ground state was measured by β -NMR spectroscopy, yielding a value of $Q_{3/2^+} = +0.086(3)$ eb [80]. This quadrupole moment was included in the calculation as diagonal matrix element $\langle 3/2^+ || E2 || 3/2^+ \rangle = 0.121(4)$ eb. For the 72 keV state the diagonal matrix element was assumed to be $\langle 5/2^+ || E2 || 5/2^+ \rangle = 0.039(3)$ eb within a rotational model with $K = 3/2$.

Including this information the GOSIA calculation yielded a reduced transition probability of $B(E2, 3/2^+ \rightarrow 5/2^+) = 150(20) \text{ e}^2\text{fm}^4$ for the Coulomb excitation of the $5/2^+$ state at 72 keV. The quoted error is dominated by the statistical error of almost 10% for the measured γ -ray yield, but also includes a 6% error for the correction for the X-ray radiation background and a 5% error for unobserved feeding from higher-lying excited states. Uncertainties of the beam composition and target excitation were included with 3% and 2%, respectively. The code CLX yields a consistent value of $B(E2) \uparrow = 159(21) \text{ e}^2\text{fm}^4$ to reproduce the measured Coulomb-excitation cross section of 212(28) mb for the $5/2^+$ state. The obtained values agree very well with the transition strength of $B(E2) \uparrow = 140(26) \text{ e}^2\text{fm}^4$, which was published by Hurst *et al.* [58].

De-excitation of the 72 keV state had to proceed via a strong $M1$ transition, to reproduce the estimated lifetime of less than 2 ns, described above. The GOSIA calculation yielded a lower limit of $B(M1, 5/2^+ \rightarrow 3/2^+) > 0.06 \mu_N^2$ for the $M1$ strength. Using the equation

$$\delta^2 = \frac{3}{100} \left(\frac{E_\gamma}{\hbar c} \right)^2 \frac{B(E2, J_i \rightarrow J_f)}{B(M1, J_i \rightarrow J_f)},$$

given in [24], where E_γ is given in MeV and the reduced transition probabilities are given in units of e^2b^2 for $E2$ and μ_N^2 for $M1$, this corresponds to a multipole mixing ratio $|\delta| < 0.025$.

From Figure 5.16 an upper limit can be calculated for the excitation of the 1588 keV state, known from β -decay studies [81, 83]. The spin and parity of this state are assigned to $1/2^+$, $3/2^+$, or $5/2^+$ due to the measured $\log ft = 4.64$ value in combination with the $3/2^+$ ground state of ^{29}Ne [83, 137]. However, the calculated excitation strength differed only marginally ($\sim 5\%$) on the spin value of the 1588 keV state, yielding $B(E2, 3/2^+ \rightarrow (5/2_2^+)) = 70(40) \text{ e}^2\text{fm}^4$. For the proposed $7/2^+$ state [54], as well as for any other higher-lying excited state in ^{29}Na , only an upper limit could be given for the reduced transition probability. Therefore a detection limit of 2.5 counts was assumed for a transition on an average background of almost 0.1 counts/keV, measured in this experiment with the MINIBALL setup in the

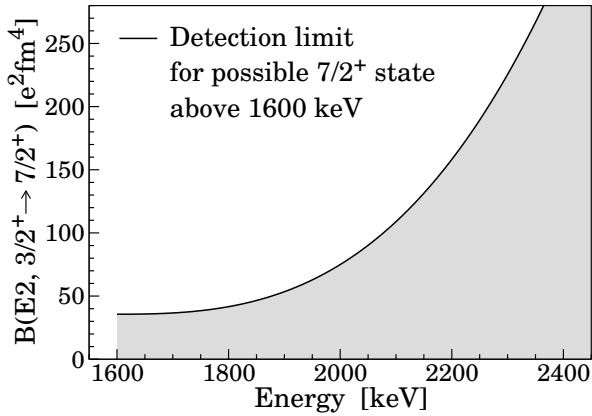


Figure 5.17: Calculated upper limit for the excitation strength of a possible $3/2^+ \rightarrow 7/2^+$ transition in ^{29}Na between 1600 keV and 2450 keV (solid line) in the present experiment in order to reproduce the measured γ -ray yields. Detailed information is given in the text.

energy range between 1600 keV and 2500 keV. It was assumed that the $7/2^+$ state had to decay to the $5/2^+$ state with a branching ratio of almost 100%. Any other branching, e.g. the direct decay into the ground state, was neglected. To reproduce the measured γ -ray yields the $E2$ excitation strength of the $3/2^+ \rightarrow 7/2^+$ transition has to be smaller than the upper limit indicated by the solid line in Figure 5.17. Thus, a transition to a $7/2^+$ state below 1900 keV would have to have a $B(E2)$ value similar to or even smaller than the predicted $57 \text{ e}^2\text{fm}^4$ [54], whereas a higher-lying $7/2^+$ state with such a moderately large value could not be detected at all in the present experiment. A $7/2^+$ state at around 2300 keV would need to be connected to the ground state with $B(E2)_{\uparrow} \approx 230 \text{ e}^2\text{fm}^4$, to be detected with 2.5 counts.

It was possible to deduce the transition strength of the $5/2^+ \rightarrow 3/2^+$ transition in agreement with the value published after proposal submission by Hurst *et al.* [58]. For transition probabilities of higher-lying deformed states the results achieved were not conclusive.

5.3 Coulomb excitation of ^{30}Na

In addition to the of ^{29}Na experiment, another Coulomb-excitation experiment on the neighboring $N = 19$ isotope ^{30}Na was carried out, using the MINIBALL setup at REX-ISOLDE, to fur-

ther study the expected transition from spherical sd-shell to deformed sd-pf-shell configurations at the island of inversion.

To achieve this a radioactive ^{30}Na beam was accelerated by the REX-LINAC up to a final energy of 2.85 MeV/u. The fraction of ^{30}Na in the radioactive $A = 30$ beam was determined to be almost 14%, but the ratio could be increased up to almost 50% in the analysis by applying a 285 ms wide time gate on the release curve (cf. Section 4.5). The average Na intensity was about 550-750 ions/s. The experiment was split into two separate parts with a break of two days in between due to another MINIBALL experiment on ^{200}Po . Two different scattering targets were employed, consisting of enriched ^{120}Sn and ^{104}Pd with thicknesses of 4.0 mg/cm^2 and 4.1 mg/cm^2 , respectively. The ^{104}Pd target was a stack of two targets (2.2 mg/cm^2 and 1.9 mg/cm^2) and was already used during the ^{29}Na experiment. The beam on target time added up to about 46 hours for the ^{120}Sn target and almost 38 hours for the ^{104}Pd target. For γ -ray detection seven MINIBALL triple cluster detectors were mounted on the support frame around the scattering chamber.

5.3.1 Measurement at 2.85 MeV/u on a 4.0 mg/cm^2 thick ^{120}Sn target

A ^{30}Na beam with an energy of 2.85 MeV/u was incident on a 4.0 mg/cm^2 thick enriched ^{120}Sn target. Scattered ^{30}Na nuclei were selected by means of the measured correlation between scattering angle θ_{CD} and energy deposited in the CD detector as shown in Figure 5.18. Apparent deviations in the detected particle energies are due to insufficient calibration data for the detector in this experiment. Nevertheless it was possible, to perform a sufficient Doppler correction of the coincident γ -ray events, using the energy and position information of the scattered particles and γ rays. The resulting background-subtracted γ -ray spectra are shown in Figure 5.19, one of them with a Doppler correction in the rest frame of the detected projectile, the other one with a Doppler correction in the rest frame of the target nucleus.

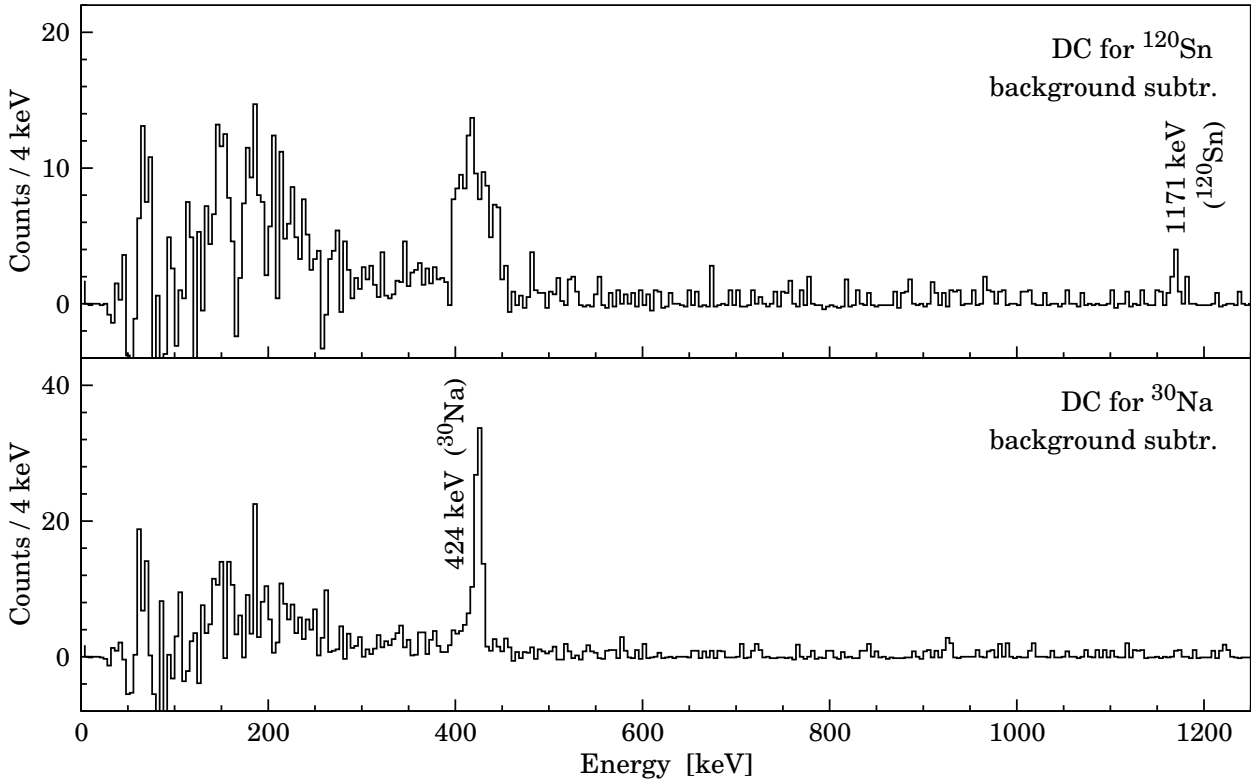


Figure 5.19: Doppler-corrected (DC) and background-subtracted γ -ray spectra in coincidence with scattered beam particles. Prompt γ -ray transitions from the Coulomb excitation of both projectile (^{30}Na) and target (^{120}Sn) nuclei were detected. Events with 511 keV coming from background radiation were suppressed in the spectra. Further information is given in the text.

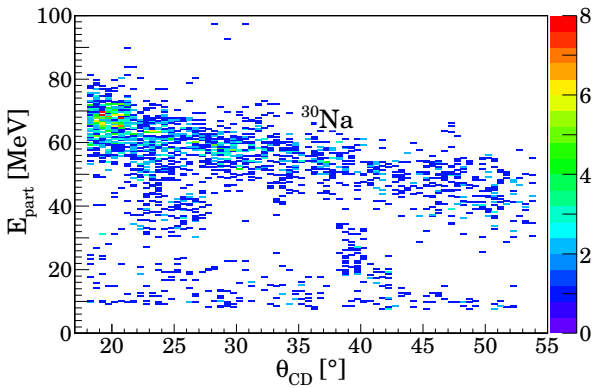


Figure 5.18: Particle energy versus scattering angle, measured in the CD detector for the $A=30$ beam, incident on the 4.0 mg/cm^2 thick ^{120}Sn target at a beam energy of 2.85 MeV/u . Only those events are plotted, which coincide with at least one prompt γ -ray event detected at MINIBALL. Apparent deviations in the detected particle energies for scattering angles around 25° and 40° are due to insufficient calibration data for the detector in this experiment.

Analysis of the γ -ray spectra

The background-subtracted γ -ray spectra taken during the experiment contain de-excitation

events of excited states of both, projectile and target nuclei. Applying Doppler correction for scattered ^{120}Sn nuclei, a weak γ -ray transition of the well-known $2_1^+ \rightarrow 0_{\text{gs}}^+$ transition was observed at 1171 keV [139] with a total intensity of 12.3(34) counts. Doppler correction for scattered $A = 30$ projectiles revealed a strong γ -ray transition at 424 keV, which was already observed by Ettenauer *et al.* [45] and assigned to the ground-state transition of an excited (3^+) state in ^{30}Na at 424 keV. De-exciting transitions of low-lying excited 1^+ states, which were known from β -decay studies of ^{30}Ne [83], were not observed in this Coulomb-excitation experiment. An accumulation of γ -ray events at around 924 keV could be interpreted as a possible candidate for the proposed (4^+) state in ^{30}Na . Its identification and placement in the level scheme will be presented later on in the analysis of the experiment using the palladium target (see Section 5.3.2).

Reduced transition probabilities

The reduced excitation probability from the ground state to the (3^+) state of ^{30}Na at 424 keV was determined by means of the measured intensity of the depopulating $(3^+) \rightarrow 2^+$ γ -ray transition, relative to the well-known cross section for Coulomb exciting the 2_1^+ state in ^{120}Sn . The de-excitation yield of the 1171 keV transition of ^{120}Sn had to be corrected for the excitation cross sections of the beam contaminants. CLX calculations yielded an effective fraction of 50.8(30)% for target excitation caused by ^{30}Na . The fit of the experimental data was performed using the coupled-channels Coulomb-excitation code GOSIA, integrating over the energy loss of the projectiles in the target material and integrating over the scattering angle range of $\Theta_{\text{CM}} = 20.5\text{--}64.8^\circ$, which was covered by the DSSSD. Position and efficiency of the MINIBALL detectors were taken into account as well as calculated internal conversion coefficients [140] and corrections for angular distribution effects.

To get the correct Coulomb-excitation cross section of the 2_1^+ state of ^{120}Sn all excited states up to the 3^- state at 2400 keV were included into the calculation, together with the data of all known transitions and transition probabilities [139]. Finally, a value of $\sigma_{\text{CE},2_1^+} = 49.5$ mb was determined for Coulomb exciting the 2_1^+ state at 1171 keV.

The spin and parity of the 424 keV state in ^{30}Na are not fixed experimentally, but recent shell-model calculations favor a deformed 3^+ state at this energy [54]. The quadrupole moment of the 2^+ ground state was predicted to be $Q_0 = 58 \text{ efm}^2$ [54]. Thus, within a rotational model applied to the $K = 2$ yrast band, a value of $|\langle 2^+ || E2 || 2^+ \rangle| = 0.219 \text{ eb}$ was assumed for the diagonal matrix element of the ground state. The MCSM calculations predicted a rather large $M1$ contribution for the $2^+ \rightarrow 3^+$ transition with a transition strength of $B(M1) \uparrow = 0.268 \mu_N^2$ [45], which was included in the present calculations. All information on low-lying levels up to 1 MeV, e.g. energy, spin, parity, branching ratio, etc., which were determined by β -decay studies [83], was taken into account carefully. Finally, the GOSIA calculation yielded a reduced transition probability of

$B(E2, 2^+ \rightarrow 3^+) = 320(100) \text{ e}^2\text{fm}^4$ for the excitation of the 424 keV state in ^{30}Na . The quoted error is dominated by the statistical errors of 28% and 9.6% for the measured de-excitation yields of target and projectile, respectively. Systematic errors arising from uncertainties of the deduced beam composition and of the calculated target excitation cross section, were taken into account with 7% and 2%, respectively.

The transition probability deduced in the present experiment, exceeded the published value of $B(E2, 2^+ \rightarrow 3^+) = 147(21) \text{ e}^2\text{fm}^4$, which was obtained by intermediate-energy Coulomb excitation of ^{30}Na [45] by more than a factor of 2. Thus, it was necessary, to perform another independent and precise Coulomb-excitation measurement on ^{30}Na .

5.3.2 Measurement at 2.85 MeV/u on a 4.1 mg/cm² thick ^{104}Pd target

In order to solve the puzzling discrepancy in the previously measured $B(E2)$ values and to further investigate higher-lying excited states a second Coulomb-excitation experiment on ^{30}Na was performed with MINIBALL at REX-ISOLDE. Therefore the $A = 30$ beam was accelerated up to 2.85 MeV/u and shot at a ^{104}Pd target with a total thickness of 4.1 mg/cm². The amount of sodium in the beam was 48.2(12)% for the analyzed data. The absolute sodium beam intensity was 550(60) ions/s on average, which

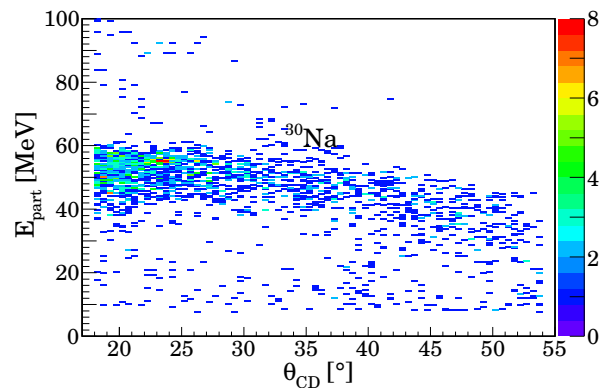


Figure 5.20: Particle energy versus scattering angle, measured in the CD detector for the $A=30$ beam, incident on the 4.1 mg/cm² thick ^{104}Pd target at a beam energy of 2.85 MeV/u. Only those events are plotted, which coincide with at least one prompt γ -ray event detected at MINIBALL.

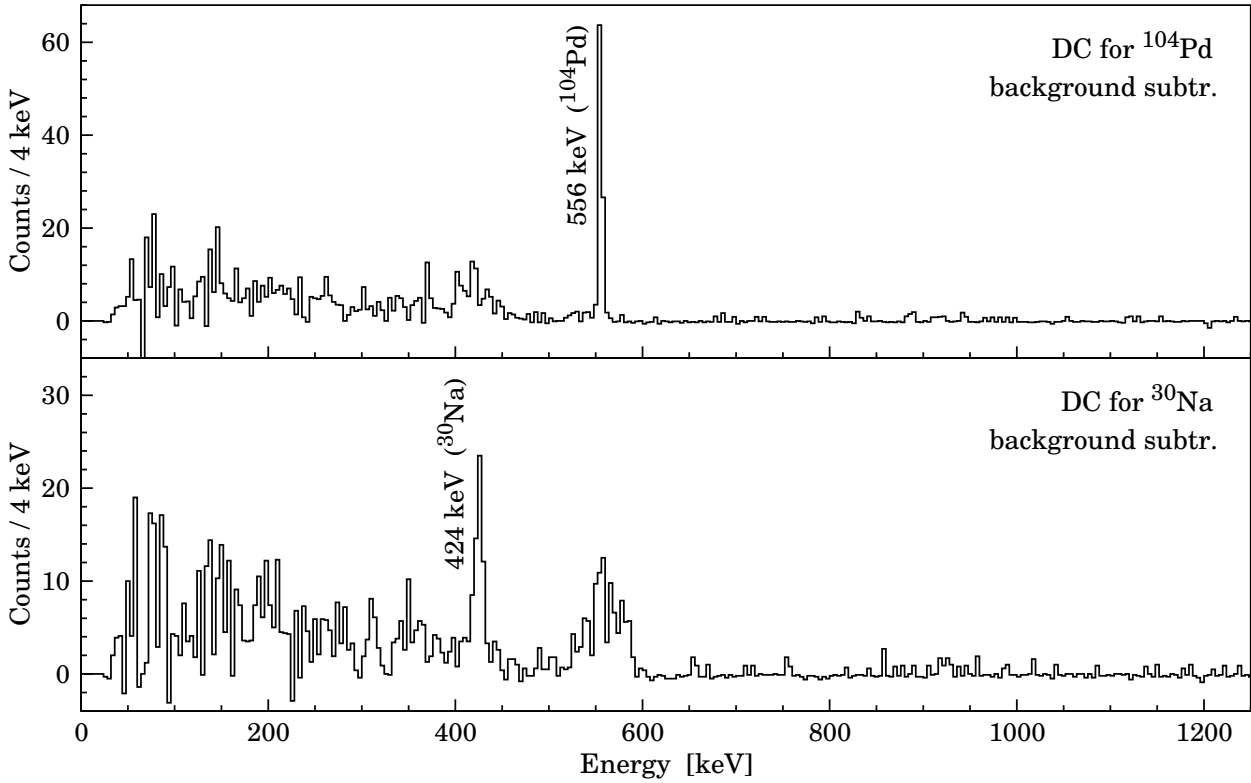


Figure 5.21: Doppler-corrected (DC) and background-subtracted γ -ray spectra in coincidence with scattered beam particles. Prompt γ -ray transitions from the Coulomb excitation of both projectile (^{30}Na) and target (^{104}Pd) nuclei were detected. Events with 511 keV coming from background radiation were suppressed in the spectra. Further information is given in the text.

was more than five times less than originally expected. More information on the experimental details and the beam composition is given in Chapter 4.5.

Scattered ^{30}Na ions were identified and selected by means of the measured correlation between scattering angle θ_{CD} and particle energy in the CD detector, as shown in Figure 5.20. Using the position information of the scattered particle and the coincident γ ray, which were provided by the segmentation of the DSSSD and the MINIBALL detectors, respectively, a proper Doppler correction of the emitted γ rays was performed. For the projectile Doppler correction is essential due to the relatively high recoil velocities $\beta > 5\%$, whereas the scattered target nuclei can be assumed to be almost at rest due to the low momentum transfer and high stopping power. According to section 4.6 a time gate was applied on prompt particle- γ coincidences, to suppress random background events effectively. The resulting Doppler-corrected and background-subtracted γ -ray spectra for both

kinematics of projectile and target nuclei are shown in Figure 5.21.

Analysis of the γ -ray spectra

Performing the Doppler correction according to the kinematics of scattered target nuclei, the prominent transition in the resulting γ -ray spectrum at 555.8 keV is the well-known $2^+ \rightarrow 0^+$ transition in ^{104}Pd [138]. Doppler correction for beam-like nuclei gives rise to a strong transition at 424 keV, which was already observed in previous Coulomb-excitation experiments of ^{30}Na [45]. This transition was assigned to the de-excitation of an excited (3^+) state in ^{30}Na to the 2^+ ground-state. De-exciting transitions of low-lying excited 1^+ states, known from a β -decay experiment of ^{30}Ne [83], were not observed. Nevertheless, an accumulation of γ -ray events at around 924 keV was found, which could be a possible candidate for the de-excitation of a proposed (4^+) state in ^{30}Na . All these findings are in agreement with the results

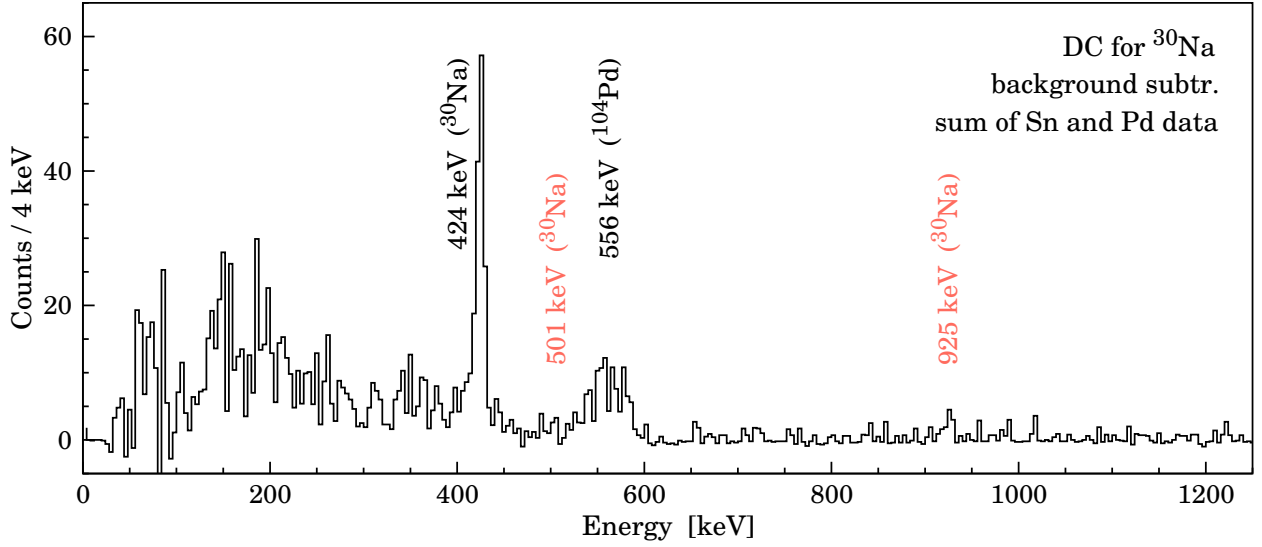


Figure 5.22: Sum spectrum of the Coulomb-excitation experiments on ^{30}Na , using the data sets taken with the ^{120}Sn target and the ^{104}Pd target, background subtracted and Doppler corrected for ^{30}Na . In addition to the known 424 keV transition there is evidence for two weak transitions at 501 keV and 925 keV, depopulating an excited state at 925 keV. These findings were confirmed by coincidence relations (see below). Events with 511 keV coming from background radiation were suppressed.

from the Coulomb-excitation experiment on a ^{120}Sn target, which was already presented in the previous section of this work.

In order to facilitate observation and identification of weak γ -ray transitions in ^{30}Na , data sets taken with both targets, i.e. ^{120}Sn and ^{104}Pd , were summed. The resulting γ -ray spectrum is shown in Figure 5.22. It revealed a new γ -ray transition at 925 keV, which could be assigned to a proposed 4^+ state in ^{30}Na , as well as a possible branching to the (3^+) state with a transition energy of 501 keV. To identify these transitions unambiguously and to allocate them in the level scheme of ^{30}Na , experimental data were sorted into a prompt particle- $\gamma\gamma$ coincidence matrix. This technique was already established successfully in the analysis of the ^{31}Mg Coulomb-excitation experiment (cf. Sec. 5.1.1). A coincidence gate was set on the $(3^+) \rightarrow 2^+$ transition at 424 keV to investigate γ -ray transitions feeding the (3^+) state. MCSM calculations predicted a strong $4^+ \rightarrow 3^+$ transition with $B(M1, 4^+ \rightarrow 3^+) = 0.43 \mu_N^2$ [45]. With the high γ -ray efficiency of the MINIBALL array a verification of this prediction should be feasible by the measured coincidence relations. The cut spectrum on the 424 keV transition showed γ -ray events at 501(5) keV, which were coincident

with the $(3^+) \rightarrow 2^+$ transition in ^{30}Na , as shown in Figure 5.23. This would be perfectly in line with the results deduced from the γ -ray singles spectra in Figure 5.22, which favored an excited state at 925 keV with about 67% γ -ray decay branching to the 2^+ ground state and about 33% branching to the (3^+) state at 424 keV. This

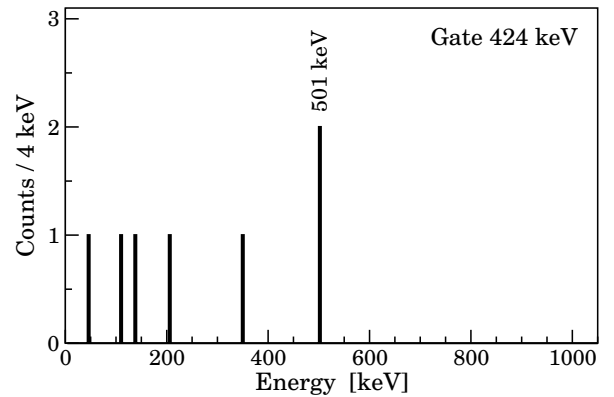


Figure 5.23: Prompt particle- $\gamma\gamma$ coincidence spectrum of the Coulomb excitation of ^{30}Na , gated on the 424 keV transition. Coincident γ -ray transitions were observed at 501(5) keV, feeding the 424 keV state. Doppler correction was performed for the detected ^{30}Na nucleus. γ rays with a detected energy between 508 keV and 514 keV were excluded from the analysis, to eliminate possible random coincidences with 511 keV γ rays.

state at 925 keV is a possible candidate for the proposed 4^+ state in ^{30}Na [54]. Moreover it is thought to form a doublet with an 1_2^+ state at 924(2) keV, which was observed by β -decay studies [83]. The known decay branches of the 1_2^+ state were not observed in this experiment.

Reduced transition probabilities

The measured intensities of the γ -ray transitions depopulating Coulomb-excited states in the ^{104}Pd target and ^{30}Na projectile nuclei, were used to determine the dedicated Coulomb-excitation cross sections. The Coulomb-excitation cross sections depend on the unknown reduced transition probabilities, which are of further interest. Therefore, the deduced cross sections of excited state in ^{30}Na are normalized to the well-known cross section for exciting the 2^+ state in ^{104}Pd , as shown in Section 3.6.3 and all the experiments previously discussed. The de-excitation yield of the 555.8 keV transition was corrected for the effective beam composition (cf. Sect. 4.5.6), yielding a fraction of 52.6(14)% on average for ^{30}Na exciting the 2^+ state in ^{104}Pd . The fit of the experimental data was performed using the coupled-channels Coulomb-excitation code GOSIA [122,123]. The calculation took into account position and efficiency of each individual MINIBALL detector, angular distribution effects of the emitted γ ray as well as internal conversion coefficients. Integration limits of the calculation were given by the scattering angle range of $\Theta_{\text{CM}} = 20.5\text{--}66.4^\circ$, which was covered by the DSSSD, and the energy loss of the projectile in the target.

For the calculation of the Coulomb-excitation cross section of the 2_1^+ state of ^{104}Pd all excited states up to the 4_2^+ state at 2082 keV were included into the calculation, together with the data of all known transitions and transition probabilities [138]. To complete the data sets for the Coulomb-excitation calculations of ^{30}Na , all information available on experimentally known low-lying excited states and electromagnetic transitions as well as on predicted quadrupole moments, transition probabilities and spin assignments, was taken into account. The spin and parity of the 424 keV state were assumed to be 3^+ [45, 54]. Furthermore, shell-

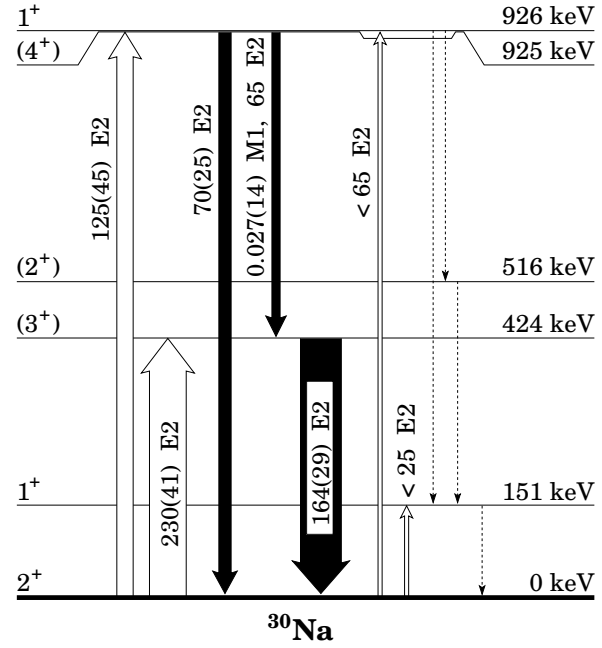


Figure 5.24: Measured reduced transition probabilities for ^{30}Na . $B(E2)$ values are given in e^2fm^4 and $B(M1)$ in μ_N^2 . The dotted transitions de-exciting the 1^+ states had not been observed in the present experiment and were taken from [83]. Thus, for those states only an upper limit of the excitation strength could be given. For detailed information see text.

model calculations favored a deformed 4^+ state at around 800 keV [54], which could be assigned to the newly observed 925 keV state. For the diagonal matrix elements of the 2^+ ground state and the 4^+ state values of $|\langle 2^+ || E2 || 2^+ \rangle| = 0.219$ eb and $|\langle 4^+ || E2 || 4^+ \rangle| = 0.112$ eb, respectively, were assumed within a rotational model applied to the $K = 2$ yrast band [54]. According to MCSM calculations de-excitation of the 3^+ is expected to proceed via a strong M1 contribution with $B(M1) \downarrow = 0.191 \mu_N^2$ [45], which was included in the present calculations. Additional information on low-lying 1^+ and (2^+) levels up to 1 MeV, e.g. level energies, transition energies, branching ratios, etc., which were determined by β -decay studies [83], was taken into account carefully. The unknown electromagnetic transition matrix elements were fitted by the GOSIA calculation using a least squares fit.

For the excitation of the 424 keV state in ^{30}Na the GOSIA calculation yielded an excitation strength of $B(E2, 2^+ \rightarrow (3^+)) = 230(41) \text{ e}^2\text{fm}^4$. The possible (4^+) state at 925 keV was populated by the Coulomb excitation with a value

of $B(E2, 2^+ \rightarrow (4^+)) = 125(45) \text{ e}^2\text{fm}^4$. De-excitation had to proceed via an $E2$ transition to the ground state, competing with a mixed $E2+M1$ transition to the (3^+) state. To reproduce the measured branching ratios the $M1$ component of the $(4^+) \rightarrow (3^+)$ transition had to be much smaller than the value of $0.43 \mu_N^2$, deduced from MCSM calculations [45]. Assuming a moderate $E2$ strength of $B(E2) = 80 \text{ e}^2\text{fm}^4$ for the 501 keV transition, the GOSIA calculation yielded an $M1$ strength of $B(M1, (4^+) \rightarrow (3^+)) = 0.027(14) \mu_N^2$. All quoted errors are mainly dominated by the statistical errors of the measured de-excitation yields of the relevant projectile and target excitations, respectively. Systematic errors arising from uncertainties of the deduced beam composition and of the calculated target excitation cross section, were minor and were taken into account with 3% and 2%, respectively.

In β -decay experiments low-lying 1^+ states were observed at 151 keV and 924(2) keV [83]. De-excitation γ rays of these 1^+ states were not observed in the present Coulomb-excitation experiment. Thus, only an upper limit of the reduced transition probabilities could be deduced. The GOSIA calculations yielded $B(E2) \uparrow < 25 \text{ e}^2\text{fm}^4$ and $B(E2) \uparrow < 70 \text{ e}^2\text{fm}^4$ for exciting the 1_1^+ and 1_2^+ state, respectively.

All reduced transition probabilities, measured in this experiment are presented in Figure 5.24. For the first time a possible 4^+ state was observed at 925 keV.

The analysis of the previous experiment using the ^{120}Sn target yielded comparable results. In that experiment the (4^+) state was excited with $B(E2) = 96(50) \text{ e}^2\text{fm}^4$. A discrepancy between the $B(E2)$ values of the 424 keV transition obtained in “safe” Coulomb-excitation experiments and those, obtained in intermediate-energy Coulomb-excitation experiments [45, 49], is observed.

5.3.3 Measurement at 2.83 MeV/u on a 3.6 mg/cm² thick ^{104}Pd target

In 2010 and 2011 further Coulomb-excitation experiments with ^{30}Na were scheduled at REX-ISOLDE, to confirm the results achieved in the previous experiments. A new 3.60(25) mg/cm²

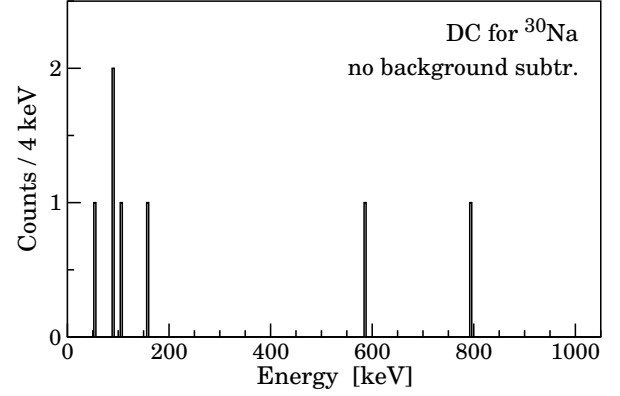


Figure 5.25: Prompt Coulomb-excitation spectrum of ^{30}Na , taken during the run in 2010. Doppler correction was performed for scattered ^{30}Na ions. No γ ray depopulating the 424 keV state was observed during 3 hours of beam time.

thick ^{104}Pd target was produced to replace the stack of the two medium-sized ^{104}Pd targets previously used, and thus to reduce uncertainties on the composition and thickness of the target. Unfortunately the experiments in 2010 and 2011 suffered from very low ^{30}Na beam intensities of less than 140 ions/s and about 60 ions/s at the MINIBALL setup, respectively. Thus, both experiments were stopped after some hours of measurement. Figure 5.25 shows the final Coulomb-excitation spectrum of the experiment scheduled in 2010.

Chapter 6

Discussion and Summary

6.1 Discussion

^{31}Mg

The measured level scheme and reduced transition probabilities of ^{31}Mg are compared to results from recently published shell-model calculations [48] and AMD+GCM calculations [76]. Both publications predicted a $5/2^+$ state at 988 keV [48] and 0.89 MeV [76], respectively, which is in very good agreement with the present results for the 945 keV state in this work, as shown in Fig. 6.1. Additionally, the 673 keV state is confirmed as $3/2_2^+$ state and the head of the $K^\pi = 3/2^+$ band with a dominant spherical $0p1h$ configuration [76,78]. A reduced coupling to the deformed $2p3h$ ground-state configuration is in very good agreement with a less collective transition with $B(E2, 1/2^+ \rightarrow 3/2_2^+) = 21(8) \text{ e}^2\text{fm}^4$ observed in this experiment.

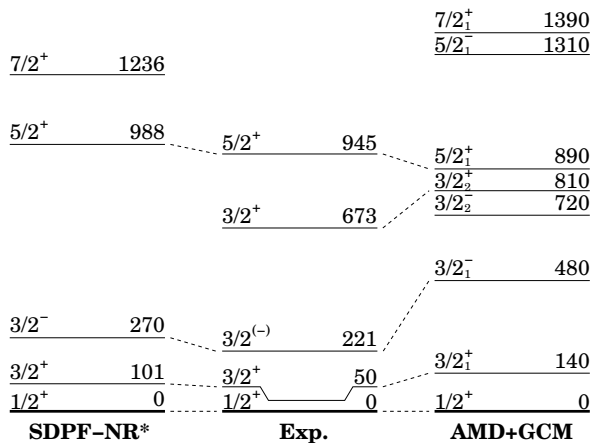


Figure 6.1: Level scheme of ^{31}Mg , as it was extracted from the Coulomb-excitation data (middle), compared to recently published shell-model calculations [48] (left) and AMD+GCM calculations [76] (right). Excitation energies are given in keV.

The measured properties of the 945 keV state agree well with the predicted $5/2^+$ state of the positive-parity yrast band in ^{31}Mg . The $5/2^+$ state has a strong coupling to the deformed ground state with $B(E2, 1/2^+ \rightarrow 5/2^+) = 182(20) \text{ e}^2\text{fm}^4$ due to its predicted dominant $2p3h$ intruder configuration. Combined with the $1/2^+$ ground state and the first excited $3/2^+$ state at 50 keV these states form a positive parity yrast band with $K = 1/2$. Moreover, intra-band decay proceeds by almost pure M1 transitions. Measured transition strengths of $B(M1, 5/2^+ \rightarrow 3/2^+) = 0.18(5) \mu_N^2$, deduced in the present work, and $B(M1, 3/2^+ \rightarrow 1/2^+) = 0.019(4) \mu_N^2$ [72] agree well with shell-model calculations done by Maréchal [48], that yield $B(M1, 5/2^+ \rightarrow 3/2^+) = 0.38 \mu_N^2$ and $B(M1, 3/2^+ \rightarrow 1/2^+) = 0.06 \mu_N^2$, respectively (see Table 6.1). For E2 transitions the shell-model calculations do not reproduce the measured values. With $B(E2, 5/2^+ \rightarrow 1/2^+) = 127 \text{ e}^2\text{fm}^4$ [48] it is in fact a factor of 2 bigger than the result of the present measurement, that gives $B(E2) = 61(7) \text{ e}^2\text{fm}^4$.

The rigid rotor approximation allows another comparison with theory [76]. This is done by assuming a purely rotational $K = 1/2$ band in ^{31}Mg , given by the sequence $1/2^+ - 3/2^+ - 5/2^+$. For transitions within such a rotational band the reduced transition probability is linked to the intrinsic quadrupole moment Q_0 by [24]

$$B(E2, I_i \rightarrow I_f)_{\text{rot}} = \frac{5}{16\pi} e^2 Q_0^2 \left| \langle I_i 2K0 | I_f K \rangle \right|^2.$$

For the $5/2^+ \rightarrow 1/2^+$ transition we get $B(E2)_{\text{rot}} = 69 \text{ e}^2\text{fm}^4$ and $B(E2)_{\text{rot}} = 114 \text{ e}^2\text{fm}^4$, calculated with predicted quadrupole moments from shell-model and rigid-rotor approximation

$I_i \rightarrow I_f$	$B(E2)_{\text{exp}}$	$B(E2)_{\text{SM}}$	$B(E2)_{\text{rot}}$	$B(M1)_{\text{exp}}$	$B(M1)_{\text{SM}}$
$5/2^+ \rightarrow 1/2^+$	61(7)	127 ^a	69 ^a / 114 ^b	—	—
$5/2^+ \rightarrow 3/2^+$			20 ^a / 32 ^b	0.18(5)	0.38 ^a
$3/2^+ \rightarrow 1/2^+$		106 ^a	140 ^a / 145 ^b	0.019(4) ^c	0.06 ^a

Table 6.1: Reduced transition probabilities of the positive-parity $K=1/2$ yrast band in ^{31}Mg , compared to recent theoretical predictions. $B(E2)$ values are given in e^2fm^4 , $B(M1)$ in μ_N^2 . For more details see text. ^a from Ref. [48]. ^b from Ref. [76]. ^c from Ref. [72].

calculations, respectively [48, 76]. The result from shell-model calculations is in reasonable agreement with the experimental result (see Table 6.1), whereas the rigid rotor approximation yields a transition strength that is too high by a factor of more than 1.8.

The deduced excitation probability $B(E2, 1/2^+ \rightarrow 5/2^+) = 182(20) \text{ e}^2\text{fm}^4$ of ^{31}Mg can be compared to the $0^+ \rightarrow 2^+$ $E2$ strengths in the neighboring even-even magnesium isotopes $^{30,32}\text{Mg}$. To avoid the effect of the different spin values for the initial (ground) states, the reduced transition matrix elements $\mathfrak{M}(E2)$ will be compared instead. For ^{32}Mg the experimental results, i.e. $B(E2)$ values, were discussed by [51], including possible feeding contributions. An $E2$ matrix element of $\mathfrak{M}(E2, 0^+ \rightarrow 2^+) = 0.210(13) \text{ eb}$ is reported without a correction for feeding, and $\mathfrak{M}(E2) = 0.182(13) \text{ eb}$ includes a correction for feeding from a higher-lying state [51], which is consistent with [66]. The new $\mathfrak{M}(E2, 1/2^+ \rightarrow 5/2^+) = 0.191(11) \text{ eb}$ value of ^{31}Mg compares well with the feeding corrected $\mathfrak{M}(E2, 0^+ \rightarrow 2^+) = 0.182(13) \text{ eb}$ of ^{32}Mg [51], and exceeds the measured $\mathfrak{M}(E2, 0^+ \rightarrow 2^+) = 0.155(10) \text{ eb}$ of ^{30}Mg [59]. This result establishes that deformed pf intruder configurations exist for the ground and low-lying states of magnesium isotopes already at $N = 19$, including a sequence of collective rotational states.

²⁹Na

The measured reduced transition probabilities of the $N = 18$ nucleus ^{29}Na are compared to very recently published experimental values [58] and MCSM predictions [54]. The transition strength of the $5/2_1^+ \rightarrow 3/2^+$ transition at 72 keV deduced in this work yielded

$B(E2, 3/2^+ \rightarrow 5/2_1^+) = 150(20) \text{ e}^2\text{fm}^4$. This value is in good agreement with the value of $B(E2) \uparrow = 140(25) \text{ e}^2\text{fm}^4$ published by Hurst and collaborators [58] a few months after the proposal for the present experiment was accepted. Recent shell-model calculations using the USD interaction and the SDPF-M interaction predict an excitation strength of $111 \text{ e}^2\text{fm}^4$ and $135 \text{ e}^2\text{fm}^4$, respectively, for the $5/2_1^+$ state [54]. Thus, the experimental results are consistent with the predictions by the MCSM calculations using the SDPF-M interaction, which yielded a mixing of intruder configurations by 42% and 32% for the wave function of the $3/2^+$ ground state and the first excited $5/2_1^+$ state, respectively [54, 83], confirming the onset of large intruder admixtures in the ground-state wave function already for the $N = 18$ isotope ^{29}Na .

Moreover, the present measurement indicates that the $3/2^+$ ground state and the $5/2_1^+$ state at 72 keV are connected by a dominant $M1$ transition with $B(M1, 5/2_1^+ \rightarrow 3/2^+) > 0.06 \mu_N^2$, i.e. multipole mixing ratio $|\delta| < 0.025$. Within a simple rotational model the measured transition strengths yielded $Q_0 = 0.542(36) \text{ eb}$ for the intrinsic electric quadrupole moment of ^{29}Na , assuming a prolate deformation. The quadrupole deformation parameter is given to first order by [24]

$$\beta_2 = \frac{\sqrt{5\pi}}{3} \frac{1}{ZR_0^2} Q_0,$$

yielding $\beta_2 = 0.48(3)$. However, this simple model overestimates the quadrupole deformation of ^{29}Na due to the different static and dynamic nuclear properties, arising from differences in the underlying single-particle configurations of the ground and first excited states. An earlier, precise β -NMR measurement pointed to slightly less deformation: $Q_0 = 0.430(15) \text{ eb}$ and $\beta_2 = 0.38(2)$ [80].

To further investigate the mechanism of intrusion in the neutron-rich sodium isotopes, the experiment searched for collective properties of possible higher-lying $3/2_2^+$, $5/2_2^+$, and $7/2_1^+$ states dominated by intruder configuration, which were predicted by MCSM calculations [54]. A possible candidate for a weak transition was observed in the present experiment at 1518(4) keV, de-exciting a known level at 1588 keV, which was assigned as $(5/2_2^+)$ state by new β -decay studies [83]. A reduced transition probability was deduced, yielding $B(E2, 3/2^+ \rightarrow (5/2_2^+)) = 70(40) \text{ e}^2\text{fm}^4$. This value is consistent with the moderately large $B(E2) \uparrow$ values predicted by theory for the intruder dominated states around 1.5-2 MeV [54]. Additionally, the measured $B(E2)$ value implies a large $2p2h$ admixture in the wave function of the 1588 keV state and a significant coupling to the ground state due to the large intruder mixing. Indeed MCSM calculations predict 77% intruder admixture for the $5/2_2^+$ state [83]. Other transitions of intruder-dominated higher-lying states predicted by theory were not observed. However, conclusive results of transition probabilities of higher-lying deformed states were not possible due to the experimental limitation and low count rates.

^{30}Na

The measured level scheme and reduced transition probabilities of ^{30}Na are compared to results from recently published experimental studies [45, 83, 141] and different shell-model predictions [54]. The excited state at 424 keV was already established in previous Coulomb-excitation experiments [45, 56] and proton inelastic scattering studies of ^{30}Na [141] to be the $J = 3$ member of the $K = 2$ rotational band built upon the 2^+ ground state. This result fits perfectly with MCSM calculations using the SDPF-M interaction, which predicted the $J = 3$ state at 430 keV excitation energy [54]. Moreover theory predicted the $J = 4$ member of the $K = 2$ rotational band at an excitation energy of around 860 keV. The newly observed γ -ray transitions at 501 keV and 924 keV were assigned as de-exciting transitions of a level at 925 keV by coincidence relations. Coulomb-excitation rela-

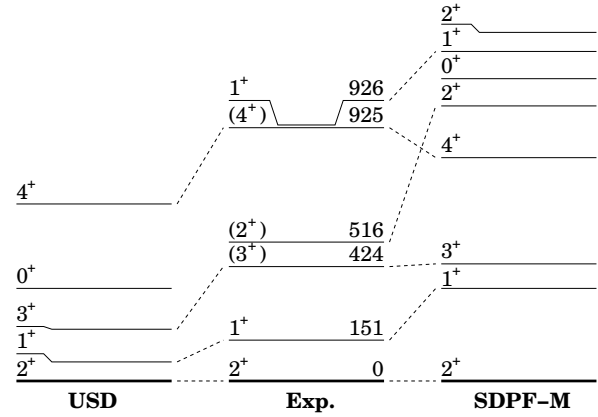


Figure 6.2: Level scheme of ^{30}Na , as it was extracted from the present Coulomb-excitation and previous β -decay data [83] (middle), compared to recently published MCSM calculations [54] using the SDPF-M interaction (right) and the USD interaction (left). Excitation energies are given in keV.

tions prefer $J^\pi = (4^+)$ for this state in agreement with the MCSM predictions (see Fig. 6.2). However, this state and its γ -ray decay were not observed in the previous Coulomb-excitation experiments [45, 56]. γ -ray events de-exciting the $K = 1$ band head at 151 keV, known as strongest γ -ray transition in β -decay studies of ^{30}Na [83], were not observed. Thus, only an upper limit for the excitation of the first 1^+ state with $B(E2) \uparrow < 25 \text{ e}^2\text{fm}^4$ could be deduced, indicating a reduced coupling of the $K = 1$ band to the $K = 2$ ground-state band. This would support the results of a proton inelastic scattering experiment on $^{30,31}\text{Na}$, assuming different proton configurations of the $K = 1$ and $K = 2$ band members [141].

The observed collective properties of excited states in ^{30}Na are in agreement with intruder-dominated configurations, predicted by recent theoretical approaches [54] (see Table 6.2). The transition strength of the $(3^+) \rightarrow 2^+$ transition was measured to be $B(E2) \uparrow = 230(41) \text{ e}^2\text{fm}^4$ in the present experiment. This value exceeds both, the previously measured $B(E2) \uparrow = 150(21) \text{ e}^2\text{fm}^4$ value published by Ettenauer *et al.* [45] and the MCSM predictions, which yield $168 \text{ e}^2\text{fm}^4$ [54]. The possible (4^+) state at 925 keV has a strong coupling to the deformed ground state with $B(E2, 2^+ \rightarrow (4^+)) = 125(45) \text{ e}^2\text{fm}^4$, in agreement with MCSM calculations, which yielded

$I_i \rightarrow I_f$	$B(E2)_{\text{exp}}$ (Pd target)	$B(E2)_{\text{exp}}$ (Sn target)	$B(E2)_{\text{SM}}$ (previous exp.)	$B(E2)_{\text{SM}}$	$B(M1)_{\text{exp}}$ (Pd target)	$B(M1)_{\text{SM}}$
$3^+ \rightarrow 2^+$	164(29)	230(70)	105(15) ^a	120 ^b	—	0.191 ^a
$4^+ \rightarrow 2^+$	70(25)	53(28)	< 20 ^a	50 ^b	—	—
$4^+ \rightarrow 3^+$					0.027(14)	0.43 ^a

Table 6.2: Experimentally deduced reduced transition probabilities of the positive-parity $K=2$ ground-state band in ^{30}Na , compared to recent theoretical predictions by MCSM calculations. The first two columns represent the results of the presented experiments using the two different scattering targets (^{104}Pd and ^{120}Sn). $B(E2)$ values are given in e^2fm^4 , $B(M1)$ in μ_N^2 . For more details see text. ^a from Ref. [45]. ^b from Ref. [54].

$B(E2) \uparrow = 90 \text{ e}^2\text{fm}^4$. Compared to the rotational band structure of the $N = 19$ isotone ^{31}Mg , presented in previous sections, the $K = 2$ band of ^{30}Na is less connected by $M1$ transitions. The $B(M1, (4^+) \rightarrow (3^+))$ value yielded $0.027(14) \mu_N^2$ and $0.43 \mu_N^2$ for the present experiment and MCSM calculations [54], respectively. Despite these differences in the observed level scheme and transition probabilities, the results of the new Coulomb-excitation experiment confirm the large quadrupole collectivity and thus, the intruder dominated $2p2h$ configuration of the ground state, for the $N = 19$ sodium isotope.

6.2 Summary

To summarize, we have investigated the Coulomb excitation of the unstable, neutron-rich nuclei ^{31}Mg and $^{29,30}\text{Na}$. The properties of a positive-parity yrast band with $K = 1/2$, built on the $1/2^+$ ground state of ^{31}Mg are in good agreement with a $5/2^+$ state at 945 keV. The determined $B(E2)$ and $B(M1)$ values support this assumption. The increased collectivity is well described by the deformed Nilsson model for excited states in ^{31}Mg [142]. Finally, the quadrupole moment supports the idea that for the $N = 19$ magnesium isotope not only the ground state but also excited states are no longer dominated by a spherical configuration. The $E2$ strength of the $5/2^+ \rightarrow 1/2^+$ transition in ^{31}Mg is quite comparable to the corresponding $2^+ \rightarrow 0^+$ transition in ^{32}Mg , which is known to have an intruder dominated $2p2h$ configuration in the ground state and a large prolate deformation with $\beta_2 = 0.52(4)$ [50].

For exotic $^{29,30}\text{Na}$ nuclei the results of previous experiments could be largely confirmed and

extended. Deduced collective properties of the first excited states are well described by MCSM calculations using the SDPF-M interaction. The measured $B(E2)$ values support the idea that in the sodium isotopic chain the ground-state wave function contains a significant intruder admixture already at $N = 18$, with $N = 19$ having an almost pure $2p2h$ deformed ground-state configuration. However, higher-lying states dominated by intruder configurations, as predicted by theory, are hardly populated in the present Coulomb-excitation experiments. The ground-state transitions of the assigned $(3/2_2^+)$ state at 1588 keV in ^{29}Na is found to have a moderately large $B(E2)$ value. In ^{30}Na a candidate for the (4^+) state is identified at 925 keV by coincidence relations. Excitation strengths and energies are well described by the MCSM calculations. Deviations found for the branching ratios and $B(M1)$ values indicate the importance to investigate the properties of excited states of exotic nuclei in the vicinity of the island of inversion further and to improve the shell-model description of odd-odd nuclei.

Chapter 7

Outlook

7.1 The HIE-ISOLDE project

During the last decade the REX-ISOLDE facility made it possible to perform intensive studies on a wide range of exotic nuclei in low-energy nuclear physics experiments, using e.g. Coulomb excitation, inelastic scattering, transfer and fusion reactions. To expand the physics program to nuclei even further from the valley of stability, reaction cross sections and beam intensities need to be increased. Therefore the “High Intensity and Energy ISOLDE” (HIE-ISOLDE) project was launched [143]. It is a major upgrade of the existing ISOLDE facility.

In a first stage the normal-conducting REX-Linac will be complemented by several superconducting cavities to increase the energy of the re-accelerated radioactive ion beam up to 5.5 MeV/u (cf. Figure 7.1). A later stage will boost the available beam energy up to 10 MeV/u. Additional improvements in the preparation and quality of the beam are intended. Furthermore ISOLDE will benefit from the increased proton beam intensity of the CERN injector chain, i.e. the new LINAC4 and upgraded PS Booster, delivering up to 6 μA to the ISOLDE target stations [143]. Therefore high-power targets and adequate ionization sources have to be developed. The increase in proton current will result in about three times higher yields for the radioactive ion production. To cope with this increased ion beam intensity, further upgrades of the charge breeding system, i.e. REXTRAP and REXEBIS, are necessary on the low-energy side of REX-ISOLDE.

The first stage of the HIE-ISOLDE upgrade, i.e. the energy upgrade to 5.5 MeV/u, is planned to become operational in 2014/2015. The full energy of 10 MeV/u as well as the increased in-

tensity of the radioactive ISOLDE beams should be available as of 2016 and 2017, respectively [145, 146].

7.2 Coulomb excitation of exotic $^{32,33}\text{Mg}$ at 5.5 MeV/u with MINIBALL at HIE-ISOLDE

Despite extensive studies the nucleus ^{32}Mg and the island of inversion [33] remains at the center of numerous ongoing experimental and theoretical efforts focusing on the evolution of shell structure far from the valley of stability. In ^{32}Mg only for the 2_1^+ and 4_1^+ excited states are quantum numbers firmly established. Recently the first excited 0_2^+ state of ^{32}Mg was measured employing the $^{30}\text{Mg}(t,p)2n$ -transfer reaction in inverse kinematics at ISOLDE [70]. A second excited 2_2^+ state is predicted to exist on the second excited 0_2^+ state in ^{32}Mg . Employing the higher beam intensities and higher beam energies of HIE-ISOLDE will allow observation of these states, which are dominated by $0p0h$ configurations [147]. Moreover, future multiple Coulomb excitation can elucidate the collectivity of the 4_1^+ and the high beam energy will also allow detecting the 3_1^- state, giving access to the size of the $\nu d_{3/2}-\nu f_{7/2}$ shell gap, if the state is of single-particle character. However, a collective excitation built on the highly deformed ground state would be of even higher relevance.

An even more intriguing case is given at the moment for the neighboring ^{33}Mg isotope. New measurements of ground-state properties of ^{33}Mg at ISOLDE unambiguously determined the spin $I = 3/2$ and a negative g factor $g = -0.4971(1)$ [148]. The quest for the parity

HIE-ISOLDE

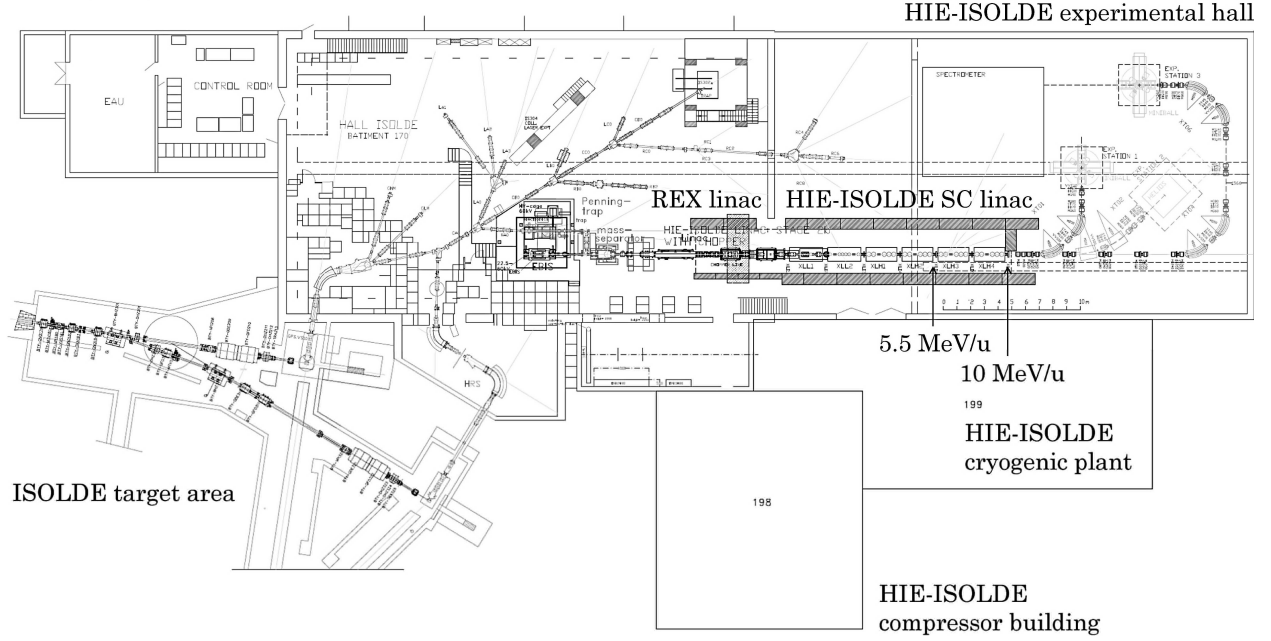


Figure 7.1: Planned layout of the new HIE-ISOLDE facility at CERN. The final stage of the superconducting accelerator has been plotted, providing post-accelerated RIBs with an energy of up to 10 MeV/u (adapted from [144]).

of the ground state and the underlying single-particle configuration is described in Ref. [149]. Excitation spectra and neutron single-particle configurations of ^{33}Mg were investigated by using antisymmetrized molecular dynamics combined with the generator coordinate method (AMD+GCM) [150]. The results show that ^{33}Mg has a strongly deformed $3/2^-$ ground state with a $3p2h$ configuration. The excitation spectra are qualitatively understood in terms of the Nilsson model and the calculation has shown the coexistence of different intruder configurations within small excitation energy. The normal $1p0h$ configuration is located at a higher excitation energy of 2.1 MeV. Due to the large

deformation the intra-band $E2$ transitions are large for the ground-state band. The calculated values are summarized in Table 7.1. The measurement of the $B(E2, 3/2_1^- \rightarrow 5/2_1^-)$ and $B(E2, 5/2_1^- \rightarrow 7/2_1^-)$ values should be feasible due to the high intrinsic quadrupole moment of the intruder state. Moreover, a multiple Coulomb-excitation experiment with a post-accelerated ^{33}Mg HIE-ISOLDE beam would preferentially populate the $5/2^-$ and $7/2^-$ levels from the $3/2^-$ ground state [149, 150]. Such an experiment would thus confirm the proposed spin and parity values for these levels.

Therefore, future Coulomb-excitation experiments of $^{32,33}\text{Mg}$ are proposed, using the HIE-ISOLDE facility coupled with the highly efficient MINIBALL array.

J_i	J_f	$B(E2, J_i \rightarrow J_f) [\text{e}^2\text{fm}^4]$
$3/2_1^-$	$5/2_1^-$	282
$3/2_1^-$	$7/2_1^-$	154
$5/2_1^-$	$7/2_1^-$	147
$5/2_1^-$	$9/2_1^-$	194
$7/2_1^-$	$9/2_1^-$	92

Table 7.1: Calculated $E2$ transition probabilities for the ground-state band in ^{33}Mg . Values are taken from Ref. [150].

Experimental setup and count rate estimate

The experimental instrument used with HIE-ISOLDE will be the MINIBALL array for in-beam γ -ray spectroscopy. In addition to the MINIBALL array the charged particle detectors of the T-REX configuration will be employed consisting of a CD-type double-sided silicon strip detector (DSSSD) and segmented Si barrel detec-

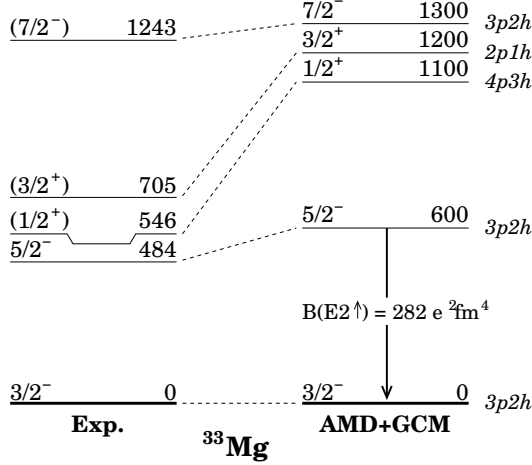


Figure 7.2: Experimentally deduced level scheme of ^{33}Mg (left) and results from an AMG+GCM calculation (right). The figure was adapted from [149, 150].

tors [151]. The detector thickness of 500 μm allows stopping completely the scattered ions. The high segmentation of the detectors allows for a kinematic reconstruction of the events and covers an angular range from 15° to 77° . A solid angle coverage of 30% is used for the count rate estimate [151].

The proposed MINIBALL experiments with unstable beams of $^{32,33}\text{Mg}$ isotopes at HIE-ISOLDE are from the ISOLDE point of view comparable with previous experiments employing $^{30,31,32}\text{Mg}$ beams. The ISOLDE yield values for Mg isotopes are 3×10^4 ions/ μC for ^{32}Mg and 3×10^3 ions/ μC for ^{33}Mg [98]. However, the yields available at HIE-ISOLDE should be slightly higher than the quoted value due to recent improvements in the RILIS laser technique.

The accelerator efficiency for the complete HIE-ISOLDE chain from REXTRAP to the MINIBALL target was estimated conservatively to be 5%. A beam intensity of ^{32}Mg and ^{33}Mg at the secondary target inside the MINIBALL of $I(^{32}\text{Mg}) = 2000$ ions/s and only $I(^{33}\text{Mg}) = 200$ ions/s can be expected with an average PSB proton beam current of 1.4 μA .

Coulomb excitation will be done at “safe” energies of 5.5 MeV/u below the Coulomb barrier of a ^{196}Pt target. A distance of closest approach of 52.0 fm is calculated for the incoming ^{33}Mg ions hitting the ^{196}Pt target nuclei with an energy of 5.5 MeV/u at an angle of 77° in the laboratory. According to the work of Cline [126] the “safe” Coulomb-excitation criterion requires distances of $d > R_p + R_t + 5 \text{ fm} = 16.2 \text{ fm}$. The target thickness can be chosen very thick with 7.5 mg/ cm^2 at this high beam energy. Nevertheless the energy differences between the kinetic energy of scattered beam and target nuclei allows for a clear separation between the scattering partners in the particle detectors. The most relevant improvements of the proposed measurements with respect to the previous result obtained for ^{33}Mg at MSU [49] are: (i) the high energy resolution of the MINIBALL HPGe detectors, (ii) the enlarged energy range for γ -ray detection, which goes down in a reliable and controlled way to a lower threshold of 50 keV and the (iii) good γ -ray efficiency of the eight triple cluster detectors of MINIBALL.

The cross sections for the excitation of the several states in $^{32,33}\text{Mg}$ were calculated with the Coulomb-excitation code CLX. A beam en-

Isotope	I_{ISOLDE} [ions/ μC]	I_{MB} [ions/s]	transition energy	$B(E2)\uparrow$ [e^2fm^4]	σ_{CE} [mb]	$I_{\gamma, \text{MB}}$ [cts/h]
^{32}Mg	3×10^4	2×10^3	$0_1^+ \rightarrow 2_1^+$, 885 keV	454	110	15
			$2_1^+ \rightarrow 4_1^+$, 1436 keV	288 ^a	50	0.5
			$0_1^+ \rightarrow 2_2^+$, 2550 keV	45 ^b	1	0.1
			$0_1^+ \rightarrow 3_1^-$, 2858 keV	2500 ^b	4	0.25 ^c
^{33}Mg	3×10^3	2×10^2	$5/2_1^- \rightarrow 3/2_1^-$, 485 keV	282 ^d	795	1.6
			$7/2_1^- \rightarrow 3/2_1^-$, 1243 keV	154 ^d	350	0.2
			$7/2_1^- \rightarrow 5/2_1^-$, 758 keV	147 ^d		0.25

Table 7.2: Rate estimates for the proposed Coulomb-excitation experiments on $^{32,33}\text{Mg}$ at HIE-ISOLDE. For more information see text. ^a Taken from Ref. [147]. ^b Estimated excitation strength. ^c Count rate of the de-exciting $3_1^- \rightarrow 2_1^+$ transition. ^d Taken from Ref. [150].

ergy value of 5.5 MeV/u was used. The cross section for projectile excitation was integrated for particle detection in the solid angle range in the CM-system of $\theta_{\text{CM}} = 25^\circ\text{-}115^\circ$. These angles are covered by the particle detectors in the laboratory frame by $\theta_{\text{lab}} = 15^\circ\text{-}77^\circ$. For γ -ray detection the measured energy dependent γ -ray efficiency was included. Effects of the γ -ray angular distribution were neglected in the estimate. As target material ^{196}Pt was used with a thickness of 7.5 mg/cm^2 .

For ^{32}Mg the $B(E2)$ value for the $0_1^+ \rightarrow 2_1^+$ transition was taken from experiment [72]. CHFB+LQRPA calculations give a value of $288 \text{ e}^2\text{fm}^4$ for the excitation strength of the next excitation step to the 4_1^+ state [147]. The excitation to a possible 3^- state at an energy of 2858 keV was assumed to occur with a strength of about 5 W.u.. Additional excitation to a distorted rotational band built on the excited 0_2^+ state in ^{32}Mg was taken into account with $B(E2, 0_1^+ \rightarrow 2_2^+) = 45 \text{ e}^2\text{fm}^4$, i.e. an order of magnitude less than the excitation of the deformed first 2_1^+ state. For the calculation of the Coulomb-excitation cross sections of ^{33}Mg the calculated excitation strengths given in Table 7.1 were used in combination with the experimentally deduced level scheme presented in Ref. [149]. Due to the deduced branching of the $7/2^-$ state, both decay transitions to the $3/2^-$ and $5/2^-$ state, respectively, need to be observed.

The estimated count rates for Coulomb-excitation experiments, employing radioactive $^{32,33}\text{Mg}$ beams at HIE-ISOLDE, are summarized in Table 7.2.

Part II

Investigating the subshell closure at $N = 32$

Lifetime measurements
in the neutron-rich isotope ^{56}Cr
with the Cologne plunger

Chapter 8

Motivation and physics case

8.1 Evolution of a neutron shell gap at $N = 32, 34$

A large number of recent experimental studies evinced changes in the shell structure for neutron-rich nuclei along the $N = 8, 20, 28$, and 40 isotonic sequences. These changes can be explained in terms of the monopole part of the nucleon-nucleon (NN) residual interaction. Schematically this is due to the $(\sigma\sigma)(\tau\tau)$ part of the NN interaction, which is strongest in the $S = 0$ (spin-flip), $\Delta L = 0$ (spin-orbit partners) and $T = 0$ (proton-neutron) channel of the two-body interaction (cf. Sec. 1.3). Monopole shifts of neutron single-particle orbits are caused by the missing $S = 0$ proton partners at large neutron excess, and new shell gaps are generated. For the sd shell this was first discussed by [5, 6] and for the pf shell by [6, 152, 153]. Moreover, for heavier nuclei and increasing spin-orbit splitting near stability the tensor part of the NN interaction creates likewise a strong monopole interaction between $S = 0$, $\Delta L = 1$ and $T = 0$ orbits of adjacent harmonic oscillator shells [34, 154, 155].

In the pf shell above the doubly magic ^{48}Ca evolution of shell-model characteristics is driven by the strong, attractive monopole part of the NN interaction between the proton $\pi 1f_{7/2}$ orbital and the neutron $\nu 1f_{5/2}$ orbital. For Ni isotopes the $\pi 1f_{7/2}$ is filled completely. Thus, the $\nu 1f_{5/2}$ orbital is lowered between the $\nu p_{3/2}$ and $\nu p_{1/2}$ orbits, opening the classical $N = 40$ shell gap between the $\nu 1p_{1/2}$ and $\nu 1g_{9/2}$ orbitals for Ni isotopes. Calculations show that when removing protons from the $\pi 1f_{7/2}$ orbital the residual interaction is weakened due to the missing $S = 0$ partner protons and the $\nu 1f_{5/2}$

orbital is rapidly shifted to higher energies, relative to the $\nu 1p_{1/2}$ and $\nu 1p_{3/2}$ single-particle states. In the Ca isotopes the proton $\pi f_{7/2}$ orbit is empty. Between the $N = 29$ isotones ^{49}Ca and ^{57}Ni this shift in energy amounts to almost 3 MeV [156]. Thus, the $N = 40$ shell gap closes and new sub-shell gaps are predicted at neutron numbers $N = 32, 34$ between the $\nu p_{3/2}$ and $\nu p_{1/2}$ and the $\nu p_{1/2}$ and $\nu f_{5/2}$ orbits [157] for the neutron-rich Ca, Ti and Cr isotopes, as illustrated in Figure 8.1. Moreover, the $N = 32$ shell gap results from the large spin-orbit splitting between the $\nu 1p_{1/2}$ and $\nu 1p_{3/2}$ orbitals [158].

Effective interactions such as KB3G [159] and GXPF1 [160] with empirically tuned monopoles mimic this NN interaction, which *a priori* is not well accounted for in G-matrix-based realistic two-body matrix elements. The full pf shell-model calculation using the effec-

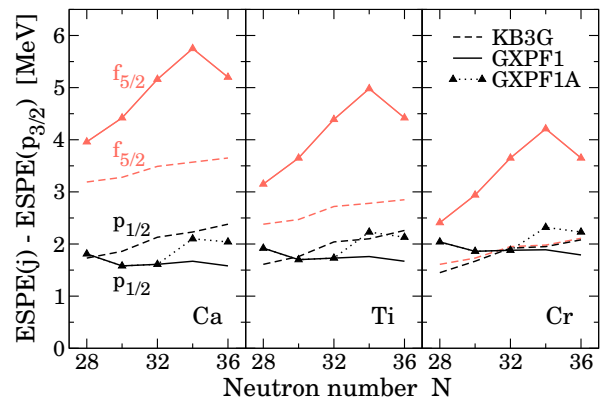


Figure 8.1: Effective single-particle energies (ESPE) of the neutron $p_{1/2}$ (black) and $f_{5/2}$ (gray) orbitals relative to the energy of the $p_{3/2}$ orbital as a function of N for even-even Ca, Ti, and Cr isotopes, calculated by the three effective interactions KB3G, GXPF1, and GXPF1A. See text for definition of the acronyms. The figure was adapted from Ref. [158].

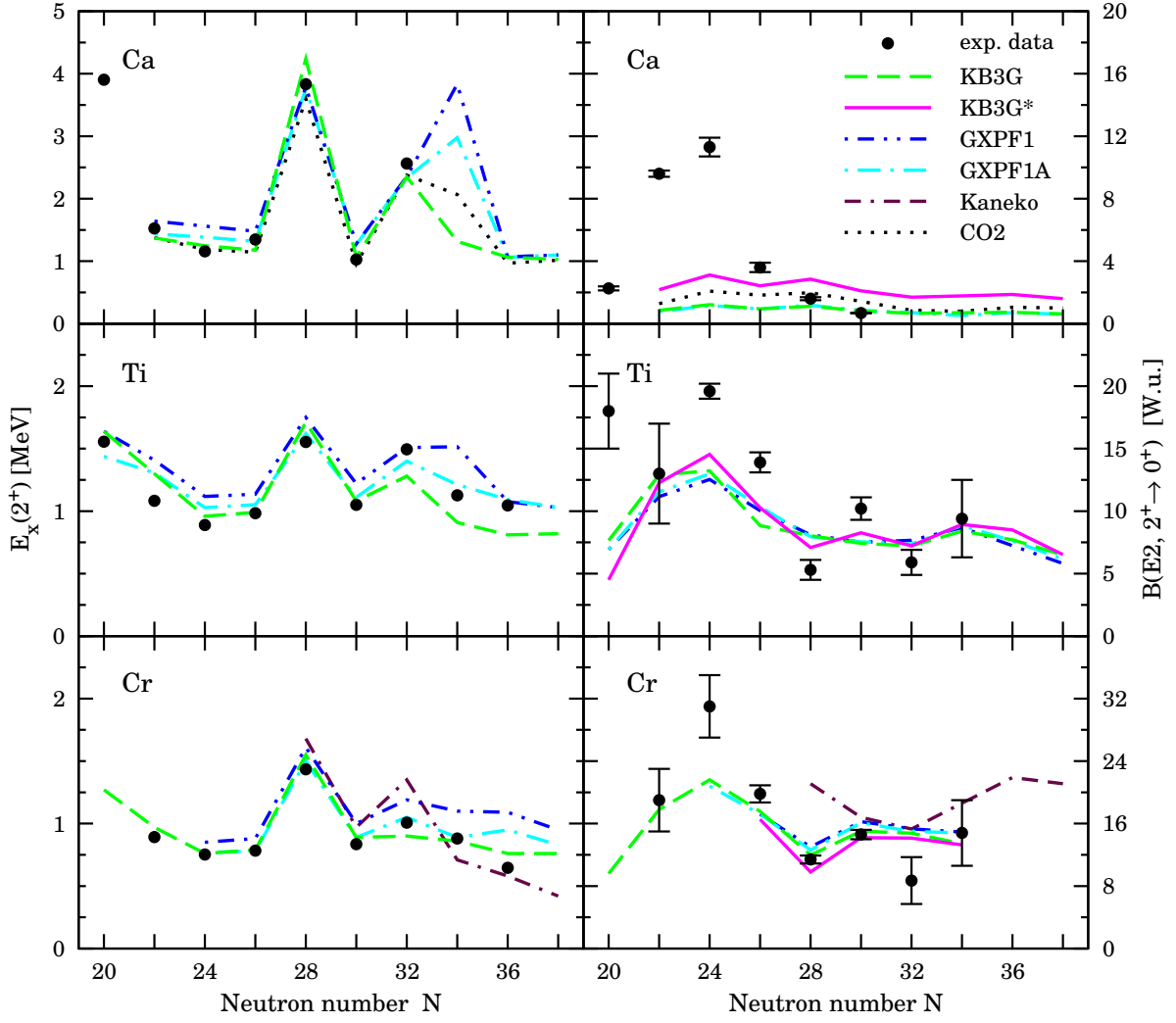


Figure 8.2: Comparison between recent shell-model calculations and experimental results in even-even Ca-, Ti- and Cr isotopes for $E_x(2^+)$ energies and $B(E2, 2^+ \rightarrow 0^+)$ values for neutron numbers between $N = 20$ and $N = 38$. See text for definition of the acronyms.

tive interaction GXPF1 shows a sub-shell gap at $N = 34$ for Cr and Ti isotopes. The newer interaction, GXPF1A [158], predicts a less pronounced $N = 34$ gap and reproduces well the known 2^+ excitation energies. To complete the list of interactions in this model space we refer as CO2 to a $V_{\text{low-k}}$ interaction with the emphasis on a good description of nuclei beyond ^{48}Ca [161], which predicts an even larger, $N = 34$, gap. Recently, a new interaction, called LNPS, has been developed to study Cr and Fe isotopes around $N = 40$ [162]. It predicts a new “island of inversion” with strong quadrupole correlations in Cr and Fe for $N \geq 38$. Similar conclusions were drawn from shell-model results for Cr isotopes employing a pairing-plus-multipole interaction [163]. Therefore the Cr isotopes with

$N \geq 28$ are a good testing ground to study the rapid shape evolution from a near-spherical to the well deformed region close to $N = 40$.

8.2 The neutron-rich Ca, Ti, and Cr isotopes

Intensive efforts were undertaken to verify the theoretical findings and predictions for the light rare neutron-rich isotopes in the pf shell. While there is no spectroscopic information available on ^{54}Ca , the less neutron rich $N = 34$ isotones have been explored to probe the subshell closure at $N = 34$. The monopole driven evolution of shell-model characteristics concurs for the neutron-rich chromium nuclei halfway between

the Ca and Ni isotopes. The status of the various predictions for $E(2_1^+)$ and $B(E2, 2^+ \rightarrow 0^+)$ vs. experiment is summarized in Figure 8.2 for the Ca, Ti and Cr isotopic chains.

In the Ca isotopes beyond $N = 28$ an increased neutron gap at $N = 32$ can be deduced from the $E(2_1^+)$ energy. However, conclusions on an $N = 34$ sub-shell are based on extrapolations [164, 165]. Detailed investigations of neutron-rich even-even Ti and Cr isotopes were performed recently with various techniques, e.g. β -decay studies [166, 167], fusion evaporation reactions [168], Coulomb excitation [169, 170], or deep inelastic reactions [166, 171]. The sub-shell closure at neutron number $N = 32$ for ^{54}Ti and ^{56}Cr was found to be apparent in both nuclei from the maximum in $E(2_1^+)$ at $N = 32$.

A crucial test for a sub-shell closure is provided by the $B(E2, 2^+ \rightarrow 0^+)$ values which are less affected than $E(2^+)$ by pairing in the ground state. Therefore Coulomb-excitation experiments with secondary beams after fragmentation reactions were performed for the $N = 32, 34$ nuclei in the Ti and Cr isotopes. The chain of $^{52,54,56}\text{Ti}$ nuclei was studied by Dinca *et al.* with intermediate-energy Coulomb excitation at MSU and established a minimum in the $B(E2, 2^+ \rightarrow 0^+)$ value for ^{54}Ti [169]. The first excited 2^+ states in $^{54,56,58}\text{Cr}$ were populated by Coulomb excitation at relativistic energies and γ rays were measured using the RISING setup at GSI [170] (see Fig. 8.3). For ^{56}Cr and ^{58}Cr the $B(E2, 2^+ \rightarrow 0^+)$ values were determined as 8.7(3.0) W.u. and 14.8(4.2) W.u., respectively. These results are consistent with an enhanced energy of the first 2_1^+ state and a local reduction of the collectivity at $N = 32$ in the Ca, Ti and Cr isotopes. The sub-shell gap is most pronounced for ^{52}Ca and decreased 2^+ energies are found in ^{54}Ti and ^{56}Cr . For the heavier isotones ^{58}Fe and ^{60}Ni neither the 2^+ energies nor the $B(E2)$ values indicate a $N = 32$ sub- pf -shell gap in agreement with theoretical predictions.

The different shell-model approaches are in line with the trend in the $E(2_1^+)$ excitation energies. But surprisingly the staggering of the $B(E2, 2^+ \rightarrow 0^+)$ values with a local minimum along the isotope chains at $N = 32$ is not reproduced, as shown in Figure 8.2. The theoret-

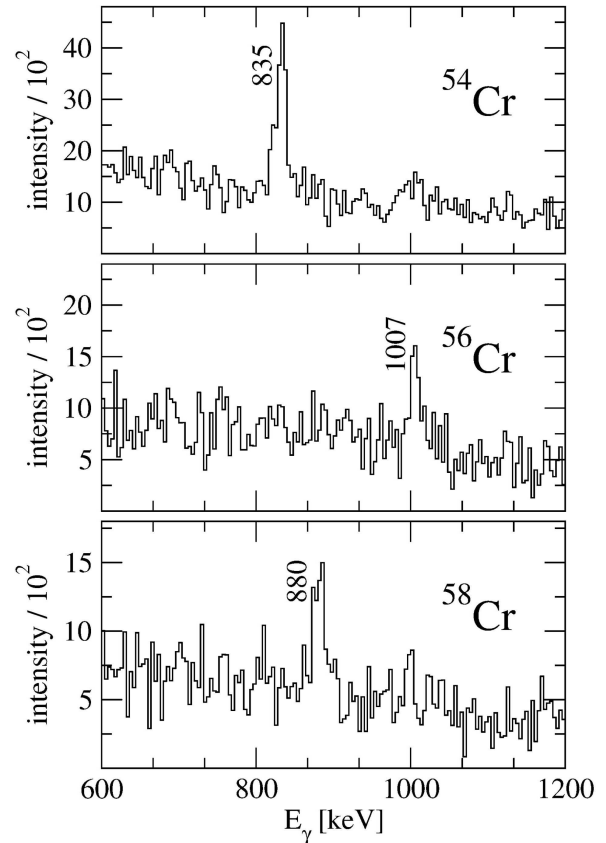


Figure 8.3: Doppler-corrected coincidence γ -ray spectra for $^{54,56,58}\text{Cr}$ obtained in a Coulomb-excitation experiment at relativistic energies performed by Bürger and collaborators at GSI. The figure was taken from the original work in Ref. [170].

ical $B(E2)$ values for the Ti and Cr isotopes are virtually unchanged and follow a more or less constant trend from $N = 30$ to 34. The experimental $B(E2)$ value of ^{56}Cr lies clearly below the shell-model predictions by about two standard deviations. The uncertainty of the value, however, does not allow to establish the discrepancy in absolute value and staggering trend with an accuracy similar to the observation in Ti isotopes.

To resolve the puzzling discrepancies between the measured and calculated $B(E2)$ values at $N = 32$ two different theoretical approaches suggested the following solutions. First of all shell-model calculations with the GXPF1 and KBG3 interaction were performed with effective charges that include a polarization isovector charge [172], referred to as KB3G* in Figure 8.2. The resulting larger neutron effective charge enhances the contribution of the

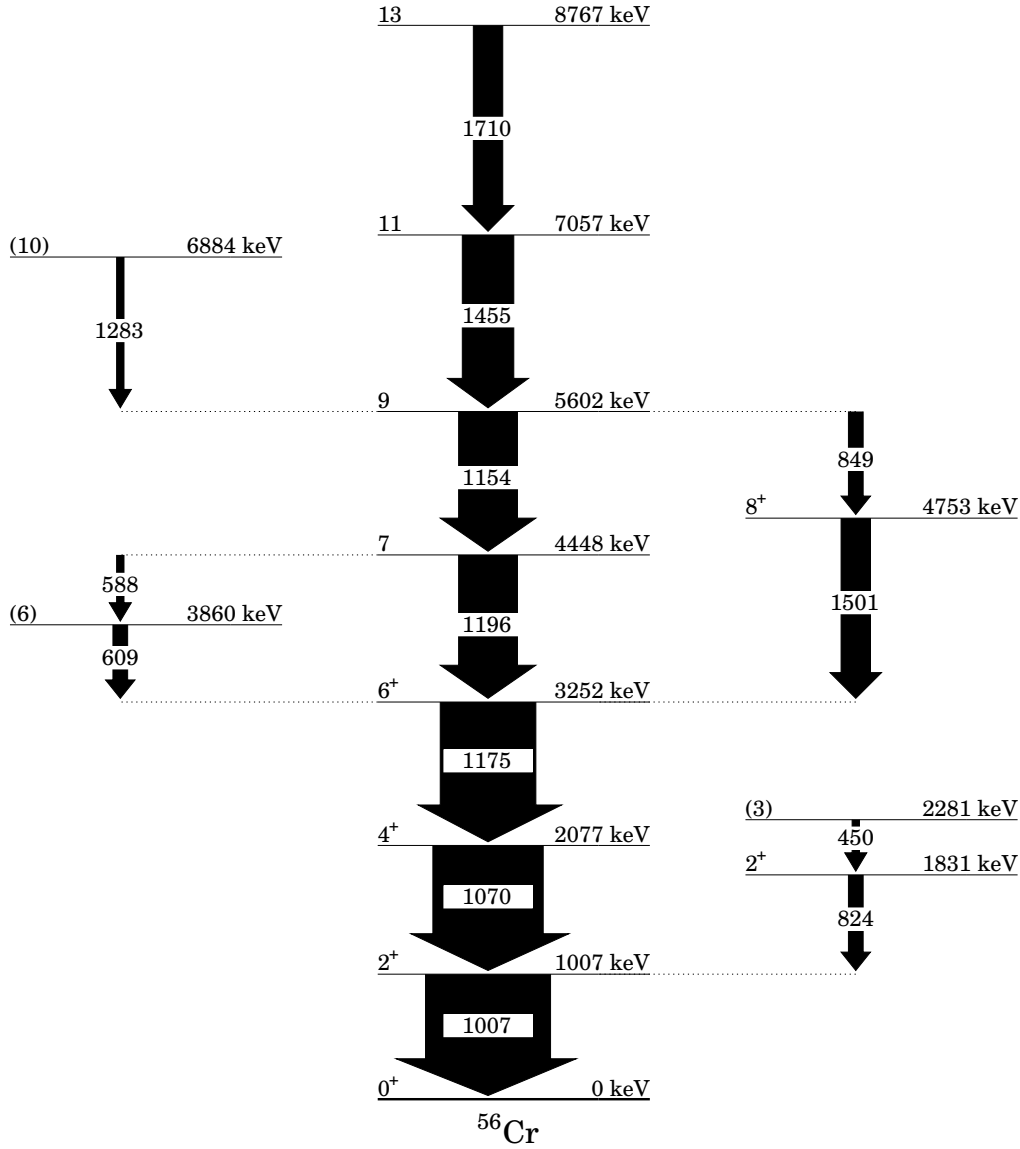


Figure 8.4: Known level-scheme of ^{56}Cr up to $J = 13$, determined by in-beam γ -ray spectroscopy [168]. The width of the arrows connecting the levels is proportional the observed intensity of the transitions. The figure was adapted from [168].

neutrons to the transition in absence of the (sub)shell closure, and it reduces the transition rate for the $N = 28$ and $N = 32$ Ti isotopes. The calculated $B(E2)$ values for the neutron rich Ti isotopes show the staggering and compare better with the experimental data points [173]. For the Cr isotopes the situation remains almost unchanged.

The second approach is based on a beyond-mean-field theory employing the finite range density dependent Gogny interaction [174]. Comparison with the experimental data for the neutron rich Ca, Ti, and Cr isotopes shows a good agreement for the excitation energies and

a reasonable one for the transition probabilities in Ca and Ti, but the decrease of the $B(E2)$ value in ^{56}Cr is not reproduced. It is important to note that these calculations support only a shell closure for $N = 32$ [174] and do not involve the use of effective charges.

In order to allow a conclusive comparison between theory and experiment, the $B(E2, 2_1^+ \rightarrow 0^+)$ value in ^{56}Cr had to be determined more precisely. This motivated a lifetime measurement with the Cologne coincidence plunger, employing the $^{48}\text{Ca}(^{11}\text{B}, p2n)^{56}\text{Cr}$ fusion evaporation reaction. $\gamma\gamma$ -coincidences of the subsequent decay of populated high spin states (cf. Fig. 8.4)

are observed in this recoil distance Doppler-shift (RDDS) measurement and are analyzed by the differential decay curve method (DDCM). In this work, level lifetimes and transition probabilities of the first excited states of ^{56}Cr will be presented and compared to recent theoretical predictions.

Chapter 9

The experimental setup and technique

In order to allow a conclusive comparison between the theory, presented in the last chapter, and experiment, the $B(E2, 2_1^+ \rightarrow 0^+)$ value in ^{56}Cr was determined very precisely by a lifetime measurement. The experiment was performed at the FN tandem accelerator of the University of Cologne combining the Cologne plunger device with a setup of one EUROBALL Cluster Ge-detector and 5 single Ge-detectors for a $\gamma\gamma$ -coincidence recoil distance measurement. Excited states in ^{56}Cr were populated by the $^{48}\text{Ca}(^{11}\text{B}, p2n)^{56}\text{Cr}$ reaction using an ^{11}B beam with an energy of 32 MeV. An overview of the setup used and the most important experimental details will be given in the following sections.

9.1 Beam production

Preparation of intense (stable) heavy ion beams starts with the ionization of neutral atoms in an ion source. In general there are two different types of ion sources, either producing positively or negatively charged ions. Positively charged ions, even at high charge states, can be produced by a large variety of ion sources, for example by plasma driven ion sources, such as a Penning ion gauge (PIG) or a vacuum arc ion source (VARIS/MEVVA), and ion sources of the electron cyclotron resonance (ECR) or electron beam (EBIS/EBIT) type. To provide negatively charged ions for an FN tandem accelerator, as in the present experiment, a sputter ion source is the most common and most versatile technique among the RF charge exchange ion source.

The ^{11}B beam used in this experiment was provided by the Cologne sputter ion source. The sputter ion source uses cesium vapor from a reservoir of cesium, heated up to approximately

90°C. The neutral Cs-atoms are thermally ionized on a tantalum ionizer, heated up to about 1000°C. Applying a voltage of some kV the positively charged Cs^+ ions are accelerated towards the sputtering target serving as cathode. In the experiment presented in this work, the cathode was made of boron. The cathode is cooled, hence it is covered by a thin layer of condensed Cs-atoms. The accelerated Cs-ions bombard the cathode, sputtering atoms from the cathode. By passing through the thin cesium coating on the cathode's surface some of the sputtered atoms gain an electron. These negatively charged ions can be extracted out of the ion source and accelerated towards the FN tandem accelerator by applying a voltage of some 10 kV.

9.2 The Cologne FN tandem Van de Graaff accelerator

The negatively charged ion beam provided by the sputter ion source is accelerated to its final beam energy by the Cologne FN tandem Van de Graaff accelerator. It is an electrostatic linear accelerator operating since 1968. The basic principle of the accelerator is quite simple. A central metal electrode, the so-called “terminal”, is charged to a high positive potential U of up to almost 11 MV. Originally the charging was done using a rubber belt, which was replaced in 2004 by a modern, inductive pelletron chain system. To isolate the highly charged electrodes of the accelerator and to prevent sparking, the FN tandem accelerator is housed in a large steel vessel, 13 m long and 3.66 m in diameter, which is filled with an insulating gas mixture of 20% SF_6 and 80% N_2 at about 12 bar (see Figure 9.1). Neg-

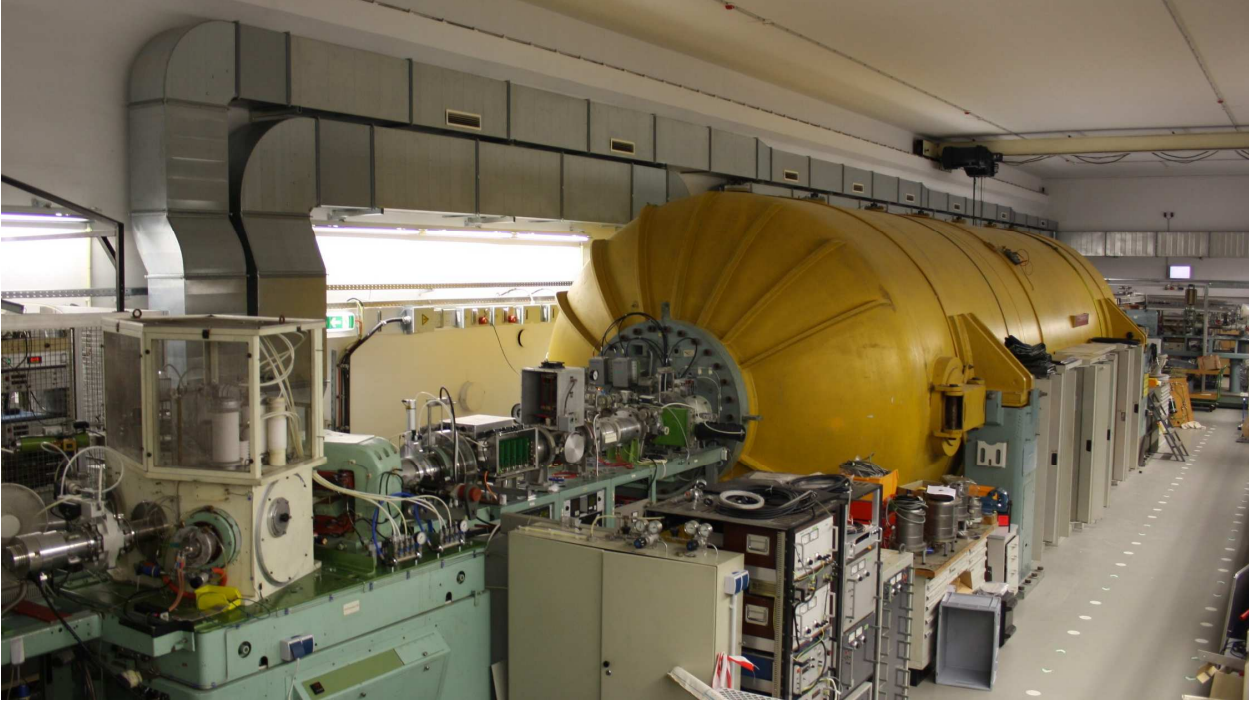


Figure 9.1: The Cologne FN tandem Van de Graaff accelerator, which accelerated the ^{11}B beam up to an energy of 32 MeV for the lifetime measurement of ^{56}Cr . The large yellow pressure tank houses the electrostatic accelerating structures.

atively charged ions of charge state 1^- are accelerated inside an evacuated beamline towards the terminal, gaining kinetic energy $E_1 = eU$. Inside the terminal the ion beam passes through a thin carbon foil (“stripper foil”) with a thickness of typically some $\mu\text{g}/\text{cm}^2$, which strips electrons from the ions, leaving it positively charged with charge state q^+ . The stripping efficiency typically exceeds 90%. The positively charged ion beam is accelerated away from the high positive potential at the terminal, gaining the kinetic energy $E_2 = qU$. Thus, the final energy of the ion beam is $E_{\text{beam}} = (q + 1)U$. Due to the population of different charge states by the stripping process, ions with different kinetic energy exit the accelerator. Therefore the ions are bent by a 90° analyzing magnet, to select a charge state, and thus, to specify the beam energy.

In the experiment presented in this work, a ^{56}Cr beam was accelerated to a final beam energy of 32 MeV, giving the maximum amount of about 2.6% for the $^{48}\text{Ca}(^{11}\text{B}, p2n)^{56}\text{Cr}$ reaction relative to the 1020 mb total reaction cross section (calculated using PACE [175]). The charge state used was 4^+ , giving rise to an average ^{11}B beam intensity of about 2.5 pA, which was provided for the plunger experiment.

9.3 The Cologne plunger setup

The accelerated ^{11}B beam was directed to the plunger setup, located at the beamline “R15”. The Cologne plunger setup was designed to allow sensitive $\gamma\gamma$ -coincidence recoil distance measurements even of weakly populated reaction channels. It combined the advanced Cologne plunger device with a set of large volume HPGe detectors in close geometry located around the target chamber. A schematic layout of the setup is shown in Figure 9.2.

9.3.1 The Cologne plunger device

The Cologne plunger apparatus was specially designed to allow for RDDS lifetime measurements of highest precision in the picosecond range.

The principal components of a plunger are the target and stopper foils and the electronic control system for precise adjustment of the distance between target and stopper. To ensure a well-defined target-to-stopper distance, both foils have to be planar and parallel. Therefore the foils are carefully stretched on conical target holders, which can be positioned by three micrometer screws. A picture of both foils mounted

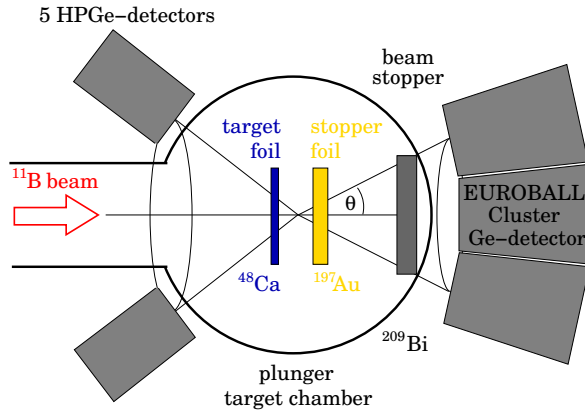


Figure 9.2: Schematic layout of the experimental setup (not to scale). The Cologne coincidence plunger device was located between five single Ge-detectors located at backward positions and an EUROBALL cluster detector at 0° forward position.

on their holders inside the plunger device is shown in Fig. 9.3. The distance between the foils is varied by a piezoelectric linear motor, the so-called inchworm. Using the inchworm motor, the distance between the foils can be roughly adjusted up to 10 mm with a global accuracy of $0.5 \mu\text{m}$. For fine-tuning an additional piezoelectric crystal is mounted between the inchworm motor and the target holder, which is capable to regulate small changes in the target-to-stopper distance up to $30 \mu\text{m}$. The relative distance between target and stopper foil is measured by two different systems. An optical metering system is coupled to the inchworm motor. To account for any changes in the distance, e.g. caused by the additional piezoelectric crystal, an independent inductive measuring system has been installed, a so-called TESA sensor.

Due to energy deposition in the target foils by the beam, the assembly of the plunger is subject to thermal expansion. Thus, the plunger apparatus used was equipped with a feedback system for compensation of slow changes in the target-to-stopper distance [176]. The isolated target and stopper foils form a parallel plate capacitor. Applying a well-defined electrical signal, the distance between the foils can be monitored continuously by means of the measured capacitance. If the capacitance, i.e. the target-to-stopper distance, exceeds a specified threshold, this is compensated automatically by the piezoelectric crystal. Thus, the accuracy of the relative distances

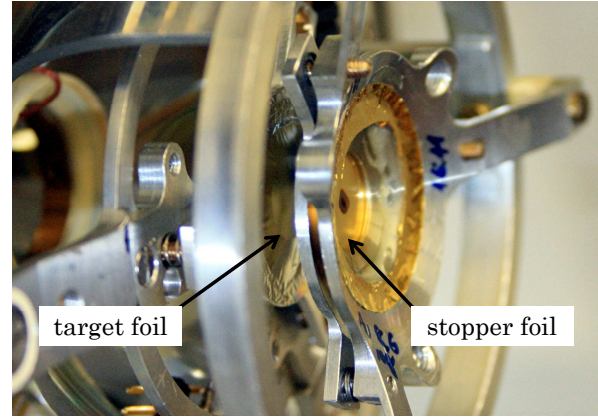


Figure 9.3: Picture of the centerpiece of the plunger device, opened for maintenance, showing the target and stopper foils mounted on their conical holders.

were measured to be better than 2-3% in the relevant range of the target and stopper foils, e.g. $0.04 \mu\text{m}$ at a distance of $1.51 \mu\text{m}$.

In the present experiment data were taken at 12 different target-to-stopper distances ranging from $0.5 \mu\text{m}$ to $80 \mu\text{m}$. The target consisted of a 0.5 mg/cm^2 thick layer of enriched ^{48}Ca which is sandwiched by two gold foils of 2.0 mg/cm^2 and $40 \mu\text{g/cm}^2$ thickness, respectively. The recoiling nuclei left the target with approximately 1% of the speed of light and were stopped in a 2.15 mg/cm^2 Au foil. The ^{11}B beam passing both foils was stopped in a 1-2 mm thick ^{209}Bi sheet.

9.3.2 γ -ray detector setup

The γ rays emitted by the fusion evaporation products were measured with one EUROBALL Cluster Ge-detector [177], containing 7 encapsulated HPGe crystals, which was positioned at a close distance of 8.5 cm between target and front side of the central Ge detector. This close distance was chosen to improve the efficiency. The original design distance between target and front side of central Ge detector for EUROBALL cluster detectors was 44.5 cm. Thus, the six crystals surrounding the central detector did not point towards the target exactly and determination of the mean γ -ray detection angle is not trivial. In this experiment the seven Ge capsules inside the EUROBALL Cluster detectors were used as seven individual detectors, arranged in forward angles of 0° and 27.4° , respectively. In

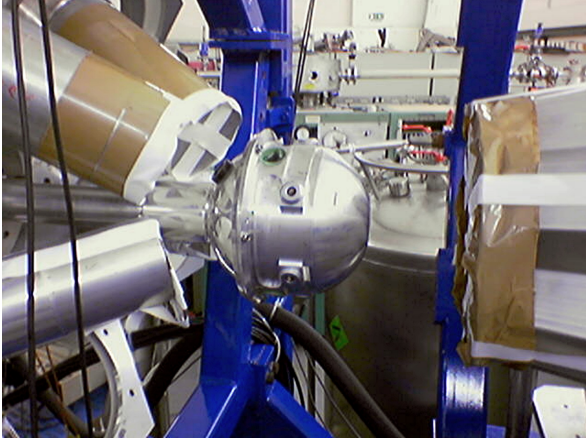


Figure 9.4: Picture of the Cologne plunger device, surrounded by five single Ge-detectors at backward angle and one EUROBALL cluster positioned at 0° for γ -ray detection. To reduce background contributions in the X-ray region the detectors were shielded by Cu, Cd, and Pb sheets. During experiment the EUROBALL cluster is positioned as close as possible to the plunger device (distance < 5 mm).

addition, 5 single Ge-detectors were arranged in one ring at backward angle with a central angle at 142.5° with respect to the beam axis. To reduce background contributions in the X-ray region and to suppress summing the Cluster Ge-detectors were shielded by copper and lead sheets of 1 mm thickness each. The backward Ge detectors were equipped individually with a small stack of 1 mm copper and 0.5 mm cadmium shielding. The total γ -ray efficiency of the setup was determined to be about 1.8% at 1.3 MeV (cf. Section 10.2.2).

During the experiment presented in this work data were recorded in $\gamma\gamma$ -coincidence mode and written to disc in listmode format.

9.4 Lifetime measurements with a plunger

To measure lifetimes of excited nuclear states in the range of about 1 ps up to several hundred picoseconds, the plunger technique is a powerful tool. Its basic principle is the application of two separate foils at variable distance, employing the recoil distance Doppler-shift (RDDS) method. Performing $\gamma\gamma$ -coincidence measurements with a plunger device, the differential decay curve method (DDCM) [178, 179] has be-

come the well-established analysis technique to extract the lifetime of a nuclear state out of the RDDS data. Both techniques were used in the present experiment and will be explained in more detail in the following sections.

9.4.1 The recoil distance Doppler-shift method

As already stated above a plunger employs the recoil distance Doppler-shift (RDDS) method. In principle a plunger is made up of two foils – a target foil and a stopper foil – mounted parallel to each other. The distance d between both foils can be varied precisely in the micrometer to millimeter range. In the target foil highly excited nuclei are produced by fusion-evaporation reactions. Due to the momentum transfer, the nuclei recoil out of the thin target foil towards the second foil (“stopper”), where they are stopped after the flight path d . Recoiling nuclei may emit de-excitation γ rays either in flight in the vacuum between both foils or at rest after implantation in the stopper foil. If de-excitation occurs in flight, the emitted γ ray will be detected with a certain Doppler shift, depending on the velocity β of the recoiling nucleus and the detection angle θ_γ :

$$E'_\gamma = \frac{\sqrt{(1 - \beta^2)}}{1 - \beta \cos \theta_\gamma} E_{\gamma,0},$$

where $E_{\gamma,0}$ is the γ -ray energy emitted in rest. Therefore in the γ -ray spectrum a Doppler-shifted component of the original transition can be observed at E'_γ additionally to the original γ -ray energy $E_{\gamma,0}$ (see Figure 9.5).

Normally the line width of the Doppler-shifted component is clearly broadened compared to the general detector resolution of the transition with E_γ . This is mainly caused by the relatively large opening angles of the HPGe detectors mounted in close geometry and the distribution of the recoil velocities around a mean value $\langle v \rangle$. This distribution can be explained by different energy loss in the target, depending whether the reaction takes place at the beginning of the target or at the end. For the present experiment the recoil velocity of ^{56}Cr was calculated to be $\langle v \rangle \approx 0.011 \pm 0.003$ c using the LISE

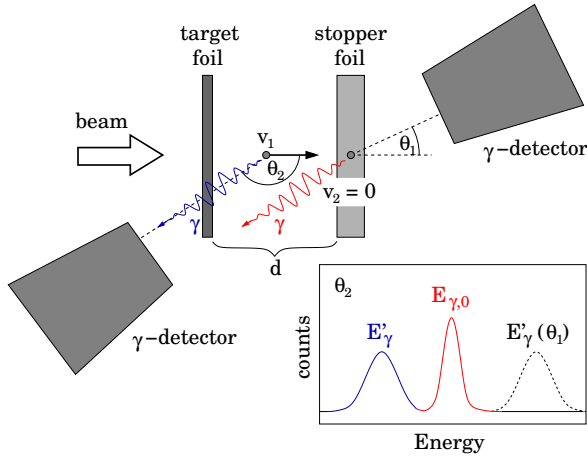


Figure 9.5: Schematic drawing of the RDDS method. Excited nuclei produced in the target recoil out of the target foil. De-excitation may occur in flight or at rest in the stopper foil. Depending on the detection angle, an additional, Doppler-shifted component of the transition can be observed in the spectrum at lower or higher energies.

code [180, 181]. Experimental verification will be given in Section 10.5.

The ratio of the shifted and unshifted component depends on the distance between the two foils, which is directly correlated to the time of flight of the nucleus between the foils, and the lifetime of the nuclear state. Thus, it is possible to extract the lifetime of an excited nuclear level by a detailed analysis of the evolution of the intensities of both components with varying distance d . A well-established tool for the analysis of those data is the differential decay curve method (cf. Section 9.4.2).

For lifetimes in the order of 1 ps or even less the effect of the Doppler-shift attenuation occurring during slowing down in the stopper has to be taken into account carefully. This effect is discussed in [182] in detail. It turns out that for $\tau > 3$ ps Doppler-shift attenuation effects can be safely neglected.

9.4.2 $\gamma\gamma$ -coincidences and the differential decay curve method

The Cologne plunger apparatus is especially advantageous for $\gamma\gamma$ -coincidence recoil distance measurements in combination with the differential decay curve method (DDCM) [178, 179] which was employed for the data analysis. In

the following paragraphs a brief summary of the method and its necessary equations will be given. Further details are given in the publications of Dewald *et al.* and Böhm *et al.*, which were quoted above.

In general the lifetime τ of an excited nuclear state can be deduced from the decay function. However, the decay function of a state depends on the time characteristics and intensities of all feeding transitions. Figure 9.6 shows a schematic drawing of a decay scheme with i the level of interest. Its lifetime is τ_i and it is depopulated by the transition A to a state j . Higher-lying states f are feeding into level i , where directly feeding transitions are labeled with B, and indirectly feeding transitions are labeled with C. The time derivative of the population $n_i(t)$ of the level i is given by

$$\frac{d}{dt}n_i(t) = -\lambda_i n_i(t) + \sum_f b_{fi} \lambda_f n_f(t),$$

where $\lambda_{i,f}$ is the decay constant and b_{fi} the branching ratio of the transition $f \rightarrow i$. After a certain time t the number of decays $N_{fi}(t)$ ($N_{ij}(t)$), which can be observed as feeding (depopulating) transitions of the level i , are given by the integrals

$$N_{fi}(t) = \int_t^\infty \lambda_f n_f(t') dt'$$

$$N_{ij}(t) = \int_t^\infty \lambda_i n_i(t') dt'.$$

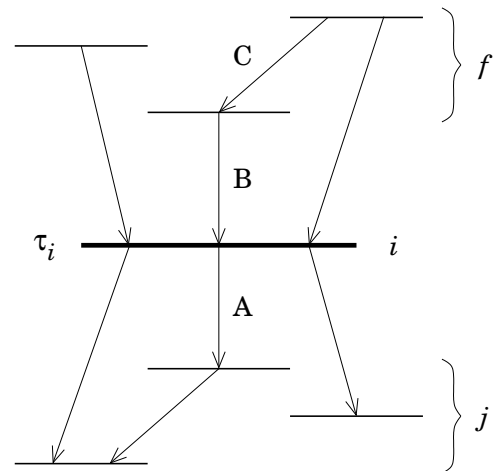


Figure 9.6: Schematic decay scheme with i the level of interest. More information is given in the text.

Thus, introducing the branching ratio b_{ij} of the depopulating transition $i \rightarrow j$, the lifetime of the level of interest can be determined by the following equation:

$$\tau_i(t) = \frac{-N_{ij}(t) + b_{ij} \sum_f b_{fi} N_{fi}(t)}{\frac{d}{dt} N_{ij}(t)}.$$

The quantities $N_{fi}(t)$ and $N_{ij}(t)$ are proportional to the intensities of the non-Doppler-shifted γ -ray transitions feeding and depopulating the state i after implantation in the stopper foil. These numbers can be deduced from the RDDS data for each measured target-to-stopper distance d , i.e. for each flight time $t = d/v$. For a measurement in singles mode the proportionality constant depends on the detection efficiency and angular distribution effects of the detector at its position. The calculation of the time derivative of $N_{ij}(t)$ is achieved by fitting a continuous sequence of second or third order polynomials to the data points and differentiating the fit function. Since the lifetimes τ are calculated for every flight time t one obtains a function $\tau(t)$ or $\tau(d)$ i.e., the so-called τ curve which is expected to be a constant. Deviations from a constant behavior indicate the presence of systematic errors.

The most important disadvantage in the DDCM analysis of RDDS data taken in singles mode, is the imperative to measure the intensities of all directly feeding transitions very precisely. It may happen that weak feeding transitions are superimposed by stronger transitions or can not be detected at all, yielding an incorrect lifetime value.

These inaccurate feeding issues (e.g. the unobserved “sidefeeding”) can be improved considerably by a $\gamma\gamma$ -coincidence measurement. In the following we will use the notation $\{X, Y\}$ for a sequence of coincident transitions X and Y :

$$\{X, Y\} \equiv f \xrightarrow{X} i \xrightarrow{Y} j$$

In RDDS measurements usually Doppler-shifted and unshifted components of a γ -ray transition are observed. The different components will be indicated by the subscripts S and U, respectively. Thus, a cascade of two coinciding RDDS events can be decomposed by

$$\{X, Y\} = \{X_S, Y_S\} + \{X_S, Y_U\} + \{X_U, Y_U\}.$$

The case $\{X_U, Y_S\}$ is not possible, because a nucleus which is at rest for the emission of X can not emit the subsequent γ ray Y in flight.

Using this nomenclature for $\gamma\gamma$ -coincidences and the definitions given in Figure 9.6 the equation for the lifetime τ , which was already derived for a measurement using singles data above, can be rewritten as

$$\tau_i(t) = \frac{\{C_{S,A_U}\}(t) - \alpha \{C_{S,B_U}\}(t)}{\frac{d}{dt} \{C_{S,A_S}\}(t)},$$

where α includes the branching ratio of a sequence of a directly feeding transition B and a directly depopulating transition A, independently from the time of flight t :

$$\alpha = \frac{\{C, A\}}{\{C, B\}} = \frac{\{C_S, A\}}{\{C_S, B\}} = \frac{\{C_S, A_U\} + \{C_S, A_S\}}{\{C_S, B_U\} + \{C_S, B_S\}}$$

Thus, applying the coincidence condition on a directly feeding transition B and applying a gate on its Doppler-shifted component, the lifetime τ_i of the state of interest can be calculated, using

$$\tau_i(t) = \frac{\{B_S, A_U\}(t)}{\frac{d}{dt} \{B_S, A_S\}(t)} = \frac{I_U(t)}{\frac{d}{dt} I_S(t)},$$

with I_S and I_U the measured intensities of the coincident depopulating transition A and its shifted and unshifted components, respectively.

Chapter 10

Data analysis

In γ -ray spectroscopy relevant information on the underlying nuclear structure can be obtained from the measured characteristics of the γ rays, i.e. their energy, time-dependence and geometrical distribution. Modern experiments with γ -ray spectrometers are capable to measure, store and analyze these information accurately on an event-by-event basis.

In the lifetime measurement presented in this work, experimental data were taken in $\gamma\gamma$ -coincidence mode. Important procedures of the analysis of the RDDS lifetime measurement, e.g. calibration measurements, normalization of the transition yields measured at different target-to-stopper distances, and determination of the mean recoil velocity, will be presented in the following sections.

10.1 Acquisition and processing of the measured data

To allow for a precise RDDS lifetime measurement of excited states in ^{56}Cr using the differential decay curve method, experimental data were taken in $\gamma\gamma$ -coincidence mode. All relevant information of the observed γ -ray events, i.e. their energy, time and detector-ID, was recorded in list mode format on event-by-event basis. For the analysis data were processed using C based codes. Processing included energy calibration, setting of prompt and background coincidence time gates, as well as sorting into $\gamma\gamma$ -matrices. Sorting was done for each measured target-to-stopper distance separately. Detectors positioned at identical angles θ_γ with respect to the beam axis were grouped into rings. Consequently the spectra measured with detectors

belonging to one ring show the same Doppler shifts. In the present experiment one EUROBALL detector was positioned at 0° (ring-ID 0), the six exterior EUROBALL detectors of the cluster were positioned at a mean angle of 27.4° (ring-ID 1) and five large volume HPGe detectors, including one 12-fold segmented MINIBALL detector, were positioned at 142.5° (ring-ID 2).

10.2 Calibration measurements

10.2.1 Energy calibration of the HPGe detectors

The analysis of an experiment always commenced by calibrating the detectors thoroughly. In order to calibrate the HPGe detectors used in the present lifetime experiment, different radioactive sources containing ^{60}Co , ^{152}Eu , and ^{226}Ra , respectively, were mounted close to the detectors. Figure 10.1 shows such a ^{226}Ra cali-

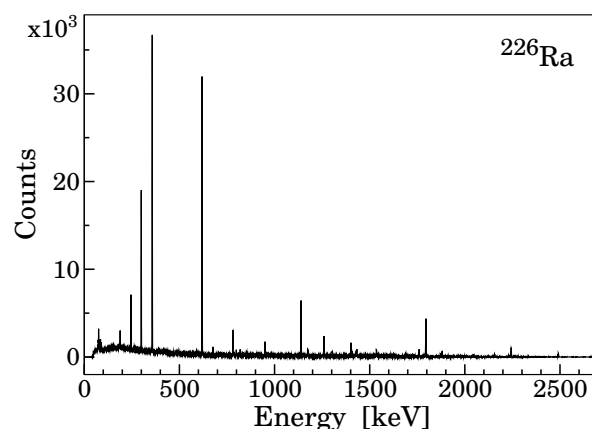


Figure 10.1: Calibration spectrum of one γ -ray detector, containing several decay transitions of ^{226}Ra and its daughter products.

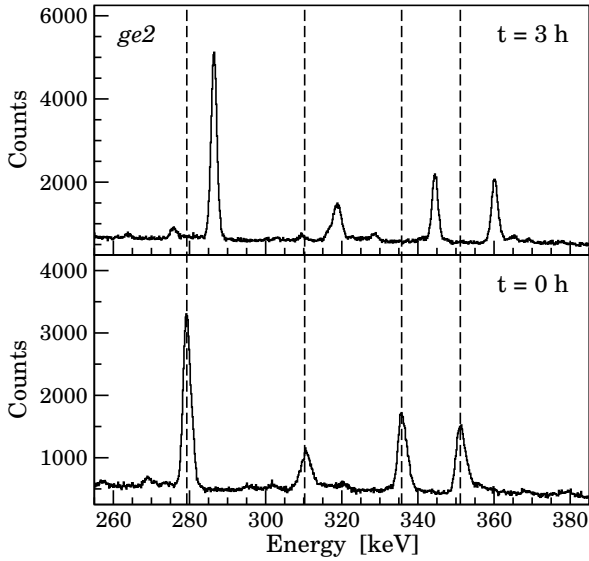


Figure 10.2: Low-energy part of the spectrum with a dominant Coulomb-excitation transition of ^{197}Au at 279 keV in the beginning of the experiment (lower part) and after 3 hours of beam time (upper part) for one EUROBALL detector. Due to instabilities in the analog amplifier electronics the gain of this particular detector was shifted by almost 3%.

bration spectrum for one of the EUROBALL detectors.

During the experiment, the gain of some amplifiers showed a long-term shift due to instabilities in the analog amplifier electronics of the detectors (cf. Fig. 10.2). A first-order approximation of these shifts yielded a linear function, fitted to the relative positions of two time-independent γ -ray transitions in the spectrum. The transitions must have a stopped component only, e.g. from Coulomb excitation, radioactive decay, nuclear isomerism, etc. In the present case the 191.44 keV transition, de-exciting a well-known Coulomb-excited $3/2_2^+$ state in ^{197}Au , and the 1460.82 keV transition of the ^{40}K decay from background radiation were used to fit the linear polynomial for each detector in each experimental run.

10.2.2 Efficiency calibration of the HPGe detectors

To determine the absolute detection efficiency ϵ_{abs} of the germanium detectors, a ^{226}Ra source was mounted at target position on the support frame of the stopper target. Its activity was

θ_γ	$\epsilon_{\text{abs}} [\%]$	comments
0°	0.20	EUROBALL detector
27.4°	0.16	EUROBALL detectors
	0.16	
	0.17	
	0.15	
	0.17	
	0.17	
142.5°	0.13	12-fold segmented MINIBALL detector
	0.14	
	0.15	
	0.10	
	0.15	
total	1.85	

Table 10.1: Absolute detection efficiencies ϵ_{abs} of the individual germanium detectors used in the setup for the 1238 keV transition of the ^{226}Ra decay.

98.7 kBq. The major γ -ray transition energies and absolute γ -ray emission intensities of ^{226}Ra and its daughter products were taken from the work of Morel *et al.* [183]. Including dead time information of the detectors, it was possible to determine the absolute detection efficiency of each individual γ -ray detector used in the setup (cf. Table 10.1). Thus, the total γ -ray detection efficiency of the detector setup is about 1.8% at 1.3 MeV.

10.2.3 Time gate for $\gamma\gamma$ -coincidences

To select real $\gamma\gamma$ -coincidences and to suppress random background events a restrictive coincidence gate had to be applied. Therefore, a $\gamma\gamma$ time-difference spectrum was generated for each of the 66 possible combinations of two Ge detectors. A prompt coincidence gate Δt_p was applied with a width of typically 40-60 ns, as shown in Figure 10.3 using the example of $\gamma\gamma$ -coincidences in a detector combination of one EUROBALL detector (ge2) and one detector positioned at backward angle (ge11). To account for random background coincidences two background gates Δt_r were applied. The total width of the background gates was identical to the width of the prompt coincidence gate.

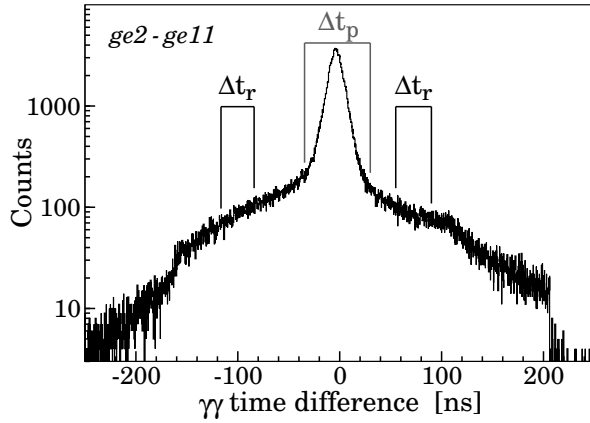


Figure 10.3: Exemplary $\gamma\gamma$ time-difference spectrum for a detector combination of one EUROBALL detector (ge2) and one backward detector (ge11). A prompt coincidence gate Δt_p was applied with a width of typically 40-60 ns. Random background coincidences were taken into account using background gates Δt_r .

10.3 Distance calibration of the plunger foils

As mentioned in the last chapter, the measurement systems for the distance between the plunger foils, i.e. the optical system at the inchworm motor and the TESA sensor, are limited to relative distance measurements. To gain an absolute value of the distance between target and stopper foil, a calibration measurement without beam had to be performed. Therefore, the target is placed at a series of different target-to-stopper distances using the inchworm motor. For each target-to-stopper distance the measured value of the TESA sensor is related to the voltage output of the capacitive measuring system (cf. 9.3.1). During the calibration measurement the additional piezoelectric crystal of the feedback system for compensation of slow changes in the target-to-stopper distance was deactivated.

Figure 10.4 shows the distance calibration of the plunger setup used. At a measured (relative) distance of $-1.51 \mu\text{m}$ the foils had contact, defining the zero point of the absolute distance. A series of continuously differentiable polynomials of third order were fitted to the data points. Thus, the voltage output continuously monitored during the experiment, could be converted into absolute target-to-stopper distances. Figure 10.5 shows the same data points as in

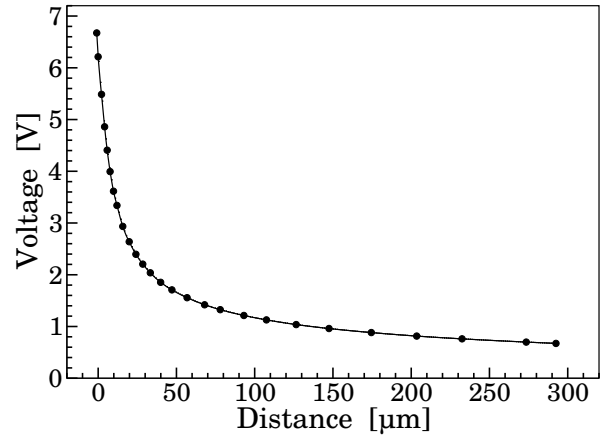


Figure 10.4: Distance calibration measurement of the plunger setup used. The voltage output of the capacitive measuring system is plotted as a function of the relative distance measured by the TESA sensor. More information is given in the text.

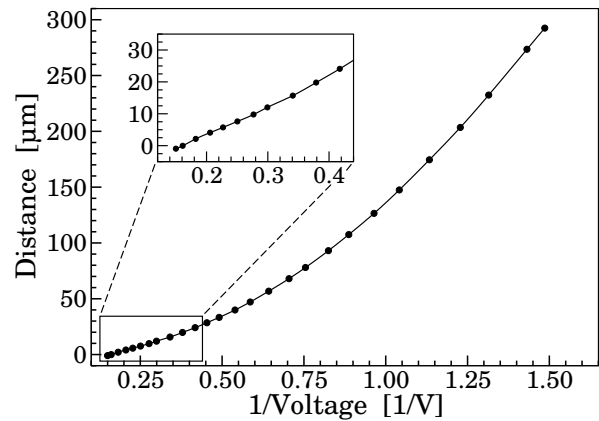


Figure 10.5: Same as in Fig. 10.4, but with the distance values of the TESA sensor plotted as a function of the reciprocal voltage output. For distances below $10 \mu\text{m}$ the fit is almost linear, just as for a parallel plate condenser.

Fig. 10.4, but with the distance values of the TESA sensor plotted as a function of the reciprocal voltage output. For distances below $10 \mu\text{m}$ the fit is almost linear. Thus, to first order the setup of the two foils is well described by a parallel plate condenser. Small deviations were due to minor unevenness of the target and stopper foils.

10.4 Yield normalization

In general the lifetime of an excited nuclear state is determined by a measurement of its decay function. In an RDDS measurement all in-

formation on the decay function is included in the measured intensities of the Doppler-shifted and unshifted components of populating and depopulating transitions. According to the equations given in Section 9.4.2 the differential decay curve method uses the developing of those quantities, measured at different target-to-stopper distances, to deduce the lifetime of the state. However, the measured intensities were not only subject to the lifetime of the state, but depended

e.g. on the duration of the measurement and the beam intensity. Thus, the measured de-excitation yields had to be normalized to ensure the same amount of reactions occurring in each measurement.

In order to account for possible time- and energy-dependent effects, e.g. varying cross sections of fusion evaporation reaction channels, it is strongly recommended to use coincident transitions of the nucleus of interest for normalization. For the experiment presented in this work this was not possible due to significant contaminations in the gated spectra of ^{56}Cr . However, time-dependent deviations in the beam energy were found to be negligible, therefore it was decided to use the γ -ray transitions of ^{56}Mn for normalization of the measured de-excitation yields. Figure 10.6 shows a partial level scheme of ^{56}Mn with the strong γ -ray cascade used for normalization. To reduce the systematic error of the deduced normalization factors, independent gated spectra were generated for different detector combinations (rings) at each target-to-stopper distance. Short-lived, coincident γ -ray transitions at 541 keV, 526 keV, 642 keV, 631 keV, and 943 keV were not affected by contamination, thus they were used for normalization. The deduced normalization factors of the measurements at the different target-to-stopper distances are shown in Figure 10.7. The weighted mean of the independently measured normalization factors reproduced very well constant γ -ray yields out of the measured transition intensities of ^{56}Mn (see Figure 10.8) and ^{56}Cr . Thus, these values were used in the DDCM lifetime analysis of the excited states of ^{56}Cr .

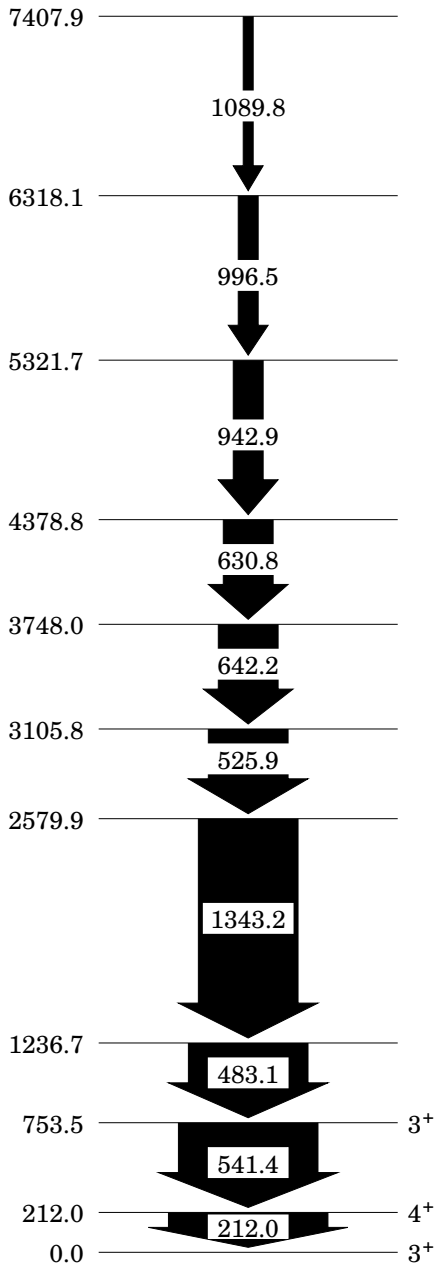


Figure 10.6: Partial level scheme of ^{56}Mn with the strong γ -ray cascade used for the normalization of the measured de-excitation yields.

10.5 Recoil velocity

Moreover the recoil velocity v of the ^{56}Cr ions was needed for the DDC method, to determine the flight time t_i out of the target-to-stopper distance d_i :

$$d_i = v \cdot t_i$$

The velocity of the recoils after the target has a certain distribution, which is mainly caused by the different energy loss in the target. Fusion evaporation products produced at the beginning

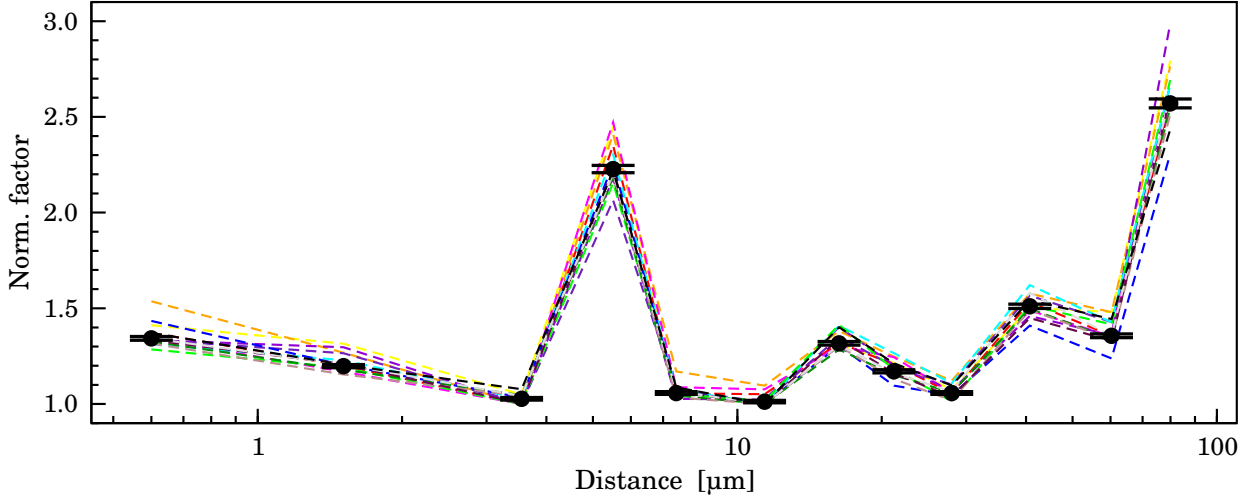


Figure 10.7: Deduced normalization factors for each target-to-stopper distance and for different coincident γ -ray transitions in ^{56}Mn (colored lines). Obviously the lines follow a very similar pattern. The black circles plus error bars mark the weighted mean values of those independently measured normalization factors, which were further used in the analysis.

of the target loose more energy than those ions produced at the end of the target. The mean recoil velocity was accurately determined via the measured Doppler shift of the γ -ray transitions emitted in flight at a certain detection angle θ_γ , using

$$\frac{v}{c} = \frac{1}{\cos \theta_\gamma} \left(\frac{E_\gamma^{(\text{sh})}}{E_\gamma^{(\text{us})}} - 1 \right),$$

where $E_\gamma^{(\text{us})}$ is the original transition energy and $E_\gamma^{(\text{sh})}$ is the Doppler-shifted transition energy. Due to the geometry of the setup used, the detection angles of two detector groups were known. The central EUROBALL detector was positioned at 0° , while all HPGe-detectors positioned at

backward angles yielded 142.5° . The mean detection angle of the detector ring formed by the six exterior EUROBALL detectors depended on the distance between target chamber and cluster, thus it was not used in this part of the analysis. The Doppler shift of the different transitions was determined for various target-to-stopper distances by fitting the peak positions of shifted and unshifted component. Table 10.2 shows the mean values of the measured transition energies and the resulting recoil velocity. Finally the experimental data yielded a value of $v/c = 1.006(9)\%$ for the mean recoil velocity of ^{56}Cr ions after the target. This agreed very well with the calculated recoil velocity of $v/c = 1.1(3)$ using the LISE code [180, 181].

	$E_\gamma^{(\text{us})}$ [keV]	$E_\gamma^{(\text{sh})}$ [keV]	v/c [%]
$\theta_\gamma = 0^\circ$	1006.47(3)	1017.20(19)	1.066(19)
	1069.42(14)	1079.52(12)	0.944(17)
	1175.53(40)	1185.85(67)	0.878(67)
		mean	0.994(13)
$\theta_\gamma = 142.5^\circ$	1006.74(4)	998.95(9)	0.975(13)
	1069.74(6)	1060.93(16)	1.038(20)
	1174.94(12)	1164.54(19)	1.116(24)
		mean	1.022(14)
		total mean	1.006(9)

Table 10.2: Mean values of the measured Doppler-shifted and unshifted transition energies and the resulting recoil velocity v/c of ^{56}Cr for different detectors positioned at forward and backward angle.

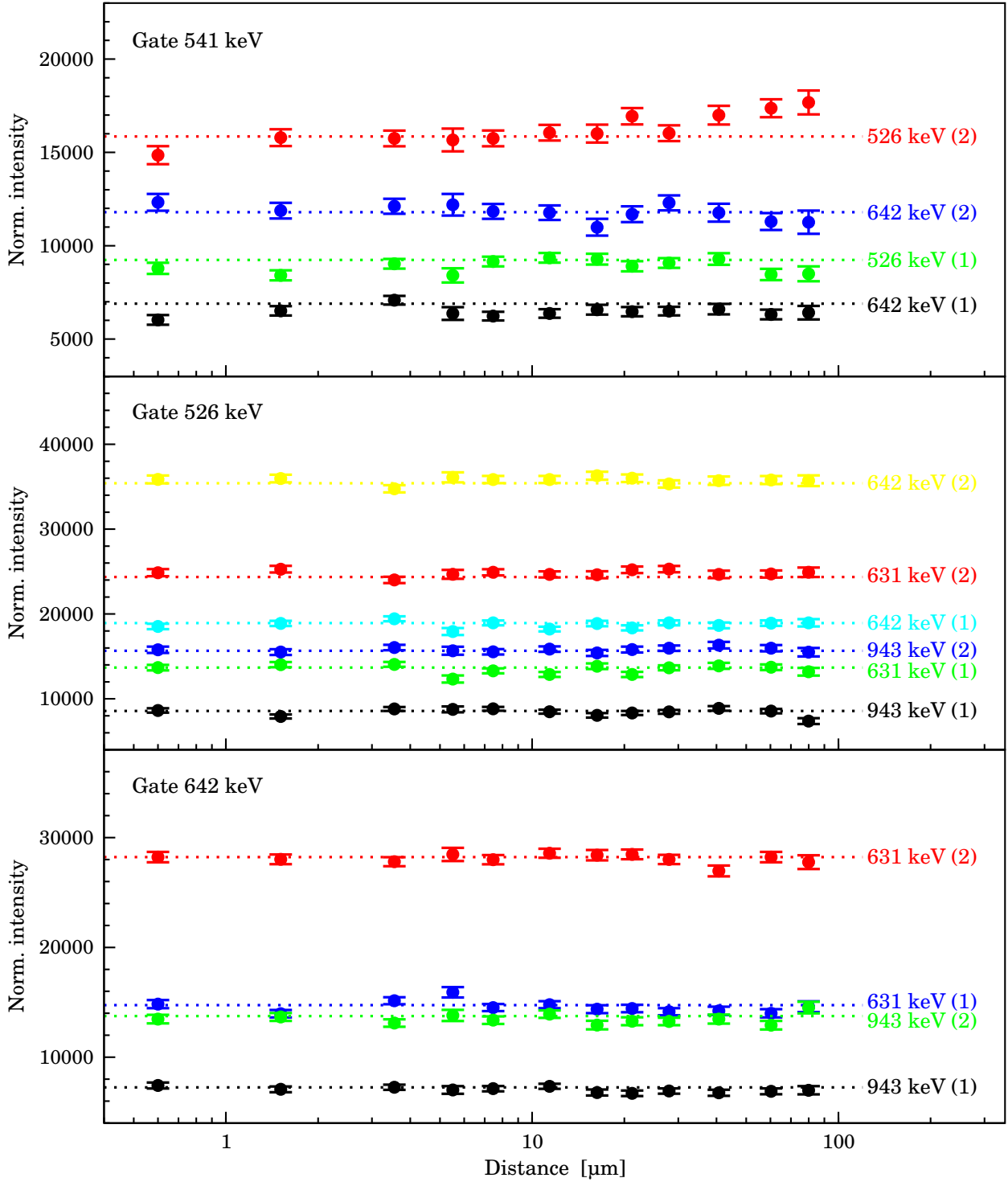


Figure 10.8: Normalized γ -ray intensities of coincident transitions in ^{56}Mn . The detectors used for the cut-spectra and yield measurements are indicated by their ring-ID (in brackets). The dotted line is the average value. Thus, the weighted mean of the independently measured normalization factors reproduces very well constant γ -ray yields for all target-to-stopper distances. More information is given in the text.

Chapter 11

Results

The results of the precise lifetime measurement of excited states in ^{56}Cr performed with the Cologne coincidence plunger will be presented in this chapter. Lifetimes of the first excited 2^+ and 4^+ states were deduced for the first time, employing the differential decay curve method (DDCM) to data of a coincidence recoil distance Doppler-shift (RDDS) measurement.

The experiment was carried out at the FN tandem accelerator of the Institute for Nuclear Physics of the University of Cologne, employing a stable ^{11}B beam at an energy of 32 MeV, incident on a 0.5 mg/cm^2 thick enriched ^{48}Ca target. The relevant fusion evaporation reaction channel $^{48}\text{Ca}(^{11}\text{B}, \text{p}2\text{n})^{56}\text{Cr}$ was populated rather weakly yielding almost 2.6% of the total reaction cross section of about $\sigma_{\text{fusion}} = 1.02 \text{ b}$. Other residual nuclei, such as ^{55}Mn and ^{56}Mn in the 4n and 3n channel, respectively, were produced much more numerously, as shown in Table 11.1. De-excitation of the odd-Z manganese isotopes proceeds by a large number of γ -ray cascades, which appeared as

nucleus	channel	σ [mb]	$\sigma/\sigma_{\text{fusion}}$ [%]
^{55}Mn	4n	472	46.3
^{56}Mn	3n	412	40.4
^{53}V	$\alpha 2\text{n}$	74	7.3
^{56}Cr	$\text{p}2\text{n}$	26	2.6
^{57}Mn	2n	11	1.1
^{55}Cr	$\text{p}3\text{n}$	10	1.0
^{54}V	αn	6	0.6
^{52}V	$\alpha 3\text{n}$	5	0.5

Table 11.1: Absolute and relative production yields of residual nuclei in the $^{48}\text{Ca}(^{11}\text{B}, \text{xpy})\text{X}$ reaction at a beam energy of 32 MeV. The values were calculated using the code PACE [175].

strong decay-transitions in the measured spectra. Moreover, in an plunger measurement the line density is almost doubled due to the observed Doppler-shifted and unshifted components of the transitions. Hence, the relevant transitions of ^{56}Cr were partly superimposed by γ -ray transitions of background reactions. To obtain almost clear spectra, $\gamma\gamma$ -coincidence information was required (see Figure 11.1 (a-c)). Despite the rather weak population of the $\text{p}2\text{n}$ -channel, the DDC method could be applied to $\gamma\gamma$ -coincidence data. To determine the lifetime of a state and to avoid systematic errors applying the DDC method it is crucial to generate cut spectra which are locally clean, i.e. the transition of interest must not be interfered with by any γ -ray transition of a background reaction. Due to the occurrence of doublets even in the gated spectra, not all possible gates and matrices generated from the different ring combinations could be used for the lifetime analysis.

For each target-to-stopper distance x_i the data were sorted into $\gamma\gamma$ -matrices corresponding to all possible ring combinations (cf. Sec. 10.1). For j different matrices the corresponding lifetimes τ_j were determined as mean value of the $\tau(x_i)$; they are statistically independent and allow for consistency checks. The weighted mean value of the independent lifetimes τ_j was finally taken as the adopted level lifetime τ .

Effects due to the deorientation of the recoiling nuclei in vacuum do not enter the DDCM analysis of a coincidence RDDS measurement as gates are set on feeding transitions of the level of interest [184]. Effects of the Doppler-shift attenuation occurring during the slowing down in the stopper account for a correction factor of less than 0.5% at a lifetime value of 2.6 ps [182]. Thus, they can be safely neglected for $\tau > 3 \text{ ps}$.

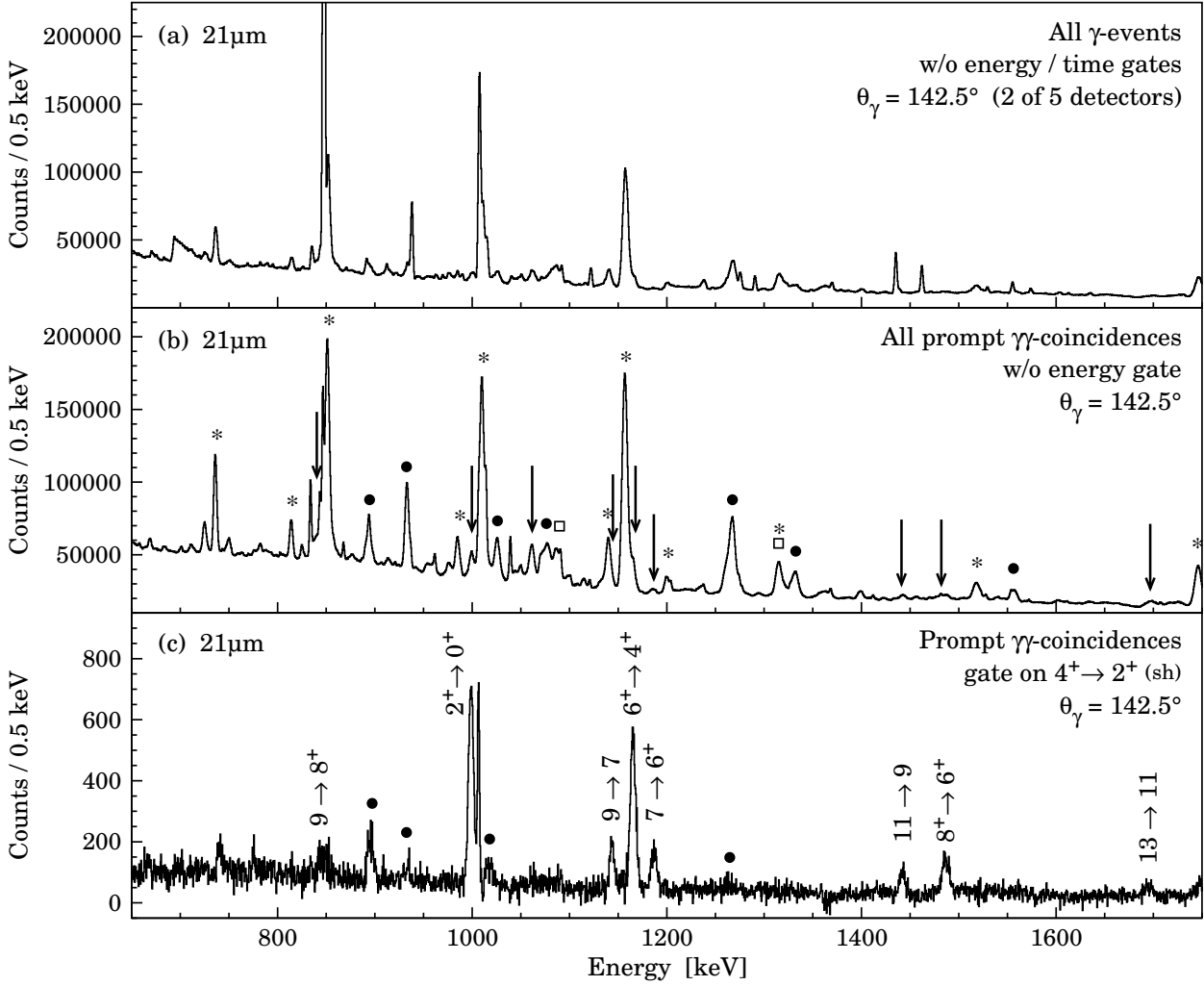


Figure 11.1: γ -ray spectra obtained during the lifetime measurement of ^{56}Cr at a target-to-stopper distance of $21\ \mu\text{m}$. (a) All γ -ray events (singles) detected in two of the five Ge detectors at backward angle. (b) Prompt coincidence spectrum of γ rays emitted in backward direction, which were coincident to a γ -ray detected in the EUROBALL detectors at forward angle. Energies of Doppler-shifted transitions in ^{56}Cr are indicated by arrows. Transitions of other residual nuclei: \bullet ^{56}Mn , $*$ ^{55}Mn , \square ^{53}V . (c) Same as (b) but with a coincidence gate applied on the Doppler-shifted component of the $4^+ \rightarrow 2^+$ transition at $1070\ \text{keV}$ in ^{56}Cr . γ rays emitted in flight, de-exciting known states up to $J = 13$, can be observed in an almost clean spectrum. For the $2^+ \rightarrow 0^+$ transition both the Doppler-shifted and the unshifted component were detected.

11.1 Lifetime of the 2^+ state

DDCM lifetime analysis always commenced by selecting appropriate $\gamma\gamma$ -coincidence gates to obtain the intensities I_{sh} and I_{us} as a function of the target-to-stopper distance. For the lifetime analysis of the 2^+ state various gated spectra were carefully investigated for contaminating transitions, interfering with the Doppler-shifted and unshifted components of the depopulating $2^+ \rightarrow 0^+$ transition at $1007\ \text{keV}$. Cut spectra of most detectors showed a transition at $1015\ \text{keV}$ coming from Coulomb excitation of

^{27}Al in random coincidence. Therefore cut spectra measured with the EUROBALL detectors at forward angles could not be used in the lifetime analysis of the 2^+ state due to the interference of the ^{27}Al γ -ray transition with the Doppler-shifted $2^+ \rightarrow 0^+$ transition. The analysis was restricted to cut spectra obtained with the Ge detectors at backward angles. Fig. 11.2 illustrates the line shape analysis of the $2^+ \rightarrow 0^+$ transition at $1007\ \text{keV}$ in ^{56}Cr and shows examples of gated spectra for different target-to-stopper distances.

Three different types of coincidence gates

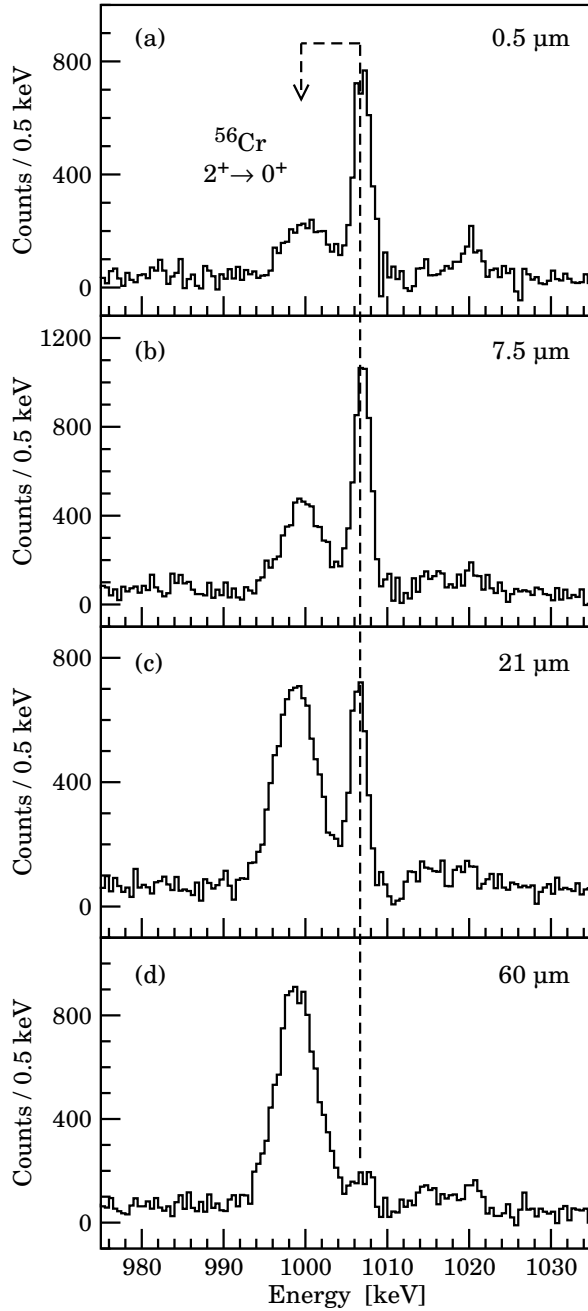


Figure 11.2: (a)-(d) Gated spectra for the $2^+ \rightarrow 0^+$ transition at 1007 keV in ^{56}Cr at the indicated distances from the five Ge detectors at backward angles. The gate was set on the shifted component of the $4^+ \rightarrow 2^+$ transition in ^{56}Cr , measured in the six EUROBALL Ge detectors at forward angles.

were used in the lifetime analysis of the 2^+ state, which will be discussed in the following. First of all a coincidence gate was applied on the Doppler-shifted component of the directly feeding transition, i.e. the $4^+ \rightarrow 2^+$ transition at 1070 keV. The intensities of the Doppler-

shifted (I_{sh}) and unshifted (I_{us}) components of the coincident depopulating $2^+ \rightarrow 0^+$ transition were determined in the corresponding cut spectra. The lifetime of the 2^+ state was deduced by the evolution of the measured intensities as a function of target-to-stopper distance according to the formulas given in Section 9.4.2, using the program “Napatau” [185]. The final τ curve is shown in Figure 11.3, yielding $\tau(2^+) = 5.49(15)$ ps.

Secondly the lifetime of the 2^+ was derived by gating on the Doppler-shifted component of the $6^+ \rightarrow 4^+$ transition at 1175 keV, indirectly feeding the 2^+ state via the $4^+ \rightarrow 2^+$ transition. The intensities of the Doppler-shifted and unshifted components of both the directly feeding $4^+ \rightarrow 2^+$ transition and the depopulating $2^+ \rightarrow 0^+$ transition had to be determined in the cut spectra. Following the analysis given in Section 9.4.2 the lifetime of the 2^+ level was measured as $\tau(2^+) = 5.48(50)$ ps (see Figure 11.4).

Another possibility to deduce the lifetime using the DDC method is to gate on the unshifted component of the depopulating 1007 keV transition and to analyze the evolution of I_{sh} and I_{us} of the directly feeding $4^+ \rightarrow 2^+$ transition at 1070 keV in the cut spectra (so-called “gate from below”). The corresponding τ curve is shown in Figure 11.5, yielding a consistent value of $\tau(2^+) = 5.49(12)$ ps for the lifetime of the 2^+ state in ^{56}Cr .

The weighted mean value of the three independently determined lifetimes was finally taken as the adopted level lifetime $\tau(2^+)_{\text{mean}} = 5.49(14)$ ps.

11.2 Lifetime of the 4^+ state

$\gamma\gamma$ -coincidence gates for the lifetime analysis of the 4^+ state in ^{56}Cr were much less affected by interfering background transitions than for the 2^+ state. Thus, all possible gates and ring combinations could be used in the analysis. The corresponding τ curves are given in Fig. 11.6-11.12 together with the quantities which were used to calculate the $\tau(x)$ values.

Gating on the Doppler-shifted component of the directly feeding $6^+ \rightarrow 4^+$ transition at 1175 keV yielded lifetime values of 2.81(23) ps

level	gate type	gated transition	θ_γ [°]	τ [ps]
2^+	direct	$4^+ \rightarrow 2^+$ (sh)	142.5	5.49(15)
	indirect	$6^+ \rightarrow 4^+$ (sh)	142.5	5.48(50)
	below	$2^+ \rightarrow 0^+$ (us)	142.5	5.49(12)
	weighted mean			5.49(14)
4^+	direct	$6^+ \rightarrow 4^+$ (sh)	27.4	2.81(23)
	direct	$6^+ \rightarrow 4^+$ (sh)	142.5	3.11(19)
	indirect	$7 \rightarrow 6^+$ (sh)	27.4	4.2(15)
	indirect	$7 \rightarrow 6^+$ (sh)	142.5	2.89(81)
	indirect	$8^+ \rightarrow 6^+$ (sh)	142.5	3.78(54)
	below	$4^+ \rightarrow 2^+$ (us)	27.4	3.39(19)
	below	$4^+ \rightarrow 2^+$ (us)	142.5	3.18(15)
	weighted mean			3.15(11)

Table 11.2: Deduced lifetimes of the 2^+ and 4^+ state of ^{56}Cr , employing the DDC method on $\gamma\gamma$ -coincidence data obtained with different coincidence gates. Gates on the Doppler-shifted component of the (in)directly feeding transitions are labeled “(in)direct”, while gates on the unshifted component of the depopulating transition are named “below”. More information is given in the text.

and 3.11(19) ps, measured at forward and backward angles, respectively, while $\tau = 4.2(15)$ ps and 2.89(81) ps were obtained applying a coincidence gate on the indirectly feeding $7 \rightarrow 6^+$ transition at 1196 keV. Another coincidence gate on the Doppler-shifted component of the indirectly feeding $8^+ \rightarrow 6^+$ transition at 1501 keV provided a lifetime value of 3.78(54)ps. By applying a gate on the unshifted component of the depopulating 1070 keV transition consistent τ values of 3.39(19) ps and 3.18(15) ps were measured at forward and backward angles, respectively.

All lifetime values deduced from the present data are summarized in Table 11.2. The weighted mean value of all independently determined lifetimes of the 4^+ state was finally taken as the adopted level lifetime $\tau(4^+)_{\text{mean}} = 3.15(11)$ ps.

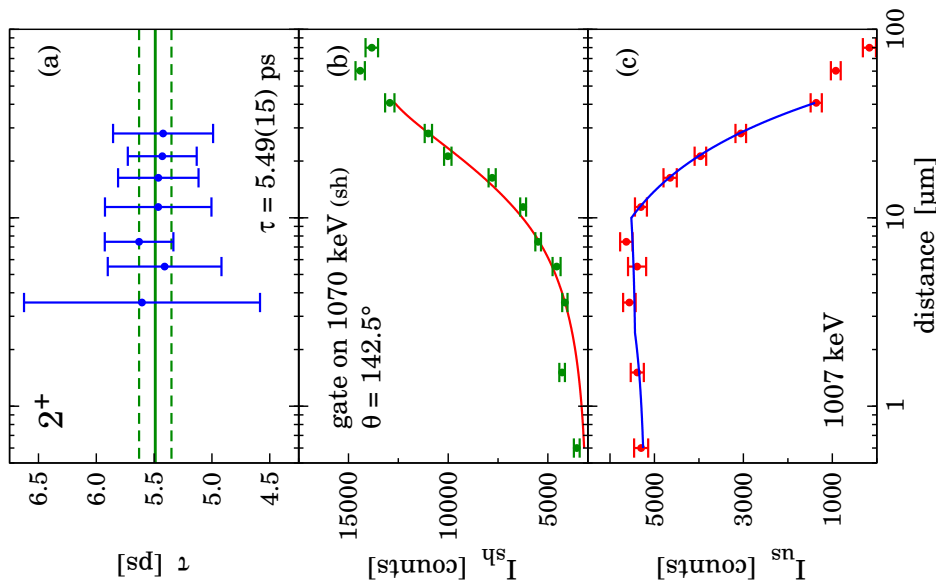


Figure 11.3: (a) Lifetime values τ as a function of target-to-stopper distance for the $2^+ \rightarrow 0^+$ transition at 1070 keV in ^{56}Cr , determined by using a coincidence gate on the Doppler-shifted component of the directly feeding transition at 1070 keV. The intensity curves of (b) the Doppler-shifted and (c) the unshifted components measured at backward angles are also shown.

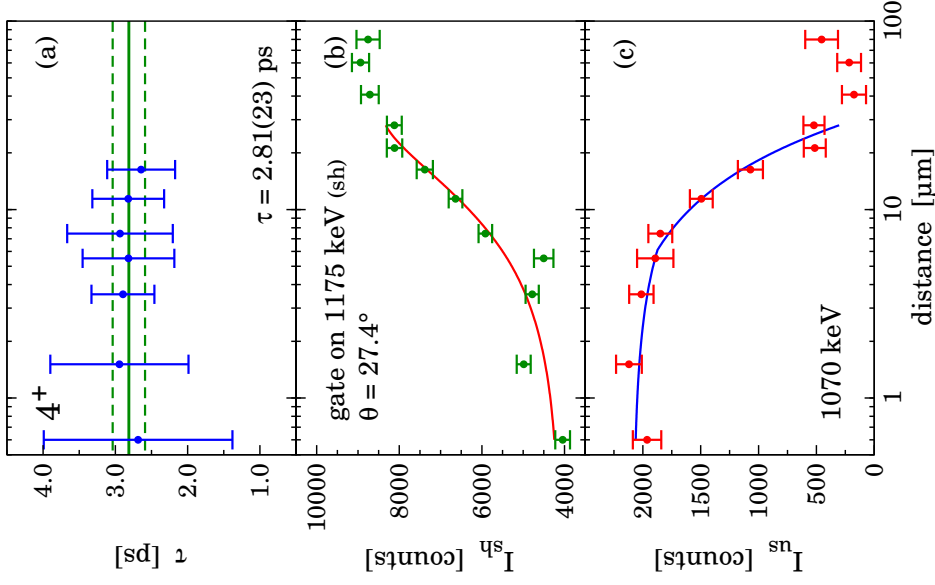


Figure 11.6: (a) Lifetime values τ as a function of target-to-stopper distance for the $4^+ \rightarrow 2^+$ transition at 1070 keV in ^{56}Cr , determined by using a coincidence gate on the Doppler-shifted component of the directly feeding transition at 1175 keV. The intensity curves of (b) the Doppler-shifted and (c) the unshifted components measured at forward angles are also shown.

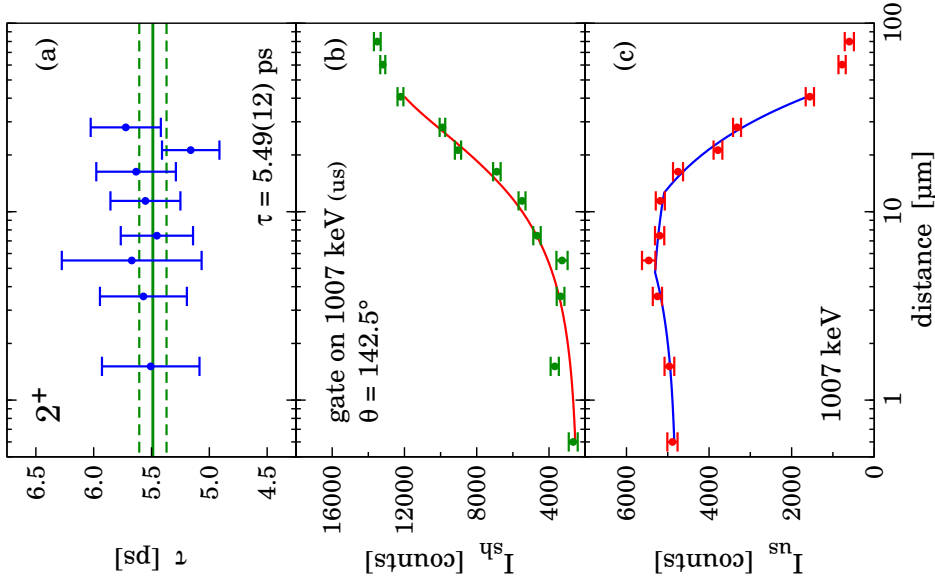


Figure 11.5: (a) Lifetime values τ as a function of target-to-stopper distance for the $2^+ \rightarrow 0^+$ transition at 1007 keV in ^{56}Cr , determined by using a coincidence gate on the Doppler-shifted component of the depopulating transition at 1007 keV. The intensity curves of (b) the Doppler-shifted and (c) the unshifted components measured at backward angles are also shown.

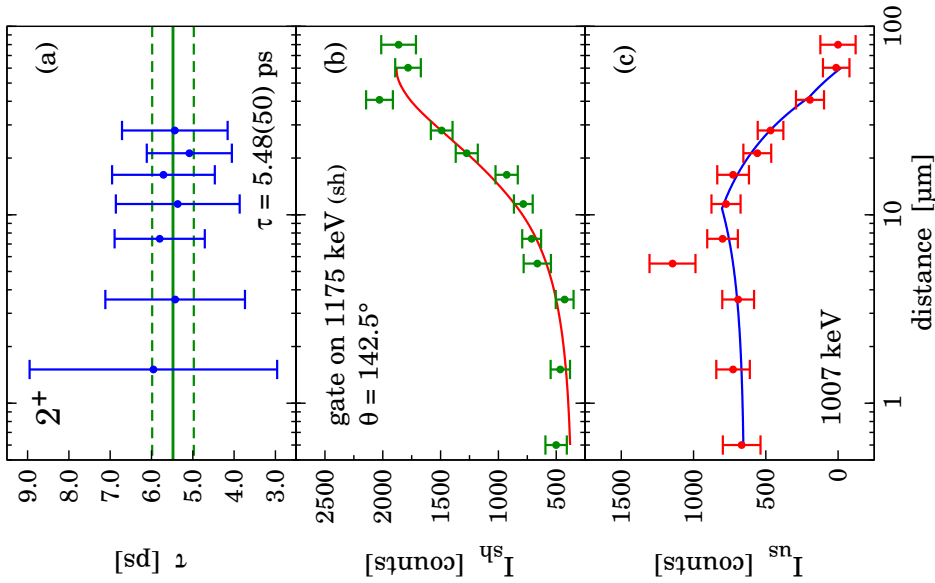


Figure 11.4: (a) Lifetime values τ as a function of target-to-stopper distance for the $2^+ \rightarrow 0^+$ transition at 1007 keV in ^{56}Cr , determined by using a coincidence gate on the Doppler-shifted component of the indirectly feeding transition at 1175 keV. The intensity curves of (b) the Doppler-shifted and (c) the unshifted components measured at backward angles are also shown.

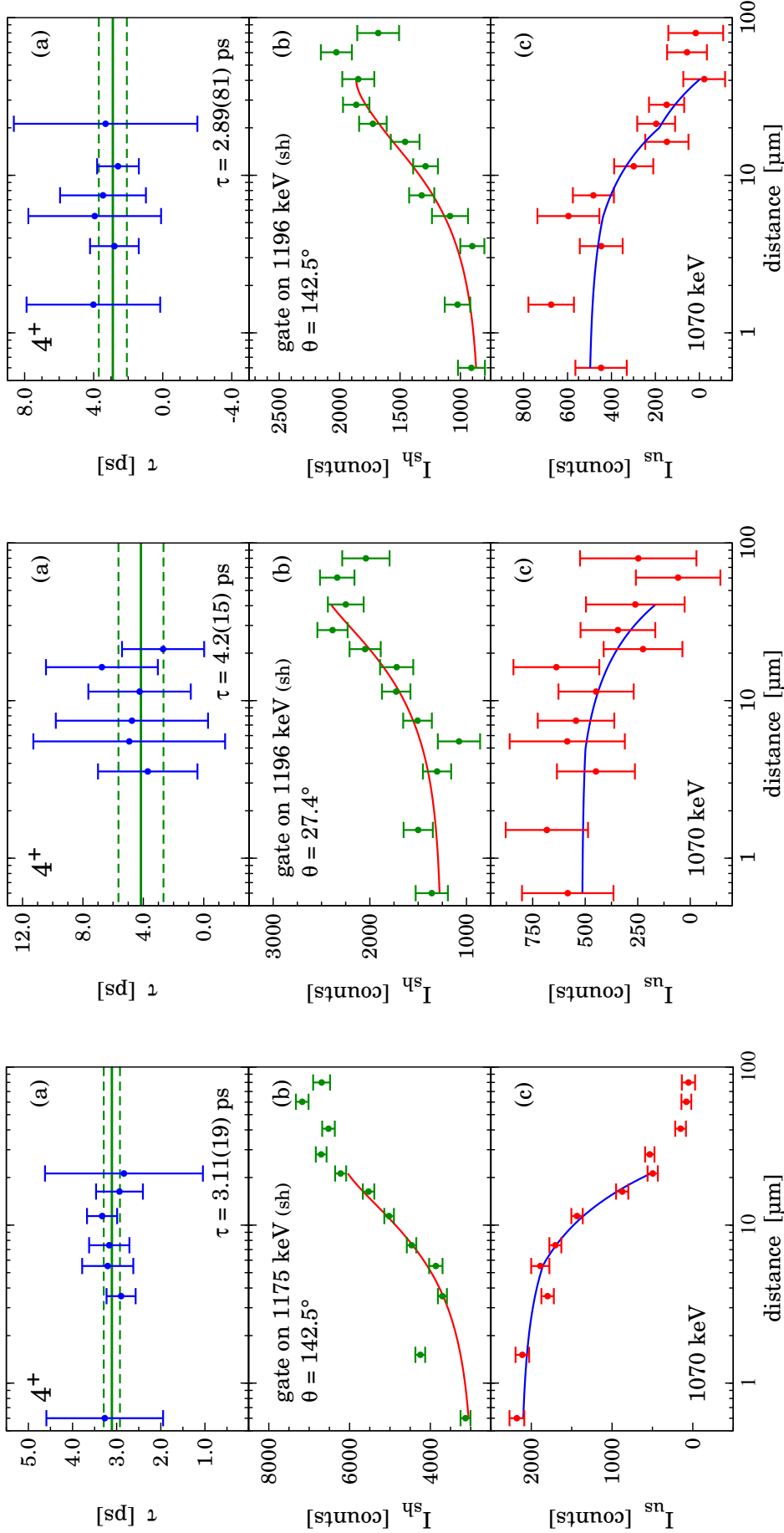


Figure 11.9: (a) Lifetime values τ as a function of target-to-stopper distance for the $4^+ \rightarrow 2^+$ transition at 1070 keV in ^{56}Cr ; determined by using a coincidence gate on the Doppler-shifted component of the indirectly feeding transition at 1196 keV. The intensity curves of (b) the Doppler-shifted and (c) the unshifted components measured at backward angles are also shown.

Figure 11.8: (a) Lifetime values τ as a function of target-to-stopper distance for the $4^+ \rightarrow 2^+$ transition at 1070 keV in ^{56}Cr ; determined by using a coincidence gate on the Doppler-shifted component of the indirectly feeding transition at 1196 keV. The intensity curves of (b) the Doppler-shifted and (c) the unshifted components measured at forward angles are also shown.

Figure 11.7: (a) Lifetime values τ as a function of target-to-stopper distance for the $4^+ \rightarrow 2^+$ transition at 1070 keV in ^{56}Cr ; determined by using a coincidence gate on the Doppler-shifted component of the directly feeding transition at 1175 keV. The intensity curves of (b) the Doppler-shifted and (c) the unshifted components measured at backward angles are also shown.

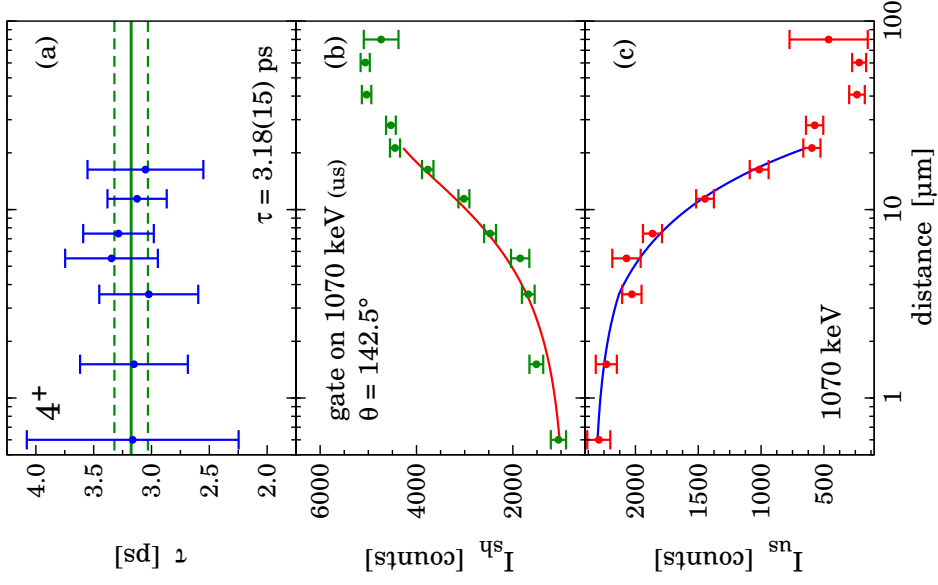


Figure 11.12: (a) Lifetime values τ as a function of target-to-stopper distance for the $4^+ \rightarrow 2^+$ transition at 1070 keV in ^{56}Cr , determined by using a coincidence gate on the unshifted component of the depopulating transition at 1070 keV. The intensity curves of (b) the Doppler-shifted and (c) the unshifted components measured at backward angles are also shown.

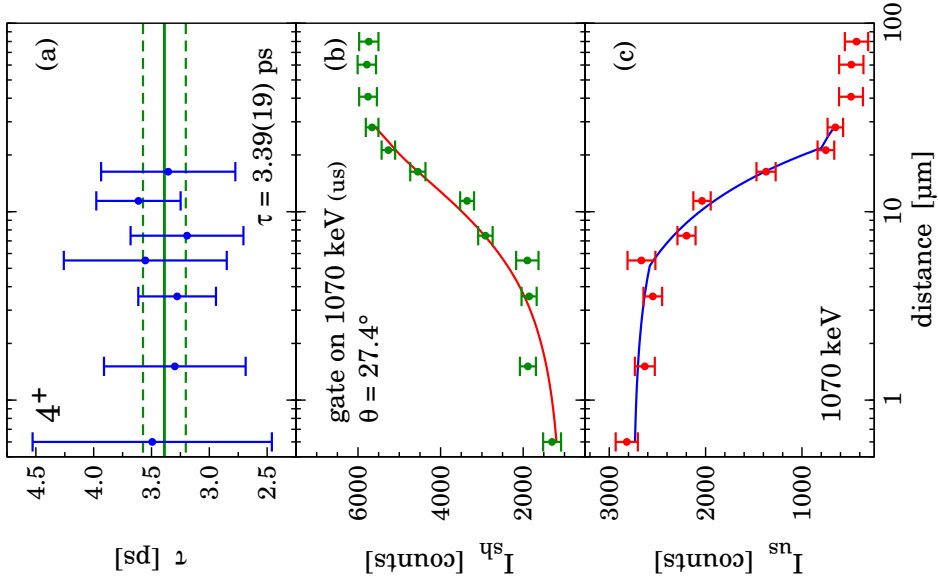


Figure 11.11: (a) Lifetime values τ as a function of target-to-stopper distance for the $4^+ \rightarrow 2^+$ transition at 1070 keV in ^{56}Cr , determined by using a coincidence gate on the Doppler-shifted component of the depopulating transition at 1070 keV. The intensity curves of (b) the Doppler-shifted and (c) the unshifted components measured at forward angles are also shown.

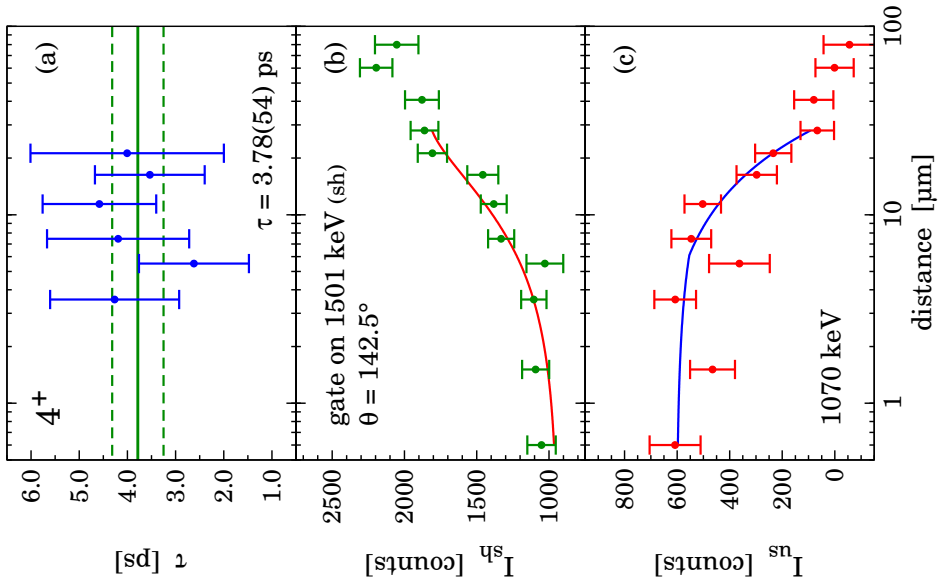


Figure 11.10: (a) Lifetime values τ as a function of target-to-stopper distance for the $4^+ \rightarrow 2^+$ transition at 1070 keV in ^{56}Cr , determined by using a coincidence gate on the Doppler-shifted component of the indirectly feeding transition at 1501 keV. The intensity curves of (b) the Doppler-shifted and (c) the unshifted components measured at backward angles are also shown.

Chapter 12

Discussion and Summary

12.1 Shell-model theory and discussion

The measured lifetime value $\tau = 5.49(14)$ ps for the first 2^+ state in ^{56}Cr corresponds to $B(E2, 2^+ \rightarrow 0^+) = 11.33(31)$ W.u.. For the $4^+ \rightarrow 2^+$ transition the precise lifetime value of $\tau = 3.15(11)$ ps would correspond to $B(E2, 4^+ \rightarrow 2^+) = 14.59(53)$ W.u. for the 4^+ state. Within errors the new and precise $B(E2, 2^+ \rightarrow 0^+)$ value is consistent with the previous result of $B(E2, 2^+ \rightarrow 0^+) = 8.7(3.0)$ W.u. from [170]. Together with the value of $B(E2, 2^+ \rightarrow 0^+) = 14.6(6)$ W.u. for ^{54}Cr [186], a considerable reduction of transition strength is observed going from $N = 30$ to $N = 32$, which is in line with the increase in $E(2^+)$. In comparison with the semimagic $N = 28$ value of $B(E2, 2^+ \rightarrow 0^+) = 11.4(5)$ W.u. for ^{52}Cr [187], an equally low result is observed for the $N = 32$ case. The accuracy of the experimental result for ^{58}Cr of $B(E2, 2^+ \rightarrow 0^+) = 14.8(4.2)$ W.u. from Ref. [170] allows only a coarse extrapolation to $N = 34$. The $B(E2, 4^+ \rightarrow 2^+)$ shows the same isotopic trend, it is smaller than in ^{54}Cr (29(6) W.u. [186]) but larger than in the semimagic ^{52}Cr (6.0(1.6) W.u. [187]). In the latter case the seniority $\nu = 2$ conserving transition $4_2^+ \rightarrow 2^+$ was chosen for comparison, as it corresponds to the $4_1^+ \rightarrow 2^+$ transitions in the isotones ^{50}Ti (proton $2p$) and ^{54}Fe (proton $2h$) which are $\nu = 2$ by definition.

These results were compared with large-scale shell-model calculations using different effective interactions in the pf shell: KB3G [159], KB3G^m [188], and the GXPF1A [155] interactions. The KB3G^m interaction was obtained by a readjustment of the KB3G monopoles. $B(E2)$

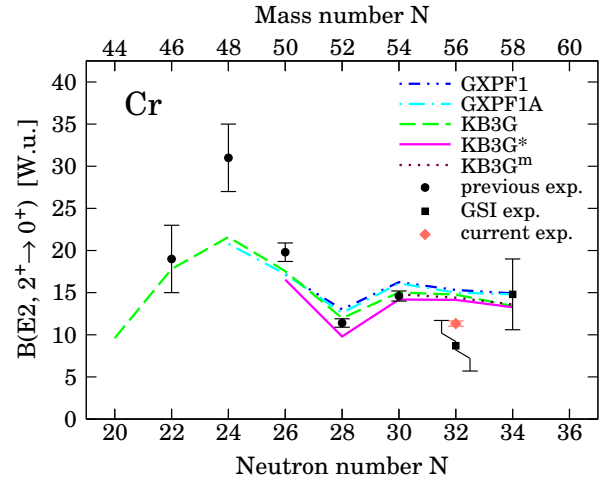


Figure 12.1: Calculated (from Ref. [155, 159, 160]) and experimental $B(E2, 2_1^+ \rightarrow 0^+)$ values (from Ref. [170, 186, 187] and this work) for Cr isotopes.

values were calculated with equal (isoscalar) polarization charges for protons and neutrons $\delta e_p = \delta e_n = 0.5e$. Although all the interactions reproduce the increase in the excitation energy of the 2^+ at $N = 32$, none of the results obtained reproduces the corresponding lowering of the $B(E2)$ value for ^{56}Cr . On the contrary, the calculations show a slight monotonic decrease in $B(E2)$ strength along the $^{54,56,58}\text{Cr}$ isotopic chain. The effective interactions that better describe both the excitation energies and the $B(E2)$ values are KB3G^m and GXPF1A. These results are reported in Figure 12.1 in comparison with the experimental values.

As stated above, in Ref. [173], it was shown that the use of different effective charges for protons and neutrons, $e_p = 1.15e$ and $e_n = 0.80e$, could reproduce a marginal staggering of the $B(E2, 2^+ \rightarrow 0^+)$ values along the chain of even-even $^{48-56}\text{Ti}$ isotopes (see Figure 8.2 on

	Spin I	exp.	GXPF1A	KB3G	KB3G ^m	GXPF1A [*]	KB3G [*]	KB3G ^{m*}
⁵⁴ Cr	2 ⁺	14.6(6) [186]	16.4	15.1	14.8	15.7	14.8	14.6
	4 ⁺	29(6) [186]	21.5	19.0	18.5	20.5	18.2	17.6
⁵⁶ Cr	2 ⁺	11.33(31)	15.2	14.7	14.4	14.5	15.2	14.6
	4 ⁺	14.59(53)	19.5	20.4	18.7	19.2	20.8	18.6
	6 ⁺		14.0	19.0				
⁵⁸ Cr	2 ⁺	14.8(4.2) [170]	15.1	13.4	13.6	14.9	13.9	13.7
	4 ⁺		18.1	15.0	14.7	16.9	15.3	14.7

Table 12.1: Experimental and calculated $B(E2, I \rightarrow I-2)$ values (in W.u.) for ^{54,56,58}Cr. Shell-model calculations with a different set of effective polarization charges ($e_p = 1.15e$, $e_n = 0.8e$) are designated by a superscripted asterisk.

page 86). These effective charges, deduced from the $T = 1/2$ mirror nuclei of mass $A = 51$ [172], result from an additional isovector polarization charge. In fact, the trend of the $B(E2)$ values in the Ti chain is correct, but the calculated values are still far from the experimental ones. Recently, it was shown that these effective charges do not reproduce the $B(E2)$ values measured in the neutron-rich nuclei ⁵⁰Ca and ⁵¹Sc [27]. For this work the $B(E2)$ values were computed for the Cr isotopes using these effective charges with the different effective interactions. The results are listed in Table 12.1 and denoted by a superscript asterisk. In all cases, the $B(E2)$ strengths remain almost unchanged; the differences amount to just a fraction of a W.u.. It is only with the GXPF1A interaction that the use of these effective charges gives a slight, relative reduction of the $B(E2)$ in ⁵⁶Cr with respect to ^{54,58}Cr but remaining still far from the experiment.

A dedicated shell-model study of neutron-rich Cr nuclei was performed recently by Kaneko *et al.* in the fpg model space [163]. This valence space comprises the full pf active proton orbitals and the $\nu p_{3/2}$, $\nu f_{5/2}$, $\nu p_{1/2}$, and $\nu g_{9/2}$ neutron orbitals. The schematic pairing-plus-multipole interaction was developed to reproduce the available data in neutron-rich Cr isotopes. For calculation of the $B(E2)$ values, standard polarization charges $\delta e_p = \delta e_n = 0.5e$ were used. Although a small relative decrease in the transition strength is obtained at $N = 32$, these calculations do not reproduce the experimental energies and $B(E2)$ of ^{56,58}Cr. Increasing $B(E2)$ values are predicted for heavier Cr nuclei until a drastic drop at $N = 46$.

The recently developed LNPS interaction describes with good accuracy the level schemes of Cr and Fe isotopes around $N = 40$ [162]. It has been applied with success to the description of recent data on lifetimes in heavy Fe isotopes [189]. The model space includes the full fp orbitals for protons and the $\nu p_{3/2}$, $\nu f_{5/2}$, $\nu p_{1/2}$, $\nu g_{9/2}$, and $\nu d_{5/2}$ shells for neutrons. This new effective interaction accounts for the development of strong quadrupole correlations that drive the Cr and Fe isotopes to large deformation towards $N = 40$. The adopted ⁴⁸Ca core in these calculations – as well as in those of Kaneko *et al.* [163] – prevents the excitation of neutrons from the $\nu f_{7/2}$ shell. While this is sensible for heavy Cr isotopes around $N = 40$, its influence in the description of the spectroscopy of lighter isotopes increases with decreasing neutron number, in particular, for ⁵⁶Cr.

The evolution of the $4^+ \rightarrow 2^+$ transition strength from $N = 28$ to $N = 32$ shows the expected increase for $N = 30$ owing to seniority mixing by proton-neutron interaction, followed by an unexpected decrease for $N = 32$. This corroborates the $B(E2, 2^+ \rightarrow 0^+)$ trend and is likewise not borne out by the shell-model results (see Table 12.1).

12.2 Summary

In summary, the decrease in $B(E2)$ values for both the 2^+ and 4^+ states in ⁵⁶Cr, and therefore their staggering from $N = 28$ to $N = 32$, is now firmly established by several standard deviations. This and the corresponding opposite trend in $E_x(2^+)$ are consistent with the obser-

vation in Ti isotopes (see Figure 8.2) and in open-shell nuclei with the Grodzins-Raman systematics [25, 190]. Despite the large difference in $E_x(2^+)$, the $B(E2)$ values in Ti and the mid-proton-shell Cr isotopes are almost identical for $N = 28$ and $N = 30$. The staggering amplitudes as defined by

$$A_{\text{st}} = B(E2)_{N=30} - \frac{B(E2)_{N=28} + B(E2)_{N=32}}{2}$$

agree in both chains within experimental uncertainties, namely, $A_{\text{st}}(\text{Ti}) = 4.2(11)$ W.u. and $A_{\text{st}}(\text{Cr}) = 3.8(6)$ W.u.. The available shell-model approaches using various interactions and/or effective charges account for the global trend of $E_x(2^+)$ and $B(E2)$ but fail to reproduce the local staggering, which, on the other hand, indicates an $N = 32$ subshell. The theoretical $B(E2)$ values in the Ca, Ti and Cr isotopic chains beyond $N = 28$ show a smooth and unstructured trend (see Figures 8.2 and 12.1). From this evidence one may conclude that the reason for the failure of the theoretical approaches lies in the neutron channel and is caused by either $T = 1$ monopoles or an imbalance in the pairing and quadrupole part of the neutron-neutron two-body matrix elements. In the former case, from the disappearance of the staggering in the Fe isotopes it can be concluded that $T = 1$ monopoles involving $\nu f_{5/2}$ orbit need retuning, as this changes position dramatically from $Z = 20$ to $Z = 28$ owing to the filling of the $\pi f_{7/2}$ shell. Core excitations of protons across the $Z = 20$ gap are unlikely to cause the observed effect beyond the Ca isotopes. The increase in the transition probabilities for heavier Cr isotopes predicted by the recent theoretical works will have to wait for the measurement of transition probabilities by means of radioactive beams.

Bibliography

- [1] W.M. Elsasser, *J. Phys. Radium* **5**, 635-639 (1934).
- [2] O. Haxel, J.H.D. Jensen, and H.E. Suess, *Phys. Rev.* **75**, 1766 (1949).
- [3] M. Goeppert-Mayer, *Phys. Rev.* **75**, 1969-1970 (1949).
- [4] K.L.G. Heyde, "The Nuclear Shell Model", Springer-Verlag, Berlin Heidelberg (1990).
- [5] T. Otsuka, R. Fujimoto, Y. Utsuno, B.A. Brown, M. Honma, and T. Mizusaki, *Phys. Rev. Lett.* **87**, 082502 (2001).
- [6] T. Otsuka, Y. Utsuno, R. Fujimoto, B.A. Brown, M. Honma, and T. Mizusaki, *Eur. Phys. J. A* **13**, 69-74 (2002).
- [7] T. Otsuka, Y. Utsuno, R. Fujimoto, B.A. Brown, M. Honma, and T. Mizusaki, *Eur. Phys. J. A* **15**, 151-155 (2002).
- [8] R. Kanungo, C. Nociforo, A. Prochazka, T. Aumann, D. Boutin, D. Cortina-Gil, B. Davids, M. Diakaki, F. Farinon, H. Geissel, R. Gernhäuser, J. Gerl, R. Janik, B. Jonson, B. Kindler, R. Knöbel, R. Krücken, M. Lantz, H. Lenske, Y. Litvinov, B. Lommel, K. Mahata, P. Maierbeck, A. Musumarra, T. Nilsson, T. Otsuka, C. Perro, C. Scheidenberger, B. Sitar, P. Strmen, B. Sun, I. Szarka, I. Tanihata, Y. Utsuno, H. Weick, and M. Winkler, *Phys. Rev. Lett.* **102**, 152501 (2009).
- [9] K.-L. Kratz, J.-P. Bitouzet, F.-K. Thielemann, P. Möller, and B. Pfeiffer, *Astrophys. J.* **403**, 216-238 (1993).
- [10] P. Cottle, *Nature (London)* **465**, 430-431 (2010).
- [11] C. Sneden and J.J. Cowan, *Science* **299**, 70-75 (2003).
- [12] T. Kautzsch, W.B. Walters, M. Hannawald, K.-L. Kratz, V.I. Mishin, V.N. Fedoseyev, W. Böhmer, Y. Jading, P. Van Duppen, B. Pfeiffer, A. Wöhr, P. Möller, I. Klökl, V. Sebastian, U. Köster, M. Koizumi, J. Lettry, and H.L. Ravn, *Eur. Phys. J. A* **9**, 201-206 (2000).
- [13] I. Dillmann, K.-L. Kratz, A. Wöhr, O. Arndt, B.A. Brown, P. Hoff, M. Hjorth-Jensen, U. Köster, A.N. Ostrowski, B. Pfeiffer, D. Seweryniak, J. Shergur, and W.B. Walters, *Phys. Rev. Lett.* **91**, 162503 (2003).
- [14] B. Pfeiffer, K.-L. Kratz, and F.-K. Thielemann, *Z. Phys. A* **357**, 235-238 (1997).
- [15] M. Moinester, J.P. Schiffer, and W.P. Alford, *Phys. Rev.* **179**, 984-995 (1969).
- [16] O. Sorlin and M.-G. Porquet, *Prog. Part. Nucl. Phys.* **61**, 602-673 (2008).
- [17] T. Otsuka, M. Honma, and D. Abe, *Nucl. Phys. A* **788**, 3c-11c (2007).
- [18] G. Audi, A.H. Wapstra, and C. Thibault, *Nucl. Phys. A* **729**, 337-676 (2003).
- [19] N.J. Stone, *At. Data Nucl. Data Tables* **90**, 75-176 (2005).
- [20] B.A. Brown and B.H. Wildenthal, *Nucl. Phys. A* **474**, 290-306 (1987).
- [21] D. Borremans, S. Teughels, N.A. Smirnova, D.L. Balabanski, N. Coulier, J.-M. Daugas, F. de Oliveira Santos, G. Georgiev, M. Lewitowicz, I. Matea, Yu.E. Penionzhkevich, W.-D. Schmidt-Ott, Yu. Sobolev, M. Stanoiu, K. Vyvey, and G. Neyens, *Phys. Lett. B* **537**, 45-50 (2002).
- [22] P. Himpe, G. Neyens, D.L. Balabanski, G. Bélier, D. Borremans, J.M. Daugas, F. de Oliveira Santos, M. De Rydt, K. Flanagan, G. Georgiev, M. Kowalska, S. Mallion, I. Matea, P. Morel, Yu.E. Penionzhkevich, N.A. Smirnova, C. Stodel, K. Turzó, N. Vermeulen, and D. Yordanov, *Phys. Lett. B* **643**, 257-262 (2006).
- [23] R.F. Casten, "Nuclear Structure from a Simple Perspective", Oxford University Press, New York Oxford (1990).
- [24] W.D. Hamilton, "The Electromagnetic Interaction in Nuclear Spectroscopy", North-Holland Publishing Company, Amsterdam Oxford (1975).
- [25] S. Raman, C.W. Nestor, Jr., and P. Tikkanen, *At. Data Nucl. Data Tables* **78**, 1-128 (2001).
- [26] P. Doornenbal, P. Reiter, H. Grawe, T. Otsuka, A. Al-Khatib, A. Banu, T. Beck, F. Becker, P. Bednarczyk, G. Benzoni, A. Bracco, A. Bürger, L. Caceres, F. Camera, S. Chmel, F.C.L. Crespi, H. Geissel, J. Gerl, M. Górská, J. Grębosz, H. Hübel, M. Kavatsyuk, O. Kavatsyuk, M. Kmiecik, I. Kojouharov, N. Kurz, R. Lozeva, A. Maj, S. Mandal, W. Meczynski, B. Million, Zs. Podolyák, A. Richard, N. Saito, T. Saito, H. Schaffner, M. Seidlitz, T. Striepling, Y. Utsuno, J. Walker, N. Warr, H. Weick, O. Wieland, M. Winkler, and H.J. Wollersheim, *Phys. Lett. B* **647**, 237-242 (2007).
- [27] J.J. Valiente-Dobón, D. Mengoni, A. Gadea, E. Farnea, S.M. Lenzi, S. Lunardi, A. Dewald, Th. Pissulla, S. Szilner, R. Broda, F. Recchia, A. Algora, L. Angus, D. Bazzacco, G. Benzoni, P.G. Bizzeti, A.M. Bizzeti-Sona, P. Boutachkov, L. Corradi, F. Crespi, G. de Angelis, E. Fioretto, A. Gorgen, A. Gorska, A. Gottardo, E. Grodner, B. Guiot, A. Howard, W. Królas, S. Leoni, P. Mason,

- R. Menegazzo, D. Montanari, G. Montagnoli, D.R. Napoli, A. Obertelli, T. Pawlat, G. Pollaro, B. Rubio, E. Şahin, F. Scarlassara, R. Silvestri, A.M. Stefanini, J.F. Smith, D. Steppenbeck, C.A. Ur, P.T. Wady, J. Wrzesiński, E. Maglione, and I. Hamamoto, *Phys. Rev. Lett.* **102**, 242502 (2009).
- [28] C. Thibault, R. Klapisch, C. Rigaud, A.M. Poskanzer, R. Prieels, L. Lessard, and W. Reisdorf, *Phys. Rev. C* **12**, 644-657 (1975).
- [29] X. Campi, H. Flocard, A.K. Kerman, and S. Koonin, *Nucl. Phys. A* **251**, 193-205 (1975).
- [30] G. Huber, F. Touchard, S. Büttgenbach, C. Thibault, R. Klapisch, H.T. Duong, S. Liberman, J. Pinard, J.L. Vialle, P. Juncar, and P. Jacquinet, *Phys. Rev. C* **18**, 2342-2354 (1978).
- [31] C. Détraz, D. Guillemaud, G. Huber, R. Klapisch, M. Langevin, F. Naulin, C. Thibault, L.C. Carraz, and F. Touchard, *Phys. Rev. C* **19**, 164-176 (1979).
- [32] D. Guillemaud-Mueller, C. Détraz, M. Langevin, F. Naulin, M. de Saint-Simon, C. Thibault, F. Touchard, and M. Epherre, *Nucl. Phys. A* **426**, 37-76 (1984).
- [33] E.K. Warburton, J.A. Becker, and B.A. Brown, *Phys. Rev. C* **41**, 1147-1166 (1990).
- [34] T. Otsuka, T. Suzuki, R. Fujimoto, H. Grawe, Y. Akaishi, *Phys. Rev. Lett.* **95**, 232502 (2005).
- [35] Y. Utsuno, T. Otsuka, T. Mizusaki, and M. Honma, *Phys. Rev. C* **60**, 054315 (1999).
- [36] K. Heyde and J.L. Wood, *J. Phys. G* **17**, 135-143 (1991).
- [37] M. Yamagami and N. Van Giai, *Phys. Rev. C* **69**, 034301 (2004).
- [38] R. Rodríguez-Guzmán, J.L. Egido, and L.M. Robledo, *Nucl. Phys. A* **709**, 201-235 (2002).
- [39] S. Péru, M. Girod, and J.F. Berger, *Eur. Phys. J. A* **9**, 35-47 (2000).
- [40] J. Terasaki, H. Flocard, P.-H. Heenen, and P. Bonche, *Nucl. Phys. A* **621**, 706-718 (1997).
- [41] P.-G. Reinhard, D.J. Dean, W. Nazarewicz, J. Dobaczewski, J.A. Maruhn, and M.R. Strayer, *Phys. Rev. C* **60**, 014316 (1999).
- [42] P. Fallon, E. Rodríguez-Vieitez, D. Bazin, C.M. Campbell, J.M. Cook, R.M. Clark, D.C. Dinca, A. Gade, T. Glasmacher, I.-Y. Lee, A.O. Macchiavelli, W.F. Mueller, S.G. Prussin, M. Wiedeking, and K. Yoneda, *J. Phys.: Conf. Ser.* **49**, 165-169 (2006).
- [43] Y. Yanagisawa, M. Notani, H. Sakurai, M. Kunibu, H. Akiyoshi, N. Aoi, H. Baba, K. Demichi, N. Fukuda, H. Hasegawa, Y. Higurashi, M. Ishihara, N. Iwasa, H. Iwasaki, T. Gomi, S. Kanno, M. Kurokawa, Y.U. Matsuyama, S. Michimasa, T. Minemura, T. Mizoi, T. Nakamura, A. Saito, M. Serata, S. Shimoura, T. Sugimoto, E. Takeshita, S. Takeuchi, K. Ue, K. Yamada, K. Yoneda, and T. Motobayashi, *Phys. Lett. B* **566**, 84-89 (2003).
- [44] P. Doornenbal, H. Scheit, N. Aoi, S. Takeuchi, K. Li, E. Takeshita, H. Wang, H. Baba, S. Deguchi, N. Fukuda, H. Geissel, R. Gernhäuser, J. Gibelin, I. Hachiuma, Y. Hara, C. Hinke, N. Inabe, K. Itahashi, S. Itoh, D. Kameda, S. Kanno, Y. Kawada, N. Kobayashi, Y. Kondo, R. Krücken, T. Kubo, T. Kuboki, K. Kusaka, M. Lantz, S. Michimasa, T. Motobayashi, T. Nakamura, T. Nakao, K. Namihiro, S. Nishimura, T. Ohnishi, M. Ohtake, N.A. Orr, H. Otsu, K. Ozeki, Y. Satou, S. Shimoura, T. Sumikama, M. Takechi, H. Takeda, K.N. Tanaka, K. Tanaka, Y. Togano, M. Winkler, Y. Yanagisawa, K. Yoneda, A. Yoshida, K. Yoshida, and H. Sakurai, *Phys. Rev. Lett.* **103**, 032501 (2009).
- [45] S. Ettenauer, H. Zwahlen, P. Adrich, D. Bazin, C.M. Campbell, J.M. Cook, A.D. Davies, D.-C. Dinca, A. Gade, T. Glasmacher, J.-L. Lecouey, W.F. Mueller, T. Otsuka, R.R. Reynolds, L.A. Riley, J.R. Terry, Y. Utsuno, and K. Yoneda, *Phys. Rev. C* **78**, 017302 (2008).
- [46] B.V. Pritychenko, T. Glasmacher, B.A. Brown, P.D. Cottle, R.W. Ibbotson, K.W. Kemper, L.A. Riley, and H. Scheit, *Phys. Rev. C* **63**, 011305(R) (2000).
- [47] G. Neyens, M. Kowalska, D. Yordanov, K. Blaum, P. Himpe, P. Lievens, S. Mallion, R. Neugart, N. Vermeulen, Y. Utsuno, and T. Otsuka, *Phys. Rev. Lett.* **94**, 022501 (2005).
- [48] F. Maréchal, D.L. Balabanski, D. Borremans, J.-M. Daugas, F. de Oliveira Santos, P. Dessagne, G. Georgiev, J. Giovino, S. Grévy, P. Himpe, C. Jollet, I. Matea, G. Neyens, F. Perrot, E. Poirier, O. Roig, M. Stanoiu, C. Stodel, J.-C. Thomas, K. Turzó, D. Yordanov, E. Caurier, F. Nowacki, and A. Poves, *Phys. Rev. C* **72**, 044314 (2005).
- [49] B.V. Pritychenko, T. Glasmacher, P.D. Cottle, R.W. Ibbotson, K.W. Kemper, L.A. Riley, A. Sakharuk, H. Scheit, M. Steiner, and V. Zelevinsky, *Phys. Rev. C* **65**, 061304(R) (2002).
- [50] T. Motobayashi, Y. Ikeda, K. Ieki, M. Inoue, N. Iwasa, T. Kikuchi, M. Kurokawa, S. Moriya, S. Ogawa, H. Murakami, S. Shimoura, Y. Yanagisawa, T. Nakamura, Y. Watanabe, M. Ishihara, T. Teranishi, H. Okuno, and R.F. Casten, *Phys. Lett. B* **346**, 9-14 (1995).
- [51] J.A. Church, C.M. Campbell, D.-C. Dinca, J. Enders, A. Gade, T. Glasmacher, Z. Hu, R.V.F. Janssens, W.F. Mueller, H. Olliver, B.C. Perry, L.A. Riley, and K.L. Yurkewicz, *Phys. Rev. C* **72**, 054320 (2005).
- [52] H. Iwasaki, T. Motobayashi, H. Sakurai, K. Yoneda, T. Gomi, N. Aoi, N. Fukuda, Z. Fülöp, U. Futakami, Z. Gacsi, Y. Higurashi, N. Imai, N. Iwasa, T. Kubo, M. Kunibu, M. Kurokawa, Z. Liu, T. Minemura, A. Saito, M. Serata, S. Shimoura, S. Takeuchi, Y.X. Watanabe, K. Yamada, Y. Yanagisawa, and M. Ishihara, *Phys. Lett. B* **522**, 227-232 (2001).
- [53] A. Gade, P. Adrich, D. Bazin, M.D. Bowen, B.A. Brown, C.M. Campbell, J.M. Cook, S. Ettenauer, T. Glasmacher, K.W. Kemper,

- S. McDaniel, A. Obertelli, T. Otsuka, A. Ratkiewicz, K. Siwek, J.R. Terry, J.A. Tostevin, Y. Utsuno, and D. Weisshaar, *Phys. Rev. Lett.* **99**, 072502 (2007).
- [54] Y. Utsuno, T. Otsuka, T. Glasmacher, T. Mizusaki, and M. Honma, *Phys. Rev. C* **70**, 044307 (2004).
- [55] H. Iwasaki, T. Motobayashi, H. Sakurai, K. Yoneda, T. Gomi, N. Aoi, N. Fukuda, Z. Fülöp, U. Futakami, Z. Gacsic, Y. Higurashi, N. Imai, N. Iwasa, T. Kubo, M. Kunibu, M. Kurokawa, Z. Liu, T. Minemura, A. Saito, M. Serata, S. Shimoura, S. Takeuchi, Y.X. Watanabe, K. Yamada, Y. Yanagisawa, and M. Ishihara, *Phys. Lett. B* **620**, 118-124 (2005).
- [56] B.V. Pritychenko, T. Glasmacher, P.D. Cottle, R.W. Ibbotson, K.W. Kemper, K.L. Miller, L.A. Riley, and H. Scheit, *Phys. Rev. C* **66**, 024325 (2002).
- [57] V. Tripathi, S.L. Tabor, C.R. Hoffman, M. Wiedeking, A. Volya, P.F. Mantica, A.D. Davies, S.N. Liddick, W.F. Mueller, A. Stolz, B.E. Tomlin, T. Otsuka, and Y. Utsuno, *Phys. Rev. C* **73**, 054303 (2006).
- [58] A.M. Hurst, C.Y. Wu, J.A. Becker, M.A. Stoyer, C.J. Pearson, G. Hackman, M.A. Schumaker, C.E. Svensson, R.A.E. Austin, G.C. Ball, D. Bandyopadhyay, C.J. Barton, A.J. Boston, H.C. Boston, R. Churchman, D. Cline, S.J. Colosimo, D.S. Cross, G. Demand, M. Djongolov, T.E. Drake, P.E. Garrett, C. Gray-Jones, K.L. Green, A.N. Grint, A.B. Hayes, K.G. Leach, W.D. Kulp, G. Lee, S. Lloyd, R. Maharaj, J.-P. Martin, B.A. Millar, S. Mythili, L. Nelson, P.J. Nolan, D.C. Oxley, E. Padilla-Rodal, A.A. Phillips, M. Porter-Peden, S.V. Rigby, F. Sarazin, C.S. Sumithrarachchi, S. Triambak, P.M. Walker, S.J. Williams, J. Wong, and J.L. Wood, *Phys. Lett. B* **674**, 168-171 (2009).
- [59] O. Niedermaier, H. Scheit, V. Bildstein, H. Boie, J. Fitting, R. von Hahn, F. Köck, M. Lauer, U.K. Pal, H. Podlech, R. Repnow, D. Schwalm, C. Alvarez, F. Ames, G. Bollen, S. Emhofer, D. Habs, O. Kester, R. Lutter, K. Rudolph, M. Pasini, P.G. Thirolf, B.H. Wolf, J. Eberth, G. Gersch, H. Hess, P. Reiter, O. Thelen, N. Warr, D. Weisshaar, F. Aksouh, P. Van den Bergh, P. Van Duppen, M. Huyse, O. Ivanov, P. Mayet, J. Van de Walle, J. Äystö, P.A. Butler, J. Cederkäll, P. Delahaye, H.O.U. Fynbo, L.M. Fraile, O. Forstner, S. Franchoo, U. Köster, T. Nilsson, M. Oinonen, T. Sieber, F. Wenander, M. Pantea, A. Richter, G. Schrieder, H. Simon, T. Behrens, R. Gernhäuser, T. Kröll, R. Krücken, M. Münch, T. Davinson, J. Gerl, G. Huber, A. Hurst, J. Iwanicki, B. Jonson, P. Lieb, L. Liljeby, A. Schempp, A. Scherillo, P. Schmidt, and G. Walter, *Phys. Rev. Lett.* **94**, 172501 (2005).
- [60] D. Kameda, H. Ueno, K. Asahi, M. Takemura, A. Yoshimi, T. Haseyama, M. Uchida, K. Shimada, D. Nagae, G. Kijima, T. Arai, K. Takase, S. Suda, T. Inoue, J. Murata, H. Kawamura, Y. Kobayashi, H. Watanabe, and M. Ishihara, *Phys. Lett. B* **647**, 93-97 (2007).
- [61] V. Tripathi, S.L. Tabor, P.F. Mantica, Y. Utsuno, P. Bender, J. Cook, C.R. Hoffman, S. Lee, T. Otsuka, J. Pereira, M. Perry, K. Pepper, J.S. Pinter, J. Stoker, A. Volya, and D. Weisshaar, *Phys. Rev. Lett.* **101**, 142504 (2008).
- [62] P. Himpe, G. Neyens, D.L. Balabanski, G. Bélier, J.M. Daugas, F. de Oliveira Santos, M. De Rydt, K.T. Flanagan, I. Matea, P. Morel, Y.E. Penionzhkevich, L. Perrot, N.A. Smirnova, C. Stodel, J.C. Thomas, N. Vermeulen, D.T. Yordanov, Y. Utsuno, and T. Otsuka, *Phys. Lett. B* **658**, 203-208 (2008).
- [63] B.V. Pritychenko, T. Glasmacher, B.A. Brown, P.D. Cottle, R.W. Ibbotson, K.W. Kemper, and H. Scheit, *Phys. Rev. C* **63**, 047308 (2001).
- [64] C. Détraz, M. Langevin, D. Guillemaud, M. Epherre, G. Audi, C. Thibault, and F. Touchard, *Nucl. Phys. A* **394**, 378-386 (1983).
- [65] N.A. Orr, W. Mittig, L.K. Fifield, M. Lewitowicz, E. Plagnol, Y. Schutz, Z.W. Long, L. Bianchi, A. Gillibert, A.V. Belozyorov, S.M. Lukyanov, Y.E. Penionzhkevich, A.C.C. Villari, A. Cunsolo, A. Foti, G. Audi, C. Stephan, and L. Tassan-Got, *Phys. Lett. B* **258**, 29-34 (1991).
- [66] B.V. Pritychenko, T. Glasmacher, P.D. Cottle, M. Fauerbach, R.W. Ibbotson, K.W. Kemper, V. Maddalena, A. Navin, R. Ronningen, A. Sakharuk, H. Scheit, and V.G. Zelevinsky, *Phys. Lett. B* **461**, 322-328 (1999).
- [67] V. Chisté, A. Gillibert, A. Lépine-Szily, N. Alamanos, F. Auger, J. Barrette, F. Braga, M.D. Cortina-Gil, Z. Dlouhy, V. Lapoux, M. Lewitowicz, R. Lichtenthäler, R. Liguori Neto, S.M. Lukyanov, M. MacCormick, F. Marie, W. Mittig, F. de Oliveira Santos, N.A. Orr, A.N. Ostrowski, S. Ottini, A. Pakou, Y.E. Penionzhkevich, P. Roussel-Chomaz, J.L. Sida, *Phys. Lett. B* **514**, 233-239 (2001).
- [68] O.T. Niedermaier, Doctoral Dissertation "Low-Energy Coulomb Excitation of the Neutron-Rich Mg Isotopes ^{30}Mg and ^{32}Mg ", University of Heidelberg (2005).
- [69] W. Schwerdtfeger, P.G. Thirolf, K. Wimmer, D. Habs, H. Mach, T.R. Rodriguez, V. Bildstein, J.L. Egido, L.M. Fraile, R. Gernhäuser, R. Hertenberger, K. Heyde, P. Hoff, H. Hübel, U. Köster, T. Kröll, R. Krücken, R. Lutter, T. Morgan, and P. Ring, *Phys. Rev. Lett.* **103**, 012501 (2009).
- [70] K. Wimmer, T. Kröll, R. Krücken, V. Bildstein, R. Gernhäuser, B. Bastin, N. Bree, J. Diriken, P. Van Duppen, M. Huyse, N. Patronis, P. Vermaelen, D. Voulot, J. Van de Walle, F. Wenander, L.M. Fraile, R. Chapman, B. Hadinia, R. Orlandi, J.F. Smith, R. Lutter, P.G. Thirolf, M. Labiche, A. Blazhev, M. Kalkühler, P. Reiter, M. Seidlitz, N. Warr, A.O. Macchiavelli, H.B. Jeppesen, E. Fiori, G. Georgiev, G. Schrieder, S. Das Gupta, G. Lo Bianco, S. Nardelli, J. Butterworth, J. Johansen, and K. Riisager, *Phys.*

- Rev. Lett. **105**, 252501 (2010).
- [71] K. Yoneda, H. Sakurai, T. Gomi, T. Motobayashi, N. Aoi, N. Fukuda, U. Futukami, Z. Gacsi, Y. Higurashi, N. Imai, N. Iwasa, H. Iwasaki, T. Kubo, M. Kunibu, M. Kurokawa, Z. Liu, T. Minemura, A. Saito, M. Serata, S. Shimoura, S. Takeuchi, Y.X. Watanabe, K. Yamada, Y. Yanagisawa, K. Yogo, A. Yoshida, and M. Ishihara, Phys. Lett. B **499**, 233-237 (2001).
 - [72] URL <http://www.nndc.bnl.gov/ensdf/>.
 - [73] B.H. Wildenthal, Prog. Part. Nucl. Phys. **11**, 5-51 (1984).
 - [74] G. Klotz, P. Baumann, M. Bounajma, A. Huck, A. Knipper, G. Walter, G. Marguier, C. Richard-Serre, A. Poves, and J. Retamosa, Phys. Rev. C **47**, 2502-2516 (1993).
 - [75] F. Maréchal, D.L. Balabanski, D. Borremans, J.-M. Daugas, F. de Oliveira Santos, P. Dessagne, G. Georgiev, J. Giovinozzo, S. Grévy, P. Himpe, C. Jollet, I. Matea, G. Neyens, F. Perrot, E. Poirier, O. Roig, M. Stanoiu, C. Stodel, J.-C. Thomas, K. Turzó, D. Yordanov, E. Caurier, F. Nowacki, and A. Poves, Phys. Rev. C **76**, 059902(E) (2007).
 - [76] M. Kimura, Phys. Rev. C **75**, 041302 (2007).
 - [77] H. Mach, L.M. Fraile, O. Tengblad, R. Boutami, C. Jollet, W.A. Plóciennik, D.T. Yordanov, M. Stanoiu, M.J.G. Borge, P.A. Butler, J. Cederkäll, P. Dessagne, B. Fogelberg, H. Fynbo, P. Hoff, A. Jokinen, A. Korgul, U. Köster, W. Kurcewicz, F. Maréchal, T. Motobayashi, J. Mrazek, G. Neyens, T. Nilsson, S. Pedersen, A. Poves, B. Rubio, and E. Ruchowska, Eur. Phys. J. A **25**, 105-109 (2005).
 - [78] D. Miller, P. Adrich, B.A. Brown, V. Moeller, A. Ratkiewicz, W. Rother, K. Starosta, J.A. Tostevin, C. Vaman, and P. Voss, Phys. Rev. C **79**, 054306 (2009).
 - [79] M. Keim, in "Proceeding of the International Conference on Exotic Nuclei and Atomic Masses (ENAM98)", AIP Conf. Proc. No. **455**, 50 (1998).
 - [80] M. Keim, U. Georg, A. Klein, R. Neugart, M. Neuroth, S. Wilbert, P. Lievens, L. Vermeeren, and B.A. Brown, Eur. Phys. J. A **8**, 31-40 (2000).
 - [81] V. Tripathi, S.L. Tabor, P.F. Mantica, C.R. Hoffman, M. Wiedeking, A.D. Davies, S.N. Liddick, W.F. Mueller, T. Otsuka, A. Stolz, B.E. Tomlin, Y. Utsuno, and A. Volya, Phys. Rev. Lett. **94**, 162501 (2005).
 - [82] M.W. Cooper, S.L. Tabor, T. Baldwin, D.B. Campbell, C. Chandler, C.R. Hoffman, K.W. Kemper, J. Pavan, A. Pipidis, M.A. Riley, and M. Wiedeking, Phys. Rev. C **65**, 051302(R) (2002).
 - [83] V. Tripathi, S.L. Tabor, P.F. Mantica, Y. Utsuno, P. Bender, J. Cook, C.R. Hoffman, Sangjin Lee, T. Otsuka, J. Pereira, M. Perry, K. Pepper, J.S. Pinter, J. Stoker, A. Volya, and D. Weisshaar, Phys. Rev. C **76**, 021301(R) (2007).
 - [84] G. Münzenberg, Nucl. Instrum. Methods **B70**, 265-275 (1992).
 - [85] H. Geissel, P. Armbruster, K.H. Behr, A. Brünle, K. Burkard, M. Chen, H. Folger, B. Franczak, H. Keller, O. Klepper, B. Langenbeck, F. Nickel, E. Pfeng, M. Pfützner, E. Roeckel, K. Rykaczewski, I. Schall, D. Schardt, C. Scheidenberger, K.-H. Schmidt, A. Schröter, T. Schwab, K. Sümmerer, M. Weber, G. Münzenberg, T. Brohm, H.-G. Clerc, M. Fauerbach, J.-J. Gaimard, A. Grewe, E. Hanelt, B. Knödler, M. Steiner, B. Voss, J. Weckenmann, C. Ziegler, A. Magel, H. Wollnik, J.P. Dufour, Y. Fujita, D.J. Vieira, and B. Sherrill, Nucl. Instrum. Methods B **70**, 286-297 (1992).
 - [86] O. Kofoed-Hansen and K.O. Nielsen, Phys. Rev. **82**, 96-97 (1951).
 - [87] M. Lindroos, Conference Proceedings of EPAC 2004, 45-49 (2004).
 - [88] D. Habs, O. Kester, T. Sieber, H. Bongers, S. Emhofer, P. Reiter, P.G. Thierolf, G. Bollen, J. Aystö, O. Forstner, H. Ravn, T. Nilsson, M. Oinonen, H. Simon, J. Cederkäll, F. Ames, P. Schmidt, G. Huber, L. Liljeby, O. Skeppstedt, K.G. Rensfelt, F. Wenander, B. Jonson, G. Nyman, R. von Hahn H. Podlech, R. Repnow, C. Gund, D. Schwalm, A. Schempp, K.-U. Kühnel, C. Welsch, U. Ratzinger, G. Walter, A. Huck, K. Kruglov, M. Huyse, P. Van den Bergh, P. Van Duppen, L. Weissman, A.C. Shotton, A.N. Ostrowski, T. Davinson, P.J. Woods, J. Cub, A. Richter, and G. Schrieder, Hyperfine Interact. **129**, 43-66 (2000).
 - [89] P. Gregers Hansen, History of CERN **3**, 327-413 (1996).
 - [90] C. Lefevre, ISOLDE brochure (English version), unpublished (2010).
 - [91] URL <http://isolde.web.cern.ch/ISOLDE/>.
 - [92] P. Van Duppen and K. Riisager, J. Phys. G: Nucl. Part. Phys. **38**, 024005 (2011).
 - [93] A. Gottberg, A. Andrighetto, P. Bricault, E. Cottureau, P. Delahaye, H. Franberg, F. Gramegna, I. Günther-Leopold, C. Jost, C. Lau, R. Luis, N. Lecesne, T. Marchi, M.G. St.-Laurant, M. Cheikh Mhamed, V. Panteleev, B. Roussiere, D. Scarpa, T. Stora, D. Stracener, and L. Tecchio, Conference Poster at ARIS 2011, unpublished (2011).
 - [94] B. Mustapha and J.A. Nolen, Nucl. Instrum. Methods B **204**, 286-292 (2003).
 - [95] U. Köster, Radiochim. Acta **89**, 749-756 (2001).
 - [96] U. Köster, Doctoral Dissertation "Ausbeuten und Spektroskopie radioaktiver Isotope bei LOHENGRIN und ISOLDE", TU Munich (2000).
 - [97] A.H.M. Evensen, R. Catherall, P. Drumm, P. Van Duppen, O.C. Jonsson, E. Kugler, J. Lettry, O. Tengblad, V. Tikhonov, and H.L. Ravn, Nucl. Instrum. Methods B **126**, 160-165 (1997).
 - [98] U. Köster, V.N. Fedoseyev, A.N. Andreyev, U.C. Bergmann, R. Catherall, J. Cederkäll, M. Dietrich, H. De Witte, D.V. Fedorov,

- L. Fraile, S. Franchoo, H. Fynbo, U. Georg, T. Giles, M. Gorska, M. Hannawald, M. Huyse, A. Joinet, O.C. Jonsson, K.L. Kratz, K. Kruglov, Ch. Lau, J. Lettry, V.I. Mishin, M. Oinonen, K. Partes, K. Peräjärvi, B. Pfeiffer, H.L. Ravn, M.D. Seliverstov, P. Thierolf, K. Van de Vel, P. Van Duppen, J. Van Roosbroeck, and L. Weissman, Nucl. Instrum. Methods B **204**, 347-352 (2003).
- [99] M.J. Dresser, J. Appl. Phys. **39**, 338-339 (1968).
- [100] V.I. Mishin, V.N. Fedoseyev, H.J. Kluge, V.S. Letokhov, H.L. Ravn, F. Scheerer, Y. Shirakabe, S. Sundell, and O. Tengblad, Nucl. Instrum. Methods B **73**, 550-560 (1993).
- [101] URL http://www.scholarpedia.org/article/The_ISOLDE_facility/.
- [102] E. Kugler, Hyperfine Interact. **129**, 23-42 (2000).
- [103] D. Habs, G. Correia, A. Jokinen, J. Lettry, M. Lindroos, E. Kugler, H. Raimbault-Hartmann, H.L. Ravn, O. Tengblad, P. Van Duppen, B. Jonson, P.G. Hansen, L. Liljeby, K.G. Rensfelt, R. Wyss, M. Grieser, T. Härtlein, R. von Hahn, C.M. Kleffner, P. Reiter, R. Repnow, D. Schwalm, P. Thierolf, H. Deitinghoff, A. Schempp, H. Backe, G. Bollen, G. Huber, K.L. Kratz, J. Kluge, U. Ratzinger, E. Nolte, J. de Boer, K.P. Lieb, M. Schumacher, G. Schrieder, P. Butler, P. Nolan, D. Warner, B. Gelletly, P. Baumann, Ph. Dessagne, A. Huck, A. Knipper, Ch. Miehé, G. Walter, G. Marguier, C. Richard-Serre, B. Visentin, J. Faure, E.D. Donets, E. Beebe, M. Huyse, D. Forkel, G. Sletten, and B. Herskind, Proposal to the ISOLDE Committee, CERN/ISC 94-25 ISC/P68, unpublished (1994).
- [104] O. Kester, T. Sieber, S. Emhofer, F. Ames, K. Reisinger, P. Reiter, P.G. Thierolf, R. Lutter, D. Habs, B.H. Wolf, G. Huber, P. Schmidt, A.N. Ostrowski, R. von Hahn, R. Repnow, J. Fitting, M. Lauer, H. Scheit, D. Schwalm, H. Podlech, A. Schempp, U. Ratzinger, O. Forstner, F. Wenander, J. Cederkäll, T. Nilsson, M. Lindroos, H. Fynbo, S. Franchoo, U. Bergmann, M. Oinonen, J. Äystö, P. Van den Bergh, P. Van Duppen, M. Huyse, N. Warr, D. Weisshaar, J. Eberth, B. Jonson, G. Nyman, M. Pantea, H. Simon, G. Schrieder, A. Richter, O. Tengblad, T. Davinson, P.J. Woods, G. Bollen, L. Weissmann, L. Liljeby, and K.-G. Rensfelt, Nucl. Instrum. Methods B **204**, 20-30 (2003).
- [105] F. Wenander, J. Inst. **5**, C10004 (2010).
- [106] R. Geller, Annu. Rev. Nucl. Sci. **40**, 15-44 (1990).
- [107] E.D. Donets, Rev. Sci. Instrum. **69**, 614-619 (1998).
- [108] P. Schmidt, F. Ames, G. Bollen, O. Forstner, G. Huber, M. Oinonen, and J. Zimmer, Nucl. Phys. A **701**, 550-556 (2002).
- [109] F. Ames, G. Bollen, P. Delahaye, O. Forstner, G. Huber, O. Kester, K. Reisinger, and P. Schmidt, Nucl. Instrum. Methods A **538**, 17-32 (2005).
- [110] A. Gustafsson, A. Herlert, and F. Wenander, Nucl. Instrum. Methods A **626-627**, 8-15 (2011).
- [111] F. Wenander, B. Jonson, L. Liljeby, and G. Nyman, CERN-OPEN-2000-320, unpublished (2000).
- [112] F. Wenander, Nucl. Phys. A **701**, 528-536 (2002).
- [113] R. Rao, O. Kester, T. Sieber, D. Habs, and K. Rudolph, Nucl. Instrum. Methods A **427**, 170-176 (1999).
- [114] J. Eberth, G. Pascovici, H.G. Thomas, N. Warr, D. Weißhaar, D. Habs, P. Reiter, P. Thierolf, D. Schwalm, C. Gund, H. Scheit, M. Lauer, P. Van Duppen, S. Franchoo, M. Huyse, R.M. Lieder, W. Gast, J. Gerl, and K.P. Lieb, Prog. Part. Nucl. Phys. **46**, 389-398 (2001).
- [115] V. Bildstein, R. Gernhäuser, Th. Kröll, R. Krücken, R. Raabe, and P. Van Duppen, Prog. Part. Nucl. Phys. **59**, 386-388 (2007).
- [116] A.N. Ostrowski, S. Cherubini, T. Davinson, D. Groombridge, A.M. Laird, A. Musumarra, A. Ninane, A. di Pietro, A.C. Shotton, and P.J. Woods, Nucl. Instrum. Methods A **480**, 448-455 (2002).
- [117] J. Cub, C. Gund, D. Pansegrau, G. Schrieder, and H. Stelzer, Nucl. Instrum. Methods A **453**, 522-524 (2000).
- [118] W. Weinzierl, Diploma Thesis "Isobarentrennung mit einer Braggkammer bei REX-ISOLDE", TU Munich (2006).
- [119] H. Bethe, Ann. Phys. (Leipzig) **397**, 325-400 (1930).
- [120] H. Ower, Doctoral Dissertation "High Spin States of ^{232}Th , ^{234}U and ^{236}U ", J.W. Goethe-University of Frankfurt a.M., unpublished (1980).
- [121] H. Ower, J. Gerl, and H. Scheit, "Multiple Coulomb Excitation Program CLX", computer code.
- [122] T. Czosnyka, D. Cline and C.Y. Wu, Bull. Am. Phys. Soc. **28**, 745 (1983).
- [123] T. Czosnyka, D. Cline and C.Y. Wu, Internal laboratory report UR/NSRL 308/1986, University of Rochester, unpublished (1986).
- [124] K. Alder, A. Bohr, T. Huus, B. Mottelson, and A. Winther, Rev. Mod. Phys. **28**, 432-542 (1956).
- [125] K. Alder and A. Winther, "Electromagnetic Excitation – Theorie of Coulomb Excitation with Heavy Ions", North-Holland Publishing Company, Amsterdam Oxford (1975).
- [126] D. Cline, Ann. Rev. Nucl. Part. Sci. **36**, 683-716 (1986).
- [127] R. Lutter, O. Schaile, K. Schöffel, K. Steinberger, and C. Broude, "MARaBQU – MBS and ROOT Based Online/Offline Utility", URL www.bl.physik.uni-muenchen.de/marabou/html/.
- [128] H.G. Essel and N. Kurz, "GSI Multi-Branch System", URL <http://www-wnt.gsi.de/daq/>.
- [129] R. Brun and F. Rademakers, "ROOT – A Data Analysis Framework", URL <http://root.cern.ch/>.
- [130] R.B. Firestone, Nucl. Data. Sheets **108**, 1-78 (2008).
- [131] J. Lettry, R. Catherall, P. Drumm, P. Van

- Duppen, A.H.M. Evensen, G.J. Focker, A. Jokinen, O.C. Jonsson, E. Kugler, and H. Ravn, *Nucl. Instrum. Methods B* **126**, 130-134 (1997).
- [132] J. Van de Walle, V. Bildstein, N. Bree, J. Cederkäll, P. Delahaye, J. Diriken, A. Ekström, V.N. Fedosseev, R. Gernhäuser, A. Gustafsson, A. Herlert, M. Huyse, O. Ivanov, T. Kröll, R. Krücken, B. Marsh, N. Patronis, P. Van Duppen, D. Voulot, N. Warr, F. Wenander, K. Wimmer, and S.M. Lenzi, *Eur. Phys. J. A* **42**, 401-406 (2009).
- [133] M. Kalkühler, Thesis submitted as part of the First State Examination “ γ -Spektroskopie von ^{31}Mg in inverser Kinematik”, University of Cologne (2008).
- [134] J. Blachot, *Nucl. Data Sheets* **107**, 355-506 (2006).
- [135] C.M. Mattoon, F. Sarazin, G. Hackman, E.S. Cunningham, R.A.E. Austin, G.C. Ball, R.S. Chakravarthy, P. Finlay, P.E. Garrett, G.F. Grinyer, B. Hyland, K.A. Koopmans, J.R. Leslie, A.A. Phillips, M.A. Schumaker, H.C. Scraggs, J. Schwarzenberg, M.B. Smith, C.E. Svensson, J.C. Waddington, P.M. Walker, B. Washbrook, and E. Zganjar, *Phys. Rev. C* **75**, 017302 (2007).
- [136] P.M. Endt, *At. Data Nucl. Data Tables* **55**, 171-197 (1993).
- [137] M. Shamsuzzoha Basunia, *Nucl. Data Sheets* **113**, 909-972 (2012).
- [138] J. Blachot, *Nucl. Data Sheets* **108**, 2035-2172 (2007).
- [139] K. Kitao, Y. Tendow, and A. Hashizume, *Nucl. Data Sheets* **96**, 241-390 (2002).
- [140] URL <http://bricc.anu.edu.au/>.
- [141] Z. Elekes, Z. Dombrádi, A. Saito, N. Aoi, H. Baba, K. Demichi, Z. Fülöp, J. Gibelin, T. Gomi, H. Hasegawa, N. Imai, M. Ishihara, H. Iwasaki, S. Kanno, S. Kawai, T. Kishida, T. Kubo, K. Kurita, Y. Matsuyama, S. Michimasa, T. Minemura, T. Motobayashi, M. Notani, T. Ohnishi, H.J. Ong, S. Ota, A. Ozawa, H.K. Sakai, H. Sakurai, S. Shimoura, E. Takeshita, S. Takeuchi, M. Tamaki, Y. Togano, K. Yamada, Y. Yanagisawa, and K. Yoneda, *Phys. Rev. C* **73**, 044314 (2006).
- [142] I. Hamamoto, *Phys. Rev. C* **76**, 054319 (2007).
- [143] A. Herlert and Y. Kadi, *J. Phys.: Conf. Ser.* **312**, 052010 (2011).
- [144] URL <http://hie-isolde.web.cern.ch/hie-isolde/>.
- [145] E. Siesling, Report at the 3rd HIE-ISOLDE Management meeting, CERN, unpublished (2012).
- [146] Y. Kadi, Report at the 3rd HIE-ISOLDE Management meeting, CERN, unpublished (2012).
- [147] N. Hinohara, K. Sato, K. Yoshida, T. Nakatsukasa, M. Matsuo, and K. Matsuyanagi, *Phys. Rev. C* **84**, 061302(R) (2011).
- [148] D.T. Yordanov, M. Kowalska, K. Blaum, M. De Rydt, K.T. Flanagan, P. Lievens, R. Neugart, G. Neyens, and H.H. Stroke, *Phys. Rev. Lett.* **99**, 212501 (2007).
- [149] G. Neyens, *Phys. Rev. C* **84**, 064310 (2011).
- [150] M. Kimura, arXiv:1105.3281v1.
- [151] V. Bildstein, R. Gernhäuser, T. Kröll, R. Krücken, K. Wimmer, P. Van Duppen, M. Huyse, N. Patronis, and R. Raabe, *Eur. Phys. J. A* **48**, 85 (2012).
- [152] H. Grawe, *Acta Phys. Pol. B* **34**, 2267-2276 (2003).
- [153] J.I. Prisciandaro, P.F. Mantica, B.A. Brown, D.W. Anthony, M.W. Cooper, A. Garcia, D.E. Groh, A. Komives, W. Kumarasiri, P.A. Lofy, A.M. Oros-Peusquens, S.L. Tabor, and M. Wiedeking, *Phys. Lett. B* **510**, 17-23 (2001).
- [154] H. Grawe, *Lect. Notes Phys.* **651**, 33-75 (2004).
- [155] T. Otsuka, T. Suzuki, R. Fujimoto, D. Abe, H. Grawe, Y. Akaishi, *Acta Phys. Pol. B* **36**, 1213-1220 (2005).
- [156] S.N. Liddick, P.F. Mantica, R.V.F. Janssens, R. Broda, B.A. Brown, M.P. Carpenter, B. Fornal, M. Honma, T. Mizusaki, A.C. Morton, W.F. Mueller, T. Otsuka, J. Pavan, A. Stolz, S.L. Tabor, B.E. Tomlin, and M. Wiedeking, *Phys. Rev. Lett.* **92**, 072501 (2004).
- [157] H. Grawe, K. Langanke, and G. Martínez-Pinedo, *Rep. Prog. Phys.* **70**, 1525-1582 (2007).
- [158] M. Honma, T. Otsuka, B.A. Brown, and T. Mizusaki, *Eur. Phys. J. A* **25**, 499-502 (2005).
- [159] E. Caurier, F. Nowacki, and A. Poves, *Eur. Phys. J. A* **15**, 145-150 (2002).
- [160] M. Honma, T. Otsuka, B.A. Brown, and T. Mizusaki, *Phys. Rev. C* **69**, 034335 (2004).
- [161] L. Coraggio, A. Covello, A. Gargano, and N. Itaco, *Phys. Rev. C* **80**, 044311 (2009).
- [162] S.M. Lenzi, F. Nowacki, A. Poves, and K. Sieja, *Phys. Rev. C* **82**, 054301 (2010).
- [163] K. Kaneko, Y. Sun, M. Hasegawa, and T. Mizusaki, *Phys. Rev. C* **78**, 064312 (2008).
- [164] A. Gade, R.V.F. Janssens, D. Bazin, R. Broda, B.A. Brown, C.M. Campbell, M.P. Carpenter, J.M. Cook, A.N. Deacon, D.-C. Dinca, B. Fornal, S.J. Freeman, T. Glasmacher, P.G. Hansen, B.P. Kay, P.F. Mantica, W.F. Mueller, J.R. Terry, J.A. Tostevin, and S. Zhu, *Phys. Rev. C* **74**, 021302(R) (2006).
- [165] M. Rejmund, S. Bhattacharyya, A. Navin, W. Mittig, L. Gaudefroy, M. Gelin, G. Mukherjee, F. Rejmund, P. Roussel-Chormaz, and C. Theisen, *Phys. Rev. C* **76**, 021304(R) (2007).
- [166] R.V.F. Janssens, B. Fornal, P.F. Mantica, B.A. Brown, R. Broda, P. Bhattacharyya, M.P. Carpenter, M. Cinausero, P.J. Daly, A.D. Davies, T. Glasmacher, Z.W. Grabowski, D.E. Groh, M. Honma, F.G. Kondev, W. Królas, T. Lauritsen, S.N. Liddick, S. Lunardi, N. Marginean, T. Mizusaki, D.J. Morrissey, A.C. Morton, W.F. Mueller, T. Otsuka, T. Pawlat, D. Seweryniak, H. Schatz, A. Stolz, S.L. Tabor, C.A. Ur, G. Viesti, I. Wiedenhöfer, and J. Wrzesiński, *Phys. Lett. B*

- 546, 55-62 (2002).
- [167] P.F. Mantica, A.C. Morton, B.A. Brown, A.D. Davies, T. Glasmacher, D.E. Groh, S.N. Liddick, D.J. Morrissey, W.F. Mueller, H. Schatz, A. Stolz, S.L. Tabor, M. Honma, M. Horoi, and T. Otsuka, *Phys. Rev. C* **67**, 014311 (2003).
 - [168] D.E. Appelbe, C.J. Barton, M.H. Muikku, J. Simpson, D.D. Warner, C.W. Beausang, M.A. Caprio, J.R. Cooper, J.R. Novak, N.V. Zamfir, R.A.E. Austin, J.A. Cameron, C. Malcolmson, J.C. Waddington, and F.R. Xu, *Phys. Rev. C* **67**, 034309 (2003).
 - [169] D.-C. Dinca, R.V.F. Janssens, A. Gade, D. Bazin, R. Broda, B.A. Brown, C.M. Campbell, M.P. Carpenter, P. Chowdhury, J.M. Cook, A.N. Deacon, B. Fornal, S.J. Freeman, T. Glasmacher, M. Honma, F.G. Kondev, J.-L. Lecouey, S.N. Liddick, P.F. Mantica, W.F. Mueller, H. Olliver, T. Otsuka, J.R. Terry, B.E. Tomlin, and K. Yoneda, *Phys. Rev. C* **71**, 041302(R) (2005).
 - [170] A. Bürger, T.R. Saito, H. Grawe, H. Hübel, P. Reiter, J. Gerl, M. Górska, H.J. Wollersheim, A. Al-Khatib, A. Banu, T. Beck, F. Becker, P. Bednarczyk, G. Benzoni, A. Bracco, S. Brambilla, P. Bringel, F. Camera, E. Clément, P. Doornenbal, H. Geissel, A. Görge, J. Grębosz, G. Hammond, M. Hellström, M. Honma, M. Kavatsyuk, M. Kmiecik, I. Kojouharov, W. Korten, N. Kurz, R. Lozeva, A. Maj, S. Mandal, B. Million, S. Muralithar, A. Neußer, F. Nowacki, T. Otsuka, Z. Podolyák, N. Saito, A.K. Singh, H. Weick, C. Wheldon, O. Wieland, and M. Winkler, *Phys. Lett. B* **622**, 29-34 (2005).
 - [171] B. Fornal, S. Zhu, R.V.F. Janssens, M. Honma, R. Broda, P.F. Mantica, B.A. Brown, M.P. Carpenter, P.J. Daly, S.J. Freeman, Z.W. Grabowski, N.J. Hammond, F.G. Kondev, W. Królas, T. Lauritsen, S.N. Liddick, C.J. Lister, E.F. Moore, T. Otsuka, T. Pawlat, D. Seweryniak, B.E. Tomlin, and J. Wrzesiński, *Phys. Rev. C* **70**, 064304 (2004).
 - [172] R. du Rietz, J. Ekman, D. Rudolph, C. Fahlander, A. Dewald, O. Möller, B. Saha, M. Axiotis, M.A. Bentley, C. Chandler, G. de Angelis, F. Della Vedova, A. Gadea, G. Hammond, S.M. Lenzi, N. Mărginean, D.R. Napoli, M. Nespolo, C. Rusu, and D. Tonev, *Phys. Rev. Lett.* **93**, 222501 (2004).
 - [173] A. Poves, F. Nowacki, and E. Caurier, *Phys. Rev. C* **72**, 047302 (2005).
 - [174] T.R. Rodriguez and J.L. Egido, *Phys. Rev. Lett.* **99**, 062501 (2005).
 - [175] A. Gavron, *Phys. Rev. C* **21**, 230-236 (1980).
 - [176] A. Dewald, in "Proceedings: The '98 Seminar on Nuclear Physics with Radioactive Ion Beam and High Spin Nuclear Structure, Lanzhou, China", Atomic Energy Press, Beijing (1999).
 - [177] J. Eberth, H.G. Thomas, P. Von Brentano, R.M. Lieder, H.M. Jäger, H. Kämmerling, M. Berst, D. Gutknecht, and R. Henck, *Nucl. Instrum. Methods A* **369**, 135-140 (1996).
 - [178] A. Dewald, S. Harissopulos, and P. von Brentano, *Z. Phys. A* **334**, 163-175 (1989).
 - [179] G. Böhm, A. Dewald, P. Petkov, and P. von Brentano, *Nucl. Instrum. Methods A* **329**, 248-261 (1993).
 - [180] D. Bazin, O. Tarasov, M. Lewitowicz, and O. Sorlin, *Nucl. Instrum. Methods A* **482**, 307-327 (2002).
 - [181] O. Tarasov and D. Bazin, *Nucl. Phys. A* **746**, 411-414 (2004).
 - [182] B. Saha, A. Dewald, O. Möller, R. Peusquens, K. Jessen, A. Fitzler, T. Klug, D. Tonev, P. von Brentano, J. Jolie, B.J.P. Gall, and P. Petkov, *Phys. Rev. C* **70**, 034313 (2004).
 - [183] J. Morel, S. Sepman, M. Rasko, E. Terechtchenko, and J.U. Delgado, *Appl. Radiat. Isotopes* **60**, 341-346 (2004).
 - [184] P. Petkov, *Nucl. Instrum. Methods A* **349**, 289-291 (1994).
 - [185] B. Saha, "Napatau – or Tk-Lifetime-Analysis", Institut für Kernphysik der Universität zu Köln, unpublished (2003).
 - [186] J. Huo and S. Huo, *Nucl. Data Sheets* **107**, 1393-1530 (2006).
 - [187] J. Huo, S. Huo, and C. Ma, *Nucl. Data Sheets* **108**, 773-882 (2007).
 - [188] E. Caurier and F. Nowacki, (to be published) private communication (2006).
 - [189] W. Rother, A. Dewald, H. Iwasaki, S.M. Lenzi, K. Starosta, D. Bazin, T. Baugher, B.A. Brown, H.L. Crawford, C. Fransen, A. Gade, T.N. Ginter, T. Glasmacher, G.F. Grinyer, M. Hackstein, G. Ilie, J. Jolie, S. McDaniel, D. Miller, P. Petkov, T. Pissulla, A. Ratkiewicz, C.A. Ur, P. Voss, K.A. Walsh, D. Weisshaar, and K.O. Zell, *Phys. Rev. Lett.* **106**, 022502 (2011).
 - [190] L. Grodzins, *Phys. Lett.* **2**, 88-91 (1962).

Acknowledgments

My gratitude goes to many people, who gave support to this thesis and made it a success:

my supervisor Prof. P. Reiter for giving me the great opportunity to work in this exciting field of nuclear structure physics. Many results of this work originate from fruitful discussions with him and his colleagues;

Dr. O. Möller, Dr. D. Mücher, and Dr. J. Van de Walle for their effort and patience to explain all the steps of careful data analysis;

Dr. F. Wenander, D. Voulot and E. Piselli – representative for the REX-ISOLDE collaboration – for the challenging preparation of the radioactive ion beams and its operation day and night;

L. Steinert, O. Rudolph, and U. Werner for operating the Cologne tandem accelerator;

Dr. N. Warr, Dr. J. Pakarinen, Dr. C. Fransen, Dr. T. Davinson, R. Lutter, Dr. H. Hess, and Dr. H. De Witte, preparing the experimental setups at CERN and Cologne;

Dr. K.O. Zell, as well as the personnel of the target labs of the TU Munich and GSI, for the preparation of the targets;

Dr. A. Blazhev, Dr. V. Bildstein, N. Bree, Dr. B. Bruyneel, S. Christen, Dr. E. Clément, Dr. D.D. DiJulio, Dr. J. Diriken, Dr. A. Ekstrøm, F. Finke, Dr. L.P. Gaffney, Dr. K. Geibel, A. Holler, Dr. G. Ilie, N. Kesteloot, Dr. T. Kotthaus, Prof. T. Kröll, Dr. P. Kudejová, Dr. B. Melon, Dr. J.-M. Régis, Dr. B. Saha, Dr. M. Scheck, B. Siebeck, Dr. I. Stefanescu, J. Taprogge, Dr. A. Wendt, Dr. A. Wiens, Dr. K. Wimmer, and Dr. K. Wrzosek-Lipska for taking shifts during the different experiments at CERN and Cologne;

Prof. H. Grawe and Prof. S.M. Lenzi performing shell model calculations included in this work;

Prof. P.A. Butler, Prof. J. Cederkäll, Dr. A. Dewald, Prof. L.M. Fraile, Prof. R. Gernhäuser, Prof. M. Huyse, Prof. J. Jolie, Prof. R. Krücken, Prof. P. Van Duppen, and Prof. P. von Brentano for their critical questions and constructive input to the publications, which are part of this thesis;

all present and former colleagues of the working group of Prof. P. Reiter and all members of the Institute for Nuclear Physics of the University of Cologne: Thank you for being such good colleagues.

Special thanks go to my wife Marijke and my family, giving support in all my studies, especially during the last months of my work on this doctoral thesis. I know that these have been stressful and busy times for you. I love you.

This work has been supported by the German BMBF under contracts 06K-167, 06KY205I, 05P09PKCI5, and 05P12PKFNE, by the EUROpean Nuclear Structure Integrated Infrastructure Initiative (EURONS, RII3-CT-2004-506065), and by the European Nuclear Science and Applications Research (ENSAR) under project number 262010.

Erklärung

Ich versichere, dass ich die von mir vorgelegte Dissertation selbstständig angefertigt, die benutzten Quellen und Hilfsmittel vollständig angegeben und die Stellen der Arbeit – einschließlich Tabellen, Karten und Abbildungen –, die anderen Werken im Wortlaut oder dem Sinn nach entnommen sind, in jedem Einzelfall als Entlehnung kenntlich gemacht habe; dass diese Dissertation noch keiner anderen Fakultät oder Universität zur Prüfung vorgelegen hat; dass sie – abgesehen von unten angegebenen Teilpublikationen – noch nicht veröffentlicht worden ist sowie, dass ich eine solche Veröffentlichung vor Abschluss des Promotionsverfahrens nicht vornehmen werde. Die Bestimmungen dieser Promotionsordnung sind mir bekannt. Die von mir vorgelegte Dissertation ist von Prof. Dr. P. Reiter betreut worden.

Köln, 29.10.2012

Michael Seidlitz

Teilpublikationen:

M. Seidlitz, D. Mücher, P. Reiter, V. Bildstein, A. Blazhev, N. Bree, B. Bruyneel, J. Cederkäll, E. Clément, T. Davinson, P. Van Duppen, A. Ekstrøm, F. Finke, L.M. Fraile, K. Geibel, R. Gernhäuser, H. Hess, A. Holler, M. Huyse, O. Ivanov, J. Jolie, M. Kalkühler, T. Kotthaus, R. Krücken, R. Lutter, E. Piselli, H. Scheit, I. Stefanescu, J. Van de Walle, D. Voulot, N. Warr, F. Wenander, and A. Wiens

Coulomb excitation of ^{31}Mg

Physics Letters B **700**, 181-186 (2011).

M. Seidlitz, P. Reiter, A. Dewald, O. Möller, B. Bruyneel, S. Christen, F. Finke, C. Fransen, M. Górska, H. Grawe, A. Holler, G. Ilie, T. Kotthaus, P. Kudejová, S.M. Lenzi, S. Mandal, B. Melon, D. Mücher, J.-M. Régis, B. Saha, P. von Brentano, A. Wiens, and K.O. Zell

Precision lifetime measurements of the first 2^+ and 4^+ states in ^{56}Cr at the $N=32$ subshell closure

Physical Review C **84**, 034318 (2011).

Curriculum vitae

Personalia

Name: Michael Seidlitz
Geburtsdatum: 8. Dezember 1982
Geburtsort: Hachenburg
Eltern: Klaus Seidlitz
Margit Seidlitz, geb. Siegmund
Familienstand: verheiratet
Staatsangehörigkeit: Deutsch

Schul Ausbildung

08/1989 – 07/1993 Grundschule Wolfsteinschule, Bad Marienberg
08/1993 – 07/1996 Privates Gymnasium Marienstatt
08/1996 – 06/2002 Städtisches Hölderlin-Gymnasium, Köln
Abschluss mit Abitur

Hochschulstudium

10/2001 – 09/2002 Vorlesungen und Übungen zu Physik I + II
im Rahmen der Teilnahme am Projekt „Schüler an der Universität“ der
Hochbegabtenstiftung der Kreissparkasse Köln und der Universität zu Köln
10/2002 Immatrikulation an der Universität zu Köln
im Diplomstudiengang Physik
04/2005 Abschluss des Vordiploms im Fach Physik
10/2008 Verleihung des Diploms im Fach Physik
Thema der Diplomarbeit: „Coulomb-Anregung von instabilen, ungeraden
Mg-Isotopen“
seit 11/2008 Promotionsstudium am Institut für Kernphysik der Universität zu Köln

Arbeitsverhältnisse

01/2005 – 10/2008 Studentische Hilfskraft
am Institut für Kernphysik der Universität zu Köln
seit 11/2008 Wissenschaftlicher Mitarbeiter
am Institut für Kernphysik der Universität zu Köln